Doctoral Thesis

Layered perovskites as electrocatalysts for energy conversion and storage systems

Areum Jun

Department of Energy Engineering

(Energy Engineering)

Graduate School of UNIST

2017

Layered perovskites as electrocatalysts for energy conversion and storage systems

Areum Jun

Department of Energy Engineering
(Energy Engineering)

Graduate School of UNIST

Layered perovskites as electrocatalysts for energy conversion and storage systems

A dissertation
submitted to the Graduate School of UNIST
in partial fulfillment of the
requirements for the degree of
Doctor of Philosophy

Areum Jun

1. 11. 2017
Approved by

Advisor
Prof. Guntae Kim

Layered perovskites as electrocatalysts for energy conversion and storage systems

Areum Jun

This certifies that the dissertation of Areum Jun is approved.

1. 11. 2017

signature

Advisor: Guntae Kim

signature

Jong-Beom Baek

signature

Hyun-Kon Song

signature

JunHee Lee

signature

Jeeyoung Shin

Abstract

With growing concerns over energy and environmental issues, sustainable and environmentally-friendly energy conversion and storage devices have received significant attention from both the academic and industrial communities. Solid oxide fuel cells (SOFCs) and solid oxide electrolysis cells (SOECs), which are collectively referred to as solid oxide cells (SOCs), are attractive energy conversion and storage systems with high energy conversion efficiency and environmental benefits. SOFCs, which directly convert chemical energy (such as H_2, CH_4, C_3H_8, *etc*) into electricity, represent an efficient alternative combustion system for the production of electricity. Similarly, SOECs, which convert water to hydrogen, are a clean and efficient hydrogen production system.

Ideally, SOFCs and SOECs should meet several criteria, such as high performance, long term stability, and relatively inexpensive cost. However, the operation of SOFCs and SOECs still accompanies several problems, especially in relation to the electrode materials. Conventional electrode materials suffer from insufficient performance, performance degradation, redox instability, coarsening, electrode delamination, and the formation of a secondary phase. In this regard, the development of electrode materials with both high conductivity and high and stable electrocatalytic activity is a vital step for the commercialization of SOFCs and SOECs.

This dissertation focuses on layered perovskite based electrode materials for SOFCs and SOECs with an aim to overcome the problems noted above. These materials show outstanding performance and stability with fast electrochemical reaction kinetics.

I first discuss basic principles and present a theoretical overview of solid oxide fuel cells and solid oxide electrolysis cells in chapter 1 and then describe the experimental techniques for the fabrication and characterization of electrode materials for SOFCs and SOECs in chapter 2. Finally, my research papers on the properties of electrode materials for SOFCs and SOECs are presented as outlined below,

1. Thermodynamic and electrical properties of $Ba_{0.5}Sr_{0.5}Co_{0.8}Fe_{0.2}O_{3-\delta}$ and $La_{0.6}Sr_{0.4}Co_{0.2}Fe_{0.8}O_{3-\delta}$ for intermediate-temperature solid oxide fuel cells.
2. Optimization of Sr content in layered $SmBa_{1-x}Sr_xCo_2O_{5+\delta}$ perovskite cathodes for intermediate-temperature solid oxide fuel cells.
3. High redox and performance stability of layered $SmBa_{0.5}Sr_{0.5}Co_{1.5}Cu_{0.5}O_{5+\delta}$ perovskite cathodes for intermediate-temperature solid oxide fuel cells.
4. Electrochemical properties of B-site Ni-doped layered perovskite cathodes for IT-SOFCs.
5. Correlation between fast oxygen kinetics and enhanced performance in Fe doped layered perovskite cathode for solid oxide fuel cells.
6. Achieving high efficiency and eliminating degradation in solid oxide electrochemical cells by

using high oxygen capacity perovskite.

7. Novel hydrogen production system: Dual Solid Oxide Electrolyzer.

Contents

List of Figures

List of Tables

Chapter 1. Introduction

1.1 Motivation and Research Objective

In recently years, there has been strong interest in clean and sustainable energy conversion and storage devices with high efficiency, low cost, and low pollutants due to the growing global energy demand related with the finite fossil fuels and related environmental problems.[1] One promising energy conversion and storage device is the solid oxide cell (SOC), which can operate in two ways – as fuel cells, converting fuels to electricity, and as electrolysis cells, producing fuels from electricity.

Ideally, SOCs should meet several criteria, such as high performance, long term stability, and relatively inexpensive cost. However, the operation of SOCs still accompanies several problems, especially in relation to the electrode materials. Conventional electrode materials suffer from insufficient performance, performance degradation, redox instability, coarsening, electrode delamination, and the formation of a secondary phase. In this regard, the development of electrode materials with both high conductivity and high and stable electrocatalytic activity is a vital step for the commercialization of SOCs. Therefore, my research has focused on the development and investigation of layered perovskites as robust electrode materials with outstanding electrocatalytic activity and high efficiency to overcome limitations of current SOCs.

Chapter 2 gives a detailed description of material preparation and experimental techniques, including the structural, electrical, electrochemical, redox properties.

Chapter 3 deals with thermodynamic and electrical properties of $Ba_{0.5}Sr_{0.5}Co_{0.8}Fe_{0.2}O_{3-\delta}$ (BSCF) and $La_{0.6}Sr_{0.4}Co_{0.2}Fe_{0.8}O_{3-\delta}$ (LSCF) for solid oxide fuel cells. The variation of oxygen non-stoichiometry and its effect on the electrical conductivity of the BSCF and LSCF were investigated by coulometric titration in a wide range of $p(O_2)$.

Chapter 4 reports the optimization of Sr content in layered $SmBa_{1-x}Sr_xCo_2O_{5+\delta}$ perovskite cathodes for intermediate-temperature solid oxide fuel cells. $SmBa_{1-x}Sr_xCo_2O_{5+\delta}$ is optimized at $x = 0.75$ in terms of obtaining the best performance for IT-SOFCs.

Chapter 5 shows the high redox and performance stability of layered $SmBa_{0.5}Sr_{0.5}Co_{1.5}Cu_{0.5}O_{5+\delta}$ perovskite cathodes for intermediate-temperature solid oxide fuel cells. $SmBa_{0.5}Sr_{0.5}Co_{1.5}Cu_{0.5}O_{5+\delta}$ presents reduced coefficients of thermal expansion and enhanced redox and performance stability, as well as suitable electrical conductivity and electrochemical performance under typical fuel cell operating conditions.

Chapter 6 presents electrochemical properties of B-site Ni-doped layered $SmBa_{0.5}Sr_{0.5}Co_2O_{5+\delta}$ perovskite cathodes for IT-SOFCs.

Chapter 7 discusses correlation between fast oxygen kinetics and enhanced performance in Fe

doped layered perovskite cathode for solid oxide fuel cells. The optimal Fe substitution shows the enhanced performance, high redox stability, and satisfactory electrical properties due to its fast oxygen kinetics under operating conditions.

Chapter 8 reports achieving high efficiency and eliminating degradation in solid oxide electrochemical cells by using high oxygen capacity perovskite. I firstly design and demonstrate the SOEC using layered perovskites as both-side electrodes.

Finally, in chapter 9, a novel hydrogen production system: Dual Solid Oxide Electrolyzer is demonstrated.

1.2 Solid Oxide Fuel Cell and Solid Oxide Electrolysis Cell Overview

1.2.1 General Fuel Cell

With the growing concerns regarding energy crisis and environmental issues, sustainable and environmentally-friendly energy conversion and storage devices such as solar cells, fuel cells, batteries, and capacitors have received great attention from both the academic and industrial communities.[1,2] Among these devices, fuel cells, which convert chemical energy directly into electrical energy, have been heralded recently as a keystone of the future energy economy due to their high efficiency and low emission of pollutants.[3] There are mainly five types of fuel cells depending on their electrolyte as shown in Figure 1.1:

(1) Phosphoric acid fuel cell (PAFC)
(2) Polymer electrolyte membrane fuel cell (PEMFC)
(3) Alkaline fuel cell (AFC)
(4) Molten carbonate fuel cell (MEFC)
(5) Solid oxide fuel cell (SOFC)

	PEMFC (Polymer Electrolyte Membrane Fuel Cell)	DMFC (Direct Methanol Fuel Cell)	AFC (Alkaline Fuel Cell)	PAFC (Phosphoric Acid Fuel Cell)	MCFC (Molten Carbonate Fuel Cell)	SOFC (Solid Oxide Fuel Cell)
Electrolyte	Polymer membrane	Polymer membrane	Alkali	Phosphoric acid	Molten carbonate	Ceramic
Mobile ion	H^+	H^+	OH^-	H^+	CO_3^{2-}	O^{2-}
Operating temperature (°C)	50 - 100	50 - 110	50 - 200	150 - 200	600 - 700	600 - 1000
Efficiency (%)	45 - 60	40	45 - 60	35 - 40	45 - 60	50 - 65
Cell components	Carbon based	Carbon based	Carbon based	Carbon based	Stainless based	Ceramic based
Fuel	Hydrogen	Methanol	Hydrogen	Hydrogen	Hydrogen or methane	Hydrogen, Hydrocarbon based fuel (CH_4, C_3H_8, JP-8)
Possible application	Backup power, Portable power, Vehicles	Potable electronic systems, mobile electronic devices	Military, Space	Distributed generation system	Electric utility, Distributed generation system	Auxiliary power, Electric utility, Distributed generation system, Transportation

Figure 1.1 Summary of fuel cell types.

They operate at different temperature regimens, incorporate different materials, and often differ in their fuel tolerance and performance properties. AFCs, PEMFCs, PAFCs essentially require pure hydrogen to be supplied to the fuel electrode. Therefore, to use hydrocarbon or alcohol fuels, an external fuel reformer and purification system are incorporated into the fuel cell system. This part leads to not only the increase of the complexity and cost but also the decrease of the total efficiency. In contrast, MCFCs and SOFCs operating at higher temperatures have the advantage that both hydrocarbon and

hydrogen can be electrochemically oxidized at the fuel electrode. Accordingly, the fuel-processing reaction can be accomplished without external reformer system, which allows to enhance efficiencies (~50%).[4] Among those types of fuel cells, SOFCs is one of the most promising fuel cell with the high energy conversion efficiency and the excellent flexibility to utilize a wide range of fuels such as hydrogen, syngas, bio-gas, and coal gas.[5]

1.2.2 Operating Principle of SOFCs

A schematic diagram of a typical SOFC is shown in Figure 1.2. SOFCs is made up of three major components: a ceramic dense electrolyte, an anode, and a cathode. The ceramic electrolyte separates each electrodes fed with different gases, is ionically conductive and is electronically insulating. The dense electrolyte could provide high stability in the reducing and oxidizing atmospheres and structural and chemical compatibility with electrode materials. The anode should be able to undergo the highly reducing conditions, while the cathode must be stable in the highly oxidizing environment under a high operating temperature.

When air is supplied to the cathode side, oxygen from the air reduced to oxygen anions (O^{2-}) which is transported to anode through the electrolyte. And then, at the anode side, the oxygen anions react with the fuel to produce electrons and water. The reactions in the anode and cathode sides are:[6]

$$O_2 + 4e^- \rightarrow 2O^{2-} \qquad \text{Eqn. 1.1}$$

$$H_2 + O^{2-} \rightarrow \ H_2O + 2e^- \qquad \text{Eqn. 1.2}$$

The difference in oxygen chemical potential between the anode and cathode sides leads to an electromotive force, and this force can be used to generate power when the electrodes are connected to an external circuit.[7]

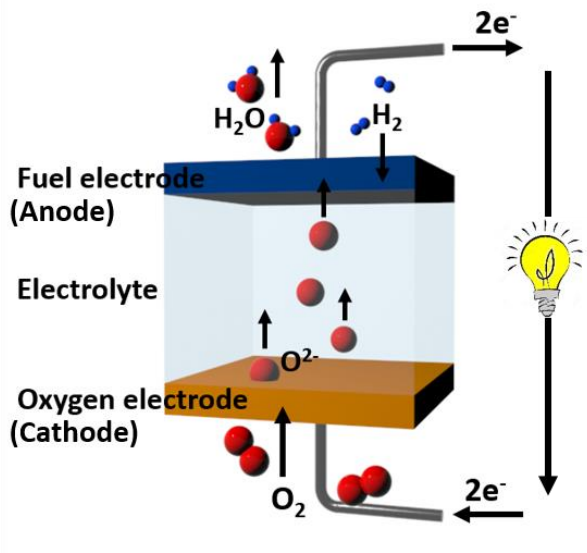

Figure 1.2 Schematic diagram of typical SOFCs.

1.2.3 Operating Principle of SOECs

The SOFC is known to be reversible, *i.e.*, it can be operated under dual modes: electricity generation mode and electrolysis mode. In electricity generation mode, SOFCs convert the chemical energy in fuel to electricity. Reversibly, in electrolysis modes, SOFCs act as an electrolyzer (referred to as solid oxide electrolysis cells or SOECs) convert the electrical energy to hydrogen through water electrolysis.[8-10] As shown in Figure 1.3, in SOECs, hydrogen is produced from water with electrons at the fuel electrode (cathode) side, and then oxygen anions (O^{2-}) pass through the electrolyte toward the air electrode (anode) side. These anions are oxidized to oxygen gas to complete the reaction. The reactions in the fuel and the air electrode can be expressed as:[11]

$$H_2O + 2e^- \rightarrow H_2(g) + O^{2-} \qquad \text{Eqn. 1.3}$$

$$O^{2-} \rightarrow \frac{1}{2}O_2(g) + 2e^- \qquad \text{Eqn. 1.4}$$

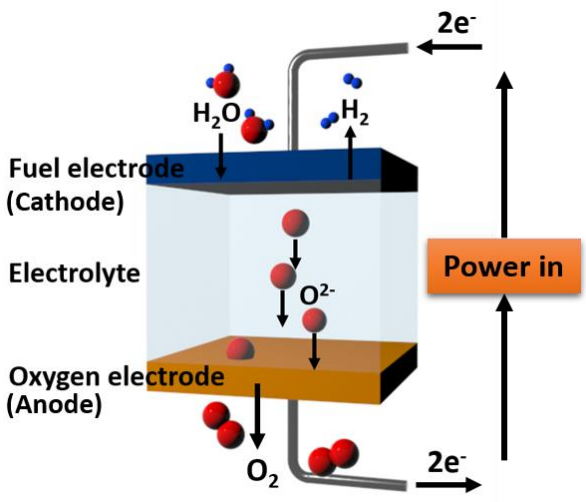

Figure 1.3 Scheme of the working mechanism of typical SOECs.

SOFCs and SOECs, which are referred to as solid oxide cells (SOCs), are considered as a highly promising technology for the future energy economy.[12-14]

1.3 Theoretical Background of SOFCs and SOECs

1.3.1. Performance of SOCs

The performance of fuel cells can be summarized with a graph of current-voltage characteristics called a current-voltage (*I-V*) curve. An ideal fuel cell would supply any amount of current, while retaining a constant voltage predicted by thermodynamics. But, the actual voltage of real fuel cell is lower than the ideal voltage because of unavoidable losses such as electrolyte thickness, operating temperature, electrode/electrolyte materials, electrode microstructure and gas flow rate. The difference between the actual voltage (E_{act}) and the theoretical voltage (E_{th}) can be defined as polarization or over-potential (η).[15]

$$\eta = E_{act} - E_{th} \qquad \text{Eqn. 1.4}$$

Figure 1.4 shows a typical current-voltage (*I-V*) curve in fuel cell. There are various kinds of polarization losses in fuel cell and are composed of three major contributions caused by following factors:

- Activation polarization (η_{act})
- Ohmic polarization (η_{ohmic})
- Concentration polarization (η_{conc})

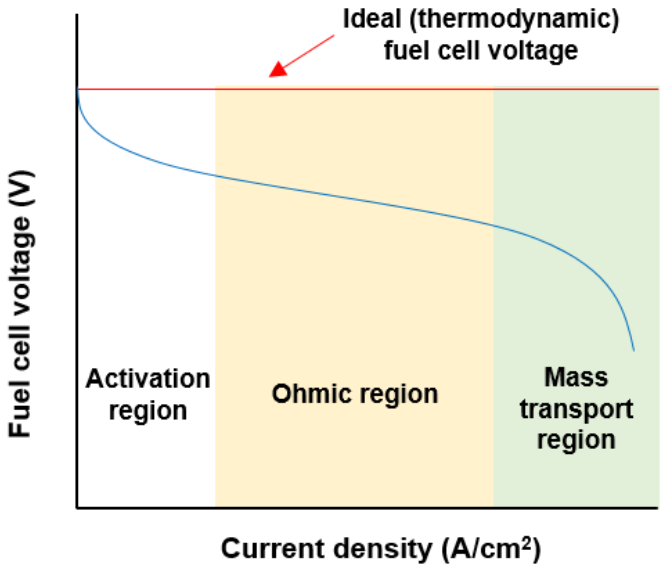

Figure 1.4 Scheme of typical *I-V* curve in fuel cell.

The activation polarization (or charge transfer polariazation, η_{act}) is associated with the rate determining step, charge transfer or the surface exchange reactions in the electrode. For the electrode reaction, the activation polarization is interpreted as the overpotential consumed to deliver the activation energy for the redox reactions in the electrode. The activation polarization (η_{act}) can be derived from the Butler-Volmer equation as follows:

$$i = i_0 \left[\exp\left(\frac{(1-\alpha)nF\eta_{act}}{RT}\right) - \exp\left(\frac{-\alpha nF\eta_{act}}{RT}\right)\right] \quad \text{Eqn. 1.5}$$

where i_0 is the exchange current density, α is the charge transfer coefficient, and η is the overpotential to drive the reaction. When the irreversibility is small, Eqn 1.5 is generalized in the form as the Tefel equation:

$$\eta_{act} = a \pm b \log i \quad \text{Eqn. 1.6}$$

It is known as the Tafel equation, and b is called the Tafel slope which related to the catalytic activity; a smaller slope indicates the better catalytic activity.

The ohmic polarization (or *IR* drop, η_{ohmic}) arises from electrical resistances of cell components including the electrolyte, electrode, interface between electrodes and electrolyte, and wire in the external circuit. Among them, the electrolyte, which is generally pure ionic conductor, contributes to the large portion of ohmic polarization.[16]

$$\eta_{ohmic} = I \cdot R_{tot} \quad \text{Eqn. 1.7}$$

The concentration polarization (or mass transfer polarization, η_{conc}) is caused by the transport limitation of the reactant approaching the reaction site and the product leaving the reaction site.[17] The concentration polarization can be expresses as:

$$\eta_{conc} = \frac{RT}{nF}\ln\left(1 - \frac{i}{i_l}\right) \quad \text{Eqn. 1.7}$$

where i_l is described as the limiting current at which the reactant concentration is near zero at the electrode/electrolyte interfaces.

Therefore, the total polarization (η_{Total}) in the fuel cell is the sum of these three polarization as

$$\eta_{Total} = \eta_{act} + \eta_{ohmic} + \eta_{conc} \quad \text{Eqn. 1.8}$$

1.3.2. Thermodynamics of SOFCs

A SOFC system converts directly the Gibbs free enthalpy of the combustion reaction for a fuel and an air into electricity. The first and the second law of thermodynamics could explain a reversible fuel cell, while the second low governs the reversibility of the transport processes in particular. The first law of the thermodynamics expressed by the equation[18]

$$q + w = \Delta H \qquad \text{Eqn. 1.9}$$

The molar reaction enthalpy ΔH of the oxidation consists of work (w) and heat energy (q). The second law of thermodynamics applied on reversible processes yields

$$\oint \Delta S = 0 \rightarrow q = q_{rev} = T\Delta S \qquad \text{Eqn. 1.10}$$

where the reversible heat exchange with the environment equalizes the generated reaction entropy. This allow to rewrite as below

$$q_{rev} + w_{rev} = \Delta H \qquad \text{Eqn. 1.11}$$

The reaction entropy (ΔS) is a result of different opportunities of the species to save thermal energy between the absolute zero level of temperature and temperature level of the reactor.

From Eqns. (1.10) and (1.11),

$$w_{rev} = \Delta H - T\Delta S \qquad \text{Eqn. 1.12}$$

Using the ambient temperature as a reference for the calculation of the Gibbs free energy (ΔG), the reversible work of the reaction (w_{rev}) is the equal to the Gibbs free energy of the reaction

$$w_{rev} = \Delta G = \Delta H - T\Delta S \qquad \text{Eqn. 1.13}$$

From the first and second laws of thermodynamics, the energy transfer from one form to another can be identified through thermodynamic potentials. When combine the first and the second laws of thermodynamics, an equation for internal energy (U) is derived from the variation of two independent variables of entropy (S) and volume (V) :[19]

$$dU = TdS - pdV \quad \text{Eqn. 1.14}$$

Tds is the reversible heat transfer and *pdV* represents the mechanical work. The following relations explain how the dependent variables (*T* and *p*) are associated with variations in the independent variables (*S* and *V*):

$$\left(\frac{dU}{dS}\right)_v = T \quad \text{Eqn. 1.15}$$

$$\left(\frac{dU}{dV}\right)_s = -p \quad \text{Eqn. 1.16}$$

A transformation of U using a *Legendre transform* starts with defining the new thermodynamic potential *G* (*T, p*) as follows:

$$G = U - \left(\frac{dU}{dS}\right)_v S - \left(\frac{dU}{dV}\right)_s V \quad \text{Eqn. 1.17}$$

From Eqns. (1.15) and (1.16), we obtain

$$G = U - TS + pV \quad \text{Eqn. 1.18}$$

This function is called the Gibbs free energy. The variation of G results in

$$dG = dU - TdS - SdT + pdV + Vdp \quad \text{Eqn. 1.19}$$

Since $dU = TdS - pdV$, we obtain

$$dG = -SdT + Vdp \quad \text{Eqn. 1.20}$$

Analogously to Eqn. (1.17), the new thermodynamic potential (*H*) is defined as

$$H = U - \left(\frac{dU}{dV}\right)_s V \quad \text{Eqn. 1.21}$$

Since Eqn. (1.16), we obtain

$$H = U + pV \quad \text{Eqn. 1.22}$$

where H is enthalpy. Through differentiation, H is a function of S and p:

$$dH = dU + pdV + Vdp \quad \text{Eqn. 1.23}$$

$$dH = TdS + Vdp \quad \text{Eqn. 1.24}$$

The overall and simple reaction encountered in SOFC is,

$$H_2 + \frac{1}{2}O_2 \rightarrow \ H_2O \quad \text{Eqn. 1.25}$$

The difference in Gibbs free energy of formation of ΔG during the reaction can be described below

$$\Delta G = \ \Delta G_{H_2O} - \ \Delta G_{H_2} - \ \frac{1}{2}\Delta G_{O_2} \quad \text{Eqn. 1.26}$$

If all the Gibbs free energy is consumed to electrical work, the Gibbs free energy for the fuel cell reaction is indicated by the equation

$$\Delta G = \ -nFE \quad \text{Eqn. 1.27}$$

where n is the number of moles of electrons involved in the chemical reaction, E is the reversible potential, and F is Faraday's constant.

If reactants and products are all in their standard states, the equation can be represented as

$$\Delta G^0 = \ -nFE^0 \quad \text{Eqn. 1.28}$$

The value of ΔG is 2379000 J mol^{-1}, $n = 2$, $F = 96485$ C mol^{-1}, and hence the calculated standard electrode potential E^0 is 1.23 V.

Beyond the standard condition, the theoretical reversible potential E_{th} can be expressed by the Nernst equation as

$$E_{th} = \ E^0 - \ \left(\frac{RT}{2F}\right)\ln\left(\frac{p_{H_2O}}{p_{H_2}p_{O_2}^{\frac{1}{2}}}\right) \quad \text{Eqn. 1.29}$$

where R is the gas constant, T is the absolute temperature, p is the partial pressure of each gas.

1.3.3. Thermodynamics of SOECs

Electrochemical reactions in an SOEC are reverse reactions in an SOFC. The overall reaction of the steam electrolysis is:

$$H_2O \rightarrow H_2 + \frac{1}{2}O_2 \qquad \text{Eqn. 1.30}$$

The electrical energy demand (ΔG) of Eqn. (1.30) can be expressed as:

$$\Delta G = \Delta H - T\Delta S \qquad \text{Eqn. 1.31}$$

where ΔH is the total energy demand and $T\Delta S$ is the heat energy demand. Figure 1.5 shows thermodynamic data of the steam electrolysis at atmospheric pressure. The heat consumption for the steam electrolysis increases with elevated temperature. Accordingly, the electrical energy demand is decreased significantly with the compensation of the heat energy demand. Therefore, the SOEC efficiency for hydrogen production can be increased, leading to reduce the hydrogen production cost.[20]

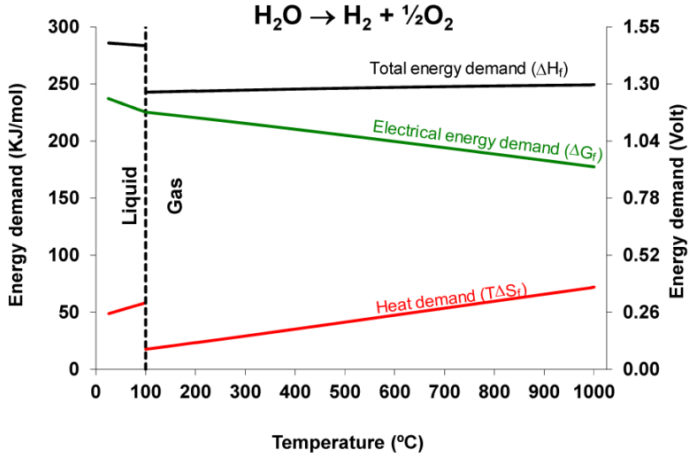

Figure 1.5 Electrical, thermal and total energy demand for steam H_2O electrolysis as a function of temperature.[20]

For electrolyzers, the thermoneutral voltage (E_{tn}) is defined as the voltage at which the electricity input into the cell and the total energy demand for electrolysis reaction are equal:[11]

$$E_{tn} = \frac{\Delta H_f}{nF} \qquad \text{Eqn. 1.31}$$

where ΔH_f is the total energy demand for electrolysis reaction, n is the number of electrons involved in the reaction (n is equal to 2 in the case of H_2O electrolysis), and F is the Faraday constant (96485 C mol^{-1}). For H_2O electrolysis, E_{tn} is 1.48 and 1.29 V at 25 and 850 °C, respectively. Therefore, at 1.29 V, the SOEC can be theoretically operated at thermal equilibrium with the electricity-to-hydrogen conversion efficiency of 100 %.[21]

1.3.4. Electrochemical Reaction Mechanisms of SOCs

The availability of reaction sites to the electrochemical reaction is an important feature for the electron transfer reaction to occur and therefore in turn critical for the performance of the SOCs. It is well known that the electron transfer reaction occurs at the triple phase boundary (TPB) where gas, the ionic conductor, and the electronic conductor are in contact. A schematic diagram of a TPB is presented in Figure 1.6.

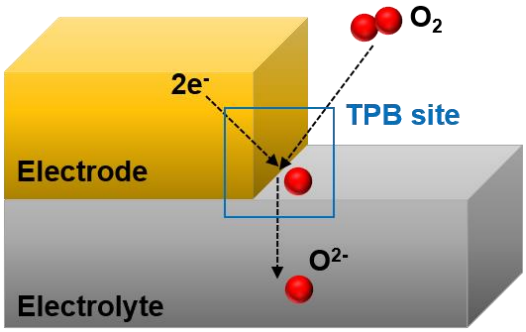

Figure 1.6 Schematic diagram of triple phase boundary TPB (triple phase boundary).

A general electrode material is an electronic conductor which contacts with an electrolyte (an ionic conductor). The edge of interface between the electrode and electrolyte is exposed to the gas phase. The electronic conductor is connected at some point away from the interface to a source of electronic current, contributing to provide a conduction path for electrons to the interface. The ionic conductor phase (*i.e.*, the electrolyte) is connected by a continuous ionic path to the electrolyte membrane, offering a sink for the oxygen ions produced from the reaction.[22]

In SOFC, at the cathode (*i.e.*, air electrode) side, the oxygen reduction reaction (ORR) occurs in a series of elementary electrochemical steps including adsorption, dissociation, surface diffusion, and charge transfer, resulting in the formation of oxygen ions as below Eqn. 1.32.[23]

$$\frac{1}{2}O_2 + V_O^{\bullet\bullet} + 2e' \rightarrow O_O^x \qquad \text{Eqn. 1.32}$$

where, in Kroger-Vink notation, $V_O^{\bullet\bullet}$ is a vacant oxygen site and O_O^x is an oxygen ion on a regular oxygen site in the ionic conducting electrolyte lattice. From Eqn. (1.32), the ORR process requires the existence of oxygen and electrons as well as the possibility for generated oxide ions to be transported from the reaction site of the electrode into the bulk of the electrolyte.

Adler *et al.*[24] proposed a mechanism for the oxygen reduction in SOFC cathodes. This Adler-Lane-Steele model (ALS model) suggests the mechanism in which the oxygen molecule is chemically reduced at the gas/mixed conductor interface and is transported through the mixed conductor by solid state diffusion. The chemical exchange of oxygen at the gas/mixed conductor interface is considered as a non-charge transfer process. Figure 1.7 shows simplified schematics of mechanisms either known or theorized in the literature to be important in determining the rate of the ORR at cathodes.[22]

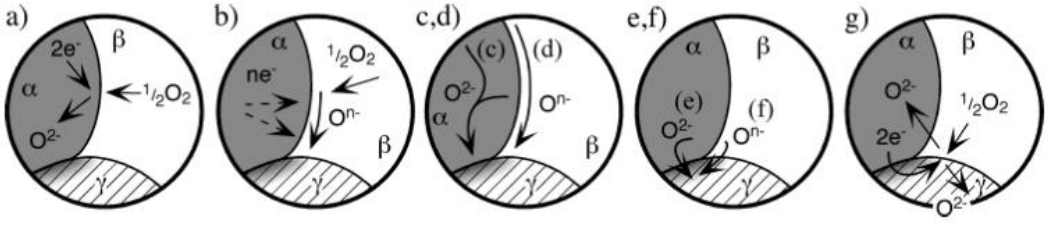

Figure 1.7 Schematics of mechanisms for the ORR in SOFC cathodes. Phases α, β, and γ refer to as the electronic phase, gas phase, and ionic phase, respectively: (a) Incorporation of oxygen gas into the bulk of the electronic phase (if mixed conducting); (b) adsorption and/or partial reduction of oxygen on the surface of the electronic phase; (c) bulk or (d) surface transport of O^{2-} or O^{n-}, respectively, to the α/γ interface, and (g) rates of one or more of these mechanisms wherein the electrolyte itself is active for generation and transport of electro-active oxygen species.[22]

1.3.5. Charge and Mass Transport Process of SOCs

Charge transport completes the circuit in an electrochemical system, moving charges from the electrode where they are produced to the electrode where they are used. There are mainly two types of charge species *i.e.*, electrons and ions. The transport of electrons as against that of ions is essentially different because of the large difference of mass between the two. In most SOCs, ion charge transport is more difficult than electron charge transport, therefore, the ionic contribution to R_{ohmic} tends to dominate and ionic conductivity should be mainly concerned. The resistance of charge transport results in a voltage loss for SOCs because this voltage loss obeys Ohm's law. The voltage loss called *ohmic* or *IR* loss relates with the electronic (R_{elec}) and ionic (R_{ionic}) contributions as follows:

$$\eta_{ohmic} = iR_{ohmic} = i(R_{elec} + R_{ionic}) \qquad \text{Eqn. 1.33}$$

Ohmic losses are minimized by reducing electrolyte thickness as thin as possible and introducing high ionic conductivity materials.

The rate at which charges move through a material is quantified in terms of flux (*J*). Charge flux is the amount of charge that flows through a material per unit area per unit time. Typical units of charge flux are

$$\frac{C}{cm^2 s} = \frac{A}{cm^2} \qquad \text{Eqn. 1.34}$$

The quantity $_{Zi}F$ is required to convert from molar flux *J* to charge flux *j*, where $_{Zi}$ is the charge number for the carrier (*e.g.*, -2 for O^{2-}) and F is Faraday's constant:

$$j = z_i F J \qquad \text{Eqn. 1.34}$$

If there is no force acting on the charge carriers (*i.e.*, the mobile electrons or ions in the material), there is no reason for them to move. The governing equation for transport can be written as

$$J_i = \sum_k M_{ik} F_k \qquad \text{Eqn. 1.35}$$

where J_i is a flux of species *i*, F_k is the *k* difference forces acting on *i*, and the M_{ik} represents the coupling coefficients which reflect the relative ability of a species to respond to a given force with movement as well as the effective strength of the driving force itself. In SOCs, there are three major driving forces that give rise to charge transport such as electrical (dV/dx), chemical ($d\mu/dx$) and mechanical (dP/dx) driving forces.

For the case where charge transport is dominated by electrical driving forces, Eqn. (1.35) can be rewritten as below

$$j = \sigma \frac{dV}{dx} \qquad \text{Eqn. 1.36}$$

where *j* is the charge flux, dV/dx is the electrical driving force for charge transport, and σ is the conductivity.

The conductivity is the ability of a material to flow the charge when driven by an electric field. The conductivity of a material is influenced by two factors: how many carriers are available to transport charge and the mobility of those carriers within the material. The conductivity can be written as:

$$\sigma_i = (|z_i|F)c_i u_i \quad \text{Eqn. 1.37}$$

where c_i is the molar concentration of charge carriers and u_i represents the mobility of the charge carries within the material. Therefore, the conductivity of material is determined by the product of carrier concentration c_i and carrier mobility u_i.

For operating SOCs, the penalty for charge transport is a loss in cell voltage due to the presence of an intrinsic resistance to charge flow. The voltage loss associated with charge transport can be expressed by the equation:

$$\eta_{\text{ohmic}} = j(\text{ASR}_{\text{ohmic}}) \quad \text{Eqn. 1.38}$$

where ASR represents for area specific resistance and carries unit of Ω cm^2.

Under SOC operation, fuel and oxidant are supplied continuously to produce electricity or hydrogen. At the same time, products must be removed to avoid "strangling" the cell. The process of supplying reactants and removing products is termed mass transport. For the case of SOCs, mass transfer mainly related with diffusion and transport of gas species.

Diffusion is a spontaneous process that is a result of the second law of thermodynamics, which requires thermodynamic processes proceed in away, maximizing entropy. Fick's law of diffusion can be described by[15]

$$\dot{n}_{j,i} = -D_{j,i} A \frac{\partial c_j}{\partial x_i} \quad \text{Eqn. 1.39}$$

where $D_{j,i}$ represents the diffusion coefficient of sepecies j with units of cubic meters per second, A is the diffusion area, c_j is the molar concentration of j, x_i is the direction of transport (x, y, or z direction), and $\dot{n}_{j,i}$ is the molar rate of transport of j in the i direction.

For 1 direction, it can be rewritten as:

$$\dot{n}_j = -D_j A \frac{\partial c_j}{\partial x} \quad \text{Eqn. 1.40}$$

where $D_j = 0.1$ cm^{2}s^{-1} for gases.

From the concentration variations, the Nernst potential changes (η_{conc}) can be calculated using c_R^* (catalyst layer reactant concentration) instead of c_R^0 (bulk reactant concentration):

$$\begin{aligned}\eta_{conc} = \; & E^0_{Nernst} - E^*_{Nernst} \\ = \; & \left(E^0 - \frac{RT}{nF}\ln\frac{1}{c^0_R}\right) - \left(E^0 - \frac{RT}{nF}\ln\frac{1}{c^*_R}\right) \\ = \; & \frac{RT}{nF}\ln\frac{c^0_R}{c^*_R}\end{aligned} \qquad \text{Eqn. 1.41}$$

where E^0_{Nernst} is the Nernst voltage using c^0 and E^*_{Nernst} is the Nernst voltage using c^*.

c^0_R can be described in terms of the limiting current density (j_L). The concentration concerns with the reaction rate that plays a key factor to determine cell performances. The reaction kinetics is described by the simplified expression of Butler-Volmer equation:

$$j = j^0_0\left(\frac{c^*_R}{c^{0*}_R}e^{-\alpha nF\eta_{act}/(RT)}\right) \qquad \text{Eqn. 1.42}$$

where j^0_0 is the exchange current density at a standard concentration, c^*_R and c^{0*}_R are arbitrary and reference reactant concentration, respectively, η_{act} represents the activation loss, and α is the transfer coefficient which measures how the change in the electrical potential across the reaction interface changes the sized of the forward versus reverse activation barrier ($0 < \alpha < 1$).

Written in the activation overvoltage, this becomes

$$\eta_{act} = \frac{RT}{\alpha nF}\ln\frac{jc^{0*}_R}{j^0_0 c^*_R} \qquad \text{Eqn. 1.43}$$

We can calculate how much the activation overvoltage changes using c^*_R

$$\eta_{act} = \eta^*_{act} - \eta^0_{act} = \left(\frac{RT}{\alpha nF}\ln\frac{jc^{0*}_R}{j^0_0 c^*_R}\right) - \left(\frac{RT}{\alpha nF}\ln\frac{jc^{0*}_R}{j^0_0 c^0_R}\right) = \frac{RT}{\alpha nF}\ln\frac{c^0_R}{c^*_R} \qquad \text{Eqn. 1.44}$$

The ratio $\frac{c^0_R}{c^*_R}$ equals $\frac{j_L}{j_L - j}$, therefore, we can write the total concentration loss (η_{conc}) as follows

$$\eta_{conc} = \frac{RT}{\alpha nF}\ln\frac{j_L}{j_L - j} \qquad \text{Eqn. 1.45}$$

1.4 Materials for SOFCs and SOECs

The typical SOFC and SOEC consist of a dense electrolyte, and a porous fuel electrode (anode in SOFC, cathode in SOEC), a porous air electrode (cathode in SOFC, anode in SOEC), and electrical interconnect layers. These components should have chemical and phase stability under the operating conditions, chemical compatibility with other components and a suitable conductivity.

1.4.1 Electrolytes

The practical requirements of electrolyte for SOCs are high ionic conductivity, low electronic conductivity, redox stability in both oxidizing and reducing conditions, excellent mechanical durability. Three electrolyte such as YSZ (yttria stabilized zirconia), GDC (gadolinium doped ceria), and LSGM (strontium, magnesium-doped lanthanum gallate) have been widely used for SOCs. The operating temperature range depends on both the ionic conductivity and the electrolyte thickness. The estimated minimum operating temperatures of YSZ, LSGM, and GDC are ~ 700 °C, ~ 550 °C, and ~ 550 °C, respectively. Figure 1.8 shows ionic conductivities of YSZ, GDC, and LSGM at various temperatures.[25]

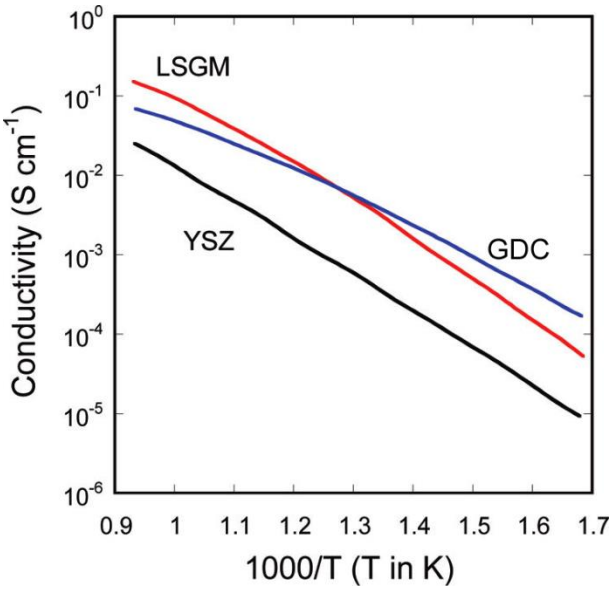

Figure 1.8 Conductivity of YSZ, GDC, LSGM.[25]

Each material have some advantages and disadvantages under SOC operating conditions. YSZ shows the sufficient electrical conductivity and good mechanical properties at high operating temperature (~ 700 °C). However, it has problems associated with reactivity with perovskite structure based electrode materials containing lanthanum, resulting in the formation of $La_2Zr_2O_7$ insulator layers. LSGM shows better ionic conductivity than YSZ and good compatibility with lanthanum based

perovskite electrodes. But, lanthanum in LSGM easily diffused to the electrode side, leading to the formation of an insulator at the interface.[26] GDC has received attractive attention as an alternative electrolyte with its high conductivity at lower temperature. GDC is generally stable under operating conditions but, Ce^{4+} is reduced to Ce^{3+} under reducing conditions ($pO_2 \approx 1\times10^{-19}$ atm). This reduction reaction leads to the increase of electronic conductivity with the occurrence of current leakage and decrease the fuel cell efficiency.

1.4.2 Air Electrodes

In SOFC, air electrodes (cathodes) should have sufficient electrochemical activity on the surface for an oxygen reduction reaction (ORR) and fast diffusivity for the transfer of oxygen ions into the air electrode.[27] Whereas, in SOEC, air electrodes (anode) should be able to undergo highly oxidizing environments. Air electrodes should have in common following properties for SOC applications.

(1) Sufficient catalytic activity for oxygen reduction/oxidation reaction.
(2) Chemical stability and compatibility with the electrolyte at high operating temperatures.
(3) Thermodynamically stability under oxidizing conditions.
(4) Sufficient electrical conductivity (> 100 S cm^{-1}).
(5) Low mismatch of thermal expansion between the cell components.

In this regards, among various materials as electrodes, electrodes based on mixed ionic and electronic conductors (MIECs) have been studied because the MIEC shows the widespread electrochemical reaction site from the three phase boundary to the entire exposed surface in SOCs. The relevant characteristics of perovskite based MIEC ceramics as air electrodes such as a simple and layered perovskite will be discussed.

1.4.2.1 Simple perovskites

Perovskite, calcium titanium oxide ($CaTiO_3$), was named after the Russian mineralogist Lev Perovski. Combination of the large oxide ion with a smaller radius metal ion gives a cubic close-packed crystal structure of oxygen ions along with interstitial metal ions. For the general chemical formula ABO_3, the crystal structure is the perovskite obtained by the partial replacement of the oxygen with cation as shown in Figure 1.9.[28] A simple cubic structure exhibits that the A site cation is 12-fold-coordinated with oxygen ions while the B site cation is 6-fold-coordinated.[29] A tolerance factor *t* is important factor to determine the stability and the crystal structure.[30] The tolerance factor t can be expressed as follows,

$$t = \frac{(R_A+R_O)}{\sqrt{2}(R_B+R_O)} \qquad \text{Eqn. 1.46}$$

where R_A, R_B, and R_O are the ionic radius of A, B, O ions, respectively. A range of t within 0.89 - 1.0 sustains the cubic structure and t values over 1.0 cause the structure change to tetragonal or orthorhombic structure.

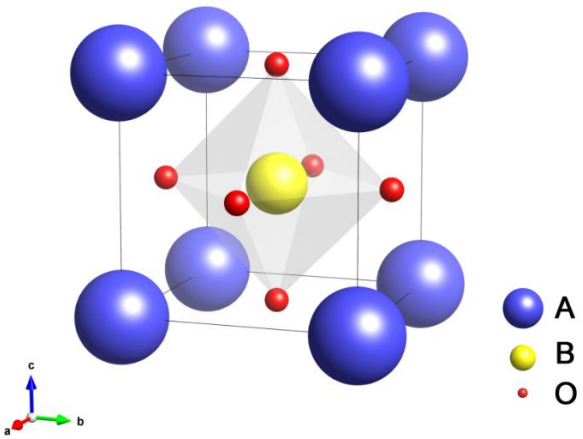

Figure 1.9 Structure of ABO_3 perovskite.

The $La_{1-x}Sr_xMnO_3$ (LSM) is considered to be general air electrodes for SOCs because of its good thermal and chemical compatibility with YSZ.[31] However, LSM exhibits inadequate performance, poor electrical conductivity and low oxygen kinetics at intermediate temperatures. Among MIECs, cobalt containing simple perovskites such as $Ba_{0.5}Sr_{0.5}Co_{0.8}Fe_{0.2}O_{3-\delta}$,[32] $La_{0.6}Sr_{0.4}Co_{0.2}Fe_{0.8}O_{3-\delta}$,[33] $Pr_{1-x}Sr_xCoO_{3-\delta}$,[34] and $Sm_{0.5}Sr_{0.5}CoO_3$[35] have been widely studied based on their high electrocatalytic activity.

1.4.2.2 A-site ordered Layered perovskites

Layered perovskites have recently been studied by numerous research groups based on their much higher chemical diffusion and surface exchange coefficients. The general formula of A site ordering layered perovskite is $AA'B_2O_{5+\delta}$, where the A is occupied by a trivalent lanthanide ion, A′ is a rare earth metal, and B is assigned a 3d transition metal ion (Mn, Fe, Co, Ni Cu, *etc*). In particular, the $LnBaCo_2O_{5+\delta}$, cobalt containing layered perovskite oxides, have stacking sequence of …$[LnO_\delta]$-$[CoO_2]$-[BaO]-$[CoO_2]$… along the *c*-axis as presented in Figure 1.10. According to modeling results obtained by density functional theory (DFT), the layered structure possesses pore channels in the [Ln-O] and [Co-O] planes that provide fast paths for oxygen transport, which in turn improves the kinetics of surface oxygen exchange.[36] Moreover, layered perovskite can accommodate more oxygen as oxygen

interstitials, which can improve the durability for SOEC operation. Because electrolysis operating conditions undergo high partial oxygen pressure ($p(O_2)$) at the interface between air electrode and electrolyte.[14] Kim *et al.* reported that $PrBaCo_2O_{5+\delta}$ exhibits faster oxygen ion diffusion and surface exchange kinetics, which lead to very low area specific resistance and high performance at intermediate temperature (500–700 °C).[37] Recently, some research groups have investigated that the effect of various cation substitution for Ba or Co site in $LnBaCo_2O_{5+\delta}$. Sr or Ca substitution for Ba show the improvement of electrochemical performance, electrical conductivity and structural stability.[38-41] Also, 3d transition metal ions have been introduced into the Co site, leading to enhance the oxygen ion kinetics, performance, and stability. [42-45]

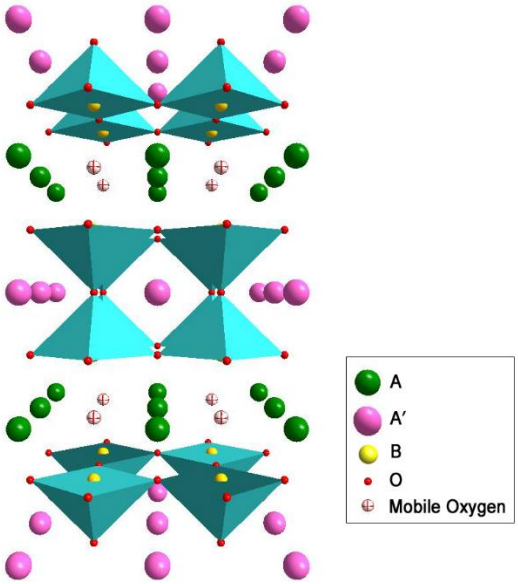

Figure 1.10 Structure of $AA'B_2O_{5+\delta}$ perovskite.

1.4.2.3 Ruddlesden-Popper type oxides

Among MIEC materials, layered A_2BO_4 oxides with a K_2NiF_4-type structure referred to as Ruddlesden-Popper (RP) phase have been investigated alternatives to perovskites. The general formula for RP phases is $A_{n+1}B_nO_{3n+1}$, where A is assigned a lanthanide or alkaline earth ion, B is occupied by transition metal ions, and n indicates the number of perovskite layers.[46] The RP phase related intergrowth oxides is composed of rock-salt AO layers alternating perovskite $(ABO_3)_n$ layers along the crystallographic *c*-axis as exhibited in Figure 1.11. This RP phase can accommodate hyperstoichiometric oxygen in interstitial sites (in the rock-salt AO layers), offering advantages related to oxygen kinetics. La_2NiO_4 offers several advantages such as high ionic and electrical conductivity, reasonable TEC values matching with general electrolyte materials and excellent electrocatalytic

activity for ORR.[47]

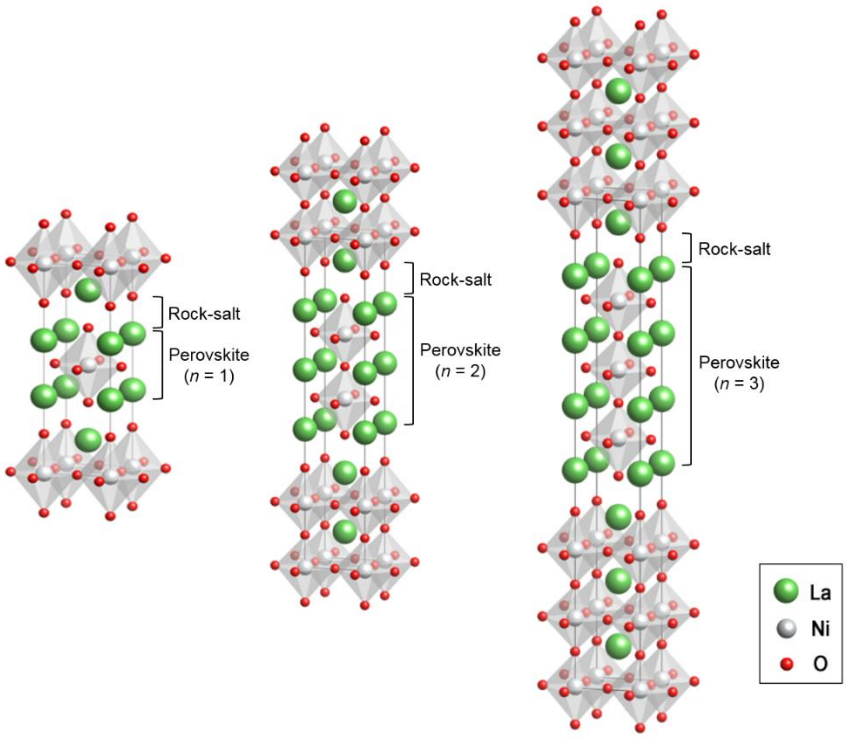

Figure 1.11 Structure of $A_{n+1}B_nO_{3n+1}$ Ruddlesden-Popper phases

1.4.3 Fuel Electrodes

Fuel electrodes, in common with air electrodes, should have thermal and chemical compatibility with contacting components. Furthermore, fuel electrodes should be able to transport a gas from fuel, oxygen ions from the electrolyte and electrons to interconnect. In this regards, fuel electrodes should be met following requirements for SOC applications.[12]

(1) Good carbon and sulfur tolerance when hydrocarbon based fuels are used without reformer systems.
(2) Sufficient porosity to avoid the fuel mass transport limitation.
(3) High electrical conductivity and catalytic activity in SOC operating conditions.
(4) Good durability on reducing and oxidizing (redox) cycles.

The conventional fuel electrodes is Ni/electrolyte composite cermet, which exhibits high catalytic activity and sufficient ionic and electrical conductivity. However, this composite cermet encounter critical problems such as carbon coking, sulfur poisoning, nickel coarsening, and the redox instability.[48-

[52] To overcome these problems, various materials and/or material combinations such as Cu-CeO_2-YSZ, Ru-CeO_2-YSZ, Cu-Ni alloy, and Ir-GDC, have been studied as alternative fuel electrodes.[53-56] But, there has been no material that possesses satisfactory solution to either of these problems. In recent years, perovskite based materials (*e.g.*, $La_{0.8}Sr_{0.2}Sc_xMn_{1-x}O_3$, $La_{0.4}Sr_{0.4}Ni_{0.06}Ti_{0.94}O_3$, $(Pr_{0.4}Sr_{0.6})_3(Fe_{0.85}Nb_{0.15})_2O_7$, $PrBaMn_2O_{5+\delta}$, $Sr_2Fe_{1.3}Ni_{0.2}Mo_{0.5}O_6$) have been focused as alternative fuel electrodes to enhance the redox stability.[57-60] In particular, the A-site layered $PrBaMn_2O_{5+\delta}$ (PBMO) perovskites is fabricated by *in situ* annealing $Pr_{0.5}Ba_{0.5}MnO_{3-\delta}$ in SOC operating conditions. The layered PBMO exhibits sufficient electrical conductivity, high performance, and remarkable durability without carbon coking and sulfur poisoning under various hydrocarbon fuels.[9]

References

(1) Chu, S.; Majumdar, A. Opportunities and Challenges for a Sustainable Energy Future. *Nature* **2012**, *488*, 294–303.

(2) Zhu, Y.; Zhou, W.; Sunarso, J.; Zhong, Y.; Shao, Z. Phosphorus-Doped Perovskite Oxide as Highly Efficient Water Oxidation Electrocatalyst in Alkaline Solution. *Adv. Funct. Mater.* **2016**, *26* (32), 5862–5872.

(3) Atkinson, A.; Barnett, S.; Gorte, R. J.; Irvine, J. T. S.; Mcevoy, A. J.; Mogensen, M.; Singhal, S. C.; Vohs, J. Advanced Anodes for High-Temperature Fuel Cells. *Nat. Mater.* **2004**, *3*, 17–27.

(4) Steele, B. C.; Heinzel, A. Materials for Fuel-Cell Technologies. *Nature* **2001**, *414*, 345–352.

(5) Ge, X. M.; Chan, S. H.; Liu, Q. L.; Sun, Q. Solid Oxide Fuel Cell Anode Materials for Direct Hydrocarbon Utilization. *Adv. Energy Mater.* **2012**, *2* (10), 1156–1181.

(6) Lashtabeg, A.; Skinner, S. J. Solid Oxide Fuel Cells-a Challenge for Materials Chemists? *J. Mater. Chem.* **2006**, *16* (31), 3161.

(7) Kilner, J. A.; Burriel, M. Materials for Intermediate-Temperature Solid-Oxide Fuel Cells. *Annu. Rev. Mater. Res.* **2014**, *44* (1), 365–393.

(8) Minh, N. Q. Solid Oxide Fuel Cells for Power Generation and Hydrogen Production. *J. Korean Ceram. Soc.* **2010**, *47* (1), 1–7.

(9) Sengodan, S.; Choi, S.; Jun, A.; Shin, T. H.; Ju, Y.-W.; Jeong, H. Y.; Shin, J.; Irvine, J. T. S.; Kim, G. Layered Oxygen-Deficient Double Perovskite as an Efficient and Stable Anode for Direct Hydrocarbon Solid Oxide Fuel Cells. *Nat. Mater.* **2014**, *14* (2), 205–209.

(10) Irvine, J. T. S.; Neagu, D.; Verbraeken, M. C.; Chatzichristodoulou, C.; Graves, C.; Mogensen, M. B. Evolution of the Electrochemical Interface in High-Temperature Fuel Cells and Electrolysers. *Nat. Energy* **2016**, *1* (1), 15014.

(11) Laguna-Bercero, M. A. Recent Advances in High Temperature Electrolysis Using Solid Oxide Fuel Cells: A Review. *J. Power Sources* **2012**, *203*, 4–16.

(12) Cowin, P. I.; Petit, C. T. G.; Lan, R.; Irvine, J. T. S.; Tao, S. Recent Progress in the Development of Anode Materials for Solid Oxide Fuel Cells. *Adv. Energy Mater.* **2011**, *1* (3), 314–332.

(13) Orera, A.; Slater, P. R. New Chemical Systems for Solid Oxide Fuel Cells. *Chem. Mater.* **2010**, *22* (3), 675–690.

(14) Jun, A.; Kim, J.; Shin, J.; Kim, G. Achieving High Efficiency and Eliminating Degradation in Solid Oxide Electrochemical Cells Using High Oxygen-Capacity Perovskite. *Angew. Chemie Int. Ed.* **2016**, *55*, 12512–12515.

(15) Bard, A. J.; Faulkner, L. R. *Electrochemical Methods: Fundamentals and Applications*; John Wiley & Sons: New York, 2000.

(16) Moçoteguy, P.; Brisse, A. A Review and Comprehensive Analysis of Degradation Mechanisms of Solid Oxide Electrolysis Cells. *Int. J. Hydrogen Energy* **2013**, *38* (36), 15887–15902.

(17) Ni, M.; Leung, M. K. H.; Leung, D. Y. C. An Electrochemical Model of a Solid Oxide Steam Electrolyzer for Hydrogen Production. *Chem. Eng. Technol.* **2006**, *29* (5), 636–642.

(18) Bove, R.; Ubertini, S. *Modeling Solid Oxide Fuel Cells: Chapter 2. Thermodynamics of Fuel Cells*; Springer, 2008.

(19) Brett, C. M. A.; Brett, A. M. O. *Electrochemistry: Principles, Methods, and Applications.*; Oxford University Press Inc.: New York, 1993.

(20) Ebbesen, S. D.; Jensen, S. H.; Hauch, A.; Mogensen, M. B. High Temperature Electrolysis in Alkaline Cells, Solid Proton Conducting Cells, and Solid Oxide Cells. *Chem. Rev.* **2014**, *114* (21), 10697–10734.

(21) Minh, N. Q. Reversible Solid Oxide Fuel Cell Technology for Hydrogen/Syngas and Power Production. In *Hydrogen Science and Engineering : Materials, Processes, Systems and Technology*; Prof. Dr. D. Stolten and Dr. B. Emonts, Ed.; Wiley-VCH Verlag GmbH & Co. KGaA: Weinheim, Germany, 2016; pp 359–390.

(22) Adler, S. B. Factors Governing Oxygen Reduction in Solid Oxide Fuel Cell Cathodes †. *Chem. Rev.* **2004**, *104*, 4791–4843.

(23) Dyer, C. K.; Moseley, P. T.; Ogumi, Z.; Rand, D. A. J.; Scrosati, B. *Encyclopedia of Electrochemical Power Sources*; Garche, J., Ed.; Elsevier B.V., 2013.

(24) Adler, S. B.; Lane, J. A.; Steele, B. C. H. Electrode Kinetics of Porous Mixed-Conducting Oxygen Electrodes. *J. Electrochem. Soc.* **1996**, *143* (11), 3554–3564.

(25) Jacobson, A. J. Materials for Solid Oxide Fuel Cells. *Chem. Mater.* **2010**, *22* (3), 660–674.

(26) Ju, Y.-W.; Jun, A.; Inoishi, A.; Ida, S.; Lim, T.; Kim, G.; Ishihara, T. Growth of Thin-Film Layered Perovskite Cathodes by Pulsed Laser Deposition and Their Electrochemical Studies in IT-SOFCs. *J. Electrochem. Soc.* **2014**, *161* (6), F698–F702.

(27) Jun, A.; Kim, J.; Shin, J.; Kim, G. Perovskite as a Cathode Material: A Review of Its Role in Solid-Oxide Fuel Cell Technology. *ChemElectroChem* **2016**, 511–530.

(28) Li, K. *Mixed Conducting Ceramic Membranes for Oxygen Separation*; 2007.

(29) Liu, Y.; Tan, X.; Li, K. Mixed Conducting Ceramics for Catalytic Membrane Processing. *Catal. Rev.* **2006**, *48* (2), 145–198.

(30) Li, C.; Lu, X.; Ding, W.; Feng, L.; Gao, Y.; Guo, Z. Formability of ABX_3 (X = F, Cl, Br, I) Halide Perovskites. *Acta Crystallogr. Sect. B* **2008**, *B64*, 702–707.

(31) Lynch, M. E.; Yang, L.; Qin, W.; Choi, J.-J.; Liu, M.; Blinn, K.; Liu, M. Enhancement of $La_{0.6}Sr_{0.4}Co_{0.2}Fe_{0.8}O_{3-\delta}$ Durability and Surface Electrocatalytic Activity by $La_{0.85}Sr_{0.15}MnO_{3\pm\delta}$ Investigated Using a New Test Electrode Platform. *Energy Environ. Sci.* **2011**, *4* (6), 2249–2258.

(32) Shao, Z.; Haile, S. M. A High-Performance Cathode for the next Generation of Solid-Oxide Fuel Cells. *Nature* **2004**, *431* (7005), 170–173.

(33) Jun, A.; Yoo, S.; Gwon, O.; Shin, J.; Kim, G. Thermodynamic and Electrical Properties of

$Ba_{0.5}Sr_{0.5}Co_{0.8}Fe_{0.2}O_{3-\delta}$ and $La_{0.6}Sr_{0.4}Co_{0.2}Fe_{0.8}O_{3-\delta}$ for Intermediate-Temperature Solid Oxide Fuel Cells. *Electrochim. Acta* **2013**, *89*, 372–376.

(34) Park, S.; Choi, S.; Shin, J.; Kim, G. Electrochemical Investigation of Strontium Doping Effect on High Performance $Pr_{1-x}Sr_xCoO_{3-\delta}$ (x = 0.1, 0.3, 0.5, and 0.7) Cathode for Intermediate-Temperature Solid Oxide Fuel Cells. *J. Power Sources* **2012**, *210*, 172–177.

(35) Yoo, S.; Lim, T.-H.; Shin, J.; Kim, G. Comparative Characterization of Thermodynamic, Electrical, and Electrochemical Properties of $Sm_{0.5}Sr_{0.5}Co_{1-x}Nb_xO_{3-\delta}$ (x = 0, 0.05, and 0.1) as Cathode Materials in Intermediate Temperature Solid Oxide Fuel Cells. *J. Power Sources* **2012**, *226*, 1–7.

(36) Choi, S.; Yoo, S.; Kim, J.; Park, S.; Jun, A.; Sengodan, S.; Kim, J.; Shin, J.; Jeong, H. Y.; Choi, Y.; et al. Highly Efficient and Robust Cathode Materials for Low-Temperature Solid Oxide Fuel Cells: $PrBa_{0.5}Sr_{0.5}Co_{2-x}Fe_xO_{5+\delta}$. *Sci. Rep.* **2013**, *3*, 2426.

(37) Kim, G.; Wang, S.; Jacobson, A. J.; Reimus, L.; Brodersen, P.; Mims, C. A. Rapid Oxygen Ion Diffusion and Surface Exchange Kinetics in $PrBaCo_2O_{5+x}$ with a Perovskite Related Structure and Ordered A Cations. *J. Mater. Chem.* **2007**, *17* (24), 2500–2505.

(38) Lim, C.; Jun, A.; Jo, H.; Ok, K. M.; Shin, J.; Ju, Y.-W.; Kim, G. Influence of Ca-Doping in Layered Perovskite $PrBaCo_2O_{5+\delta}$ on the Phase Transition and Cathodic Performance of a Solid Oxide Fuel Cell. *J. Mater. Chem. A* **2016**, *4*, 6479–6486.

(39) Yoo, S.; Jun, A.; Ju, Y.; Odkhuu, D.; Hyodo, J.; Jeong, H. Y.; Park, N.; Shin, J.; Ishihara, T.; Kim, G. Development of Double-Perovskite Compounds as Cathode Materials for Low-Temperature Solid Oxide Fuel Cells. *Angew. Chemie Int. Ed.* **2014**, *53*, 13064–13067.

(40) Jun, A.; Kim, J.; Shin, J.; Kim, G. Optimization of Sr Content in Layered $SmBa_{1-x}Sr_xCo_2O_{5+\delta}$ Perovskite Cathodes for Intermediate-Temperature Solid Oxide Fuel Cells. *Int. J. Hydrogen Energy* **2012**, *37* (23), 18381–18388.

(41) Kim, J. H.; Cassidy, M.; Irvine, J. T. S.; Bae, J. Electrochemical Investigation of Composite Cathodes with $SmBa_{0.5}Sr_{0.5}Co_2O_{5+\delta}$ Cathodes for Intermediate Temperature-Operating Solid Oxide Fuel Cell. *Chem. Mater.* **2010**, *22* (3), 883–892.

(42) Jun, A.; Yoo, S.; Ju, Y.-W.; Hyodo, J.; Choi, S.; Jeong, H. Y.; Shin, J.; Ishihara, T.; Lim, T.; Kim, G. Correlation between Fast Oxygen Kinetics and Enhanced Performance in Fe Doped Layered Perovskite Cathodes for Solid Oxide Fuel Cells. *J. Mater. Chem. A* **2015**, *3*, 15082–15090.

(43) Kim, Y. N.; Manthiram, A. Layered $LnBaCo_{2-x}Cu_xO_{5+\delta}$ ($0 \le x \le 1.0$) Perovskite Cathodes for Intermediate-Temperature Solid Oxide Fuel Cells. *J. Electrochem. Soc.* **2011**, *158* (3), B276–B282.

(44) Jun, A.; Shin, J.; Kim, G. High Redox and Performance Stability of Layered $SmBa_{0.5}Sr_{0.5}Co_{1.5}Cu_{0.5}O_{5+\delta}$ Perovskite Cathodes for Intermediate-Temperature Solid Oxide Fuel

Cells. *Phys. Chem. Chem. Phys.* **2013**, *15* (45), 19906–19912.

(45) Kim, J. H.; Manthiram, A. Layered $NdBaCo_{2-x}Ni_xO_{5+\delta}$ Perovskite Oxides as Cathodes for Intermediate Temperature Solid Oxide Fuel Cells. *Electrochim. Acta* **2009**, *54* (28), 7551–7557.

(46) Kim, S.; Choi, S.; Jun, A.; Shin, J.; Kim, G. Scale-Down and Sr-Doping Effects on $La_4Ni_3O_{10}$--YSZ Nanocomposite Cathodes for IT-SOFCs. *J. Electrochem. Soc.* **2014**, *161* (14), F1468–F1473.

(47) Kim, J.-H.; Manthiram, A. Layered $LnBaCo_2O_{5+\delta}$ Perovskite Cathodes for Solid Oxide Fuel Cells: An Overview and Perspective. *J. Mater. Chem. A* **2015**, *3*, 24195–24210.

(48) Nikooyeh, K.; Clemmer, R.; Alzate-Restrepo, V.; Hill, J. M. Effect of Hydrogen on Carbon Formation on Ni/YSZ Composites Exposed to Methane. *Appl. Catal. A Gen.* **2008**, *347* (1), 106–111.

(49) Rasmussen, J. F. B.; Hagen, A. The Effect of H_2S on the Performance of Ni-YSZ Anodes in Solid Oxide Fuel Cells. *J. Power Sources* **2009**, *191* (2), 534–541.

(50) Iwata, T. Characterization of Ni-YSZ Anode Degradation for Substrate-Type Solid Oxide Fuel Cells. *J. Electrochem. Soc.* **1996**, *143* (5), 1521–1525.

(51) Cassidy, M.; Lindsay, G.; Kendall, K. The Reduction of Nickel-Zirconia Cermet Anodes and the Effects on Supported Thin Electrolytes. *J. Power Sources* **1996**, *61*, 189–192.

(52) Lay-Grindler, E.; Laurencin, J.; Villanova, J.; Cloetens, P.; Bleuet, P.; Mansuy, A.; Mougin, J.; Delette, G. Degradation Study by 3D Reconstruction of a Nickel-Yttria Stabilized Zirconia Cathode after High Temperature Steam Electrolysis Operation. *J. Power Sources* **2014**, *269*, 927–936.

(53) Park, S.; Vohs, J. M.; Gorte, R. J. Direct Oxidation of Hydrocarbons in a Solid-Oxide Fuel Cell. *Nature* **2000**, *404*, 265–267.

(54) Zhan, Z.; Barnett, S. A. An Octane-Fueled Solid Oxide Fuel Cell. *Science* **2005**, *308*, 844–847.

(55) Kim, H.; Lu, C.; Worrell, W. L.; Vohs, J. M.; Gorte, R. J. Cu-Ni Cermet Anodes for Direct Oxidation of Methane in Solid-Oxide Fuel Cells. *J. Electrochem. Soc.* **2002**, *149* (3), A247–A250.

(56) Wisniewski, M.; Boréave, A.; Gélin, P. Catalytic CO_2 Reforming of Methane over $Ir/Ce_{0.9}Gd_{0.1}O_{2-x}$. *Catal. Commun.* **2005**, *6*, 596–600.

(57) Sengodan, S.; Ahn, S.; Shin, J.; Kim, G. Oxidation–reduction Behavior of $La_{0.8}Sr_{0.2}Sc_yMn_{1-y}O_{3\pm\delta}$ (y = 0.2, 0.3, 0.4): Defect Structure, Thermodynamic and Electrical Properties. *Solid State Ionics* **2012**, *228*, 25–31.

(58) Tsekouras, G.; Neagu, D.; Irvine, J. T. S. Step-Change in High Temperature Steam Electrolysis Performance of Perovskite Oxide Cathodes with Exsolution of B-Site Dopants. *Energy Environ. Sci.* **2013**, *6* (1), 256–266.

(59) Yang, C.; Li, J.; Lin, Y.; Liu, J.; Chen, F.; Liu, M. In Situ Fabrication of CoFe Alloy

Nanoparticles Structured $(Pr_{0.4}Sr_{0.6})_3(Fe_{0.85}Nb_{0.15})_2O_7$ Ceramic Anode for Direct Hydrocarbon Solid Oxide Fuel Cells. *Nano Energy* **2015**, *11*, 704–710.

(60) Wang, Y.; Liu, T.; Li, M.; Xia, C.; Zhou, B.; Chen, F. (Frank). Exsolved Fe-Ni Nano-Particles from $Sr_2Fe_{1.3}Ni_{0.2}Mo_{0.5}O_6$ Pervoskite Oxides as Cathodes for Solid Oxide Steam Electrolysis Cells. *J. Mater. Chem. A* **2016**, *4*, 14163–14169.

Chapter 2. Experimental

2.1. Sample Preparation

The perovskite based electrode materials were prepared by the Pechini method. The general procedures are covered in this Chapter and the detailed information will be provided in the relevant Chapters. The desired composition was obtained by each dissolving nitrate salts in distilled water with the addition of quantitative amounts of citric acid and ethylene glycol. In addition, citric acid and ethylene glycol were used as complexing agents. After a viscous resin was formed, the mixture was heated to roughly 250 ^{o}C in air, followed by combustion to form powders, which were calcined at 600 ^{o}C for 4 h and ball-milled in acetone for 24 h.

2.2. Cell Fabrication

2.2.1. GDC Electrolyte Based Cell

The $Ce_{0.9}Gd_{0.1}O_{2-\delta}$ (GDC) powder was pressed into pellets and sintered at 1350 ^{o}C for 4 h in air to obtain a ~ 1 mm-thick electrolyte substrate. Slurries of electrode materials were screen-printed onto both sides of the dense GDC electrolyte to form a symmetrical cell, which was then sintered at 950 ^{o}C for 4 h. The silver paste was used as the current collector for the electrodes.

A NiO-GDC anode-supported single cell was fabricated to measure the electrochemical performance. The NiO-GDC anode was prepared by a mixture of nickel oxide, GDC, and starch at a weight ratio of 6:4:1.5 after being ball milled in ethanol for 24 h. The GDC electrolyte was pressed onto the pelletized disk of the NiO-GDC cermet anode. This NiO-GDC|GDC anode-supported cell was sintered at 1350 ^{o}C for 5 h and cathode slurries were applied onto the surface of the GDC electrolyte layer by screen printing. A tri-layer air electrode|GDC|NiO-GDC cell with an active electrode area of 0.36 cm^2 was finally sintered at 950 ^{o}C for 4 h in air. The electrolyte and cathode thickness of a single cell were about 15 μm with a 500 μm thick anode.

2.2.2. LSGM Electrolyte Supported Single Cell

$La_{0.9}Sr_{0.1}Ga_{0.8}Mg_{0.2}O_{3-\delta}$ (LSGM) powder was prepared by the solid state reaction method and a dense electrolyte substrate was prepared by dry pressing followed by sintering at 1475 ^{o}C. Stoichiometric amounts of La_2O_3 (Sigma 99.99%), $SrCO_3$ (Sigma, 99.99%), Ga_2O_3 (Sigma, 99.99%), and MgO (Sigma, 99.9%) powders were ball milled in ethanol for 24 h. After drying, the mixture was

calcined at 1000 ºC for 6 h. The thickness of the LSGM electrolyte was adjusted to about 250 μm by polishing. $La_{0.4}Ce_{0.6}O_{2-\delta}$ (LDC) was also prepared by ball milling stoichiometric amounts of La_2O_3 and CeO_2 (Sigma, 99.99%) in ethanol and then calcined for 6 h. The LSGM electrolyte-supported cell was fabricated to measure the electrolysis performance. The LDC layer was used as the buffer layer between the air electrode and the electrolyte to prevent inter-diffusion of ionic species between electrode material and LSGM.[1] The electrode slurry was applied on the LSGM pellet by the screen printing method, and then sintered at 950 ºC in air for 4 hours.

2.2.3. BZCYYb Electrolyte Based Anode Supported Single Cell

$BaZr_{0.1}Ce_{0.7}Y_{0.1}Yb_{0.1}O_{3-\delta}$ (BZCYYb) powders were synthesized by the typical solid state reaction method. Stoichiometric amounts of barium carbonate, zirconium oxide, cerium oxide, ytterbium oxide, and yttrium oxide powders (all from Aldrich Chemicals) were mixed by ball milling and then sintered at 1100 ºC in air for 10 h. The NiO powders for the fuel electrode were synthesized by the glycine nitrate process (GNP). Stoichiometric amount of metal nitrate was dissolved in distilled water. Glycine was added into the mixed nitrate solutions at a molar ratio of 1.5:1.0 for glycine and metal nitrate. The solutions were heated up to 350 ºC and followed by combustion to form fine powders. NiO-BZCYYb supported cells were fabricated using the drop-coating method. The NiO-BZCYYb fuel electrode was prepared by a mixture of NiO and BZCYYb (weight ratio of 6.5:3.5) after being ball-milled in ethanol for 24 hours. The BZCYYb suspension was applied to a NiO-BZCYYb support by drop-coating, followed by drying in air and subsequent co-sintering at 1400 ºC for 4 hours. Air electrode slurries were applied onto the surface of the BZCYYb electrolyte by screen printing and were finally sintered 950 ºC for 4 hours in air.

2.3. Basic Characterization

2.3.1. Structural Analysis

The crystalline structure was characterized by using an X-ray diffractometer (Rigaku diffractometer, Cu Kα radiation). The powder pattern and lattice parameters were analyzed by Rietveld refinement using the GSAS program. to determine the phase stability in air from 100 to 800 ºC, it was also analyzed using an *in-situ* X-ray diffractometer (Bruker AXS D8 Advance diffractometer, Cu Kα radiation). The microstructures of electrodes and cross-sections of single cells were investigated using a field emission scanning electron microscope (Nova Nano SEM, FEI, USA).

2.3.2. Thermal Analysis

A thermogravimetric analysis (TGA) was performed using a thermogravimetric analyzer (SDT-Q600, TA Instruments, USA) from 100 to 900 °C with a heating/cooling rate of 2 °C min^{-1} in air. The initial oxygen content of samples was determined by iodometric titration. The thermal expansion curve of the samples was measured from 100 to 900 °C with a heating/cooling rate of 5 °C min^{-1} in air. The coefficient of thermal expansion was calculated as below,

$$\alpha = \frac{1}{L_0}\frac{dL}{dT} \qquad \text{Eqn 2.1}$$

where α is the thermal expansion coefficient (TEC), L_0 represents the length of the specimen at a specific temperature, and T is the absolute temperature.

2.3.3. Electrical and Electrochemical Analysis

For the measurement of electrical conductivity, the powder was pressed into a cylindrical shape and sintered to dense pellets (>98 % density). The electrical conductivities of samples were measured by a four-terminal DC arrangement technique. The current and the voltage were recorded by a BioLogic Potentiostat from 100 to 750 °C at intervals of 50 °C in air.

Electrochemical impedance spectroscopy of the materials was carried out using a symmetrical cell. Impedance spectra were recorded under OCV in a frequency range of 1 mHz to 500 kHz with AC perturbation of 14 mA.

For the single-cell performance test, Ag wires were attached at both electrodes of the single cell using Ag paste as a current collector. The single cell was fixed on an alumina tube using a ceramic adhesive (Aremco, Ceramabond 552). Humidified hydrogen (3 % H_2O) was supplied as fuel through a water bubbler with a flow rate of 20 mL min^{-1} and ambient air was used as an oxidant during single cell tests. *I-V* curves and impedance spectra were examined using a BioLogic Potentiostat at operating temperature.

2.3.4. Redox Property and Oxygen Non-stoichiometric Analysis

The redox property and oxygen non-stoichiometry were measured using coulometric titration as a function of the oxygen partial pressure, $p(O_2)$. Coulometric titration was used to accurately quantify the oxidation/reduction state of the sample as a function of $p(O_2)$. The coulometric titration rig was mainly composed of an YSZ tube (McDanel Advanced Ceramic Technologies, Z15410630) with Ag-

paste electrodes plastered on both sides. The yittria-stabilized zirconia (YSZ) tube was used both to electrochemically pump oxygen out of the system and to detect the equilibrium $p(O_2)$ inside the tube. Electrodes on either side of the YSZ tube were used to measure the potential across the membrane and the potential could be related to the $p(O_2)$ through the Nernst Equation. After passing 5% O_2-Ar gas over the sample in the tube, the sample was isolated in the tube and the equilibrium $p(O_2)$ was measured with an OCV sensor. The OCV sensor was integrated onto the tube surface and could be used to add or remove oxygen from the system through the application of a potential across the ion-conducting YSZ tube. The sample was considered to be equilibrated when the potential varied in a range of less than 1 mV per hour. Oxygen non-stoichiometry was decided through this process at operating temperature over a wide range of oxygen partial pressure. The oxygen partial pressure dependence of the electrical conductivity was also measured by the four-probe DC method with a BioLogic Potentiostat on the sintered bar of the sample.

2.3.5. Oxygen kinetics determination

Isotope oxygen exchange was carried out using a closed circulation system with >96% $^{18}O_2$. The concentration of $^{18}O_2$ in the gas phase was measured by using a mass analyzer (Anelva, M-100-QA-F). The measured samples were polished using diamond paste and the final diameter of diamond paste was 0.25 μm. Naturally abundant O_2 under pressure of 200 mbar was introduced into the system with a measured sample, and the sample was heated to 590 ºC. The measured samples were annealed for more than ten times longer than the isotope oxygen exchanging time.[2] The sample was cooled to the room temperature, and residual oxygen was removed from the system. Subsequently, $^{18}O_2$ at a pressure of 200 mbar was introduced for oxygen exchange. The sample was then heated rapidly to room temperature. After isotope oxygen exchanging for 40 min, the sample was quenched to room temperature. The obtained sample was cut into a bar shape, and the cut surface was polished with diamond paste. The isotope oxygen diffusion profile was obtained by secondary ion mass spectrometry (SIMS) using an ATOMICA 4100 quadrupole-base analyzer, with the line-scan mode at the cross-section of the sample using a cesium ion primary source (Cs^+) at 10 keV. The tracer diffusion coefficient (D^*) and the oxygen surface exchange coefficient (k) were estimated by fitting to the semi-infinite diffusion model.[3]

References

(1) Sengodan, S.; Choi, S.; Jun, A.; Shin, T. H.; Ju, Y.-W.; Jeong, H. Y.; Shin, J.; Irvine, J. T. S.; Kim, G. Layered Oxygen-Deficient Double Perovskite as an Efficient and Stable Anode for Direct Hydrocarbon Solid Oxide Fuel Cells. *Nat. Mater.* **2014**, *14* (2), 205–209.

(2) De Souza, R. A.; Chater, R. J. Oxygen Exchange and Diffusion Measurements: The Importance of Extracting the Correct Initial and Boundary Conditions. *Solid State Ionics* **2005**, *176* (23–24), 1915–1920.

(3) Crank, J. T. The Mathematics of Diffusion. Oxford. Clarendon press 1975.

Chapter 3. Thermodynamic and electrical properties of $Ba_{0.5}Sr_{0.5}Co_{0.8}Fe_{0.2}O_{3-\delta}$ and $La_{0.6}Sr_{0.4}Co_{0.2}Fe_{0.8}O_{3-\delta}$ for intermediate-temperature solid oxide fuel cells

3.1. Introduction

The solid oxide fuel cell (SOFC) is a new power generation device with high energy conversion efficiency and excellent fuel flexibility. The requirement for high operating temperatures of 1073-1273 K, however, results in crucial issues such as high costs and material compatibility challenges. The focus of research on SOFC technology, consequently, has shifted toward the operation in intermediate operating temperatures (873-1073 K) to improve material compatibility and practical applicability.[1,2] This decrease of operating temperature leads to a serious deterioration in electrode activity. As a result, cathode materials with high electrocatalytic activity for oxygen reduction should be developed because the polarization loss on the cathode limits the cell performances at intermediate temperatures.[3]

The iron-cobalt-based perovskite oxides are good candidates for intermediate-temperature SOFCs (IT-SOFCs) because of their high electrical conductivity and good electrochemical performance. Mixed conductors with both electronic and ionic conductivity (MIECs) [4] also can be considered as promising cathode materials for IT-SOFCs because of their extended electrochemically active area. The reaction site of MIECs can be extended to a remarkably larger cathode area because the oxygen exchange reaction occurs not only on the triple-phase boundary between electrolyte, cathode, and gas phase but also on two phase boundary between electrode and gas phase.[5,6]

The $Ba_{0.5}Sr_{0.5}Co_{0.8}Fe_{0.2}O_{3-\delta}$ (BSCF) and $La_{0.6}Sr_{0.4}Co_{0.2}Fe_{0.8}O_{3-\delta}$ (LSCF) are commonly proposed as cathode materials for SOFCs at intermediate temperatures because of their sufficiently high electronic conductivity for current pickup and a high catalytic activity for the oxygen exchange reaction. BSCF and LSCF cathodes have shown to improve the electrical conductivity and stability by the combined effect of the substitution of Sr and Fe on A and B site. Shao et al. discovered BSCF as a novel cathode material for intermediate temperature SOFC operation with excellent performance at temperatures lower than 873 K.[2] The LSCF is known to show suitable stability ranges and to have good electrochemical performance at intermediate temperature.[7] Their physical and chemical properties such as electrical conductivity, electronic structure, catalytic activity, stability and thermal expansion have been studied so far.[8-11]

In this study, we evaluate the redox behavior of the BSCF and LSCF under same conditions by the coulometric titration. Furthermore, the electrical conductivity in an actual cathode operating condition less than the oxygen partial pressure in the atmosphere (0.21 atm) is investigated simultaneously during the coulometric titration.

3.2. Experimental

The $Ba_{0.5}Sr_{0.5}Co_{0.8}Fe_{0.2}O_{3-\delta}$ and $La_{0.6}Sr_{0.4}Co_{0.2}Fe_{0.8}O_{3-\delta}$ powders were synthesized by Pechini method. Stoichiometric amounts of $Sr(NO_3)_2$ (Aldrich, 99+%), $Ba(NO_3)_2$ (Aldrich, 99+%), $La(NO_3)_3 \cdot 6H_2O$ (Aldrich, 99+%), $Co(NO_3)_2 \cdot 6H_2O$ (Aldrich, 98+%), $Fe(NO_3)_3 \cdot 9H_2O$ (Aldrich, 99+%) and citric acid were dissolved in distilled water to form an aqueous mixed solution. An adequate amount of ethylene glycol was added into the beaker after the mixture was dissolved. After a viscous resin was formed, the mixture was heated to roughly 523 K. The resultant powder was calcined at 873 K for 4 h and ball milled in acetone for 24 h. The powder was pressed into pellet and then sintered in air at 1473 K for 12 h.

The structure of the prepared samples were characterized by X-ray diffractometer (Rigaku diffractometer, Cu Ka radiation) at a scanning rate of 0.5 ^{o} min^{-1} and a range $20 < 2\theta < 60$ ^{o}.

For electrical conductivity measurement, the powder was pressed into a cylinder shape and sintered at 1473 K for 12 h. The electrical conductivities of the BSCF and LSCF pellets were measured by a four-probe DC conductivity technique. The current and the voltage were evaluated by BioLogic Potentiostat from 373 to 1023 K at intervals of 50 K in air.

Coulometric titration was used to accurately quantify the oxidation/reduction state of the BSCF and LSCF as a function of $p(O_2)$. The coulometric titration rig in Fig. 1was mainly composed of an YSZ tube with Ag-paste electrodes plastered on both sides, which has been explained sufficiently elsewhere.[12] The yittria-stabilized zirconia (YSZ) tube was used both to electrochemically pump oxygen out of the system and to detect the equilibrium $p(O_2)$ inside the tube. Electrodes on either side of the YSZ tube were used to measure the potential across the membrane and the potential could be related to the $p(O_2)$ through the Nernst Equation. After passing 5% O_2-Ar gas over the sample in the tube, the sample was isolated in the tube and the equilibrium $p(O_2)$ was measured with the OCV sensor. The OCV sensor was a part of the tube surface and could be used to add or remove oxygen from the system through the application of a potential across the ion-conducting YSZ tube. The sample was considered to equilibrate when the potential varied in a range of less than 1 mV per hour. Oxygen nonstoichiometry was decided through this process at 923, 973 and 1023 K over a wide range of oxygen partial pressure. The oxygen partial pressure dependence of the electrical conductivity was also measured by the four-probe DC method with a BioLogic Potentiostat on sintered bars of BSCF and LSCF as illustrated in Figure. 3.1.

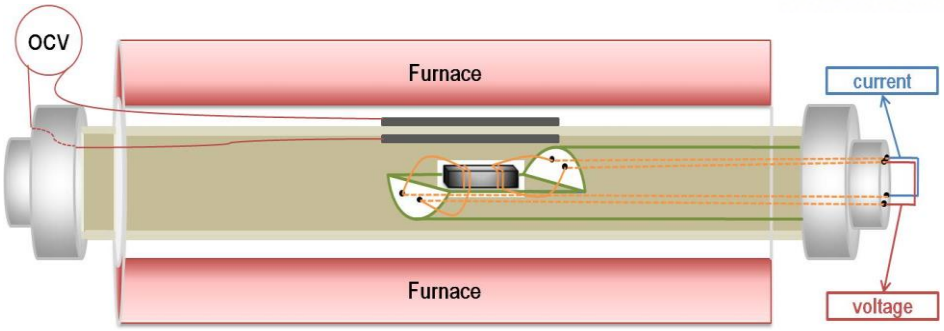

Figure. 3.1. Schematic diagram of the coulometric titration unit.

3. 3. Results and Discussions

The XRD patterns of the BSCF and LSCF pellets sintered at 1473 K for 12 h were measured to determine the phases present. Figure 3.2 reveals the presence of intense peaks indicating a well-defined crystallized perovskite structure obtained after calcinations. All the peaks are well indexed as a cubic perovskite structure and sharp lines reflect well-developed crystallization without any detectable impurity phases. These results are in agreement with other references elsewhere forming BSCF and LSCF phases.[13,14]

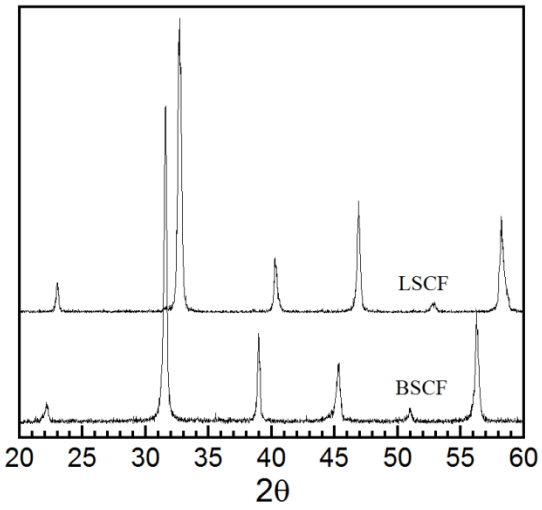

Figure. 3.2. XRD analysis of $Ba_{0.5}Sr_{0.5}Co_{0.8}Fe_{0.2}O_{3-\delta}$ and $La_{0.6}Sr_{0.4}Co_{0.2}Fe_{0.8}O_{3-\delta}$ sintered at 1473 K.

The electrical conductivities in air of BSCF and LSCF were measured in the temperature range 373-1023 K as in Figure 3.3. The conductivity of BSCF increases gradually and reaches a 14.87 S cm^{-1} at 773 K. It decreases slightly to 823 K and remains almost constant until 1023 K. The electrical conductivity of LSCF reaches a maximum of 215.58 S cm^{-1} around 823 K and then decreases continuously. Such an increase of the electrical conductivity at lower temperature was typical for the semi-conductors, while both BSCF and LSCF samples show metallic behavior at higher temperature.

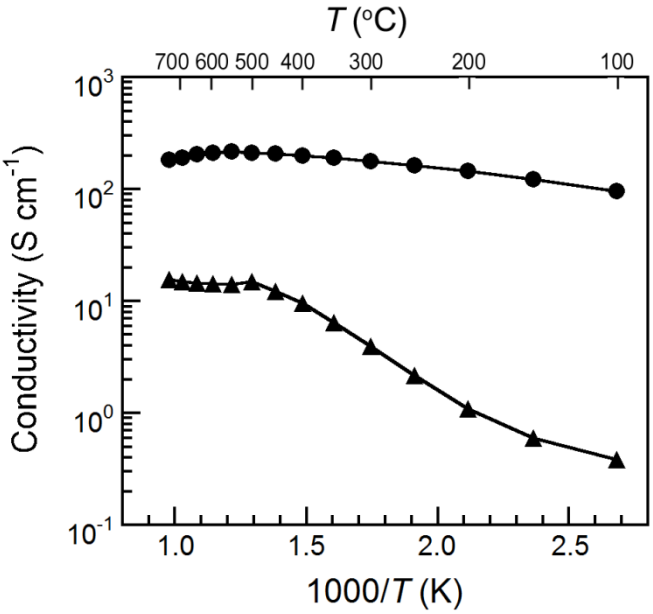

Figure 3.3. The electrical conductivities of $Ba_{0.5}Sr_{0.5}Co_{0.8}Fe_{0.2}O_{3-\delta}$ (▲) and $La_{0.6}Sr_{0.4}Co_{0.2}Fe_{0.8}O_{3-\delta}$ (●) at various temperatures from 373 to 1023 K in air.

The higher redox stability is an important factor for stable electrochemical properties of a cathode material for IT-SOFCs at operating conditions. Figures 3.4 and 3.5 show the equilibrium oxygen nonstoichiometries for BSCF and LSCF determined by coulometric titration as a function of $p(O_2)$ in a temperature range of 923-1023 K.[12,15] The oxidation isotherms of BSCF and LSCF for three different temperatures (923, 973, and 1023 K) have similar shapes suggesting that the oxidation/reduction mechanisms of both materials are quite similar. As temperature decreases, the decomposition $p(O_2)$ at which the sharp drop of oxygen content occurs, are shifted to the lower $p(O_2)$ side. LSCF, therefore, can be considered more stable than BSCF reflecting the $p(O_2)$ range of decomposition. In all cases over the entire temperature range, the BSCF sample starts to decay at a $p(O_2)$ of approximately10^{-5} atm and appears to decompose thoroughly at a $p(O_2)$ of 10^{-6} atm. The LSCF sample starts to experience chemical and/or structural change at a $p(O_2)$ of approximately 10^{-6} atm and occurs to decompose thoroughly at a $p(O_2)$ of 10^{-7} atm. The isotherms indicate that BSCF and LSCF operating at 10^{-5}-10^{-6} atm and 1023 K are subject to steep oxygen non-stoichiometry gradients and may undergo corresponding structural instability with significant consequences. The suitability for cathode materials of BSCF and LSCF should be cautiously reviewed concerning the instability predicted from the isotherm.

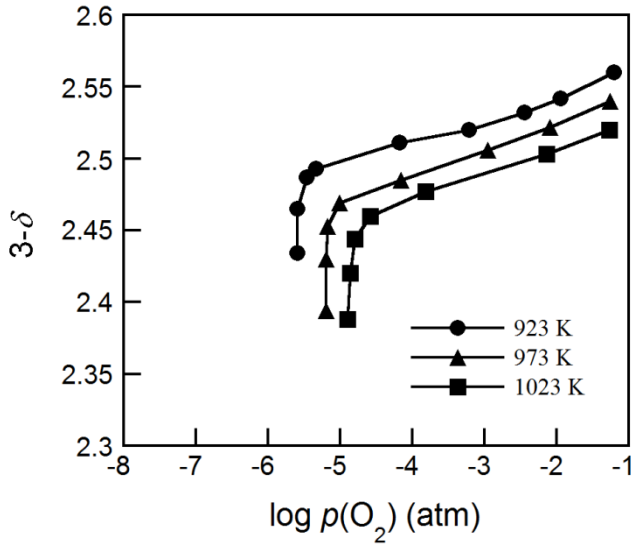

Figure 3.4. Isotherms of $Ba_{0.5}Sr_{0.5}Co_{0.8}Fe_{0.2}O_{3-\delta}$.

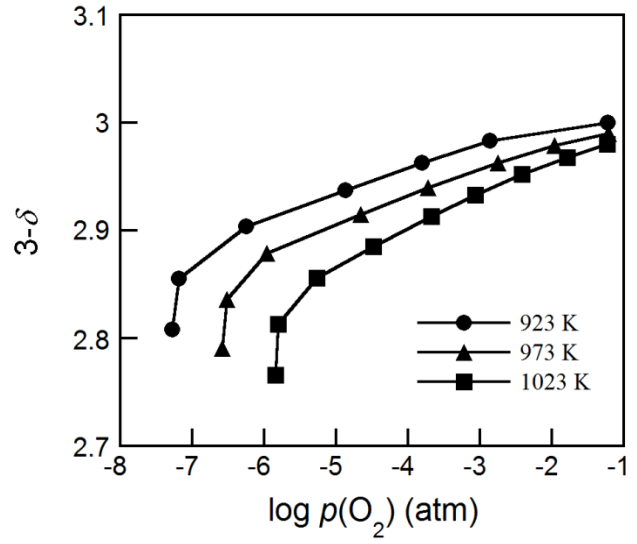

Figure 3.5. Isotherms of $La_{0.6}Sr_{0.4}Co_{0.2}Fe_{0.8}O_{3-\delta}$.

In general, the cathode experiences a lower $p(O_2)$ under operating conditions due to cathodic polarization Therefore, sufficient electrical conductivity at relatively low $p(O_2)$ is also important to ensure efficient current collection and long-term stability.[16] The $p(O_2)$ dependence of the 4-probe electrical conductivities for BSCF and LSCF at various temperatures ($923 < T(K) < 1023$) are displayed in Figures 3.6 and 3.7. The slope of electrical conductivity in BSCF and LSCF becomes much steeper below 10^{-5} and 10^{-6} atm. This suggests that the electrical properties are also closely related with the chemical and/or structural change of the material, which can be estimated from the oxidation isotherm.

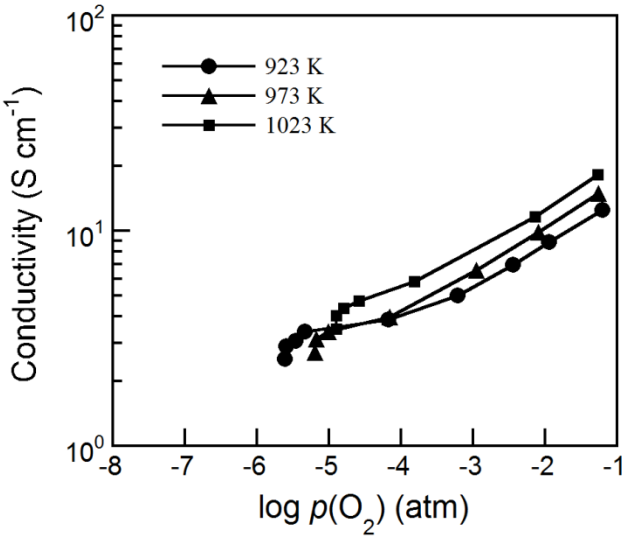

Figure 3.6. Electrical conductivities of $Ba_{0.5}Sr_{0.5}Co_{0.8}Fe_{0.2}O_{3-\delta}$ in various $p(O_2)$ (atm).

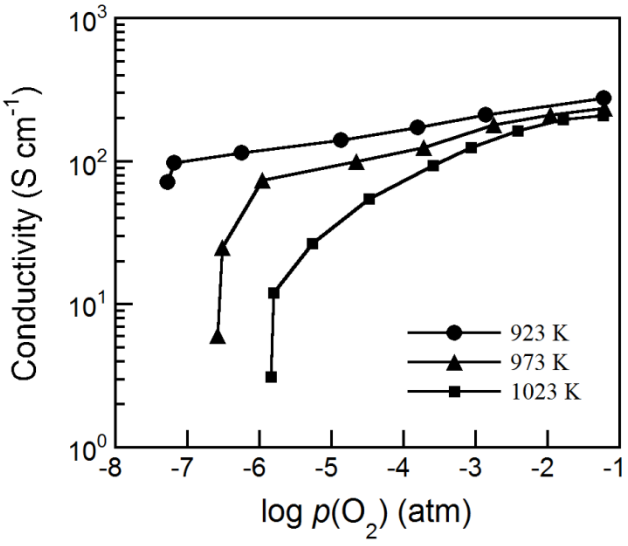

Figure 3.7. Electrical conductivities of $La_{0.6}Sr_{0.4}Co_{0.2}Fe_{0.8}O_{3-\delta}$ in various $p(O_2)$ (atm).

The predominant defects in BSCF and LSCF are oxygen vacancies ($V_o^{\bullet\bullet}$), Co^{4+} in Co^{3+} ($Co_{Co}^{\bullet}$) and Fe^{4+} in Fe^{3+} ($Fe_{Fe}^{\bullet}$). Eqns. (3.1) and (3.2) can express the pseudo-chemical reaction between the surrounding gas and the oxygen vacancies using the Kröger-Vink notation.[17]

$$2Co_{Co}^{\bullet} + O_o^{x} \leftrightarrow 2Co_{Co}^{x} + V_o^{\bullet\bullet} + \frac{1}{2}O_2 \qquad \text{Eqn. 3.1}$$

$$2Fe_{Fe}^{\bullet} + O_o^{x} \leftrightarrow 2Fe_{Fe}^{x} + V_o^{\bullet\bullet} + \frac{1}{2}O_2 \qquad \text{Eqn. 3.2}$$

The decrease in conductivity with decreasing $p(O_2)$ could be due to the loss of lattice oxygen and the creation of oxygen vacancies as indicated by L. Ge *et al.*[18] The formation of oxide ion vacancies is accompanied by a reduction of high valence state of Co^{4+} and Fe^{4+} to lower trivalent of Co^{3+} and Fe^{3+}, which results in a decrease of the charge carrier concentration.[19] As an oxygen partial pressure is lower, it would lead to an increase in concentration of oxygen vacancies and a decrease in the concentration of electronic holes, which would in turn *p*-type electrical conductivity.

The partial molar enthalpy and entropy of oxidation are related with the slopes of the isotherms. The Gibbs free energy, ΔG, is calculated as Eqn. (3.3) with the equilibrium constant K.

$$\Delta G = -RT\ln K = \frac{1}{2}RT\ln p(O_2) \qquad \text{Eqn. 3.3}$$

At a constant δ, the partial molar enthalpy of oxidation at various temperatures is shown by the Gibbs-Helmholtz equation.[20]

$$\Delta H = \frac{\partial\left(\frac{\Delta G}{T}\right)}{\partial\left(\frac{1}{T}\right)} = \frac{R}{2}\frac{\partial \ln[p(O_2)]}{\partial\left(1/T\right)}\Bigg|_{\delta} \qquad \text{Eqn. 3.4}$$

And the partial molar entropy can be obtained by using the Maxwell relation as follows;

$$-\Delta S = \frac{\partial \Delta G}{\partial T} = \left(\frac{R}{2}\right)\left(\frac{\partial\, T\ln[p(O_2)]}{\partial T}\right)\Bigg|_{\delta} \qquad \text{Eqn. 3.5}$$

The partial enthalpies of oxidation for BSCF and LSCF are calculated from Eqn. (3.4) and presented in Figure 3.8. The partial enthalpies of oxidation for the BSCF range from -240 to -170 kJ mol^{-1} and those of the LSCF range from -210 to -160 kJ mol^{-1}. The partial molar enthalpies become higher for higher δ, implying higher energy is needed for the lift-off of the oxygen inside the lattice as the reduction proceeds.

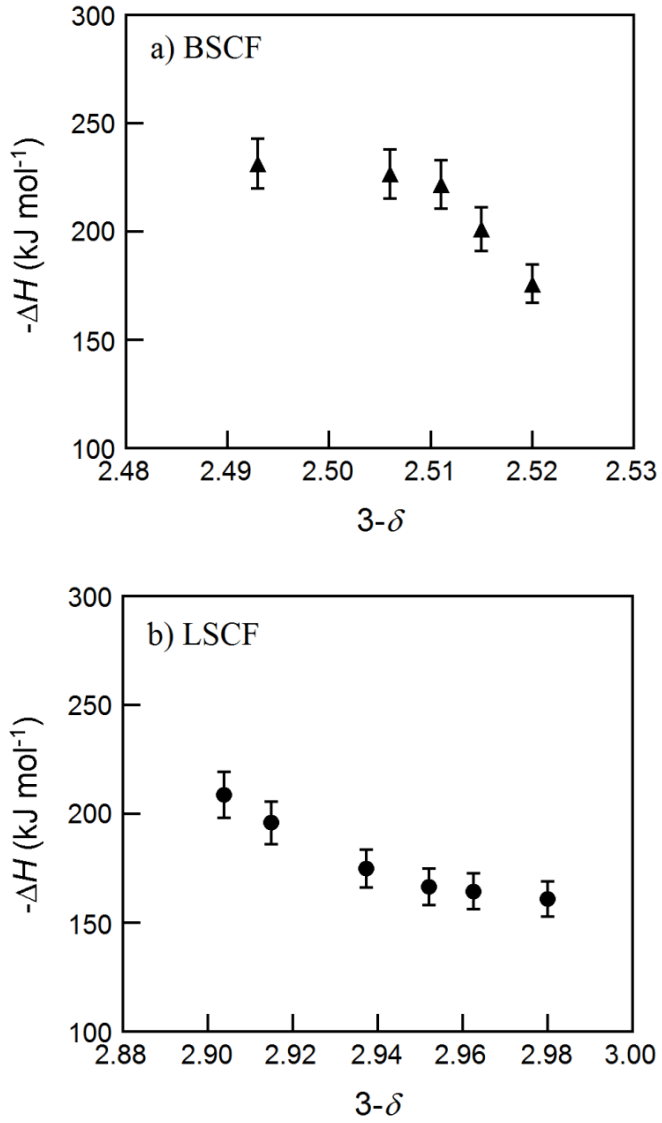

Figure 3.8. Partial molar enthalpy of oxidation (ΔH) at 973 K of (a) $Ba_{0.5}Sr_{0.5}Co_{0.8}Fe_{0.2}O_{3-\delta}$ and (b) $La_{0.6}Sr_{0.4}Co_{0.2}Fe_{0.8}O_{3-\delta}$.

The partial molar entropies of oxidation calculated from the differences in the Gibbs free energies and the enthalpies are shown in Figure 3.9. The partial molar entropies of oxidation for BSCF range from -200 to -150 J mol^{-1} K^{-1}, and the LSCF range from -170 to -140 J mol^{-1} K^{-1}. The partial molar entropies of BSCF and LSCF are not much different, which means that the probability of oxygen vacancy formation reaction is similar.

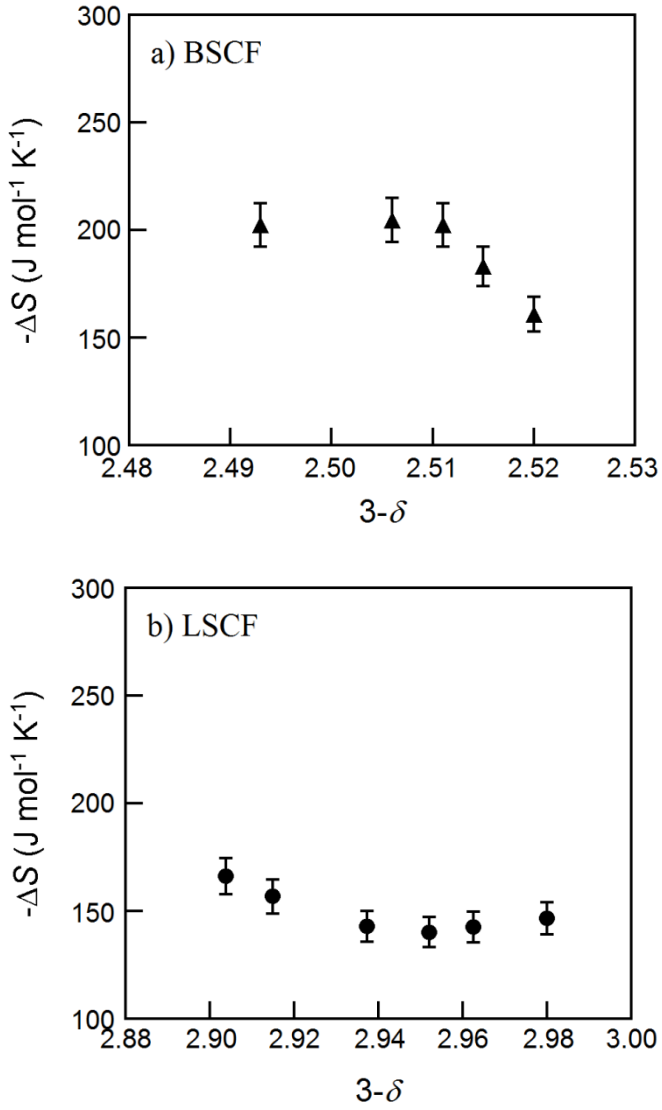

Figure 3.9. Partial molar entropy of oxidation (ΔS) at 973 K of (a) $Ba_{0.5}Sr_{0.5}Co_{0.8}Fe_{0.2}O_{3-\delta}$ and (b) $La_{0.6}Sr_{0.4}Co_{0.2}Fe_{0.8}O_{3-\delta}$.

3. 4. Conclusions

The redox properties of BSCF and LSCF perovskite were investigated using coulometric titration. The isotherms indicate that BSCF and LSCF operating around 10^{-5} atm and 1023 K can be stable without experiencing steep change in chemical stability because the decomposition is expected to occur around 10^{-5}-10^{-6} atm. The partial enthalpies of oxidation for the BSCF range from -240 to -170 kJ mol^{-1} and those of the LSCF range from -210 to -160 kJ mol^{-1}. The partial molar entropies of oxidation for BSCF and LSCF vary between -200 to -150 J mol^{-1} K^{-1} and between -170 to -140 J mol^{-1} K^{-1}, respectively. The electrical conductivity of BSCF and LSCF was increased with $p(O_2)$ in all cases over the entire temperature range, indicating that this material is a *p*-type electronic conductor. The BSCF and LSCF

are considered to be a suitable cathode material of IT-SOFC in terms of electrical conductivity and redox stability.

References

(1) Steele, B. C.; Heinzel, A. Materials for Fuel-Cell Technologies. *Nature* **2001**, *414*, 345–352.

(2) Shao, Z.; Haile, S. M. A High-Performance Cathode for the next Generation of Solid-Oxide Fuel Cells. *Nature* **2004**, *431*, 170–173.

(3) Brandon, N. P.; Skinner, S.; Steele, B. C. H. Recent Advances in Materials for Fuel Cells. *Annu. Rev. Mater. Res.* **2003**, *33* (1), 183–213.

(4) Petric, A.; Huang, P.; Tietz, F. Evaluation of La-Sr-Co-Fe-O Perovskites for Solid Oxide Fuel Cells and Gas Separation Membranes. *Solid State Ionics* **2000**, *135*, 719–725.

(5) Adler, S. B.; Lane, J. A.; Steele, B. C. H. Electrode Kinetics of Porous Mixed-Conducting Oxygen Electrodes. *J. Electrochem. Soc.* **1996**, *143* (11), 3554–3564.

(6) Ried, P.; Holtappels, P.; Wichser, A.; Ulrich, A.; Graule, T. Synthesis and Characterization of $La_{0.6}Sr_{0.4}Co_{0.2}Fe_{0.8}O_{3-\delta}$ and $Ba_{0.5}Sr_{0.5}Co_{0.8}Fe_{0.2}O_{3-\delta}$. *J. Electrochem. Soc.* **2008**, *155* (10), B1029–B1035.

(7) Stevenson, J. W.; Armstrong, T. R.; Carneim, R. D.; Pederson, L. R.; Weber, W. J. Electrochemical Properties of Mixed Conducting Perovskites $La_{1-x}M_xCo_{1-y}Fe_yO_{3-\delta}$ (M=Sr,Ba,Ca). *J. Electrochem. Soc.* **1996**, *143* (9), 2722–2729.

(8) Wei, B.; Lü, Z.; Li, S.; Liu, Y.; Liu, K.; Su, W. Thermal and Electrical Properties of New Cathode Material $Ba_{0.5}Sr_{0.5}Co_{0.8}Fe_{0.2}O_{3-\delta}$ for Solid Oxide Fuel Cells. *Electrochem. Solid-State Lett.* **2005**, *8* (8), A428–A431.

(9) Niedrig, C.; Taufall, S.; Burriel, M.; Menesklou, W.; Wagner, S. F.; Baumann, S.; Ivers-Tiffée, E. Thermal Stability of the Cubic Phase in $Ba_{0.5}Sr_{0.5}Co_{0.8}Fe_{0.2}O_{3-\delta}$ (BSCF)1. *Solid State Ionics* **2011**, *197*, 25–31.

(10) Esquirol, A.; Brandon, N. P.; Kilner, J. A.; Mogensen, M. Electrochemical Characterization of $La_{0.6}Sr_{0.4}Co_{0.2}Fe_{0.8}O_3$ Cathodes for Intermediate-Temperature SOFCs. *J. Electrochem. Soc.* **2004**, *151* (11), A1847–A1855.

(11) Tai, L. W.; Nasrallah, M. M.; Anderson, H. U. Thermochemical Stability, Electrical-Conductivity, and Seebeck Coefficient of Sr-Doped $LaCo_{0.2}Fe_{0.8}O_{3-\delta}$. *Journal of Solid State Chemistry*. 1995, *118*, 117–124.

(12) Yoo, S.; Shin, J. Y.; Kim, G. Thermodynamic and Electrical Characteristics of $NdBaCo_2O_{5+\delta}$ at Various Oxidation and Reduction States. *J. Mater. Chem.* **2011**, *21* (2), 439–44.

(13) Chen, Z.; Ran, R.; Zhou, W.; Shao, Z.; Liu, S. Assessment of $Ba_{0.5}Sr_{0.5}Co_{1-y}Fe_yO_{3-\delta}$ (y = 0.0-1.0) for Prospective Application as Cathode for IT-SOFCs or Oxygen Permeating Membrane. *Electrochim. Acta* **2007**, *52* (25), 7343–7351.

(14) Liu, Z.; Han, M. F.; Miao, W. T. Preparation and Characterization of Graded Cathode $La_{0.6}Sr_{0.4}Co_{0.2}Fe_{0.8}O_{3-\delta}$ *J. Power Sources* **2007**, *173*, 837–841.

(15) Yoo, S.; Shin, J. Y.; Kim, G. Thermodynamic and Electrical Properties of Layered Perovskite

$NdBaCo_{2-x}Fe_xO_{5+\delta}$−YSZ ($x$ = 0, 1) Composites for Intermediate Temperature SOFC Cathodes. *J. Electrochem. Soc.* **2011**, *158* (6), B632–B638.

(16) Bastidas, D. M.; Tao, S.; Irvine, J. T. S. A Symmetrical Solid Oxide Fuel Cell Demonstrating Redox Stable Perovskite Electrodes. *J. Mater. Chem.* **2006**, *16* (17), 1603–1605.

(17) Shao, Z.; Xiong, G.; Tong, J.; Dong, H.; Yang, W. Ba Effect in Doped $Sr(Co_{0.8}Fe_{0.2})O_{3-\delta}$ on the Phase Structure and Oxygen Permeation Properties of the Dense Ceramic Membranes. *Sep. Purif. Technol.* **2001**, *25*, 419–429.

(18) Ge, L.; Zhou, W.; Ran, R.; Liu, S.; Shao, Z.; Jin, W.; Xu, N. Properties and Performance of A-Site Deficient $(Ba_{0.5}Sr_{0.5})_{1-x}Co_{0.8}Fe_{0.2}O_{3-\delta}$ for Oxygen Permeating Membrane. *J. Memb. Sci.* **2007**, *306*, 318–328.

(19) Tai, L.-W.; Nasrallah, M. M.; Anderson, H. U.; Sparlin, D. M.; Sehlin, S. R. Structure and Electrical Properties of $La_{1-x}Sr_xCo_{1-y}Fe_yO_3$. Part 1. The System $La_{0.8}Sr_{0.2}Co_{1-y}Fe_yO_3$. *Solid State Ionics* **1995**, *76*, 273–283.

(20) Nakamura, T.; Yashiro, K.; Sato, K.; Mizusaki, J. Thermodynamic Quantities and Defect Equilibrium in $La_{2-x}Sr_xNiO_{4+\delta}$ *J. Solid State Chem.* **2009**, *182* (5), 1121–1128.

Chapter 4. Optimization of Sr content in layered $SmBa_{1-x}Sr_xCo_2O_{5+\delta}$ perovskite cathodes for intermediate-temperature solid oxide fuel cells

4.1. Introduction

Solid oxide fuel cells (SOFCs) are a new power generation device with high energy conversion efficiency and excellent fuel flexibility. High operating temperature of 800-1000 °C, however, leads to crucial issues such as high costs and material compatibility challenges. The focus of research on SOFC technology has shifted toward operation at intermediate operating temperature (500-700 °C) in order to improve material compatibility and practical applicability.[1,2] The lower operating temperature, however, results in a serious decline in electrode activity. Therefore, cathode materials with high electrocatalytic activity for the oxygen reduction reaction should be developed, because the polarization loss on the cathode limits the cell performance at intermediate operating temperature.[3]

In this regard, mixed ionic electronic conductors (MIECs), with both electronic and ionic conductivity,[4] are promising cathode materials for intermediate temperature solid oxide fuel cells (IT-SOFCs). The reaction sites of MIECs can extend the electrochemically active area, because the oxygen exchange reaction occurs not only on the triple-phase boundary (TPB) between the electrolyte, cathode, and gas phase but also on the two phase boundary between the electrode and gas phase.[5,6] In particular, cobalt containing MIECs such as $Ba_{0.5}Sr_{0.5}Co_{0.8}Fe_{0.2}O_{3-\delta}$,[7] $La_{0.6}Sr_{0.4}Co_{0.2}Fe_{0.8}O_{3-\delta}$,[8] $Pr_{1-x}Sr_xCoO_{3-\delta}$,[9] and $Sm_{0.5}Sr_{0.5}CoO_3$[10] have been proposed as cathode materials for SOFCs at intermediate temperatures owing to their high electrical conductivity and high catalytic activity for the oxygen reduction reaction (ORR).

Recently, many researchers also have focused on layered perovskite oxides, based on their much higher chemical diffusion and surface exchange coefficients relative to those of ABO_3-type perovskite oxides. The general formula of LnBCO oxides is $AA'B_2O_{5+\delta}$, where the A and A′ sites are assigned as lanthanides and Ba, respectively, and they have stacking layers of $[CoO_2]$-$[LnO_\delta]$-$[CoO_2]$-[BaO] along the *c*-axis.[11] It can be speculated that alternating lanthanide and alkali-earth planes will enhance the oxygen transport kinetics compared with the ABO_3-type perovskite oxides,[12] as layered perovskites were reported to provide reduced oxygen bonding strength and disorder-free channels for ion motion.[13]

On the basis of these promising properties, several groups have studied the structural and physical properties of layered perovskites, including $LnBaCo_2O_{5+\delta}$ (LnBCO, Ln = Pr, Sm, and Gd).[14-16] Kim *et al*.[17] also reported that $PrBaCo_2O_{5+\delta}$ offers faster oxygen ion diffusion and surface exchange kinetics compared with $La_{0.5}Sr_{0.5}CoO_{3-\delta}$ at intermediate temperature (500-700 °C), which are reflected in very low area specific resistance.

Some researchers have reported that the substitution of Sr for Ba in LnBCO can improve the

conductivity and the catalytic activity for the ORR of layered perovskite oxides.[18,19] The substitution of Sr for Ba in a $GdBaCo_2O_{5+\delta}$ cathode enhanced the chemical stability between the electrode and electrolyte as well as the oxygen transport.[20] In addition, Mckinlay *et al*.[21] found that Sr substitution in $YBa_{1-x}Sr_xCo_2O_{5+\delta}$ causes a structural change from orthorhombic to tetragonal and a roughly 32-fold increase of electrical conductivity compared to that of a Sr-free sample. Kim *et al*.[22] have shown that a layered $SmBa_{0.5}Sr_{0.5}Co_2O_{5+\delta}$ perovskite has advanced electrochemical properties and can be potentially utilized as a cathode material for IT-SOFC applications. Their studies, however, focus on only one composition, x = 0.5, in $SmBa_{1-x}Sr_xCo_2O_{5+\delta}$ and do not provide a systematic investigation of the strontium effect. In this study, we investigate the effects of strontium doping on crystal characteristics, electrical properties, and electrochemical performance of $SmBa_{1-x}Sr_xCo_2O_{5+\delta}$ (x = 0, 0.25, 0.5, 0.75, and 1.0) in relation to its application as an IT-SOFC cathode material.

4.2. Experimental

Table 4.1. Abbreviations of Specimens.

Chemical composition	Abbreviations
$Ce_{0.9}Gd_{0.1}O_{2-\delta}$	GDC
$SmBaCo_2O_{5+\delta}$	SBCO
$SmBa_{0.75}Sr_{0.25}Co_2O_{5+\delta}$	SBSCO25
$SmBa_{0.5}Sr_{0.5}Co_2O_{5+\delta}$	SBSCO50
$SmBa_{0.25}Sr_{0.75}Co_2O_{5+\delta}$	SBSCO75
$SmSrCo_2O_{5+\delta}$	SSCO

The $SmBa_{1-x}Sr_xCo_2O_{5+\delta}$ cathodes were synthesized by the Pechini method. Stoichiometric amounts of $Sm(NO_3)_3 \cdot 6H_2O$(Aldrich, 99+%, metal basis), $Ba(NO_3)_2$ (Aldrich, 99+%), $Sr(NO_3)_2$ (Aldrich, 99+%), $Co(NO_3)_2 \cdot 6H_2O$ (Aldrich, 98+%), and citric acid were dissolved in distilled water to form an aqueous mixed solution. An adequate amount of ethylene glycol was added into the beaker after the mixture was dissolved. After a viscous resin was formed, the mixture was heated to roughly 250 ºC. The resultant powder was calcined at 600 ºC for 4 h and ball milled in acetone for 24 h. For the final step to form a phase, the powder was pressed into pellets and then sintered in air at various temperatures. SBCO was sintered in air at 1100 ºC for 12 h, while SBSCO25, SBSCO50, SBSCO75, and SSCO were sintered at 1150 ºC for 12 h. The abbreviations used to identify the various samples are summarized in Table 4.1. For the cathode slurry, $SmBa_{1-x}Sr_xCo_2O_{5+\delta}$ and GDC powders were thoroughly mixed together at a weight ratio of 6:4 and the mixed powders were blended with an organic binder (Heraeus V006) to form slurries thereafter.

The structure of $SmBa_{1-x}Sr_xCo_2O_{5+\delta}$ was characterized by using an X-ray diffractometer (Rigaku diffractometer, Cu Ka radiation) at a scanning rate of 0.6 ° min^{-1} and a range 20 ° < 2θ < 100 °. The powder pattern and lattice parameters were analyzed by Rietveld refinement using the GSAS program. The microstructures of the $SmBa_{1-x}Sr_xCo_2O_{5+\delta}$ composites and cross sections of single cells were investigated using a field emission scanning electron microscope (Nova SEM). A thermogravimetric analysis (TGA) was performed using a SDT-Q600 (TA instrument, USA) from 100 to 900 °C with a heating/cooling rate of 2 °C min^{-1} in air. The initial oxygen contents of the $SmBa_{1-x}Sr_xCo_2O_{5+\delta}$ oxides were determined by iodometric titration.

For measurement of electrical conductivity, the powder was pressed into a cylindrical shape and sintered to dense pellets (>98 % density). The electrical conductivities of $SmBa_{1-x}Sr_xCo_2O_{5+\delta}$ samples were measured by a four-terminal DC arrangement technique. The current and the voltage were recorded by a BioLogic Potentiostat from 100 to 750 °C at intervals of 50 °C in air.

Impedance spectroscopy of $SmBa_{1-x}Sr_xCo_2O_{5+\delta}$ was carried out using a symmetric cell. The $Ce_{0.9}Gd_{0.1}O_{2-\delta}$ (GDC) powder was pressed into pellets and sintered at 1350 °C for 4 h in air to obtain a ~ 1 mm-thick electrolyte substrate. Slurries of the $SmBa_{1-x}Sr_xCo_2O_{5+\delta}$-GDC composite were screen-printed onto both sides of the dense GDC electrolyte to form a symmetrical cell, which was then heated at 950 °C for 4 h. The silver paste was used as the current collector for the electrodes.

A NiO-GDC anode-supported cell was fabricated to measure the electrochemical performance of $SmBa_{1-x}Sr_xCo_2O_{5+\delta}$. The NiO-GDC cermet anode was prepared by a mixture of nickel oxide, GDC, and starch at a weight ratio of 6:4:1.5 after being ball milled in ethanol for 24 h. The GDC electrolyte was pressed onto the pelletized disk of the NiO-GDC cermet anode. This NiO-GDC|GDC anode-supported cell was sintered at 1350 °C for 5 h and cathode slurries were applied onto the surface of the GDC electrolyte layer by screen printing. A tri-layer $SmBa_{1-x}Sr_xCo_2O_{5+\delta}$-GDC|GDC|NiO-GDC cell with an active electrode area of 0.36 cm^2 was finally sintered at 950 °C for 4 h in air. The electrolyte and cathode thickness of a single cell were about 15 μm with a 500 μm thick anode. For the single-cell performance test, Ag wires were attached at both electrodes of the single cell using Ag paste as a current collector. The single cell was fixed on an alumina tube using a ceramic adhesive (Aremco, Ceramabond 552). Humidified hydrogen (3 % H_2O) was supplied as fuel through a water bubbler with a flow rate of 20 mL min^{-1} and the ambient air was used as an oxidant during single cell tests. *I-V* curves and impedance spectra were examined using a BioLogic Potentiostat at operating temperature from 500 to 650 °C. Impedance spectra were recorded under OCV in a frequency range of 1 mHz to 500 kHz with AC perturbation of 14 mA from 500 to 650 °C.

4.3. Results and Discussions

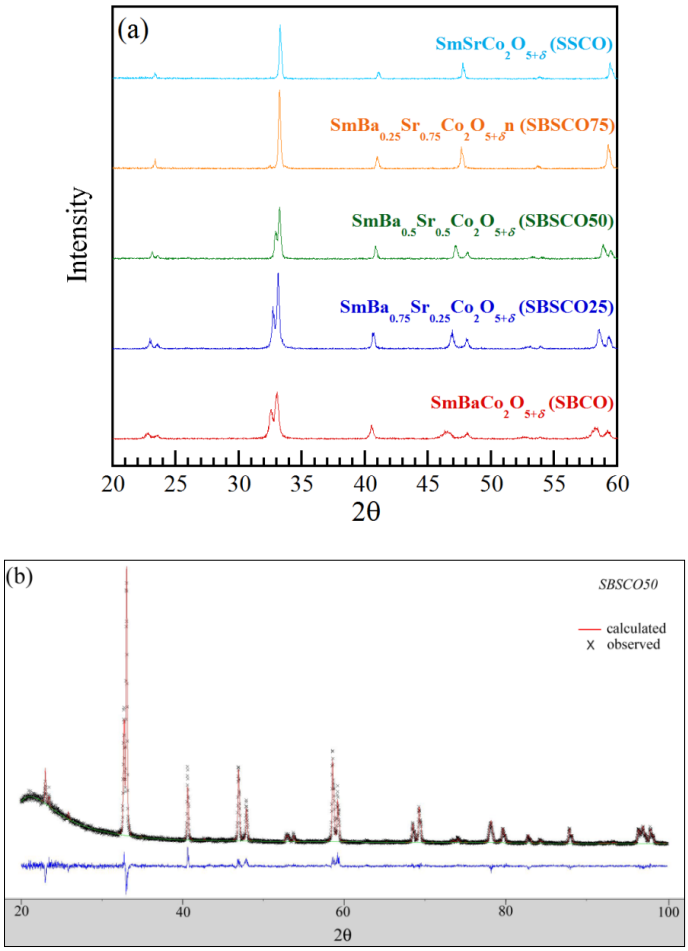

Figure 4.1. (a) XRD patterns of $SmBa_{1-x}Sr_xCo_2O_{5+\delta}$ (x = 0, 0.25, 0.5, 0.75, and 1.0) powders, (b) observed and calculated XRD profiles and the difference between them for SBSCO50.

XRD patterns of $SmBa_{1-x}Sr_xCo_2O_{5+\delta}$ samples for different strontium content (x = 0, 0.25, 0.5, 0.75, and 1.0) are shown in Figure 4.1(a) and structural data are given in Table 4.2. The XRD patterns indicate that all $SmBa_{1-x}Sr_xCo_2O_{5+\delta}$ specimens are single-phase perovskite without any detectable impurity phases. The Rietveld refinement data reveal that the diffraction pattern of SBCO and SBSCO25 samples could be indexed to an orthorhombic structure (space group: *Pmmm*) while those of SBSCO50 and SBSCO75 cathodes reflect a tetragonal structure (space group: *P4/mmm*),[23,24] with all samples being an ordered perovskite structure. For SSCO in which Ba is fully replaced by Sr, the diffraction pattern is indexed with an orthorhombic structure (space group: *Pbnm*) and identified as a disordered perovskite structure. The data in Table 4.2 indicate that the lattice parameters and the unit cell volume of $SmBa_{1-x}Sr_xCo_2O_{5+\delta}$ samples decrease with increasing Sr content due to the substitution of the smaller ionic radii of Sr^{2+} for Ba^{2+}. As an example illustrating the refinement of SBSCO50, Figure 4.1(b) shows the measured XRD data, the calculated profile, and the difference between them for SBSCO50. There is excellent agreement between the experimental data and the calculated profiles,

suggesting that cations are well ordered between Sm^{3+} and Ba^{2+}/Sr^{2+} ions in the ordered perovskite lattice.

Table 4.2. Structural parameters and oxygen content of the $SmBa_{1-x}Sr_xCo_2O_{5+\delta}$ oxides.

	Space Group	*a* (Å)	*b* (Å)	*c* (Å)	V (Å^3)	Oxygen content (5 + δ)
SBCO	*Pmmm*	3.8997	3.9183	7.5908	115.9889	5.62
SBSCO25	*Pmmm*	3.8858	3.8912	7.5889	114.7473	5.70
SBSCO50	*P4/mmm*	3.8674	3.8674	7.5857	113.4576	5.76
SBSCO75	*P4/mmm*	3.8344	3.8344	7.6640	112.6809	5.87
SSCO	*Pbnm*	5.4025	5.3830	7.6264	221.7883 (110.8941)	6.00

In general, the phase reaction between an electrode and electrolyte can generate an undesired insulating layer at the interface, which obstructs the oxide-ionic and electronic transport.[25] The chemical reactivity between $SmBa_{1-x}Sr_xCo_2O_{5+\delta}$ and GDC is therefore examined by sintering the corresponding powders in a 6:4 weight ratio at 950 °C for 4 h. The XRD spectra of $SmBa_{1-x}Sr_xCo_2O_{5+\delta}$-GDC are illustrated in Figure 4.2 to confirm the absence of chemical reactivity, and there are no observed interfacial reactions or apparent secondary phases between them.

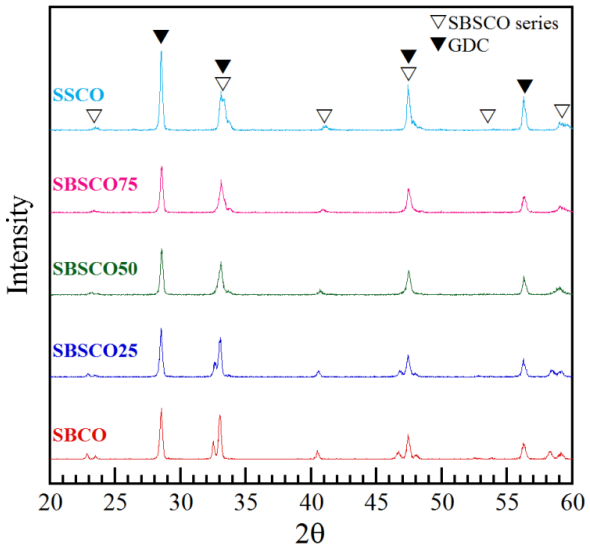

Figure 4.2. XRD patterns of $SmBa_{1-x}Sr_xCo_2O_{5+\delta}$-GDC mixture sintered at 950 °C for 4 h.

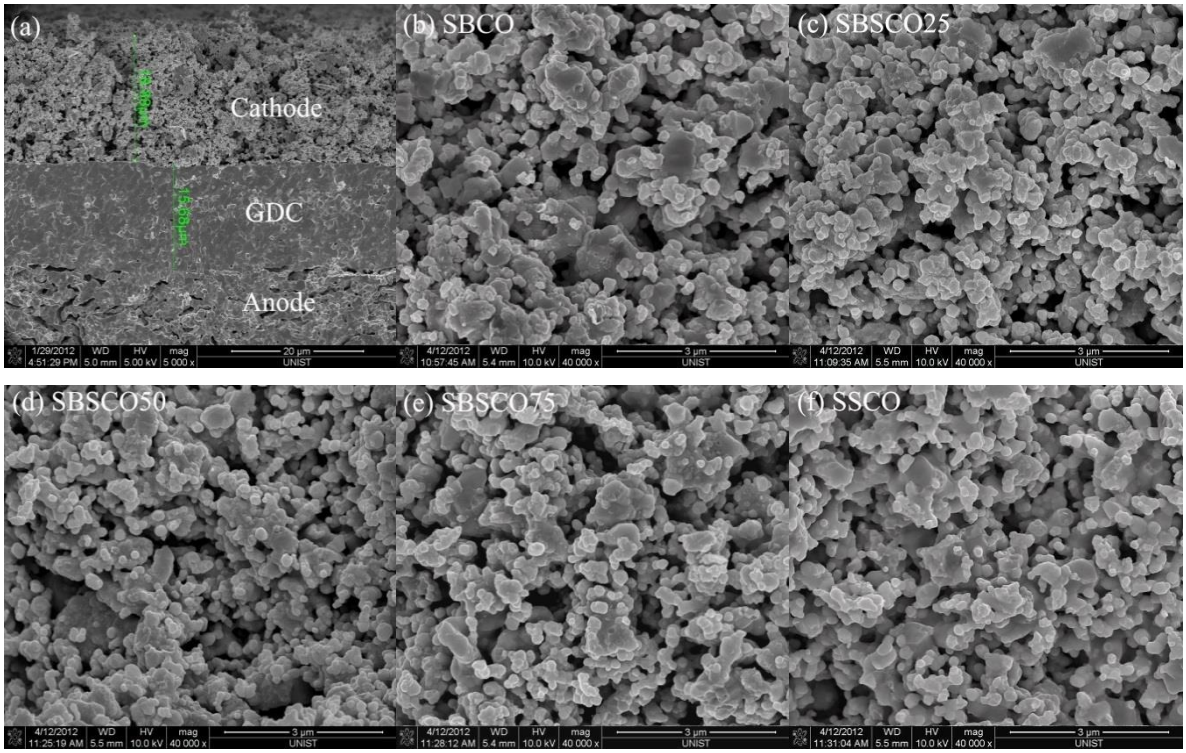

Figure 4.3. SEM micrographs showing (a) the cross section of SBSCO75-GDC|GDC|NiO-GDC and (b)-(f) $SmBa_{1-x}Sr_xCo_2O_{5+\delta}$-GDC cathodes; (b) SBCO, (c) SBSCO25, (d) SBSCO50, (e) SBSCO75, and (f) SSCO.

The electrode microstructure is linked to the characteristics of the surface, the TPB area, the volume fraction of chemical phases present, and electron transport. These properties affect the fuel cell performance through the reaction kinetics, charge transport, and mass transport processes.[26,27] Figure 4.3(a) shows the microstructure of a cross section of SBSCO75-GDC|GDC|NiO-GDC, showing a 15-μm cathode and 15-μm electrolyte. The adhesion between the cathode and electrolyte appears to be very good and the electrolyte is dense with no cracks or pores. Furthermore, the cathode has a porous microstructure, which will result in fast transport of gases and high electro-catalyst reactions. As seen in Figures 4.3(b)-(f), the microstructure of all $SmBa_{1-x}Sr_xCo_2O_{5+\delta}$-GDC composites ($x$ = 0, 0.25, 0.5, 0.75, and 1.0) samples are similar, and thus this factor appears to be insensitive to Sr substitution.

Figure 4.4 shows the variation of the oxygen content with temperature in air for $SmBa_{1-x}Sr_xCo_2O_{5+\delta}$ ($0 \leq x \leq 1.0$) samples. The inset in Figure 4.4 shows TGA data collected by the weight change of $SmBa_{1-x}Sr_xCo_2O_{5+\delta}$ samples upon heating to 900 °C in air. All $SmBa_{1-x}Sr_xCo_2O_{5+\delta}$ samples show initial weight change above 200 °C due to the release of lattice oxygen, with weight loss of 1.3-1.7 % from 25 to 900 °C. According to the iodometric titration data presented in Table 4.2, the initial oxygen content increases gradually from 5.62 to 6.00 with increasing Sr content at room temperature.

This is attributed to the smaller size difference between Sr^{2+} (1.44 Å) and Sm^{3+} (1.24 Å) as compared to that between Ba^{2+} (1.60 Å) and Sm^{3+} (1.24 Å). The smaller size difference and consequent alteration of the ordering between Ba and Sm layer result in a tendency to increase the coordination number of Sm and consequently the oxygen content values.[20]

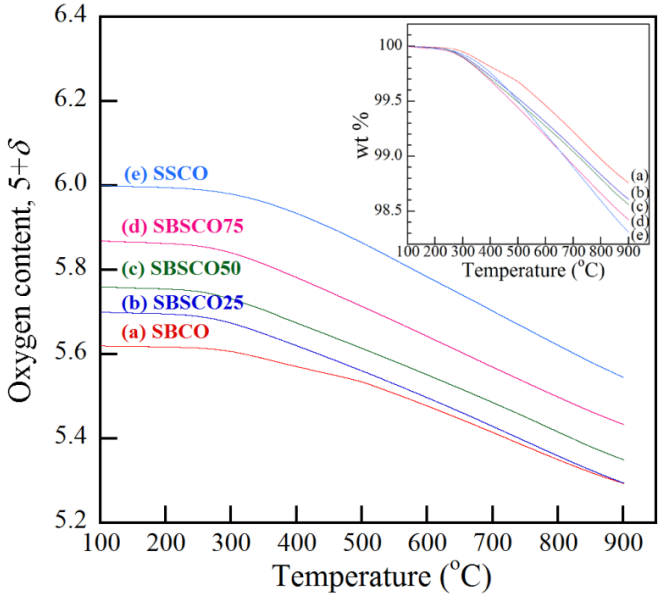

Figure 4.4. Variations of oxygen contents in $SmBa_{1-x}Sr_xCo_2O_{5+\delta}$ with temperature in air. The inset shows thermogravimetric analysis data by the weight change with temperature in air; (a) SBCO, (b) SBSCO25, (c) SBSCO50, (d) SBSCO75, and (e) SSCO.

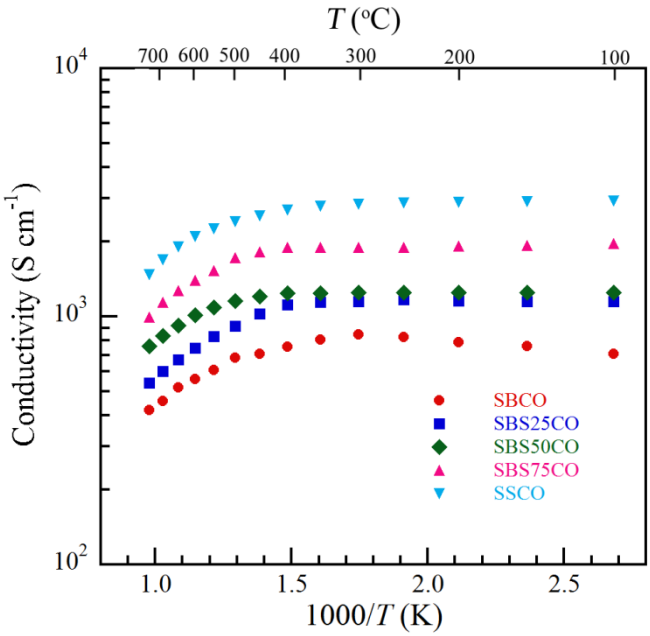

Figure 4.5. Electrical conductivities of $SmBa_{1-x}Sr_xCo_2O_{5+\delta}$ at various temperatures from 100 to 750 °C in air.

The electrical conductivity of $SmBa_{1-x}Sr_xCo_2O_{5+\delta}$ cathodes in air is displayed by an Arrhenius plot in Figure 4.5. High electrical conductivity is one of the fundamental requirements for a good cathode material at intermediate operating temperature. The lowest electrical conductivity of all $SmBa_{1-x}Sr_xCo_2O_{5+\delta}$ samples is still higher than 400 S cm^{-1} from 100 to 750 °C. This means that all $SmBa_{1-x}Sr_xCo_2O_{5+\delta}$ samples could satisfy the requirements of electrical conductivity for use as an IT-SOFC cathode.[28] All $SmBa_{1-x}Sr_xCo_2O_{5+\delta}$ samples show decreasing electrical conductivity with increasing temperature, indicating metallic conducting behavior. There is a significant drop of electrical conductivity over 400 °C due to the loss of oxygen atoms from the lattice.[29] Electrical conductivity is proportional to Sr content at a given temperature, which can be interpreted as the effect of the mobile interstitial oxygen as follows. The predominant defects in $SmBa_{1-x}Sr_xCo_2O_{5+\delta}$ samples are the interstitial oxygen, O_i'', and the electronic holes, $h^{\bullet}$.[30-32] The following pseudo-chemical reaction takes place between the defects and the atmosphere, using the Kröger-Vink notation.[33]

$$\frac{1}{2}O_2(g) + V_i^x + 2Co_{Co}^x \rightleftarrows O_i'' + 2Co_{Co}^{\bullet} \qquad \text{Eqn. 4.1}$$

The electroneutrality leads to the following equation:

$$2[O_i''] = [h^{\bullet}] \qquad \text{Eqn. 4.2}$$

The increase in the interstitial oxygen concentration with Sr content results in an increase of electronic holes, which is finally responsible for the higher electronic conductivities.

The area specific resistance (ASR) of $SmBa_{1-x}Sr_xCo_2O_{5+\delta}$ is obtained by AC impedance spectroscopy for $SmBa_{1-x}Sr_xCo_2O_{5+\delta}$-GDC|GDC|$SmBa_{1-x}Sr_xCo_2O_{5+\delta}$-GDC symmetrical cells. The ASR values are determined by the impedance intercept between high-frequency and low-frequency with the real axis of the Nyquist plot, and representative impedance spectra are presented in Figure 4.6(a). Figure 4.6(b) shows the various ASRs of $SmBa_{1-x}Sr_xCo_2O_{5+\delta}$ measured at 600 °C in air. The ASRs of $SmBa_{1-x}Sr_xCo_2O_{5+\delta}$ decrease with Sr content up to $x = 0.75$ and increases suddenly for SSCO ($x = 1$). The ASRs of SBCO, SBSCO25, SBSCO50, SBSCO75, and SSCO are 0.192, 0.168, 0.141, 0.138, and 0.284 Ω cm^2, respectively, at 600 °C. According to the Adler-Lane-Steele (ALS) model, the ASR is related to oxygen kinetics, such as bulk diffusion (D_o^*) and surface exchange (k_o^0);[5] this can be expressed as

$$R_{cathode} = \frac{RT}{2F^2}\left[\frac{\tau}{(1-\emptyset)Sc_0^2 D_0^* k_0^0}\right]^{1/2} \qquad \text{Eqn. 4.3}$$

where $\emptyset$, S, and τ are the porosity, surface area, and tortuosity, respectively. On the assumption that the parameters of microstructure, such as porosity, cathode surface area, and tortuosity, are similar, high bulk diffusion and surface exchange lead to lower ASR values. Therefore, SBSCO75 is expected to provide fast oxygen diffusion in the bulk and high surface kinetics on the surface of the electrode among the $SmBa_{1-x}Sr_xCo_2O_{5+\delta}$ samples.

Arrhenius plots of 1/ASR at various Sr content are shown in Figure 4.6(c). The activation energy is directly related to the cathode properties including oxygen adsorption, dissociation, and surface/bulk diffusion.[17,34] The activation energies of $SmBa_{1-x}Sr_xCo_2O_{5+\delta}$ are calculated from the Arrhenius plots of the fitted line. The activation energy of $SmBa_{1-x}Sr_xCo_2O_{5+\delta}$ (x = 0, 0.25, 0.5, and 0.75) is around 110 kJ mol^{-1} and that of SSCO is 120.6 kJ mol^{-1}. The activation energy of the ABO_3-type perovskite oxide SSCO is similar to that of $La_{0.6}Sr_{0.4}Co_{0.2}Fe_{0.8}O_{3-\delta}$ (LSCF6428), which is reported to be 121.6 kJ mol^{-1}.[35] It is suggested that, due to the difference in the activation energy, the oxygen reduction mechanism in $SmBa_{1-x}Sr_xCo_2O_{5+\delta}$ (x = 0, 0.25, 0.5, and 0.75) might be different from that of SSCO.

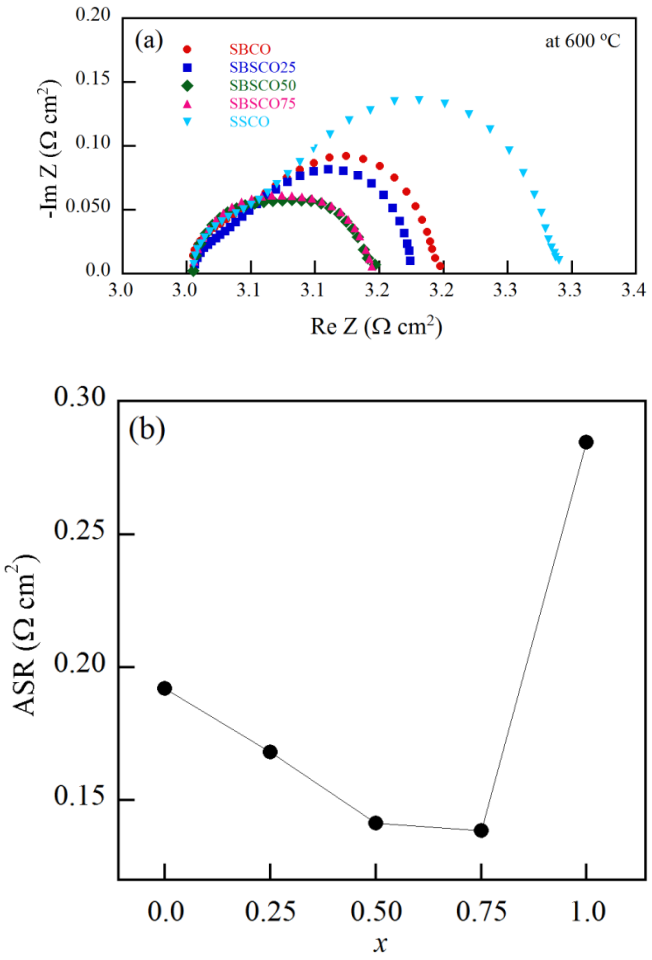

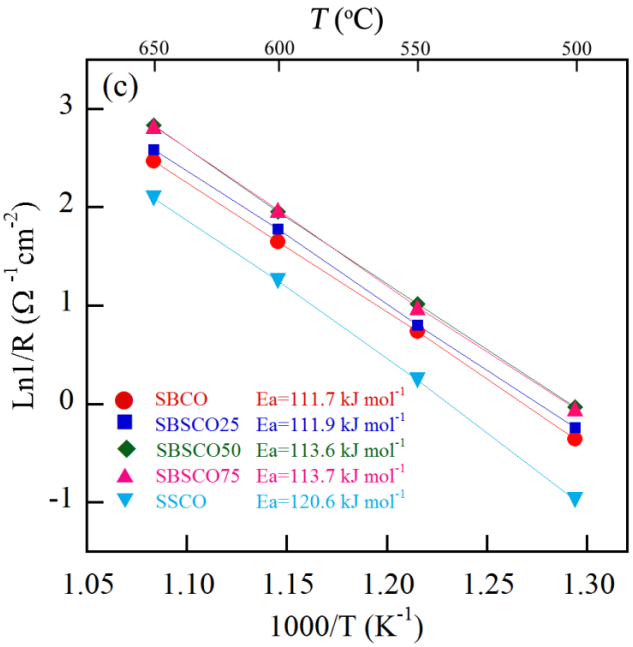

Figure 4.6. (a) Impedance spectra of $SmBa_{1-x}Sr_xCo_2O_{5+\delta}$-GDC|GDC|$SmBa_{1-x}Sr_xCo_2O_{5+\delta}$-GDC at 600 °C under OCV; (b) The ASRs of a symmetric cell measured at 600 °C in air, (c) Arrhenius plots of 1/ASR at various Sr contents.

Figure 4.7 shows the power density and voltage as a function of current density for the $SmBa_{1-x}Sr_xCo_2O_{5+\delta}$-GDC|GDC|NiO-GDC cells using humidified H_2 (3 % H_2O) as a fuel and ambient air as an oxidant in a temperature range of 500-650 °C. The full cell performances improve with increasing strontium content up to x = 0.75 in the $SmBa_{1-x}Sr_xCo_2O_{5+\delta}$ oxides, while SSCO shows a sudden reduction of cell performance. For example, the maximum power density of SBCO, SBSCO25, SBSCO50, SBSCO75, and SSCO is 0.848, 0.875, 0.964, 1.039, and 0.713 W cm^{-2}, respectively, at 600 °C. The maximum power densities of SBSCO50 and SBSCO75 are remarkably high, thus showing that the strontium in $SmBa_{1-x}Sr_xCo_2O_{5+\delta}$ layered perovskites can enhance the electrochemical performance of a single cell.

This can be explained by the finding that SBSCO50 and SBSCO75 could be indexed to tetragonal lattice geometry while SBCO and SBSCO25 reflect an orthorhombic structure. Generally, a tetragonal structure is characterized by faster oxygen diffusion in the bulk and surface and higher catalytic activity for the ORR as compared to an orthorhombic structure.[36] The ABO_3-type perovskite oxide SSCO exhibits a sudden drop in cell performance, which is associated with a higher ASR value in symmetric impedance measurement. Therefore, the layered perovskite oxides with higher Sr content in the A site (x = 0.5 and 0.75) are thought to have rapid oxygen kinetics due to reduced oxygen bonding strength in the [AO] layer and a disorder-free channel for ion diffusion.[37]

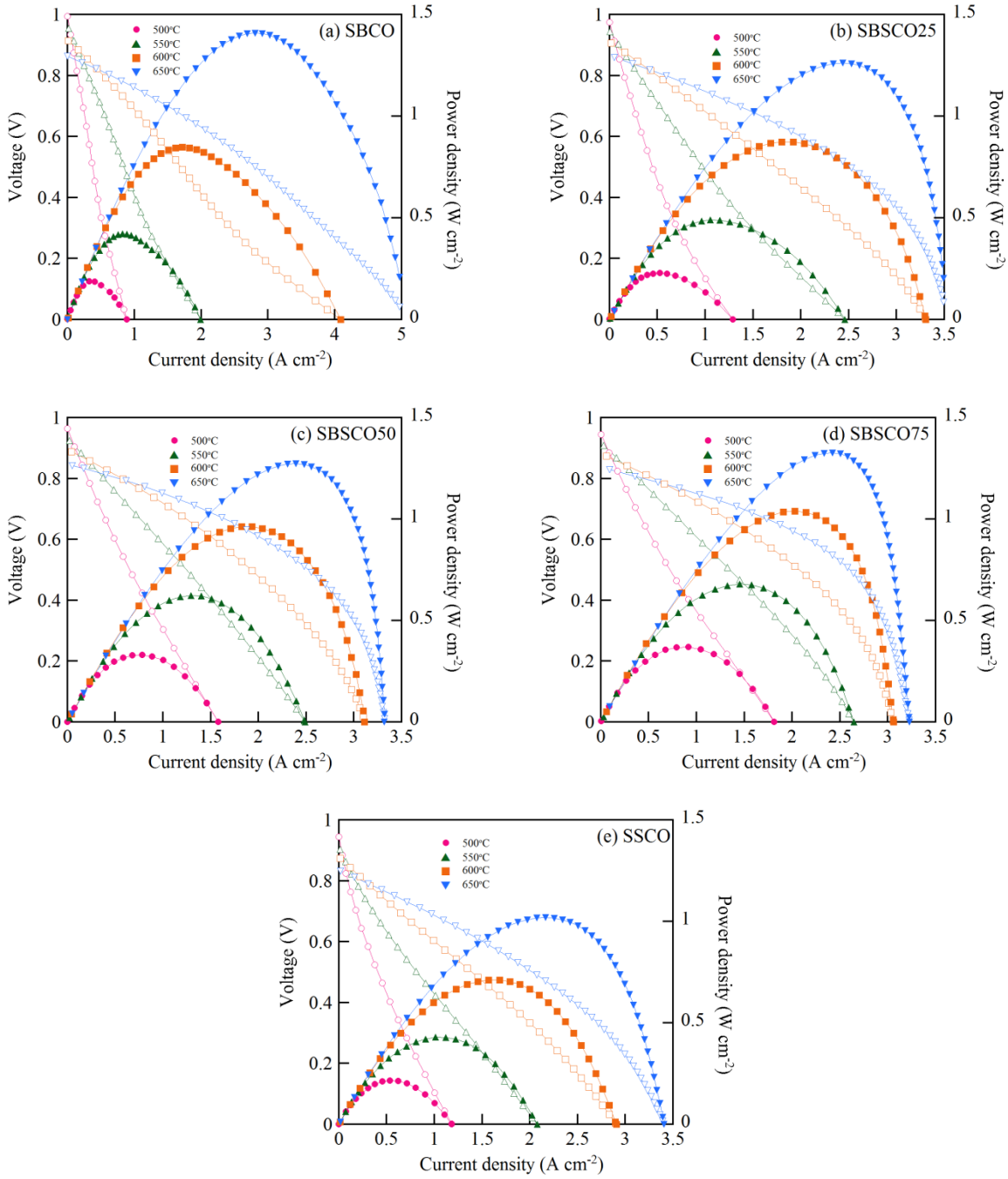

Figure 4.7. *I-V* curve for $SmBa_{1-x}Sr_xCo_2O_{5+\delta}$-GDC|GDC|NiO-GDC at different temperatures: (a) SBCO, (b) SBSCO25, (c) SBSCO50, (d) SBSCO75, and (e) SSCO.

4.4. Conclusions

$SmBa_{1-x}Sr_xCo_2O_{5+\delta}$ (x = 0, 0.25, 0.5, 0.75, and 1.0) oxides are considered promising cathode materials for IT-SOFCs. The electrical conductivity improves with increasing Sr content due to the increased concentration of mobile interstitial oxygen and electronic holes. The ASR of $SmBa_{1-}$

$_xSr_xCo_2O_{5+\delta}$ decreased with Sr content up to x = 0.75 and increased suddenly in the case of SSCO (x = 1). SBSCO75 showed the lowest non-ohmic resistance, 0.138 Ω cm^2 at 600 °C. The electrochemical performances of $SmBa_{1-x}Sr_xCo_2O_{5+\delta}$ were evaluated using an anode-supported cell based on a GDC electrolyte with humidified H_2 (3 % H_2O). The maximum power density of SBSCO75 was 1.039 W cm^{-2} at 600 °C, which is clear evidence of the positive effect of strontium in a $SmBa_{1-x}Sr_xCo_2O_{5+\delta}$ layered perovskite, and is associated with higher electrical conductivity and a low ASR value. Therefore, SBSCO75 is considered to be an optimized composition in the $SmBa_{1-x}Sr_xCo_2O_{5+\delta}$ system as a cathode material for IT-SOFCs.

References

(1) Steele, B. C.; Heinzel, A. Materials for Fuel-Cell Technologies. *Nature* **2001**, *414*, 345–352.

(2) Jacobson, A. J. Materials for Solid Oxide Fuel Cells. *Chem. Mater.* **2010**, *22* (3), 660–674.

(3) Brandon, N. P.; Skinner, S.; Steele, B. C. H. Recent Advances in Materials for Fuel Cells. *Annu. Rev. Mater. Res.* **2003**, *33* (1), 183–213.

(4) Petric, A.; Huang, P.; Tietz, F. Evaluation of La-Sr-Co-Fe-O Perovskites for Solid Oxide Fuel Cells and Gas Separation Membranes. *Solid State Ionics* **2000**, *135*, 719–725.

(5) Adler, S. B.; Lane, J. A.; Steele, B. C. H. Electrode Kinetics of Porous Mixed-Conducting Oxygen Electrodes. *J. Electrochem. Soc.* **1996**, *143* (11), 3554–3564.

(6) Ried, P.; Holtappels, P.; Wichser, A.; Ulrich, A.; Graule, T. Synthesis and Characterization of $La_{0.6}Sr_{0.4}Co_{0.2}Fe_{0.8}O_{3-\delta}$ and $Ba_{0.5}Sr_{0.5}Co_{0.8}Fe_{0.2}O_{3-\delta}$. *J. Electrochem. Soc.* **2008**, *155* (10), B1029–B1035.

(7) Shao, Z.; Haile, S. M. A High-Performance Cathode for the next Generation of Solid-Oxide Fuel Cells. *Nature* **2004**, *431* (7005), 170–173.

(8) Tai, L.-W.; Nasrallah, M. M.; Anderson, H. U.; Sparlin, D. M.; Sehlin, S. R. Structure and Electrical Properties of $La_{1-x}Sr_xCo_{1-y}Fe_yO3$. Part 1. The System $La_{0.8}Sr_{0.2}Co_{1-y}Fe_yO_3$. *Solid State Ionics* **1995**, *76*, 273–283.

(9) Park, S.; Choi, S.; Shin, J.; Kim, G. Electrochemical Investigation of Strontium Doping Effect on High Performance $Pr_{1-x}Sr_xCoO_{3-\delta}$ (x = 0.1, 0.3, 0.5, and 0.7) Cathode for Intermediate-Temperature Solid Oxide Fuel Cells. *J. Power Sources* **2012**, *210*, 172–177.

(10) Xia, C.; Rauch, W.; Chen, F.; Liu, M. $Sm_{0.5}Sr_{0.5}CoO_3$ Cathodes for Low-Temperature SOFCs. *Solid State Ionics* **2002**, *149* (1–2), 11–19.

(11) Pang, S.; Jiang, X.; Li, X.; Wang, Q.; Su, Z. Characterization of Ba-Deficient $PrBa_{1-x}Co_2O_{5+\delta}$ as Cathode Material for Intermediate Temperature Solid Oxide Fuel Cells. *J. Power Sources* **2012**, *204*, 53–59.

(12) Gu, H.; Chen, H.; Zheng, Y.; Guo, L. Effect of Chromium Poisoning on the Electrochemical Properties of $NdBaCo_2O_{5+\delta}$ Cathode for IT-SOFCs. *Int. J. Hydrogen Energy* **2010**, *35* (6), 2457–2462.

(13) Taskin, A. A.; Lavrov, A. N.; Ando, Y. Achieving Fast Oxygen Diffusion in Perovskites by Cation Ordering. *Appl. Phys. Lett.* **2005**, *86* (9), 1–3.

(14) Zhu, C.; Liu, X.; Yi, C.; Yan, D.; Su, W. Electrochemical Performance of $PrBaCo_2O_{5+\delta}$ Layered Perovskite as an Intermediate-Temperature Solid Oxide Fuel Cell Cathode. *J. Power Sources* **2008**, *185* (1), 193–196.

(15) Zhou, Q.; He, T.; Ji, Y. $SmBaCo_2O_{5+x}$ Double-Perovskite Structure Cathode Material for Intermediate-Temperature Solid-Oxide Fuel Cells. *J. Power Sources* **2008**, *185* (2), 754–758.

(16) Tarancon, A.; Penamartinez, J.; Marrerolopez, D.; Morata, A.; Ruizmorales, J.; Nunez, P.

Stability, Chemical Compatibility and Electrochemical Performance of $GdBaCo_2O_{5+x}$ Layered Perovskite as a Cathode for Intermediate Temperature Solid Oxide Fuel Cells. *Solid State Ionics* **2008**, *179* (40), 2372–2378.

(17) Kim, G.; Wang, S.; Jacobson, A. J.; Reimus, L.; Brodersen, P.; Mims, C. A. Rapid Oxygen Ion Diffusion and Surface Exchange Kinetics in $PrBaCo_2O_{5+x}$ with a Perovskite Related Structure and Ordered A Cations. *J. Mater. Chem.* **2007**, *17* (24), 2500–2505.

(18) Azad, A. K.; Kim, J. H.; Irvine, J. T. S. Structure–property Relationship in Layered Perovskite Cathode $LnBa_{0.5}Sr_{0.5}Co_2O_{5+\delta}$ (*Ln* = Pr, Nd) for Solid Oxide Fuel Cells. *J. Power Sources* **2011**, *196* (17), 7333–7337.

(19) Kim, J. H.; Cassidy, M.; Irvine, J. T. S.; Bae, J. Advanced Electrochemical Properties of $LnBa_{0.5}Sr_{0.5}Co_2O_{5+\delta}$ (*Ln* = Pr, Sm, and Gd) as Cathode Materials for IT-SOFC. *J. Electrochem. Soc.* **2009**, *156* (6), B682–B689.

(20) Kim, J.-H.; Prado, F.; Manthiram, A. Characterization of $GdBa_{1-x}Sr_xCo_2O_{5+\delta}$ ($0 \leq x \leq 1.0$) Double Perovskites as Cathodes for Solid Oxide Fuel Cells. *J. Electrochem. Soc.* **2008**, *155* (10), B1023–B1028.

(21) Mckinlay, A.; Connor, P.; Irvine, J. T. S.; Zhou, W. Structural Chemistry and Conductivity of a Solid Solution of $YBa_{1-x}Sr_xCo_2O_{5+\delta}$. *J. Phys. Chem. C* **2007**, *111* (51), 19120–19125.

(22) Kim, J. H.; Cassidy, M.; Irvine, J. T. S.; Bae, J. Electrochemical Investigation of Composite Cathodes with $SmBa_{0.5}Sr_{0.5}Co_2O_{5+\delta}$ Cathodes for Intermediate Temperature-Operating Solid Oxide Fuel Cell. *Chem. Mater.* **2010**, *22* (3), 883–892.

(23) Maignan, A.; Martin, C.; Pelloquin, D.; Nguyen, N.; Raveau, B. Structural and Magnetic Studies of Ordered Oxygen-Deficient Perovskites$LnBaCo_2O_{5+\delta}$, Closely Related to the "112" Structure. *J. Solid State Chem.* **1999**, *142* (2), 247–260.

(24) Martin, C.; Maignan, A.; Pelloquin, D.; Nguyen, N.; Raveau, B. Magnetoresistance in the Oxygen Deficient $LnBaCo_2O_{5.4}$ (*Ln* = Eu, Gd) Phases. *Appl. Phys. Lett.* **1997**, *71* (10), 421.

(25) Rossignol, C.; Ralph, J. M.; Bae, J. M.; Vaughey, J. T. $Ln_{1-x}Sr_xCoO_3$ (*Ln* = Gd, Pr) as a Cathode for Intermediate-Temperature Solid Oxide Fuel Cells. *Solid State Ionics* **2004**, *175* (1–4), 59–61.

(26) Nam, J. H.; Jeon, D. H. A Comprehensive Micro-Scale Model for Transport and Reaction in Intermediate Temperature Solid Oxide Fuel Cells. *Electrochim. Acta* **2006**, *51* (17), 3446–3460.

(27) Andersson, M.; Yuan, J.; Sundén, B. Review on Modeling Development for Multiscale Chemical Reactions Coupled Transport Phenomena in Solid Oxide Fuel Cells. *Appl. Energy* **2010**, *87* (5), 1461–1476.

(28) Boehm, E.; Bassat, J. M.; Steil, M. C.; Dordor, P.; Mauvy, F.; Grenier, J. C. Oxygen Transport Properties of $La_2Ni_{1-x}Cu_xO_{4+\delta}$ Mixed Conducting Oxides. *Solid State Sci.* **2003**, *5* (7), 973–981.

(29) Moon, J. W.; Masuda, Y.; Seo, W. S.; Koumoto, K. Influence of Ionic Size of Rare-Earth Site

on the Thermoelectric Properties of $RCoO_3$-Type Perovskite Cobalt Oxides. *Mater. Sci. Eng. B Solid-State Mater. Adv. Technol.* **2001**, *85* (1), 70–75.

(30) Yoo, S.; Shin, J. Y.; Kim, G. Thermodynamic and Electrical Characteristics of $NdBaCo_2O_{5+\delta}$ at Various Oxidation and Reduction States. *J. Mater. Chem.* **2011**, *21* (2), 439–44.

(31) Mauvy, F.; Bassat, J.-M.; Boehm, E.; Manaud, J.-P.; Dordor, P.; Grenier, J.-C. Oxygen Electrode Reaction on $Nd_2NiO_{4+\delta}$ Cathode Materials: Impedance Spectroscopy Study. *Solid State Ionics* **2003**, *158* (1–2), 17–28.

(32) Vashook, V. .; Tolochko, S. .; Yushkevich, I. .; Makhnach, L. .; Kononyuk, I. .; Altenburg, H.; Hauck, J.; Ullmann, H. Oxygen Nonstoichiometry and Electrical Conductivity of the Solid Solutions $La_{2-x}Sr_xNiO_y$ ($0 \leq x \leq 0.5$). *Solid State Ionics* **1998**, *110* (3–4), 245–253.

(33) Kröger, F. A.; Vink, H. J. Relations between the Concentrations of Imperfections in Crystalline Solids. *Solid State Phys.* **1956**, *3*, 307–435.

(34) Lü, S.; Meng, X.; Ji, Y.; Fu, C.; Sun, C.; Zhao, H. Electrochemical Performances of $NdBa_{0.5}Sr_{0.5}Co_2O_{5+x}$ as Potential Cathode Material for Intermediate-Temperature Solid Oxide Fuel Cells. *J. Power Sources* **2010**, *195* (24), 8094–8096.

(35) Leng, Y.; Chan, S. H.; Liu, Q. Development of LSCF-GDC Composite Cathodes for Low-Temperature Solid Oxide Fuel Cells with Thin Film GDC Electrolyte. *Int. J. Hydrogen Energy* **2008**, *33* (14), 3808–3817.

(36) Tarancón, A.; Skinner, S. J.; Chater, R. J.; Hernández-Ramírez, F.; Kilner, J. a. Layered Perovskites as Promising Cathodes for Intermediate Temperature Solid Oxide Fuel Cells. *J. Mater. Chem.* **2007**, *17* (30), 3175.

(37) Taskin, A. A.; Lavrov, A. N.; Ando, Y. Fast Oxygen Diffusion in A-Site Ordered Perovskites. *Prog. Solid State Chem.* **2007**, *35* (2–4 SPEC. ISS.), 481–490.

Chapter 5. High redox and performance stability of layered $SmBa_{0.5}Sr_{0.5}Co_{1.5}Cu_{0.5}O_{5+\delta}$ perovskite cathodes for intermediate-temperature solid oxide fuel cells

5.1. Introduction

Solid oxide fuel cells (SOFCs) are a new power generation device with high energy conversion efficiency, environmental affinity, and low sensitivity to impurities in the fuel.[1,2] While high operating temperatures of 800 - 1000 ^{o}C enhance the electrochemical performance, they give rise to crucial issues such as high costs and material compatibility challenges. These problems have motivated researchers to lower device operating temperature in order to improve material compatibility and practical applicability.[3,4] Lower operating temperature, however, causes slow oxygen reduction kinetics and high over-potential at the cathode.[5] Therefore, cathode materials with high electrocatalytic activity for the oxygen reduction reaction, as reflected by their oxygen transport and surface exchange properties, at intermediate operating temperature should be developed.[6]

The conventional cathode material $La_{1-x}Sr_xMnO_3$ is considered to be one of the most promising cathode materials for high temperature SOFCs due to its satisfactory thermal and chemical stability with YSZ.[7] However, $La_{1-x}Sr_xMnO_3$ does not provide adequate performance for intermediate temperature solid oxide fuel cells (IT-SOFCs) because of its poor oxide-ion conductivity and lower catalytic activity at intermediate temperature ranges.[8]

In this regard, mixed ionic electronic conductors (MIECs), exhibiting both electronic and ionic conductivity,[9] have received considerable attention as possible candidate cathode materials for IT-SOFCs. Among those MIECs, many researchers have recently focused on $LnBaM'M''O_{5+\delta}$ layered perovskite oxides, wherein the B site occupied by equal amounts of different 3d transition metal cations (M′, M″ = Mn, Fe, Co, Ni, Cu), based on their much higher chemical diffusion and surface exchange coefficients relative to those of ABO_3-type perovskite oxides. In particular, $LnBaCo_2O_{5+\delta}$, cobalt containing layered oxides, have stacking layers of $[CoO_2]$-$[LnO_\delta]$-$[CoO_2]$-[BaO] along the *c*-axis, and it can be speculated that alternating lanthanide and alkali-earth planes of the layered oxide will enhance the oxygen transport kinetics compared with ABO_3-type perovskite oxides.[10] Kim *et al*.[11] reported that $PrBaCo_2O_{5+\delta}$ offers faster oxygen ion diffusion and surface exchange kinetics, which are reflected in very low area specific resistance, compared with $La_{0.5}Sr_{0.5}CoO_{3-\delta}$ at intermediate temperature (500 - 700 ^{o}C).

Furthermore, some researchers have reported that the substitution of Sr for Ba in $LnBaCo_2O_{5+\delta}$ can improve the conductivity and the catalytic activity for the ORR of layered perovskite oxides.[12,13] The substitution of Sr for Ba in a $GdBaCo_2O_{5+\delta}$ cathode enhanced the chemical stability between the electrode and electrolyte as well as the oxygen transport.[14] In addition, Mckinlay *et al*.[15] found that

substituted Sr in $YBa_{1-x}Sr_xCo_2O_{5+\delta}$ causes a structural change from orthorhombic to tetragonal and a roughly 32-fold increase of electrical conductivity compared to that of a Sr-free sample Kim *et al.*[16] have also shown that a layered $SmBa_{0.5}Sr_{0.5}Co_2O_{5+\delta}$ perovskite has favorable electrochemical properties and can be potentially utilized as a cathode material for IT-SOFC applications.

However, cobalt-containing cathodes encounter problems such as high thermal expansion coefficients (TEC), poor stability, and the high cost of cobalt, making them unsuitable for practical use as a cathode material for SOFCs. The high TEC is related with transformation of the low-spin (t_{2g}^6) cobalt ions to the paramagnetic high-spin state ($t_{2g}^4 e_g^2$) transition associated with Co^{3+}.[17]Furthermore, the thermal expansion mismatch between the cell components makes this system unsuitable as a cathode material for IT-SOFCs subject to repeated thermal cycling.[18] Therefore, in order to solve these problems of cobalt containing cathodes, partial substitution of other elements for cobalt in these materials is considered a possible means to compensate these disadvantages while maintaining adequate electrochemical activity of cobalt-containing cathode materials,[19] such as $LnBaCo_{2-x}Cu_xO_{5+\delta}$ (Ln = Nd, Gd), $YBaCo_{2-x}Cu_xO_{5+\delta}$, $GdBaCo_{2/3}Fe_{2/3}Cu_{2/3}O_{5+\delta}$, and $PrBaMCoO_{5+\delta}$ (M = Cu, Fe).[20-23]

In this study, we focus on the effects of Cu doping on the Co site in $SmBa_{0.5}Sr_{0.5}Co_2O_{5+\delta}$ in the aspects of structural characteristics, electrical properties, electrochemical performance, redox properties, and performance stability of $SmBa_{0.5}Sr_{0.5}Co_{2-x}Cu_xO_{5+\delta}$($x$ = 0 and 0.5) in relation to its application as an IT-SOFC cathode material.

5.2. Experimental

The $SmBa_{0.5}Sr_{0.5}Co_{2-x}Cu_xO_{5+\delta}$ (x = 0 and 0.5) cathodes were synthesized by the Pechini method. Stoichiometric amounts of $Sm(NO_3)_3 \cdot 6H_2O$ (Aldrich, 99+%, metal basis), $Ba(NO_3)_2$ (Aldrich, 99+%), $Sr(NO_3)_2$ (Aldrich, 99+%), $Co(NO_3)_2 \cdot 6H_2O$ (Aldrich, 98+%), $Cu(NO_3)_2 \cdot 2.5H_2O$ (Aldrich,99+%), and citric acid were dissolved in distilled water to form an aqueous mixed solution. An adequate amount of ethylene glycol was added into the beaker after the mixture was dissolved. After a viscous resin was formed, the mixture was heated to roughly 250 °C. The powder was calcined at 600 °C for 4 h and ball-milled in acetone for 24 h. For the final step to form a phase, the powder was pressed into pellets and then sintered in air at various temperatures. $SmBa_{0.5}Sr_{0.5}Co_2O_{5+\delta}$(SBSCO) was sintered in air at 1100 °C for 12 h, while $SmBa_{0.5}Sr_{0.5}Co_{1.5}Cu_{0.5}O_{5+\delta}$(SBSCCu50) was sintered at 1000 °C for 12 h. For the cathode slurry, $SmBa_{0.5}Sr_{0.5}Co_{2-x}Cu_xO_{5+\delta}$ and $Ce_{0.9}Gd_{0.1}O_{2-\delta}$ (GDC) powders were thoroughly mixed together at a weight ratio of 6:4 and the mixed powders were blended with an organic binder (Heraeus V006) to form slurries thereafter.

The structure of $SmBa_{0.5}Sr_{0.5}Co_{2-x}Cu_xO_{5+\delta}$was characterized by using an X-ray diffractometer (Rigaku diffractometer, Cu Kα radiation) at a scanning rate of 0.6 ° min^{-1} and a range 20 ° $< 2\theta <$ 100

°. The powder pattern and lattice parameters were analyzed by Rietveld refinement using the GSAS program. SBSCCu50 was analyzed also by in situ X-ray diffractometer (Bruker AXS D8 Advance diffractometer, Cu Kα radiation) to determine phase stability at a scanning rate of 0.6 ° min^{-1} and a range of 20 ° < 2θ < 60 ° in air from 100 to 800 °C. The microstructures of the $SmBa_{0.5}Sr_{0.5}Co_{2-x}Cu_xO_{5+\delta}$ composites and cross sections of single cells were investigated using field emission scanning electron microscopy (Nova Nano SEM, FEI, USA). A thermogravimetric analysis (TGA) was performed using a thermogravimetric analyzer (SDT-Q600, TA Instruments, USA) from 100 to 900 °C with a heating/cooling rate of 2 °C min^{-1} in air. The initial oxygen content of the $SmBa_{0.5}Sr_{0.5}Co_{2-x}Cu_xO_{5+\delta}$ oxides was determined by iodometric titration. The thermal expansion curve of the samples was measured from 100 to 900 °C with a heating/cooling rate of 5 °C min^{-1} in air.

For the measurement of electrical conductivity, the powder was pressed into a cylindrical shape and sintered to dense pellets (>98 % density). The electrical conductivities of $SmBa_{0.5}Sr_{0.5}Co_{2-x}Cu_xO_{5+\delta}$ samples were measured by a four-terminal DC arrangement technique. The current and the voltage were recorded by a BioLogic Potentiostat from 100 to 750 °C at intervals of 50 °C in air.

Coulometric titration was used to accurately quantify the oxidation/reduction state of the $SmBa_{0.5}Sr_{0.5}Co_{2-x}Cu_xO_{5+\delta}$ as a function of $p(O_2)$. The coulometric titration rig was mainly composed of an YSZ tube with Ag-paste electrodes plastered on both sides, which has been explained sufficiently elsewhere.[24] The yittria-stabilized zirconia (YSZ) tube was used both to electrochemically pump oxygen out of the system and to detect the equilibrium $p(O_2)$ inside the tube. Electrodes on either side of the YSZ tube were used to measure the potential across the membrane and the potential could be related to the $p(O_2)$ through the Nernst Equation. After passing 5% O_2-Ar gas over the sample in the tube, the sample was isolated in the tube and the equilibrium $p(O_2)$ was measured with an OCV sensor. The OCV sensor was integrated onto the tube surface and could be used to add or remove oxygen from the system through the application of a potential across the ion-conducting YSZ tube. The sample was considered to be equilibrated when the potential varied in a range of less than 1 mV per hour. Oxygen nonstoichiometry was decided through this process at 700 °C over a wide range of oxygen partial pressure. The oxygen partial pressure dependence of the electrical conductivity was also measured by the four-probe DC method with a BioLogic Potentiostat on sintered bars of $SmBa_{0.5}Sr_{0.5}Co_{2-x}Cu_xO_{5+\delta}$.

Impedance spectroscopy of $SmBa_{0.5}Sr_{0.5}Co_{2-x}Cu_xO_{5+\delta}$ was carried out using a symmetric cell. The GDC powder was pressed into pellets and sintered at 1350 °C for 4 h in air to obtain a ~ 1 mm-thick electrolyte substrate. Slurries of the $SmBa_{0.5}Sr_{0.5}Co_{2-x}Cu_xO_{5+\delta}$-GDC composite were screen-printed onto both sides of the dense GDC electrolyte to form a symmetrical cell, which was then heated at 950 °C for 4 h. The silver paste was used as the current collector for the electrodes.

A NiO-GDC anode-supported cell was fabricated to measure the electrochemical performance of $SmBa_{0.5}Sr_{0.5}Co_{2-x}Cu_xO_{5+\delta}$. The NiO-GDC cermet anode was prepared by a mixture of nickel oxide,

GDC, and starch at a weight ratio of 6:4:1.5 after being ball-milled in ethanol for 24 h. The GDC electrolyte was pressed onto the pelletized disk of the NiO-GDC cermet anode. This NiO-GDC|GDC anode-supported cell was sintered at 1350 °C for 5 h and cathode slurries were applied onto the surface of the GDC electrolyte layer by screen printing. A tri-layer $SmBa_{0.5}Sr_{0.5}Co_{2-x}Cu_xO_{5+\delta}$-GDC|GDC|NiO-GDC cell with an active electrode area of 0.36 cm^2 was finally sintered at 950 °C for 4 h in air. The electrolyte and cathode thickness of a single cell were both about ~ 20 μm with a 500 μm thick anode. For the single-cell performance test, Ag wires were attached at both electrodes of the single cell using Ag paste as a current collector. The single cell was fixed on an alumina tube using a ceramic adhesive (Aremco, Ceramabond 552). Humidified hydrogen (3 % H_2O) was supplied as fuel through a water bubbler with a flow rate of 20 mL min^{-1} and ambient air was used as an oxidant during single cell tests. *I-V* curves and impedance spectra were examined using a BioLogic Potentiostat at operating temperature from 500 to 650 °C. Impedance spectra were recorded under OCV in a frequency range of 1 mHz to 500 kHz with AC perturbation of 14 mA from 500 to 650 °C.

The long term stability for $SmBa_{0.5}Sr_{0.5}Co_{2-x}Cu_xO_{5+\delta}$-GDC|GDC|NiO-GDC was examined using humidified H_2 as the fuel and stationary air as an oxidant at a constant cell ampere of -0.4 A cm^{-2} at 600 °C.

5.3. Results and Discussions

Table 5.1. Structural parameters and oxygen content of the $SmBa_{0.5}Sr_{0.5}Co_{2-x}Cu_xO_{5+\delta}$ oxides.

	Space Group	*a* (Å)	*b* (Å)	*c* (Å)	*V* (Å^3)	Oxygen content (5 + δ)
SBSCO	*P4/mmm*	3.8674	3.8674	7.5857	113.4576	5.76
SBSCCu50	*P4/mmm*	3.8697	3.8697	7.6062	113.8996	5.71

The Rietveld refinement data of $SmBa_{0.5}Sr_{0.5}Co_{1.5}Cu_{0.5}O_{5+\delta}$ (SBSCCu50) samples are shown in Figure 5.1(a) and structural data of $SmBa_{0.5}Sr_{0.5}Co_2O_{5+\delta}$ (SBSCO) and SBSCCu50 are given in Table 5.1. There is excellent agreement between the experimental data and the calculated profiles, suggesting that cations are well ordered between Sm^{3+} and Ba^{2+}/Sr^{2+} ions in the ordered perovskite lattice. The Rietveld refinement data reveal that the diffraction pattern of SBSCO and SBSCCu50 samples could be indexed to a tetragonal structure (space group: *P4/mmm*),[25] with all samples being an ordered perovskite structure. The data in Table 1 indicate that the lattice parameters and the unit cell volume of the $SmBa_{0.5}Sr_{0.5}Co_{2-x}Cu_xO_{5+\delta}$ samples increase with Cu doping, because the cell volume of the samples with B-site substitution depends on the size of the substituting cations. Comparing the ionic radius of

substituting cations, Cu^{2+}(0.730 Å) is larger than Co^{3+}(0.545 Å for low spin and 0.61 Å for high spin) and Co^{4+}(0.530 Å),[26] which explains the increased volume of the Cu doped SBSCO.

To confirm the phase stability of SBSCCu50 in the operating conditions of a SOFC cathode, *in-situ* X-ray diffraction measurement was carried out in air from 100 to 800 °C and the results are presented in Figure 5.1(b). SBSCCu50 is a single phase perovskite structure without any detectable decomposition in the entire temperature range of measurements, indicating that SBSCCu50 is thermally stable. The inset in Figure 5.1(b) shows the dependence of temperature on unit cell volume V (Å ^{3}) that the shift of the main diffraction peaks towards lower 2θ with increasing temperature indicates a volume increase of the unit cell.

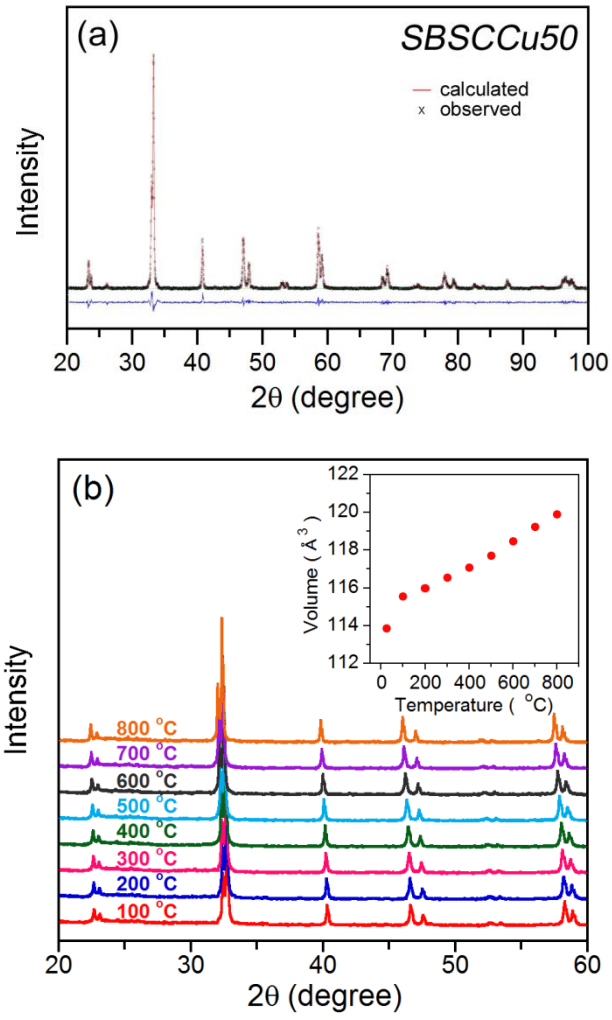

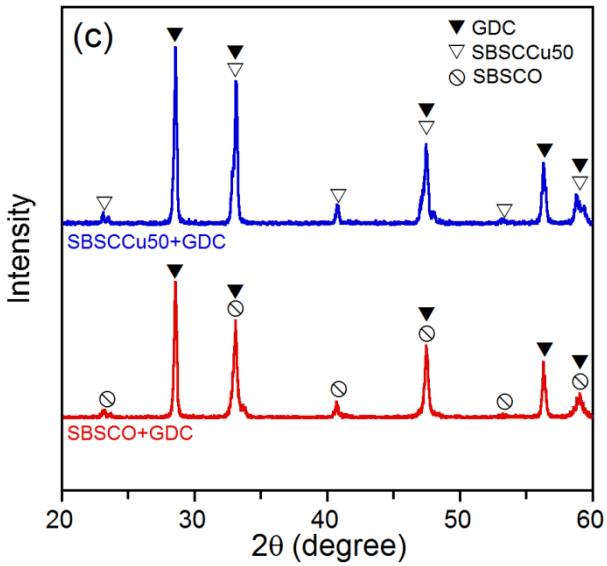

Figure 5.1. (a) Observed and calculated XRD profiles and the difference between them for SBSCCu50. (b) *In-situ* X-ray diffraction patterns for SBSCCu50 in air from 100 to 800 °C. The inset shows the dependence of temperature on unit cell volume V (Å^3). (c) XRD patterns between SBSCO-GDC and SBSCCu50-GDC mixture sintered at 950 °C for 4 h.

In general, the phase reaction between the electrode and electrolyte can generate an undesired insulating layer at the interface, which obstructs the oxide-ionic and electronic transport.[27] The chemical stability between $SmBa_{0.5}Sr_{0.5}Co_{2-x}Cu_xO_{5+\delta}$ and GDC in contact with the GDC electrolyte is therefore examined with the corresponding powders in a 6:4 weight ratio sintered at 950 °C for 4 h. The XRD spectra of $SmBa_{0.5}Sr_{0.5}Co_{2-x}Cu_xO_{5+\delta}$-GDC are illustrated in Figure 5.1 (c) to confirm the absence of chemical reactivity, and there are no observed interfacial reactions or distinct secondary phases between them.

The electrode microstructure is linked to the characteristics of the surface, the TPB area, the volume fraction of chemical phases present, and electron transport. These properties affect the fuel cell performance through the reaction kinetics, charge transport, and mass transport preprocess.[28] Figure 5.2(a) shows the microstructure of a cross section of SBSCCu50-GDC|GDC|Ni O-GDC, showing a 15-μm cathode and 20-μm electrolyte. The adhesion between the cathode and electrolyte appears to be very good and the electrolyte is dense with no cracks or pores. The particle size of the SBSCCu50-GDC composites is larger than that of SBSCO-GDC composites, indicating that Cu doping improves the sintering characteristics of these composites.[29]

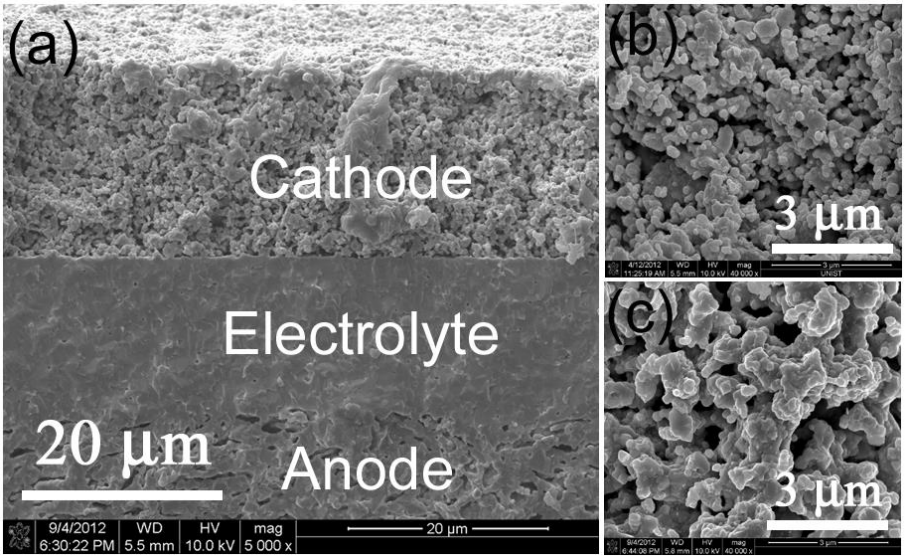

Figure 5.2. SEM micrographs showing (a) the cross section of SBSCCu50-GDC|GDC|NiO-GDC and (b) SBSCO-GDC composite cathode and (c) SBSCCu50-GDC composite cathode.

Figure 5.3 shows thermogravimetric analysis data collected by the weight change of SBSCO and SBSCCu50 samples upon heating to 900 °C in air. SBSCO and SBSCCu50 samples show slight weight changes above 300 °C due to the release of lattice oxygen, with weight loss of 1.2 - 1.5 % from 25 to 900 °C. The TGA data indicate that the oxygen loss decreases with Cu substitution upon increasing temperature in relation to the thermal stability of Cu and Co ions and the Cu-O and Co-O bond strength. This suggests that the Cu-O bond strength is stronger as compared to the Co-O bond, which would suppress oxygen loss of the samples with substitution of Cu.

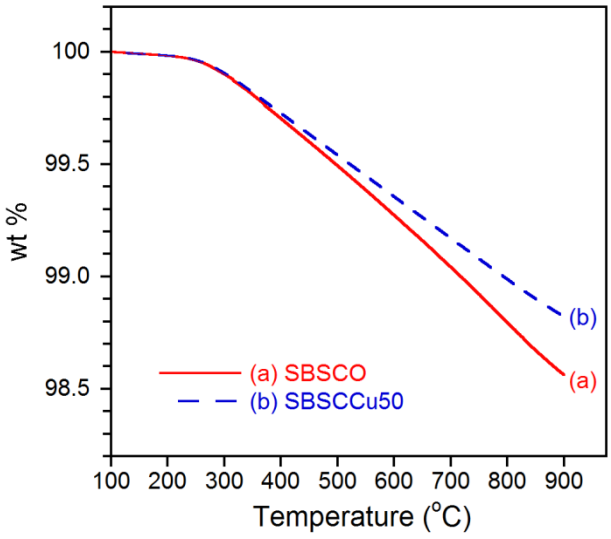

Figure 5.3. Thermogravimetric analysis data of SBSCO and SBSCCu50 by the weight change with temperature in air.

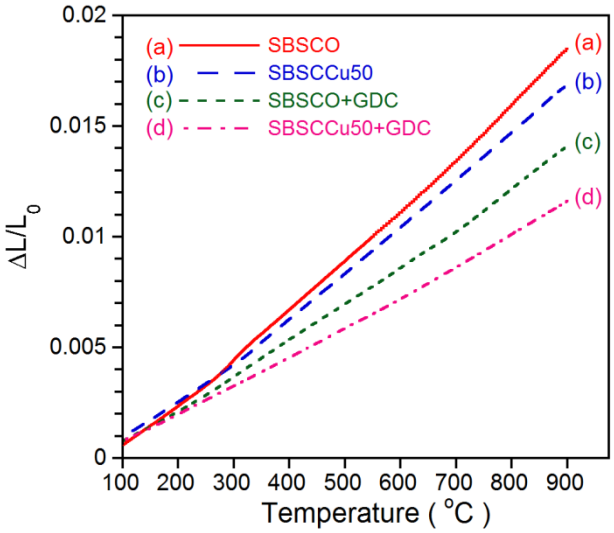

Figure 5.4. Thermal expansion curves of SBSCO, SBSCCu50, SBSCO-GDC composites, and SBSCCu50-GDC composites in a temperature range of 100 - 900 °C in air.

Figure 5.4 shows the thermal expansion curves of SBSCO, SBSCCu50, SBSCO-GDC composites, and SBSCCu50-GDC composites measured from 100 to 900 °C. The thermal expansion value of SBSCCu50 is lower than that of SBSCO. The TEC values of SBSCO and SBSCCu50 are 13.7 x 10^{-6} K^{-1} and 12.8 x 10^{-6} K^{-1} at 700 °C, respectively. In general, the larger TEC values for the cobalt-based perovskite oxides can be ascribed to the increase of the average ionic radius of Co ions during the thermal expansion measurement.[30] The larger TEC values of cobalt-based perovskite oxides are mainly attributed to the reduction of smaller Co^{4+} to larger Co^{3+} with a loss of oxygen and easy transition of the Co^{3+} ions from low-spin to high-spin with increasing temperature.[18,31] Therefore, the decreasing amount of $Co^{3+/4+}$ and the decreasing oxygen loss lead to a decrease of the TEC value.[20] Meanwhile, the values of SBSCO-GDC composites and SBSCCu50-GDC composites are 10.5 and 8.9 x 10^{-6} K^{-1}, respectively, at 700 °C. The TEC values of SBSCCu50 with added GDC significantly decrease, and these results are close to the TEC values of GDC.[32] Therefore, the SBSCCu50-GDC composite cathodes are acceptable in terms of matching thermal expansion with the GDC electrolyte in the application of IT-SOFCs.

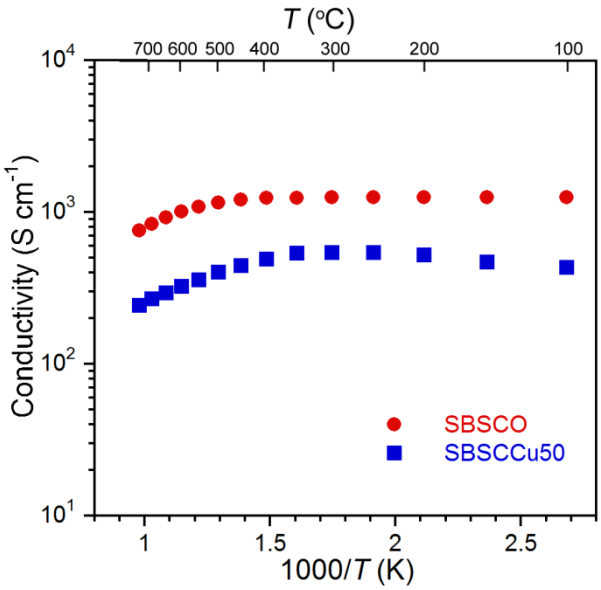

Figure 5.5. Electrical conductivities of SBSCO and SBSCCu50 at various temperatures from 100 to 750 °C in air.

Figure 5.5 shows the electrical conductivity with temperature of $SmBa_{0.5}Sr_{0.5}Co_{2-x}Cu_xO_{5+\delta}$ cathodes in air. SBSCO and SBSCCu50 samples show decreasing electrical conductivity at higher temperatures, indicating metallic conducting behavior. There is a significant drop of electrical conductivity over 350 °C due to the loss of oxygen atoms from the lattice, which corresponds to TGA data.[33] This can be explained by the fact that the holes are the majority charge carriers and hole-conductivity in cobaltites is usually related to the presence of Co^{4+} ions. The loss of oxygen atoms with increasing temperature not only decreases the hole concentration but also disturbs the (Co,Cu)-O-(Co,Cu) periodic potential and introduces hole localization.[34,35]

At a given temperature, the electrical conductivity of SBSCCu50 shows a tendency to decrease with Cu substitution in SBSCO. This can be explained by the fact that the alternation of CoO_5 pyramidal and CoO_6 octahedral planes along *a* and *b* directions in SBSCO were weakened by the substituted Cu in the Co site, which hampers the hole creation.[21] The electrical conductivity of SBSCO and SBSCCu50 exhibit 758 - 1250 S cm^{-1} and 234 - 432 S cm^{-1} in a temperature range of 100 - 750 °C, respectively. The lowest electrical conductivity of SBSCO and SBSCCu50 samples is still higher than 200 S cm^{-1} from 100 to 750 °C. This means that both the SBSCO and SBSCCu50 samples could satisfy the requirements of electrical conductivity for use as an IT-SOFC cathode.[36]

In general, the cathode was reduced at lower $p(O_2)$ under fuel cell operating conditions due to cathodic polarization.[37] Therefore, sufficient electrical conductivity at relatively low $p(O_2)$ is also important to ensure efficient current collection and long-term stability.[38] The $p(O_2)$ dependence of the 4-probe electrical conductivities for SBSCO and SBSCCu50 at 700 °C simultaneously are displayed in

Figure 5.6 (a). The electrical conductivities of SBSCO and SBSCCu50 are within a range of 40 to 550 S/cm under relatively low oxygen partial pressures, which are typical operating conditions of IT-SOFC cathodes.

Higher redox stability is an important factor for stable electrochemical properties of a cathode material for IT-SOFCs at operating conditions. Figure 5.6 (b) shows the equilibrium oxygen nonstoichiometries for SBSCO and SBSCCu50 determined by coulometric titration as a function of $p(O_2)$ at 700 ºC.[39] The oxidation isotherms of SBSCO and SBSCCu50 at 700 ºC have similar shapes, suggesting that the oxidation/reduction mechanisms of both materials are quite similar. The slope of isotherms for SBSCO decreases prominently at a $p(O_2)$ of approximately 10^{-5} atm while that for SBSCCu50 declines markedly at a $p(O_2)$ of around 10^{-7} atm. A steep decrease of the slope near 10^{-7} atm and 700 ºC implies that the operating $p(O_2)$ of SBCCCu50 should be carefully reviewed considering the structural instability predicted from the redox behavior,[37] which has also been reported in the previous studies.[40] The decomposition of SBSCCu50 starts at lower $p(O_2)$ as compared with that of SBSCO, implying that SBSCCu50 has higher redox stability or better durability under cathodic polarization and consequently a favourable property for practical applications in IT-SOFCs.

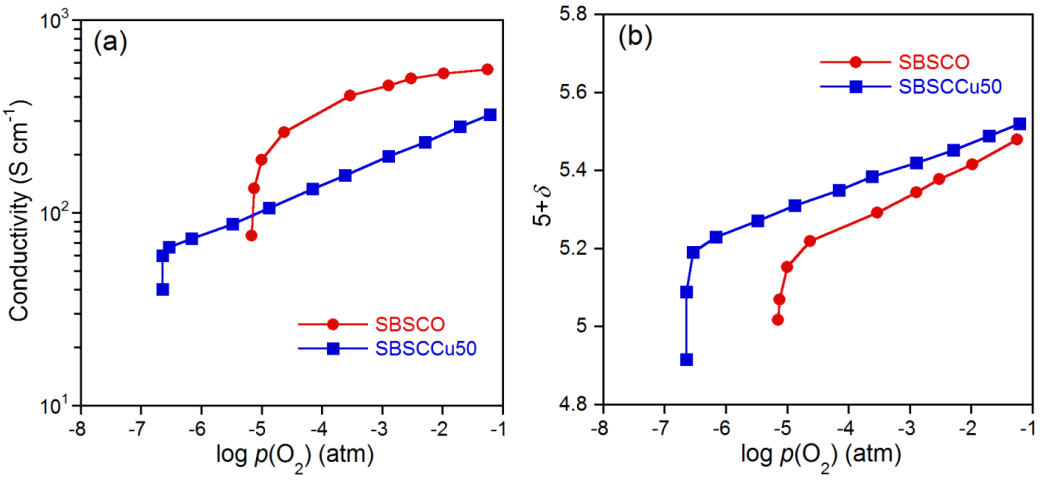

Figure 5.6. (a) Electrical conductivity of SBSCO and SBSCCu50 and (b) Oxidation isotherms of SBSCO and SBSCCu50 in various $p(O_2)$ at 700 ºC.

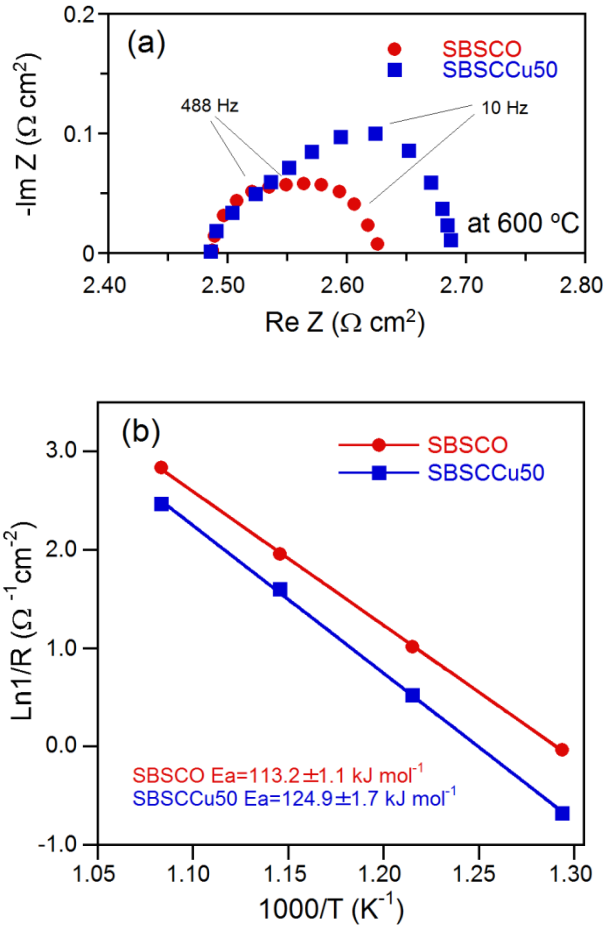

Figure 5.7 (a) Impedance spectra of symmetric cell at different temperatures under OCV for SBSCO-GDC|GDC|SBSCO-GDC and SBSCCu50- GDC|GDC|SBSCCu50-GDC at 600 °C. (b) Arrhenius plots of the ASR for SBSCO and SBSCCu50 at various temperatures.

The area specific resistance (ASR) of $SmBa_{0.5}Sr_{0.5}Co_{2-x}Cu_xO_{5+\delta}$ is obtained by AC impedance spectroscopy for $SmBa_{0.5}Sr_{0.5}Co_{2-x}Cu_xO_{5+\delta}$-GDC|GDC|$SmBa_{0.5}Sr_{0.5}Co_{2-x}Cu_xO_{5+\delta}$-GDC symmetrical cells. The ASR values are determined by the impedance intercept between high-frequency and low-frequency with the real axis of the Nyquist plot, and representative impedance spectra are presented in Figure 5.7 (a). The ASRs of SBSCCu50 are higher than that of SBSCO, and the ASRs of SBSCO and SBSCCu50 are 0.141 and 0.201 Ω cm^2, respectively, at 600 °C. Arrhenius plots of the ASR for SBSCO and SBSCCu50 are shown in Figure 5.7(b). The activation energy is directly related to the cathode properties including oxygen adsorption, dissociation, and surface/bulk diffusion.[11,41] The activation energies of $SmBa_{0.5}Sr_{0.5}Co_{2-x}Cu_xO_{5+\delta}$ are calculated from the Arrhenius plots of the fitted line. The activation energy of SBSCO is around 113.2 kJ mol^{-1} while that of SBSCCu50 is 124.9 kJ mol^{-1}.

Figure 5.8 shows the power density and cell voltage as a function of the current density for the $SmBa_{0.5}Sr_{0.5}Co_{2-x}Cu_xO_{5+\delta}$-GDC|GDC|NiO-GDC cells using humidified H_2 (3 % H_2O) as a fuel and

ambient air as an oxidant in a temperature range of 500 - 650 °C. The maximum power density of SBSCO and SBSCCu50 is 2.03 and 1.76 W cm^{-2} at 650 °C and 1.37 and 1.15 W cm^{-2} at 600 °C, respectively. The single cell performances decrease with doped Cu in the SBSCO, being consistent with the trend of the ASR and electrical conductivity results.

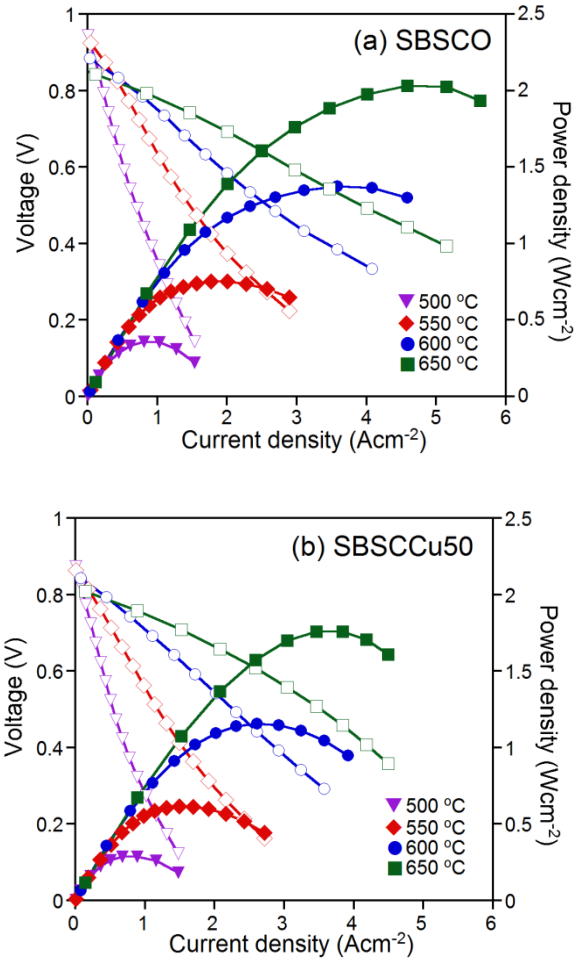

Figure 5.8. *I-V* curve for $SmBa_{0.5}Sr_{0.5}Co_{2-x}Cu_xO_{5+\delta}$-GDC|GDC|NiO-GDC at different temperatures: (a) SBSCO and (b) SBSCCu50.

To measure the long term stability of $SmBa_{0.5}Sr_{0.5}Co_{2-x}Cu_xO_{5+\delta}$-GDC|GDC|NiO-GDC single cell, the voltage of SBSCO and SBSCCu50 single cells was recorded as a function of time under a constant current load of -0.4 A cm^{-2} operating in humidified H_2 as the fuel and stationary air as the oxidant at 600 °C, as shown in Figure 5.9. The SBSCCu50 single cell shows more stable performance at 600 °C for 100 hours than SBSCO single cell, which could be explained by higher redox stability.

In conclusion, SBSCCu50 is considered a sufficient material as a cathode for IT-SOFCs considering that Cu substitution in SBSCO provides a combination of reduced TEC values and

enhanced redox and performance stability, and also shows satisfactory electrical properties and electrochemical performance under typical fuel cell operating conditions.

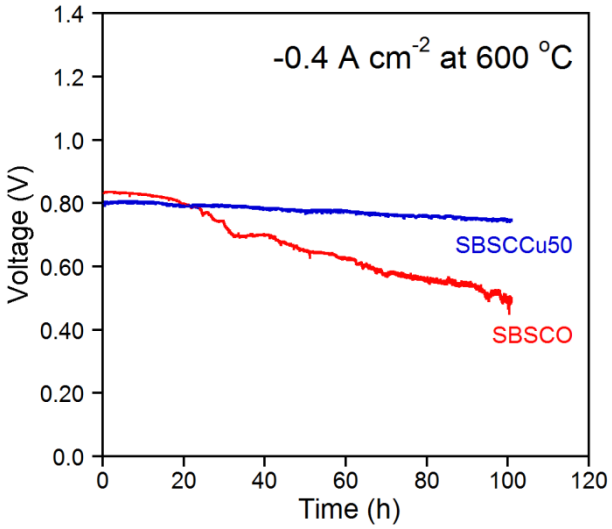

Figure 5.9. Comparison of the long term performance of SBSCO-GDC|GDC|NiO-GDC and SBSCCu50-GDC|GDC|NiO-GDC with humidified H_2 as the fuel and stationary air as oxidant under a constant current load of -0.4 A cm^{-2} at 600 °C.

5.4. Conclusions

The effects of Cu doping on the Co site in SBSCO, $SmBa_{0.5}Sr_{0.5}Co_{2-x}Cu_xO_{5+\delta}$ (x = 0 and 0.5), are investigated with respect to structural characteristics, electrical properties, electrochemical performance, redox properties, and performance stability as cathode materials for IT-SOFC applications. The TEC value of the SBSCCu50 sample is 12.8 x 10^{-6} K^{-1}, which is lower than that (13.7 x 10^{-6} K^{-1}) of the SBSCO sample at 700 °C. In coulometric titration, SBSCCu50 shows higher redox stability at lower $p(O_2)$ as compared with that of SBSCO. The single cell performance of SBSCCu50 is very stable at 600 °C for 100 hours as compared with that of SBSCO. SBSCCu50 shows satisfactory stable performance, which could be explained by higher redox stability. Cu substitution in SBSCO provides a combination of reduced TEC values and enhanced redox and performance stability, and also shows satisfactory electrical properties and electrochemical performance under typical fuel cell operating conditions. SBSCCu50 is considered a suitable cathode material for IT-SOFCs.

References

(1) Gross, M. D.; Vohs, J. M.; Gorte, R. J. Recent Progress in SOFC Anodes for Direct Utilization of Hydrocarbons. *J. Mater. Chem.* **2007**, *17* (30), 3071–3077.

(2) Ishihara, T.; Shibayama, T.; Honda, M.; Nishiguchi, H.; Takita, Y. Solid Oxide Fuel Cell Using Co Doped La(Sr)Ga(Mg)O_3 Perovskite Oxide with Notably High Power Density at Intermediate Temperature. *Chem. Commun.* **1999**, 1227–1228.

(3) Steele, B. C.; Heinzel, A. Materials for Fuel-Cell Technologies. *Nature* **2001**, *414*, 345–352.

(4) Jacobson, A. J. Materials for Solid Oxide Fuel Cells. *Chem. Mater.* **2010**, *22* (3), 660–674.

(5) Colomer, M. T.; Steele, B. C. H.; Kilner, J. a. Structural and Electrochemical Properties of the Cathode $Sr_{0.8}Ce_{0.1}Fe_{0.7}Co_{0.3}O_{3-\delta}$ Perovskite Material for ITSOFCs. *Solid State Ionics* **2002**, *147*, 41–48.

(6) Zhou, W.; Sunarso, J.; Chen, Z.-G.; Ge, L.; Motuzas, J.; Zou, J.; Wang, G.; Julbe, A.; Zhu, Z. Novel B-Site Ordered Double Perovskite $Ba_2Bi_{0.1}Sc_{0.2}Co_{1.7}O_{6-x}$ for Highly Efficient Oxygen Reduction Reaction. *Energy Environ. Sci.* **2011**, *4* (3), 872.

(7) Lynch, M. E.; Yang, L.; Qin, W.; Choi, J.-J.; Liu, M.; Blinn, K.; Liu, M. Enhancement of $La_{0.6}Sr_{0.4}Co_{0.2}Fe_{0.8}O_{3-\delta}$ Durability and Surface Electrocatalytic Activity by $La_{0.85}Sr_{0.15}MnO_{3\pm\delta}$ Investigated Using a New Test Electrode Platform. *Energy Environ. Sci.* **2011**, *4* (6), 2249–2258.

(8) Lü, S.; Long, G.; Ji, Y.; Meng, X.; Zhao, H.; Sun, C. $SmBaCoCuO_{5+x}$ as Cathode Material Based on GDC Electrolyte for Intermediate-Temperature Solid Oxide Fuel Cells. *J. Alloys Compd.* **2011**, *509* (6), 2824–2828.

(9) Petric, A.; Huang, P.; Tietz, F. Evaluation of La-Sr-Co-Fe-O Perovskites for Solid Oxide Fuel Cells and Gas Separation Membranes. *Solid State Ionics* **2000**, *135*, 719–725.

(10) Chroneos, A.; Yildiz, B.; Tarancon, A.; Parfitt, D.; Kilner, J. A. Oxygen Diffusion in Solid Oxide Fuel Cell Cathode and Electrolyte Materials: Mechanistic Insights from Atomistic Simulations. *Energy Environ. Sci.* **2011**, 2774–2789.

(11) Kim, G.; Wang, S.; Jacobson, A. J.; Reimus, L.; Brodersen, P.; Mims, C. A. Rapid Oxygen Ion Diffusion and Surface Exchange Kinetics in $PrBaCo2O_{5+x}$ with a Perovskite Related Structure and Ordered A Cations. *J. Mater. Chem.* **2007**, *17* (24), 2500–2505.

(12) Azad, A. K.; Kim, J. H.; Irvine, J. T. S. Structure–property Relationship in Layered Perovskite Cathode $LnBa_{0.5}Sr_{0.5}Co_2O_{5+\delta}$ (*Ln* = Pr, Nd) for Solid Oxide Fuel Cells. *J. Power Sources* **2011**, *196* (17), 7333–7337.

(13) Kim, J. H.; Cassidy, M.; Irvine, J. T. S.; Bae, J. Advanced Electrochemical Properties of $LnBa_{0.5}Sr_{0.5}Co_2O_{5+\delta}$ (*Ln* = Pr, Sm, and Gd) as Cathode Materials for IT-SOFC. *J. Electrochem. Soc.* **2009**, *156* (6), B682–B689.

(14) Kim, J.-H.; Prado, F.; Manthiram, A. Characterization of $GdBa_{1-x}Sr_xCo_2O_{5+\delta}$ ($0 \leq x \leq 1.0$) Double Perovskites as Cathodes for Solid Oxide Fuel Cells. *J. Electrochem. Soc.* **2008**, *155* (10),

B1023–B1028.

(15) Mckinlay, A.; Connor, P.; Irvine, J. T. S.; Zhou, W. Structural Chemistry and Conductivity of a Solid Solution of $YBa_{1-x}Sr_xCo_2O_{5+\delta}$. *J. Phys. Chem. C* **2007**, *111* (51), 19120–19125.

(16) Kim, J. H.; Cassidy, M.; Irvine, J. T. S.; Bae, J. Electrochemical Investigation of Composite Cathodes with $SmBa_{0.5}Sr_{0.5}Co_2O_{5+\delta}$ Cathodes for Intermediate Temperature-Operating Solid Oxide Fuel Cell. *Chem. Mater.* **2010**, *22* (3), 883–892.

(17) Hou, S. E.; Alonso, J. A.; Goodenough, J. B. Co-Free, Iron Perovskites as Cathode Materials for Intermediate-Temperature Solid Oxide Fuel Cells. *J. Power Sources* **2010**, *195* (1), 280–284.

(18) Huang, K.; Lee, H. Y.; Goodenough, J. B. Sr- and Ni-Doped $LaCoO_3$ and $LaFeO_3$ Perovskites. *J. Electrochem. Soc.* **1998**, *145* (9), 3220–3227.

(19) Zhou, Q.; Wei, T.; Guo, S.; Qi, X.; Ruan, R. Intermediate Temperature Solid Oxide Fuel Cells. *Ceram. Int.* **2012**, *38* (4), 2899–2903.

(20) Kim, Y. N.; Manthiram, A. Layered $LnBaCo_{2-x}Cu_xO_{5+\delta}$ ($0 \leq x \leq 1.0$) Perovskite Cathodes for Intermediate-Temperature Solid Oxide Fuel Cells. *J. Electrochem. Soc.* **2011**, *158* (3), B276–B282.

(21) Zhang, X.; Hao, H.; Hu, X. Electronic Transport Properties of $YBaCo_{2-x}Cu_xO_{5+\delta}$ ($0 \leqslant x \leqslant 1$) at High Temperature. *Phys. B Condens. Matter* **2008**, *403*, 3406–3409.

(22) Jo, S. H.; Muralidharan, P.; Kim, D. K. Enhancement of Electrochemical Performance and Thermal Compatibility of $GdBaCo_{2/3}Fe_{2/3}Cu_{2/3}O_{5+\delta}$ Cathode on $Ce_{1.9}Gd_{0.1}O_{1.95}$ Electrolyte for IT-SOFCs. *Electrochem. commun.* **2009**, *11*, 2085–2088.

(23) Klyndyuk, A. I. Structure, Thermal Expansion, and Electrical Properties of the $PrBaMCoO_{5+\delta}$ (M = Cu, Fe) Layered Oxides. *Inorg. Mater.* **2009**, *45* (8), 942–945.

(24) Yoo, S.; Shin, J. Y.; Kim, G. Thermodynamic and Electrical Characteristics of $NdBaCo_2O_{5+\delta}$ at Various Oxidation and Reduction States. *J. Mater. Chem.* **2011**, *21* (2), 439–44.

(25) Maignan, A.; Martin, C.; Pelloquin, D.; Nguyen, N.; Raveau, B. Structural and Magnetic Studies of Ordered Oxygen-Deficient Perovskites$LnBaCo_2O_{5+\delta}$, Closely Related to the "112" Structure. *J. Solid State Chem.* **1999**, *142* (2), 247–260.

(26) Nakayama, M.; Ikuta, H.; Uchimoto, Y.; Wakihara, M. Ionic Conduction of Lithium in B-Site Substituted Perovskite Compounds, $(Li_{0.1}La_{0.3})_yM_xNb_{1-x}O_3$ (M = Zr, Ti, Ta). *J. Mater. Chem.* **2002**, *12* (5), 1500–1504.

(27) Rossignol, C.; Ralph, J. M.; Bae, J. M.; Vaughey, J. T. $Ln_{1-x}Sr_xCoO_3$ (*Ln* = Gd, Pr) as a Cathode for Intermediate-Temperature Solid Oxide Fuel Cells. *Solid State Ionics* **2004**, *175*, 59–61.

(28) Andersson, M.; Yuan, J.; Sundén, B. Review on Modeling Development for Multiscale Chemical Reactions Coupled Transport Phenomena in Solid Oxide Fuel Cells. *Appl. Energy* **2010**, *87* (5), 1461–1476.

(29) Zhang, X.; Decès-Petit, C.; Yick, S.; Robertson, M.; Kesler, O.; Maric, R.; Ghosh, D. A Study

on Sintering Aids for $Sm_{0.2}Ce_{0.8}O_{1.9}$ Electrolyte. *J. Power Sources* **2006**, *162* (1), 480–485.

(30) Mori, M.; Sammes, N. M. Sintering and Thermal Expansion Characterization of Al-Doped and Co-Doped Lanthanum Strontium Chromites Synthesized by the Pechini Method. *Solid State Ionics* **2002**, *146* (3–4), 301–312.

(31) Señarís-Rodríguez, M. A.; Goodenough, J. B. $LaCoO_3$ Revisited. *Journal of Solid State Chemistry*. 1995, pp 224–231.

(32) Lee, S. J.; Yong, S. M.; Kim, D. S.; Kim, D. K. Cobalt-Free Composite Cathode for SOFCs: Brownmillerite-Type Calcium Ferrite and Gadolinium-Doped Ceria. *Int. J. Hydrogen Energy* **2012**, *37* (22), 17217–17224.

(33) Moon, J. W.; Masuda, Y.; Seo, W. S.; Koumoto, K. Influence of Ionic Size of Rare-Earth Site on the Thermoelectric Properties of $RCoO_3$-Type Perovskite Cobalt Oxides. *Mater. Sci. Eng. B Solid-State Mater. Adv. Technol.* **2001**, *85* (1), 70–75.

(34) Lee, K. T.; Manthiram, A. $LaSr_3Fe_{3-y}Co_yO_{10-\delta}$ ($0 \leq y \leq 1.5$) Intergrowth Oxide Cathodes for Intermediate Temperature Solid Oxide Fuel Cells. *Chem. Mater.* **2006**, *18*, 1621–1626.

(35) Takahashi, H.; Munakata, F.; Yamanaka, M. Ab Initio Study of the Electronic Structures in $LaCoO_3$-$SrCoO_3$ Systems. *Phys. Rev. B* **1998**, *57* (24), 15211–15218.

(36) McIntosh, S.; Gorte, R. J. Direct Hydrocarbon Solid Oxide Fuel Cells. *Chem. Rev.* **2004**, *104*, 4845–4865.

(37) Adler, S. B. Factors Governing Oxygen Reduction in Solid Oxide Fuel Cell Cathodes. *Chem. Rev.* **2004**, *104*, 4791–4843.

(38) Bastidas, D. M.; Tao, S.; Irvine, J. T. S. A Symmetrical Solid Oxide Fuel Cell Demonstrating Redox Stable Perovskite Electrodes. *J. Mater. Chem.* **2006**, *16* (17), 1603–1605.

(39) Yoo, S.; Shin, J. Y.; Kim, G. Thermodynamic and Electrical Properties of Layered Perovskite $NdBaCo_{2-x}Fe_xO_{5+\delta}$−YSZ ($x$ = 0, 1) Composites for Intermediate Temperature SOFC Cathodes. *J. Electrochem. Soc.* **2011**, *158* (6), B632–B638.

(40) Jun, A.; Yoo, S.; Gwon, O.; Shin, J.; Kim, G. Thermodynamic and Electrical Properties of $Ba_{0.5}Sr_{0.5}Co_{0.8}Fe_{0.2}O_{3-\delta}$ and $La_{0.6}Sr_{0.4}Co_{0.2}Fe_{0.8}O_{3-\delta}$ for Intermediate-Temperature Solid Oxide Fuel Cells. *Electrochim. Acta* **2013**, *89*, 372–376.

(41) Lü, S.; Meng, X.; Ji, Y.; Fu, C.; Sun, C.; Zhao, H. Electrochemical Performances of $NdBa_{0.5}Sr_{0.5}Co_2O_{5+x}$ as Potential Cathode Material for Intermediate-Temperature Solid Oxide Fuel Cells. *J. Power Sources* **2010**, *195* (24), 8094–8096.

Chapter 6. Electrochemical properties of B-site Ni-doped layered perovskite cathodes for IT-SOFCs

6.1. Introduction

Solid oxide fuel cells (SOFCs) are one of the promising power generation devices given their advantages of high energy conversion efficiency, good fuel flexibility, and low emission. High operating temperature of 800-1000 ^{o}C, however, imposes considerable restrictions on material compatibility, resulting in increased expenditure. For many years, the main approach for the development of SOFCs has consequently been lowering the operation temperatures to an intermediate (500-700 ^{o}C) range in order to improve material compatibility and practical applicability.[1,2] Reducing operating temperature, however, leads to significant polarization losses of the electrodes, a phenomenon associated with slow kinetics for the oxygen reduction reaction (ORR) and charge transport. Because the polarization loss on the electrodes limits the cell performance at intermediate operating temperature, cathode materials with high electrocatalytic activity for the ORR should therefore be developed.[3]

In this regard, mixed ionic-electronic conductors (MIECs)[4,5] have received considerable attention as promising candidate cathode materials to attain high performance in electrodes for intermediate temperature solid oxide fuel cells (IT-SOFCs). The reaction sites of MIECs extend the active ORR sites from the three-phase boundary to the entire exposed surface of MIEC cathodes, which affords low cathode polarization resistance and high performance at intermediate operating temperature.[6]

Among the MIECs studied to date, many researchers have recently focused on layered perovskite oxides, because they offer fast oxygen reduction kinetics and high electrical conductivities relative to those of ABO_3-type perovskite oxides. In particular, $LnBaCo_2O_{5+\delta}$ (Ln = Pr, Nd, Sm, Gd, and Y), cobalt containing layered oxides, have stacking layers of $[CoO_2]$-$[LnO_\delta]$-$[CoO_2]$-[BaO] along the *c*-axis, and it can be speculated that alternating lanthanide and alkali-earth planes of the layered oxide will enhance the oxygen transport kinetics compared with ABO_3-type perovskite oxides.[7-11] Kim *et al*.[12] reported that $PrBaCo_2O_{5+\delta}$ provides faster oxygen ion diffusion and surface exchange kinetics, which are reflected in very low area specific resistance, compared with $La_{0.5}Sr_{0.5}CoO_{3-\delta}$ at intermediate temperature (500 - 700 ^{o}C).

Furthermore, some researchers have reported that the substitution of Sr for Ba in $LnBaCo_2O_{5+\delta}$ can improve the conductivity and the catalytic activity for the ORR of layered perovskite oxides, such as $GdBa_{1-x}Sr_xCo_2O_{5+\delta}$ and $YBa_{1-x}Sr_xCo_2O_{5+\delta}$.[13-15] Jun *et al.* recently reported that a layered $SmBa_{0.5}Sr_{0.5}Co_2O_{5+\delta}$ perovskite oxide has favorable electrochemical properties and can be potentially utilized as a cathode material for IT-SOFC applications.[16]

However, cobalt-containing cathodes accompany problems such as high thermal expansion

coefficients (TEC) and the high cost of cobalt, making them unsuitable for practical use as a cathode material for SOFCs. In particular, the thermal expansion mismatch between the cell components makes this material unsuitable for IT-SOFC cathode applications subject to repeated thermal cycling.[17] Partial substitution of various transition metals (e.g. Mn, Fe, Ni, and Cu) for cobalt in these materials is considered a possible avenue to address the aforementioned problems of cobalt containing cathodes while maintaining adequate electrochemical activity.[18-22] In this study, among the applicable transition metals, we focus on the effects of Ni doping on the Co site in $SmBa_{0.5}Sr_{0.5}Co_2O_{5+\delta}$ in terms of structural characteristics, electrical properties, and electrochemical performance of $SmBa_{0.5}Sr_{0.5}Co_{2-x}Ni_xO_{5+\delta}$ (x = 0, 0.1, 0.2, and 0.3) in relation to its application as an IT-SOFC cathode material.

6.2. Experimental

The $SmBa_{0.5}Sr_{0.5}Co_{2-x}Ni_xO_{5+\delta}$ (x = 0, 0.1, 0.2, and 0.3) cathodes were synthesized by the Pechini method. Stoichiometric amounts of $Sm(NO_3)_3 \cdot 6H_2O$ (Aldrich, 99+%, metal basis), $Ba(NO_3)_2$ (Aldrich, 99+%), $Sr(NO_3)_2$ (Aldrich, 99+%), $Co(NO_3)_2 \cdot 6H_2O$ (Aldrich, 98+%), $Ni(NO_3)_2 \cdot 6H_2O$ (Aldrich,99+%), and citric acid were dissolved in distilled water with adequate amount of ethylene glycol. After a viscous resin was formed, the mixture was heated to roughly 250 ºC. The powder was calcined at 600 ºC for 4 h and ball-milled in acetone for 24 h. For the final step to form a phase, the powder was pressed into pellets and then sintered in air at various temperatures. The $SmBa_{0.5}Sr_{0.5}Co_{2-x}Ni_xO_{5+\delta}$ (x = 0, 0.1, 0.2, and 0.3) samples were sintered in air at 1100 ºC for 12 h. The abbreviations used to identify the various samples are summarized in Table 6.1. The reactivity of $SmBa_{0.5}Sr_{0.5}Co_{2-x}Ni_xO_{5+\delta}$+GDC was evaluated by XRD patterns of a sintered sample obtained from intimate mixing of 60 wt% of $SmBa_{0.5}Sr_{0.5}Co_{2-x}Ni_xO_{5+\delta}$ and 40 wt% of GDC. An agate mortar was used to mix fine $SmBa_{0.5}Sr_{0.5}Co_{2-x}Ni_xO_{5+\delta}$-GDC powders suspended in acetone. For the cathode slurry, $SmBa_{0.5}Sr_{0.5}Co_{2-x}Ni_xO_{5+\delta}$ and $Ce_{0.9}Gd_{0.1}O_{2-\delta}$ (GDC) powders were thoroughly mixed together at a weight ratio of 6:4 and the mixed powders were blended with an organic binder (Heraeus V006) to form slurries thereafter.

Table 6.1. Abbreviations of specimens.

Chemical composition	Abbreviations
$Ce_{0.9}Gd_{0.1}O_{2-\delta}$	GDC
$SmBa_{0.5}Sr_{0.5}Co_2O_{5+\delta}$	SBSCO
$SmBa_{0.5}Sr_{0.5}Co_{1.9}Ni_{0.1}O_{5+\delta}$	SBSCN10
$SmBa_{0.5}Sr_{0.5}Co_{1.8}Ni_{0.2}O_{5+\delta}$	SBSCN20

The structure of $SmBa_{0.5}Sr_{0.5}Co_{2-x}Ni_xO_{5+\delta}$ (x = 0, 0.1, 0.2, and 0.3) was characterized by using an X-ray diffractometer (Rigaku diffractometer, Cu Kα radiation) at a scanning rate of 0.6 ° min^{-1} and a range 20 ° < 2θ < 100 °. The powder pattern and lattice parameters were analyzed by Rietveld refinement using the GSAS program. The microstructures of the $SmBa_{0.5}Sr_{0.5}Co_{2-x}Ni_xO_{5+\delta}$ (x = 0, 0.1, 0.2, and 0.3) composites and cross sections of single cells were investigated using field emission scanning electron microscopy (Nova Nano SEM, FEI, USA). For the measurement of electrical conductivity, the powder was pressed into a cylindrical shape and sintered to dense pellets (>98 % density). The electrical conductivities of $SmBa_{0.5}Sr_{0.5}Co_{2-x}Ni_xO_{5+\delta}$ samples were measured by a four-terminal DC arrangement technique. The current and the voltage were recorded by a BioLogic Potentiostat from 100 to 750 °C at intervals of 50 °C in air.

A thermogravimetric analysis (TGA) was performed using a thermogravimetric analyzer (SDT-Q600, TA Instruments, USA) from 100 to 900 °C with a heating/cooling rate of 2 °C min^{-1} in air. The initial oxygen content of the $SmBa_{0.5}Sr_{0.5}Co_{2-x}Ni_xO_{5+\delta}$ oxides was determined by iodometric titration.

Impedance spectroscopy of $SmBa_{0.5}Sr_{0.5}Co_{2-x}Ni_xO_{5+\delta}$ was carried out using a symmetric cell. The GDC powder was pressed into pellets and sintered at 1350 °C for 4 h in air to obtain a ~ 1 mm-thick electrolyte substrate. Slurries of the $SmBa_{0.5}Sr_{0.5}Co_{2-x}Ni_xO_{5+\delta}$-GDC composite were screen-printed onto both sides of the dense GDC electrolyte to form a symmetrical cell, which was then heated at 950 °C for 4 h. The silver paste was used as the current collector for the electrodes. Impedance spectra were recorded under OCV in a frequency range of 1 mHz to 500 kHz with AC perturbation of 14 mA from 500 to 650 °C using a BioLogic Potentiostat.

A NiO-GDC anode-supported cell was fabricated to measure the electrochemical performance of $SmBa_{0.5}Sr_{0.5}Co_{2-x}Ni_xO_{5+\delta}$. The NiO-GDC cermet anode was prepared by a mixture of nickel oxide, GDC, and starch at a weight ratio of 6:4:1.5 after being ball-milled in ethanol for 24 h. After drying, the NiO-GDC mixture was pressed into a pellet (0.6 mm thick and 15 mm diameter). Thin GDC electrolyte membranes were prepared by a refined particle suspension coating technique. A GDC suspension was prepared by dispersing GDC powder (Aldrich) in ethanol with a small amount of binder (polyvinyl Butyral, B-98) and dispersant (Triethanolamine, Alfa Aesar) at a ratio of 1:10. The GDC suspension was applied to a NiO-GDC anode support by drop-coating, followed by drying in air and subsequent co-sintering at 1400 °C for 5 h. Cathode slurries were applied onto the surface of the GDC electrolyte layer by screen printing and a tri-layer $SmBa_{0.5}Sr_{0.5}Co_{2-x}Ni_xO_{5+\delta}$-GDC|GDC|NiO-GDC cell was finally sintered at 950 °C for 4 h in air. The electrolyte and cathode thickness of a single cell were both about ~ 20 μm with a 500 μm thick anode. For the single-cell performance test, Ag wires were attached at both electrodes of the single cell using Ag paste as a current collector, as illustrated in Figure 6.1. The single cell was fully sealed onto one end of an alumina tube using a ceramic adhesive (Aremco, Ceramabond 552). Humidified hydrogen (3 % H_2O) was applied to the anode side as fuel through a

water bubbler with a flow rate of 20 mL min^{-1} and ambient air was used as an oxidant during single cell tests. *I-V* curves and impedance spectra were recorded using a BioLogic Potentiostat at operating temperature from 500 to 650 °C.

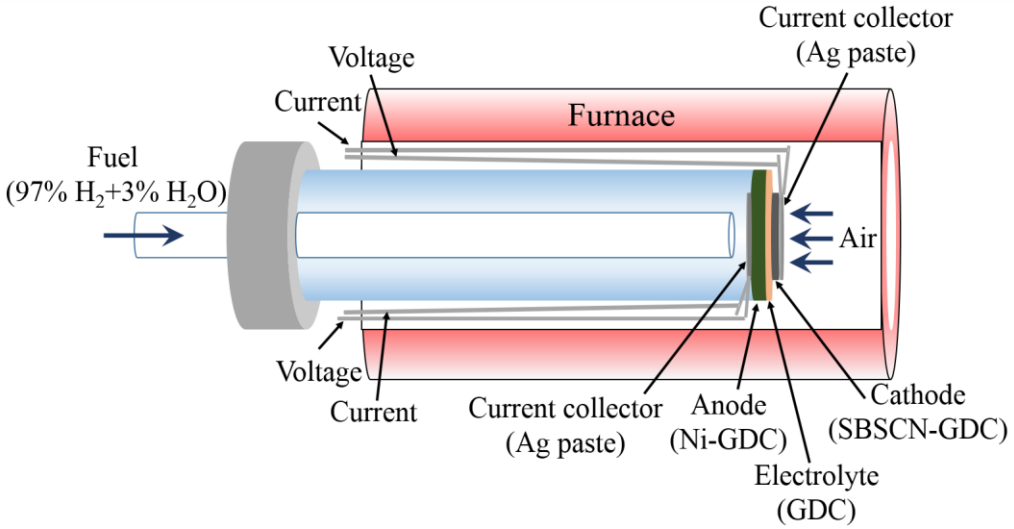

Figure 6.1. Schematic diagram of the single cell ($SmBa_{0.5}Sr_{0.5}Co_{2-x}Ni_xO_{5+\delta}$-GDC|GDC|Ni-GDC) test equipment.

6.3. Results and Discussions

Figure 6.2 (a) shows the XRD patterns of $SmBa_{0.5}Sr_{0.5}Co_{2-x}Ni_xO_{5+\delta}$ (SBSCN, x = 0, 0.1, 0.2, and 0.3) sintered at various temperatures for 12h in air. The observed peaks indicate that SBSCN(x = 0, 0.1, and 0.2) are single-phase perovskites without any detectable secondary phases. On the contrary, the XRD patterns of SBSCN30 show the formation of secondary phases, indicating a Ni solubility limit of ~ 0.2 in the $SmBa_{0.5}Sr_{0.5}Co_{2-x}Ni_xO_{5+\delta}$ system. Figure 6.2 (b) gives the Rietveld refinement data of SBSCN10 and presents good agreement between the observed and calculated profiles. For $SmBa_{0.5}Sr_{0.5}Co_{2-x}Ni_xO_{5+\delta}$, the diffraction pattern of SBSCN10 and SBSCN20 is indexed with the orthorhombic space group *Pmmm*. The lattice parameters have been extracted from Rietveld refinement of XRD data, as shown in Table 6.2. The unit cell volume of SBSCN(x = 0, 0.1, and 0.2) samples increases with increasing Ni content, because the cell volume of the samples with B-site substitution depends on the size of the substituting cations. Comparing the ionic radius of substituting cations, Ni^{3+}(0.56 Å for low spin and 0.6 Å for high spin) is similar or marginally larger than Co^{3+}(0.545 Å for low spin and 0.61 Å for high spin) and Co^{4+}(0.530 Å), which explains the slightly increased volume of the Ni doped SBSCO.[23]

Table 6.2. Space group and lattice parameters of $SmBa_{0.5}Sr_{0.5}Co_{2-x}Ni_xO_{5+\delta}$.

	Space group	*a* (Å)	*b* (Å)	*c* (Å)	*V* (Å)^3	Oxygen content (5+δ)
SBSCO	*P4/mmm*	3.867	3.867	7.585	113.423	5.76
SBSCN10	*Pmmm*	3.875	3.859	7.606	113.737	5.83
SBSCN20	*Pmmm*	3.861	3.875	7.602	113.736	5.72

The chemical compatibility between SBSCN(x = 0, 0.1, and 0.2) and GDC is also confirmed by an SBSCN(x = 0, 0.1, and 0.2)-GDC mixed powder sintered at 950 °C for 4h. Generally, the chemical reaction between the electrode and electrolyte can cause the formation of an undesired insulating layer at the interface, which hampers the ionic and electronic transport.[24] As shown in Figure 6.2 (c), the SBSCN(x = 0, 0.1, and 0.2) and GDC retain their structures without any obvious reactions between SBSCN(x = 0, 0.1, and 0.2) and GDC. SBSCN(x = 0, 0.1, and 0.2) are chemically stable cathode materials for SOFCs based on GDC when the operating temperature is below 950 °C.

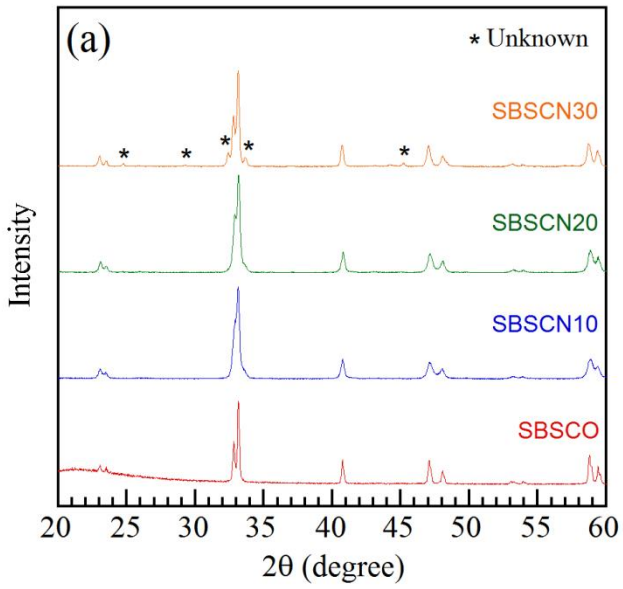

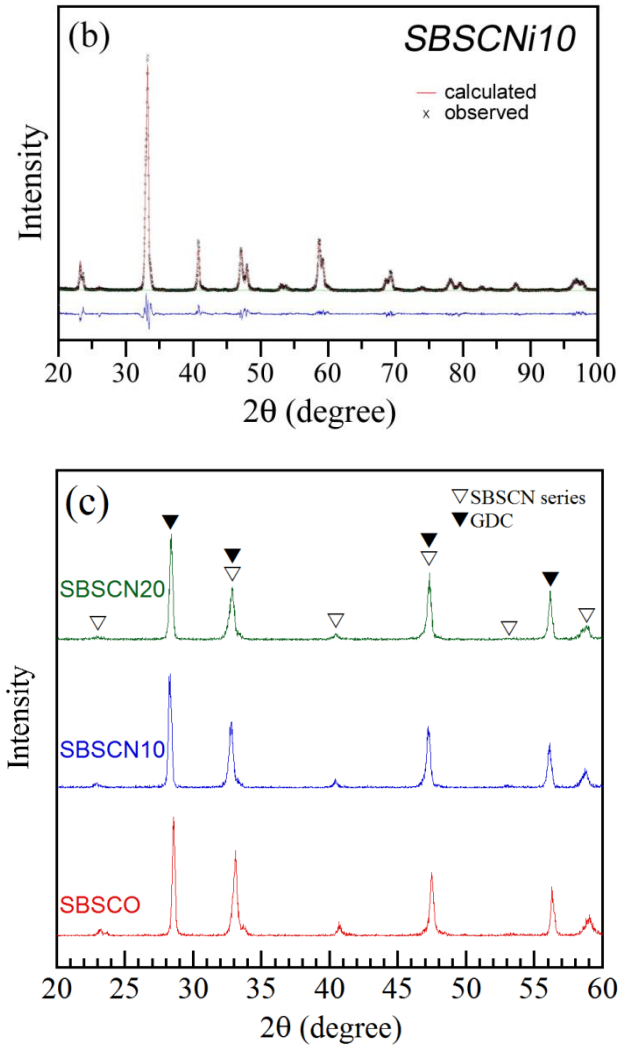

Figure 6.2. (a) XRD patterns of $SmBa_{0.5}Sr_{0.5}Co_{2-x}Ni_xO_{5+\delta}$ (x = 0, 0.1, 0.2, and 0.3) powders. (b) Observed and calculated XRD profiles and the difference between them for SBSCN10. (c) XRD patterns between $SmBa_{0.5}Sr_{0.5}Co_{2-x}Ni_xO_{5+\delta}$ (x = 0, 0.1, and 0.2) and GDC mixture sintered at 950 °C for 4 h.

Figure 6.3 (a) presents a cross-sectional SEM image of a single cell consisting of a SBSCN10-GDC composite cathode, Ni-GDC as an anode, and GDC as an electrolyte sintered at 950 °C for 4 hours. The thickness of the porous cathode and GDC electrolyte of a single cell is about 15μm, respectively. The interface between the cathode and electrolyte appears to be well connected and the electrolyte is dense with no pores or cracks. More detailed microstructural images of $SmBa_{0.5}Sr_{0.5}Co_{2-x}Ni_xO_{5+\delta}$-GDC composite cathodes (x = 0, 0.1, and 0.2) fabricated using the screen printing method are displayed in Figure 6.3 (b)-(d). The cathode has a porous and homogeneous microstructure, which results in fast transport of gases and high electro-catalyst reactions. Moreover, the microstructure of all

$SmBa_{0.5}Sr_{0.5}Co_{2-x}Ni_xO_{5+\delta}$-GDC composite cathodes (x = 0, 0.1, and 0.2) appears to be insensitive to Ni substitution.

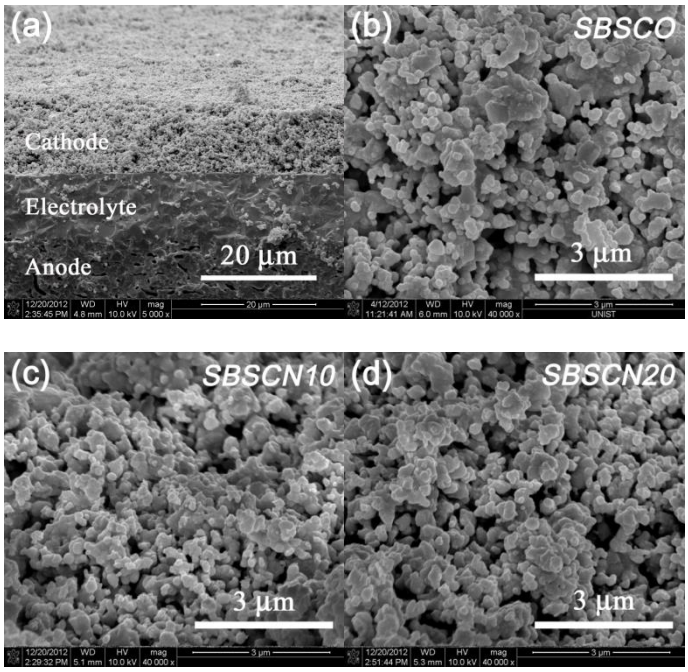

Figure 6.3. SEM micrographs showing (a) the cross section of SBSCN10-GDC|GDC|NiO-GDC and (b)-(d) $SmBa_{0.5}Sr_{0.5}Co_{2-x}Ni_xO_{5+\delta}$-GDC cathodes; (b) SBSCO, (c) SBSCN10, and (d) SBSCN20.

The temperature dependence of electrical conductivity is illustrated in Figure 6.4. All the $SmBa_{0.5}Sr_{0.5}Co_{2-x}Ni_xO_{5+\delta}$ (x = 0, 0.1, and 0.2) samples show a decrease in electrical conductivity with increasing temperature due to the loss of oxygen from the lattice over 200 ^oC, indicating metallic conducting behavior. This can be explained by the knowledge that holes are the major charge carriers and hole conductivity in cobaltites is usually related to the presence of Co^{4+} ions. At given temperature, the electrical conductivity decreases with substitution of Ni for Co, mainly due to a decrease in the covalency of the (Co-Ni)-O bond, which is consistent with previous findings.[25,26] However, all the $SmBa_{0.5}Sr_{0.5}Co_{2-x}Ni_xO_{5+\delta}$ (x = 0, 0.1, and 0.2) samples show conductivity >300 Scm^{-1} up to 800 ^oC, which satisfies the electrical conductivity requirement for IT-SOFC cathode application.[27]

The inset in Figure 6.5 compares TGA data of $SmBa_{0.5}Sr_{0.5}Co_{2-x}Ni_xO_{5+\delta}$ (x = 0, 0.1, and 0.2) samples recorded from 100 to 900 ^oC in air. All $SmBa_{0.5}Sr_{0.5}Co_{2-x}Ni_xO_{5+\delta}$ (x = 0, 0.1, and 0.2) samples start to lose weight slightly above 200 ^oC due to the oxygen released from the lattice, with weight loss of 1.5 – 1.6 % from 100 to 900 ^oC. The TGA data indicate that the oxygen loss upon increasing temperature decreases with Ni substitution in relation to the thermal stability of Ni and Co ions. Figure 6.5 shows the variation of the oxygen content with temperature in air for $SmBa_{0.5}Sr_{0.5}Co_{2-x}Ni_xO_{5+\delta}$ (x =

0, 0.1, and 0.2) samples. These curves were derived using the initial oxygen content determined by the iodometric titration data presented in Table 2. The oxygen content of the SBSCN10 samples is the highest in a temperature range of 100 – 900 °C, which results in an increase in the oxygen mobile species.

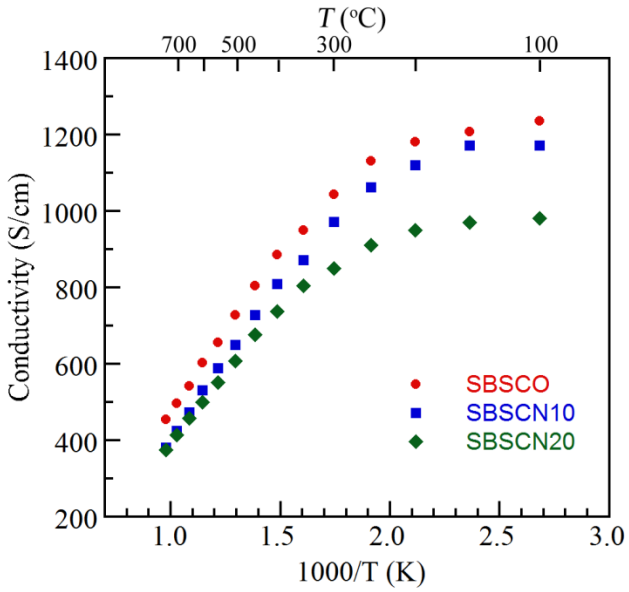

Figure 6.4. Electrical conductivities of $SmBa_{0.5}Sr_{0.5}Co_{2-x}Ni_xO_{5+\delta}$ (x = 0, 0.1, and 0.2) at various temperatures from 100 to 750 °C in air.

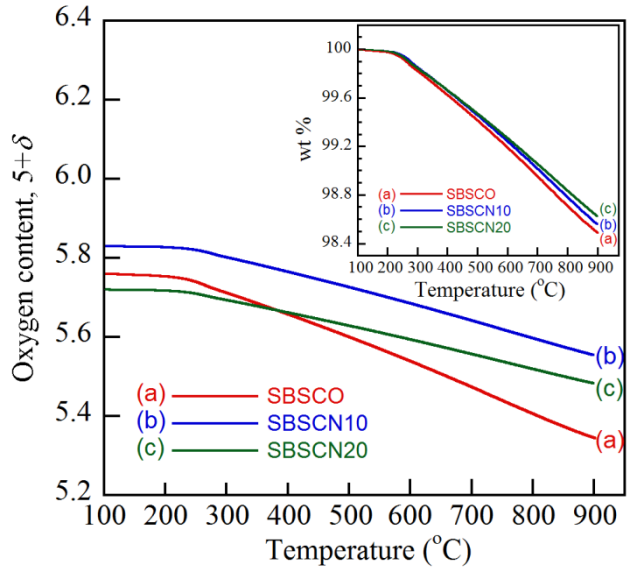

Figure 6.5. Variations of oxygen contents in $SmBa_{0.5}Sr_{0.5}Co_{2-x}Ni_xO_{5+\delta}$ (x = 0, 0.1, and 0.2) with temperature in air. The inset shows thermogravimetric analysis data by the weight change with temperature in air; (a) SBSCO, (b) SBSCN10, and (c) SBSCN20.

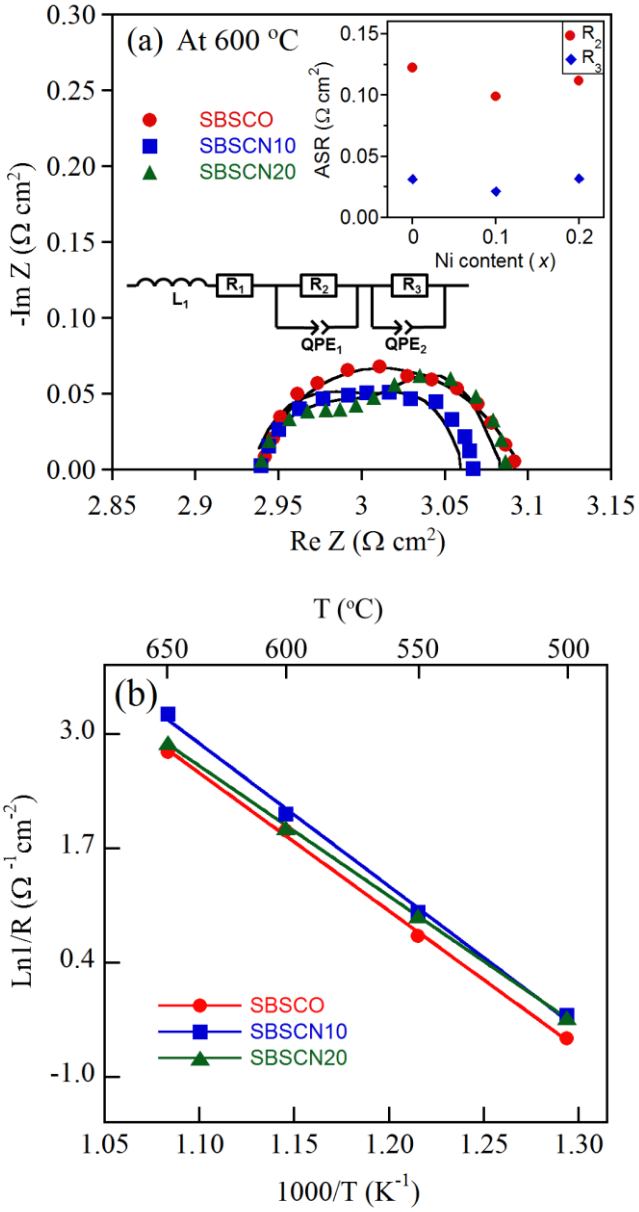

Figure 6.6 (a) Experimental and simulated impedance spectra of $SmBa_{0.5}Sr_{0.5}Co_{2-x}Ni_xO_{5+\delta}$-GDC|GDC|$SmBa_{0.5}Sr_{0.5}Co_{2-x}Ni_xO_{5+\delta}$-GDC at 600 °C under OCV by the equivalent circuit shown as an inset. The inset in Figure 6.6 (a) shows the R_2 and R_3 at various Ni content determined from the impedance spectra. (b) Arrhenius plots of 1/ASR for $SmBa_{0.5}Sr_{0.5}Co_{2-x}Ni_xO_{5+\delta}$ (x = 0, 0.1, and 0.2) at various temperatures.

The area specific resistance (ASR) of $SmBa_{0.5}Sr_{0.5}Co_{2-x}Ni_xO_{5+\delta}$ is obtained by AC impedance spectroscopy for $SmBa_{0.5}Sr_{0.5}Co_{2-x}Ni_xO_{5+\delta}$-GDC|GDC|$SmBa_{0.5}Sr_{0.5}Co_{2-x}Ni_xO_{5+\delta}$-GDC symmetrical cells. The ASR values are determined by the impedance intercept between high-

frequency and low-frequency with the real axis of the Nyquist plot. The experimental impedance spectra are presented in Figure 6.6 (a) and well fitted by the equivalent circuit model showed as an inset in Figure 6.6 (a). The inset in Figure 6.6 (a) shows the R_2 and R_3 at various Ni content determined from the impedance spectra. The ASR values of $SmBa_{0.5}Sr_{0.5}Co_{2-x}Ni_xO_{5+\delta}$-GDC are 0.152, 0.125, and 0.146 Ω cm^2 at x = 0, 0.1, and 0.2, respectively, at 600 ºC. In general, the population of oxygen mobile species may contribute to the enhanced oxygen kinetics associated with oxygen bulk diffusion and surface exchange.[4,28,29] A higher concentration of oxygen mobile species in the Ln-O layer may lead to faster oxygen kinetics and better electrochemical performance. Therefore, SBSCN10 is expected to provide fast oxygen diffusion in the bulk and high surface kinetics on the surface of the electrode among the $SmBa_{0.5}Sr_{0.5}Co_{2-x}Ni_xO_{5+\delta}$ samples. The temperature dependence of ASR with the $SmBa_{0.5}Sr_{0.5}Co_{2-x}Ni_xO_{5+\delta}$-GDC composite is illustrated by an Arrhenius plot in Figure 6.6(b). The ASR value of SBSCN10 is lower than that of SBSCO and SBSCN20 at operating temperature range (500 – 650 ºC).

Figure 6.7 shows the power density and cell voltage as a function of the current density for $SmBa_{0.5}Sr_{0.5}Co_{2-x}Ni_xO_{5+\delta}$-GDC|GDC|NiO-GDC cells using humidified H_2 (3 % H_2O) as a fu el and ambient air as an oxidant in a temperature range of 500 - 650 ºC. The maximum power density of SBSCO, SBSCN10, and SBSCN20 is 1.37, 1.78, and 1.57 W cm^{-2} at 600 ºC, respectively. The maximum power density of SBSCN10 is remarkably high, as expected from it having the lowest ASR value, thus showing that the SBSCN10 layered perovskites can enhance the electrochemical performance of a single cell.

In conclusion, SBSCN10 is considered an adequate material as a cathode for IT-SOFCs considering that Ni substitution in SBSCO provides satisfactory electrical properties and electrochemical performance under typical fuel cell operating conditions.

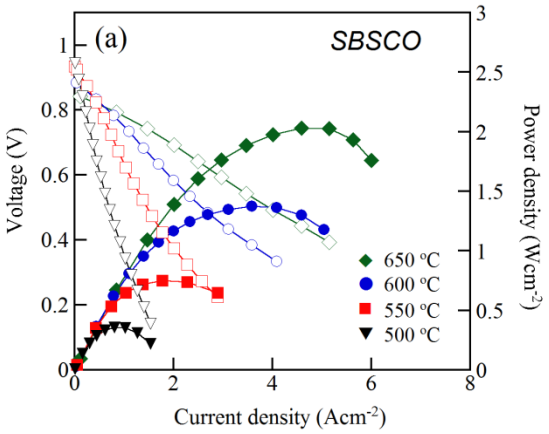

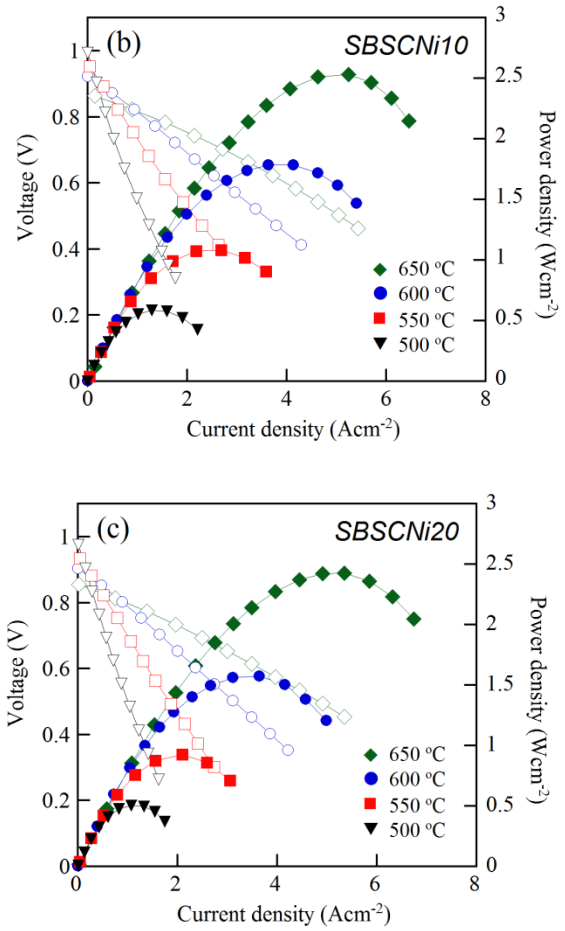

Figure 6.7. *I-V* curve for $SmBa_{0.5}Sr_{0.5}Co_{2-x}Ni_xO_{5+\delta}$-GDC|GDC|NiO-GDC at different temperatures: (a) SBSCO, (b) SBSCN10, and (c) SBSCN20.

6.4. Conclusions

The effects of Ni substitution for the Co site in $SmBa_{0.5}Sr_{0.5}Co_2O_{5+\delta}$ are investigated in terms of structural characteristics, electrical properties, and electrochemical performance of $SmBa_{0.5}Sr_{0.5}Co_{2-x}Ni_xO_{5+\delta}$($x$ = 0, 0.1, and 0.2) in relation to its application as an IT-SOFC cathode material. The electrical conductivity decreases with increasing Ni content, mainly due to a decrease in the covalency of the (Co-Ni)-O bond. The ASR values of $SmBa_{0.5}Sr_{0.5}Co_{2-x}Ni_xO_{5+\delta}$-GDC are 0.152, 0.125, and 0.146 Ω cm^2 at x = 0, 0.1, and 0.2, respectively, at 600 °C. The maximum power density of SBSCO, SBSCN10, and SBSCN20 is 1.37, 1.78, and 1.57 W cm^{-2} at 600 °C, respectively. The maximum power density of SBSCN10 is remarkably high, as expected from it having the lowest ASR value, thus showing that the SBSCN10 layered perovskites can enhance the electrochemical performance of a single cell. Ni doped $SmBa_{0.5}Sr_{0.5}Co_{2-x}Ni_xO_{5+\delta}$ is considered a suitable material as a cathode for IT-SOFCs considering that Ni substitution in SBSCO provides sufficiently high electrical conductivities and electrochemical

performance under typical fuel cell operating conditions.

References

(1) Steele, B. C.; Heinzel, A. Materials for Fuel-Cell Technologies. *Nature* **2001**, *414*, 345–352.

(2) Jacobson, A. J. Materials for Solid Oxide Fuel Cells. *Chem. Mater.* **2010**, *22* (3), 660–674.

(3) Colomer, M. T.; Steele, B. C. H.; Kilner, J. a. Structural and Electrochemical Properties of the Cathode $Sr_{0.8}Ce_{0.1}Fe_{0.7}Co_{0.3}O_{3-\delta}$ Perovskite Material for ITSOFCs. *Solid State Ionics* **2002**, *147*, 41–48.

(4) Adler, S. B.; Lane, J. A.; Steele, B. C. H. Electrode Kinetics of Porous Mixed-Conducting Oxygen Electrodes. *J. Electrochem. Soc.* **1996**, *143* (11), 3554–3564.

(5) Kim, J.; Jun, A.; Shin, J.; Kim, G. Effect of Fe Doping on Layered $GdBa_{0.5}Sr_{0.5}Co_2O_{5+\delta}$ Perovskite Cathodes for Intermediate Temperature Solid Oxide Fuel Cells. *J. Am. Ceram. Soc.* **2014**, *97* (2), 651–656.

(6) Fleig, J. On the Width of the Electrochemically Active Region in Mixed Conducting Solid Oxide Fuel Cell Cathodes. *J. Power Sources* **2002**, *105* (2), 228–238.

(7) Chroneos, A.; Yildiz, B.; Tarancon, A.; Parfitt, D.; Kilner, J. A Oxygen Diffusion in Solid Oxide Fuel Cell Cathode and Electrolyte Materials: Mechanistic Insights from Atomistic Simulations. *Energy Environ. Sci.* **2011**, 2774–2789.

(8) Zhu, C.; Liu, X.; Yi, C.; Yan, D.; Su, W. Electrochemical Performance of $PrBaCo_2O_{5+\delta}$ Layered Perovskite as an Intermediate-Temperature Solid Oxide Fuel Cell Cathode. *J. Power Sources* **2008**, *185* (1), 193–196.

(9) Gu, H.; Chen, H.; Zheng, Y.; Guo, L. Effect of Chromium Poisoning on the Electrochemical Properties of $NdBaCo_2O_{5+\delta}$ Cathode for IT-SOFCs. *Int. J. Hydrogen Energy* **2010**, *35* (6), 2457–2462.

(10) Zhou, Q.; He, T.; Ji, Y. $SmBaCo_2O_{5+x}$ Double-Perovskite Structure Cathode Material for Intermediate-Temperature Solid-Oxide Fuel Cells. *J. Power Sources* **2008**, *185* (2), 754–758.

(11) Kim, J.-H.; Manthiram, A. $LnBaCo_2O_{5+\delta}$ Oxides as Cathodes for Intermediate-Temperature Solid Oxide Fuel Cells. *J. Electrochem. Soc.* **2008**, *155* (4), B385–B390.

(12) Kim, G.; Wang, S.; Jacobson, A. J.; Reimus, L.; Brodersen, P.; Mims, C. A. Rapid Oxygen Ion Diffusion and Surface Exchange Kinetics in $PrBaCo_2O_{5+x}$ with a Perovskite Related Structure and Ordered A Cations. *J. Mater. Chem.* **2007**, *17* (24), 2500–2505.

(13) Kim, J. H.; Cassidy, M.; Irvine, J. T. S.; Bae, J. Electrochemical Investigation of Composite Cathodes with $SmBa_{0.5}Sr_{0.5}Co_2O_{5+\delta}$ Cathodes for Intermediate Temperature-Operating Solid Oxide Fuel Cell. *Chem. Mater.* **2010**, *22* (3), 883–892.

(14) Kim, J.-H.; Prado, F.; Manthiram, A. Characterization of $GdBa_{1-x}Sr_xCo_2O_{5+\delta}$ ($0 \leq x \leq 1.0$) Double Perovskites as Cathodes for Solid Oxide Fuel Cells. *J. Electrochem. Soc.* **2008**, *155* (10), B1023–B1028.

(15) Mckinlay, A.; Connor, P.; Irvine, J. T. S.; Zhou, W. Structural Chemistry and Conductivity of a

Solid Solution of $YBa_{1-x}Sr_xCo_2O_{5+\delta}$. *J. Phys. Chem. C* **2007**, *111* (51), 19120–19125.

(16) Jun, A.; Kim, J.; Shin, J.; Kim, G. Optimization of Sr Content in Layered $SmBa_{1-x}Sr_xCo_2O_{5+\delta}$ Perovskite Cathodes for Intermediate-Temperature Solid Oxide Fuel Cells. *Int. J. Hydrogen Energy* **2012**, *37* (23), 18381–18388.

(17) Huang, K.; Lee, H. Y.; Goodenough, J. B. Sr- and Ni-Doped $LaCoO_3$ and $LaFeO_3$ Perovskites. *J. Electrochem. Soc.* **1998**, *145* (9), 3220–3227.

(18) Zhou, Q.; Wang, W.; Wei, T.; Qi, X.; Li, Y.; Zou, Y.; Liu, Y.; Li, Z.; Wu, Y. $LaBaCuFeO_{5+\delta}$–$Ce_{0.8}Sm_{0.2}O_{1.9}$ as Composite Cathode for Solid Oxide Fuel Cells. *Ceram. Int.* **2012**, *38* (2), 1529–1532.

(19) Kim, J.; Choi, S.; Park, S.; Kim, C.; Shin, J.; Kim, G. Effect of Mn on the Electrochemical Properties of a Layered Perovskite $NdBa_{0.5}Sr_{0.5}Co_{2-x}Mn_xO_{5+\delta}$ (x = 0, 0.25, and 0.5) for Intermediate-Temperature Solid Oxide Fuel Cells. *Electrochim. Acta* **2013**, *112*, 712–718.

(20) Jun, A.; Shin, J.; Kim, G. High Redox and Performance Stability of Layered $SmBa_{0.5}Sr_{0.5}Co_{1.5}Cu_{0.5}O_{5+\delta}$ Perovskite Cathodes for Intermediate-Temperature Solid Oxide Fuel Cells. *Phys. Chem. Chem. Phys.* **2013**, *15* (45), 19906–19912.

(21) Hu, Y.; Bogicevic, C.; Bouffanais, Y.; Giot, M.; Hernandez, O.; Dezanneau, G. Synthesis, Physical-Chemical Characterization and Electrochemical Performance of $GdBaCo_{2-x}Ni_xO_{5+\delta}$ (x = 0 - 0.8) as Cathode Materials for IT-SOFC Application. *J. Power Sources* **2013**, *242*, 50–56.

(22) Wei, B.; Lü, Z.; Jia, D.; Huang, X.; Zhang, Y.; Su, W. Thermal Expansion and Electrochemical Properties of Ni-Doped $GdBaCo_2O_{5+\delta}$ Double-Perovskite Type Oxides. *Int. J. Hydrogen Energy* **2010**, *35* (8), 3775–3782.

(23) Shannon, B. Y. R. D.; H, M.; Baur, N. H.; Gibbs, O. H.; Eu, M.; Cu, V. Revised Effective Ionic Radii and Systematic Studies of Interatomie Distances in Halides and Chaleogenides. *Acta Crystallogr. Sect. A* **1976**, *A32*, 751–767.

(24) Park, S.; Choi, S.; Shin, J.; Kim, G. A Collaborative Study of Sintering and Composite Effects for a $PrBa_{0.5}Sr_{0.5}Co_{1.5}Fe_{0.5}O_{5+\delta}$ IT-SOFC Cathode. *RSC Adv.* **2014**, *4* (4), 1775.

(25) Kim, J. H.; Manthiram, A. Layered $NdBaCo_{2-x}Ni_xO_{5+\delta}$ Perovskite Oxides as Cathodes for Intermediate Temperature Solid Oxide Fuel Cells. *Electrochim. Acta* **2009**, *54* (28), 7551–7557.

(26) Takahashi, H.; Munakata, F.; Yamanaka, M. Ab Initio Study of the Electronic Structures in $LaCoO_3$-$SrCoO_3$ Systems. *Phys. Rev. B* **1998**, *57* (24), 15211–15218.

(27) McIntosh, S.; Gorte, R. J. Direct Hydrocarbon Solid Oxide Fuel Cells. *Chem. Rev.* **2004**, *104*, 4845–4865.

(28) Kim, J.; Seo, W.; Shin, J.; Liu, M.; Kim, G. Composite Cathodes Composed of $NdBa_{0.5}Sr_{0.5}Co_2O_{5+\delta}$ and $Ce_{0.9}Gd_{0.1}O_2$. *J. Mater. Chem. A* **2013**, *1*, 515–519.

(29) Choi, S.; Yoo, S.; Kim, J.; Park, S.; Jun, A.; Sengodan, S.; Kim, J.; Shin, J.; Jeong, H. Y.; Choi, Y.; *et al*. Highly Efficient and Robust Cathode Materials for Low-Temperature Solid Oxide Fuel

Cells: $PrBa_{0.5}Sr_{0.5}Co_{2-x}Fe_xO_{5+\delta}$. *Sci. Rep.* **2013**, *3*, 2426.

Chapter 7. Correlation between fast oxygen kinetics and enhanced performance in Fe doped layered perovskite cathode for solid oxide fuel cells

7.1. Introduction

Solid oxide fuel cells (SOFCs), which directly convert the chemical energy of a fuel gas into electrical energy, are attractive power generation systems with high energy conversion efficiency, environmental benefits, and greater fuel flexibility.[1-3] However, in spite of a number of advantages compared with conventional power generation systems, they accompany critical problems such as high cost, thermal stress, and material compatibility challenges due to the high operating temperature (800-1000 ^{o}C).[4] For many years, the development of SOFCs has focused on lowering the operating temperature to an intermediate range (500-700 ^{o}C). By lowering the device operating temperature, a wider range of materials can be used to improve the material compatibility and the practical applicability. Developing cathode materials with high electrocatalytic activity for the oxygen reduction reaction (ORR) is also a vital step toward successful operation at intermediate temperature since lower operating temperature causes slow oxygen reduction kinetics and high over-potential at the cathode.[5]

In this regard, mixed ionic electronic conducting (MIECs) cathodes, which exhibit simultaneous electronic and ionic conduction,[6] have received considerable attention for application to intermediate-temperature solid oxide fuel cells (IT-SOFCs). MIEC cathode materials show high performance at the intermediate temperature range, since the oxygen reduction reaction occurs not only at the triple-phase boundary (TPB) between the electrolyte, cathode, and gas phase but also at the two phase boundary between the electrode and gas phase.[7,8]

Among MIECs, layered perovskite oxides described with the general formula $AA'B_2O_{5+\delta}$, have recently been studied by numerous research groups based on their much higher chemical diffusion and surface exchange coefficients relative to those of ABO_3-type perovskite oxides such as $Ba_{0.5}Sr_{0.5}Co_{0.8}Fe_{0.2}O_{3-\delta}$,[9] $La_{0.6}Sr_{0.4}Co_{0.2}Fe_{0.8}O_{3-\delta}$,[10] $Pr_{1-x}Sr_xCoO_{3-\delta}$,[11] and $Sm_{0.5}Sr_{0.5}CoO_3$.[12] In particular, the $LnBaCo_2O_{5+\delta}$, cobalt containing layered perovskite oxides, have stacking layers of …$[LnO_\delta]$-$[CoO_2]$-[BaO]-$[CoO_2]$…. According to modeling results obtained by the authors using density functional theory (DFT) in a previous study, the layered structure possesses pore channels in the [Ln-O] and [Co-O] planes that provide fast paths for oxygen transport, which in turn enhances the kinetics of surface oxygen exchange.[13]

Several researchers have examined the effects of ion substitution on the characteristics of $LnBaCo_2O_{5+\delta}$. For example, Sr substitution of Ba enhances the electrochemical characteristics owing to the higher conductivity and higher oxygen content of the Sr doped layered perovskite oxides, which are considered to be favorable to the ORR.[14] Various transition metal ions also have been introduced

into the B-site such as Mn, Fe, Ni, and Cu.[15-18] In particular, Fe substitution of Co improves the oxygen ion diffusivity, ORR activity, and stability of the cathodes due to increased 3d metal-oxygen bonding energy and decreased thermal expansion.[19]

In a previous study, we investigated the effects of strontium doping on $SmBa_{1-x}Sr_xCo_2O_{5+\delta}$ and reported that the electrochemical performance of $SmBa_{0.5}Sr_{0.5}Co_2O_{5+\delta}$ is remarkably high.[14] Herein, we focus on the catalytic effect of Fe doping of $SmBa_{0.5}Sr_{0.5}Co_2O_{5+\delta}$ for the ORR and optimize the amount of Fe substitution through an investigation of the structural characteristics, electrical properties, redox properties, oxygen kinetics, and electrochemical performance of $SmBa_{0.5}Sr_{0.5}Co_{2-x}Fe_xO_{5+\delta}$ (x = 0, 0.25, 0.5, 0.75, and 1.0) in relation to its application as an IT-SOFC cathode material.

Table 7.1. Abbreviations of specimens

Chemical composition	Abbreviations
$Ce_{0.9}Gd_{0.1}O_{2-\delta}$	GDC
$SmBa_{0.5}Sr_{0.5}Co_2O_{5+\delta}$	SBSCO
$SmBa_{0.5}Sr_{0.5}Co_{1.75}Fe_{0.25}O_{5+\delta}$	SBSCF25
$SmBa_{0.5}Sr_{0.5}Co_{1.5}Fe_{0.5}O_{5+\delta}$	SBSCF50
$SmBa_{0.5}Sr_{0.5}Co_{1.25}Fe_{0.75}O_{5+\delta}$	SBSCF75
$SmBa_{0.5}Sr_{0.5}CoFeO_{5+\delta}$	SBSCF100

7.2. Experimental

Cathode materials $SmBa_{0.5}Sr_{0.5}Co_{2-x}Fe_xO_{5+\delta}$ (x = 0, 0.25, 0.5, 0.75, and 1.0) were synthesized by the Pechini method. Stoichiometric amounts of $Sm(NO_3)_3 \cdot 6H_2O$ (Aldrich, 99+%, metal basis), $Ba(NO_3)_2$ (Aldrich, 99+%), $Sr(NO_3)_2$ (Aldrich, 99+%), $Co(NO_3)_2 \cdot 6H_2O$ (Aldrich, 98+%), and $Fe(NO_3)_2 \cdot 9H_2O$ (Aldrich, 99+%) were dissolved in distilled water to form an aqueous mixed solution with a proper amount of citric acid. An adequate amount of ethylene glycol was added into the beaker after the mixture was dissolved. After a viscous resin was formed, the mixture was heated to roughly 250 °C in air, followed by combustion to form powders, which were calcined at 600 °C for 4 h and ball-milled in acetone for 24 h. For measurement of the electrical conductivity and coulometric titration, the powder was pressed into pellets and then sintered in air at 1150 °C for 12 h. For the cathode slurry, $SmBa_{0.5}Sr_{0.5}Co_{2-x}Fe_xO_{5+\delta}$ and $Ce_{0.9}Gd_{0.1}O_{2-\delta}$ (GDC) powders were thoroughly mixed together at a weight ratio of 6:4 and the mixed powders were then blended with an organic binder (Heraeus V006) to form slurries.

The crystalline structure of $SmBa_{0.5}Sr_{0.5}Co_{2-x}Fe_xO_{5+\delta}$ was characterized by using an X-ray diffractometer (Rigaku diffractometer, Cu Kα radiation). The powder pattern and lattice parameters

were analyzed by Rietveld refinement using the GSAS program. $SmBa_{0.5}Sr_{0.5}Co_{1.5}Fe_{0.5}O_{5+\delta}$(SBSCF50) was also analyzed using an in situ X-ray diffractometer (Bruker AXS D8 Advance diffractometer, Cu Kα radiation) to determine the phase stability in air from 100 to 800 ºC. The microstructures of the $SmBa_{0.5}Sr_{0.5}Co_{2-x}Fe_xO_{5+\delta}$ composites and cross sections of single cells were investigated using field emission scanning electron microscopy (Nova Nano SEM, FEI, USA). A thermogravimetric analysis (TGA) was performed using a thermogravimetric analyzer (SDT-Q600, TA Instruments, USA) from 100 to 900 ºC with a heating/cooling rate of 2 ºC min^{-1} in air. The initial oxygen content values at room-temperature were determined by iodometric titration.

The electrical conductivities of $SmBa_{0.5}Sr_{0.5}Co_{2-x}Fe_xO_{5+\delta}$ samples were measured by a four-terminal DC arrangement technique. The current and the voltage were recorded by a BioLogic Potentiostat from 100 to 750 ºC at intervals of 50 ºC in air.

Coulometric titration was used to accurately quantify the oxidation/reduction state of the $SmBa_{0.5}Sr_{0.5}Co_{2-x}Fe_xO_{5+\delta}$ specimens as a function of $p(O_2)$. The coulometric titration rig was mainly composed of an YSZ tube with Ag-paste electrodes plastered on both sides, a setup that has been described sufficiently elsewhere.[20] The sample was considered to be equilibrated when the potential varied in a range of less than 1 mV per hour. Oxygen nonstoichiometry was decided through this process at 700 ºC over a wide range of oxygen partial pressure. The oxygen partial pressure dependence of the electrical conductivity was also measured by the four-probe DC method with a BioLogic Potentiostat on sintered bars of $SmBa_{0.5}Sr_{0.5}Co_{2-x}Fe_xO_{5+\delta}$.

Impedance spectroscopy of $SmBa_{0.5}Sr_{0.5}Co_{2-x}Fe_xO_{5+\delta}$ was carried out using a symmetric cell. The GDC powder was pressed into pellets and sintered at 1350 ºC for 4 h in air to obtain a ~ 0.6 mm-thick electrolyte substrate. Slurries of the $SmBa_{0.5}Sr_{0.5}Co_{2-x}Fe_xO_{5+\delta}$-GDC composite were screen-printed onto both sides of the dense GDC electrolyte to form a symmetrical cell, which was then heated at 950 ºC for 4 h. Silver paste was used as the current collector for the electrodes.

A NiO-GDC anode-supported cell was fabricated to measure the electrochemical performance of $SmBa_{0.5}Sr_{0.5}Co_{2-x}Fe_xO_{5+\delta}$. The NiO-GDC cermet anode was prepared by a mixture of nickel oxide, GDC, and starch at a weight ratio of 6:4:1.5 after being ball-milled in ethanol for 24 h. The GDC electrolyte was pressed onto the pelletized disk of the NiO-GDC cermet anode, followed by co-sintering at 1350 ºC for 5 h. Cathode slurries were applied onto the surface of the GDC electrolyte layer by screen printing and were finally sintered at 950 ºC for 4 h in air. The electrolyte and cathode thickness of a single cell were both about ~ 20 μm with a 500 μm thick anode. For the single-cell performance test, Ag wires were attached at both electrodes of the single cell using Ag paste as a current collector. The single cell was fixed on an alumina tube using a ceramic adhesive (Aremco, Ceramabond 552). Humidified hydrogen (3 % H_2O) was supplied as fuel through a water bubbler with a flow rate of 100 mL min^{-1} and ambient air was used as an oxidant during single cell tests. *I-V* curves and impedance

spectra were examined using a BioLogic Potentiostat at operating temperature from 500 to 650 ºC. Impedance spectra were recorded under OCV in a frequency range of 1 mHz to 500 kHz with AC perturbation of 14 mV from 500 to 650 ºC.

Isotope oxygen exchange was carried out using a closed circulation system with >96 % $^{18}O_2$. The concentration of $^{18}O_2$ in the gas phase was measured by a mass analyzer (Anelva, M-100-QA-F). The measured samples were polished using diamond paste and the final diameter of diamond paste was 0.25 μm. Natural abundance O_2 under pressure of 200 mbar was introduced into the system with a measured sample, and the sample was heated to 590 ºC. The measured samples were annealed for more than ten times longer than the isotope oxygen exchanging time.[21] The sample was cooled to the room temperature, and residual oxygen was removed from the system. Subsequently, $^{18}O_2$ at pressure of 200 mbar was introduced for oxygen exchange. The sample was then heated rapidly to room temperature. After isotope oxygen exchanging for 40 min, the sample was quenched to room temperature. The obtained sample was cut into a bar shape, and the cut surface was polished by diamond paste. The isotope oxygen diffusion profile was obtained by secondary ion mass spectrometry (SIMS) using an ATOMICA 4100 quadrupole-base analyzer, with the line-scan mode at the cross section of the sample using a cesium ion primary source (Cs^+) at 10 keV. The tracer diffusion coefficient (D^*) and the oxygen surface exchange coefficient (k) were estimated by fitting to the semi-infinite diffusion model.[22]

7.3. Results and Discussions

XRD patterns of $SmBa_{0.5}Sr_{0.5}Co_{2-x}Fe_xO_{5+\delta}$ samples for different iron content (x = 0, 0.25, 0.5, 0.75, and 1.0) are shown in Figure 7.1(a) and structural data are given in Table 7.2. The XRD patterns indicate that all $SmBa_{0.5}Sr_{0.5}Co_{2-x}Fe_xO_{5+\delta}$ specimens are a single-phase perovskite without any detectable impurity phases. The Rietveld refinement data reveal that the diffraction patterns of all samples can be indexed to a tetragonal structure (space group: *P4/mmm*),[23] with those samples being an ordered perovskite structure. The data in Table 7.2 indicate that the lattice parameters and the unit cell volume of the $SmBa_{0.5}Sr_{0.5}Co_{2-x}Fe_xO_{5+\delta}$ samples increase with increasing Fe content, because the cell volume of the samples with B-site substitution depends on the size of the substituting cations. Comparing the ionic radius of the substituting cations, the crystal ionic radius of iron (r_{Fe3+} = 0.785 Å, CN = 6, and HS) is larger than that of cobalt (r_{Co3+} = 0.75 Å, CN = 6, and HS),[24] which explains the increased volume of the Fe doped SBSCO. As an example depicting the refinement of SBSCF50, Figure 7.1(b) shows the observed XRD data, the calculated profile, and the difference between them. Rietveld refinement fitting results show excellent agreement between the experimental data and the calculated profile with high reliability factors of R_{wp} = 4.8 %, and R_p = 3.8 % for the pattern with a goodness-of-fit of 1.277.

Table 7.2. Space group and lattice parameters of $SmBa_{0.5}Sr_{0.5}Co_{2-x}Fe_xO_{5+\delta}$.

	Space group	*a* (Å)	*b* (Å)	*c* (Å)	*V* (Å)^3	Oxygen content (5+δ)	Oxidation state (Co,Fe)
SBSCO	*P4/mmm*	3.862	3.862	7.571	112.921	5.76	3.26
SBSCF25	*P4/mmm*	3.863	3.863	7.759	113.354	5.87	3.37
SBSCF50	*P4/mmm*	3.866	3.866	7.616	113.809	5.98	3.48
SBSCF75	*P4/mmm*	3.870	3.870	7.653	114.612	6.00	3.50
SBSCF100	*P4/mmm*	3.870	3.870	7.695	115.247	6.00	3.50

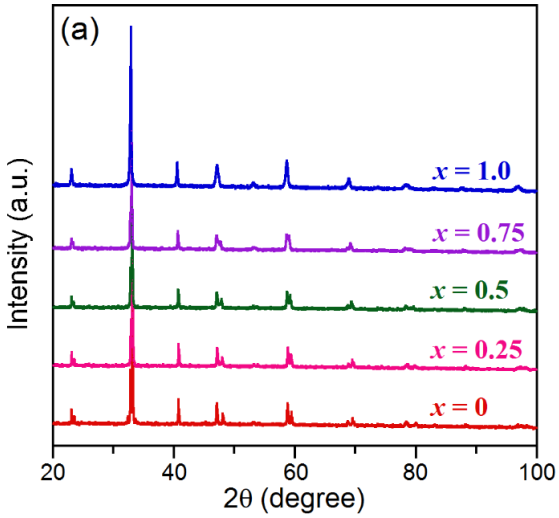

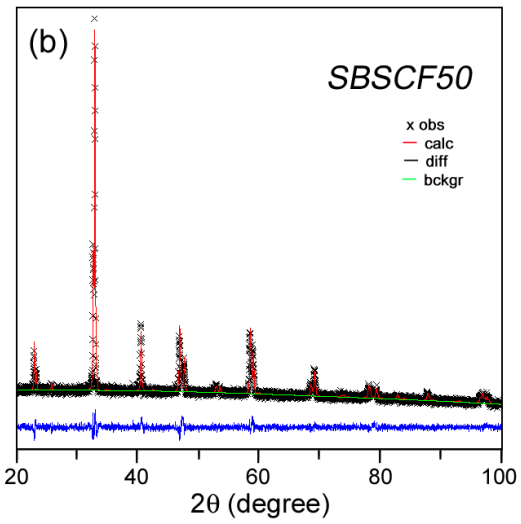

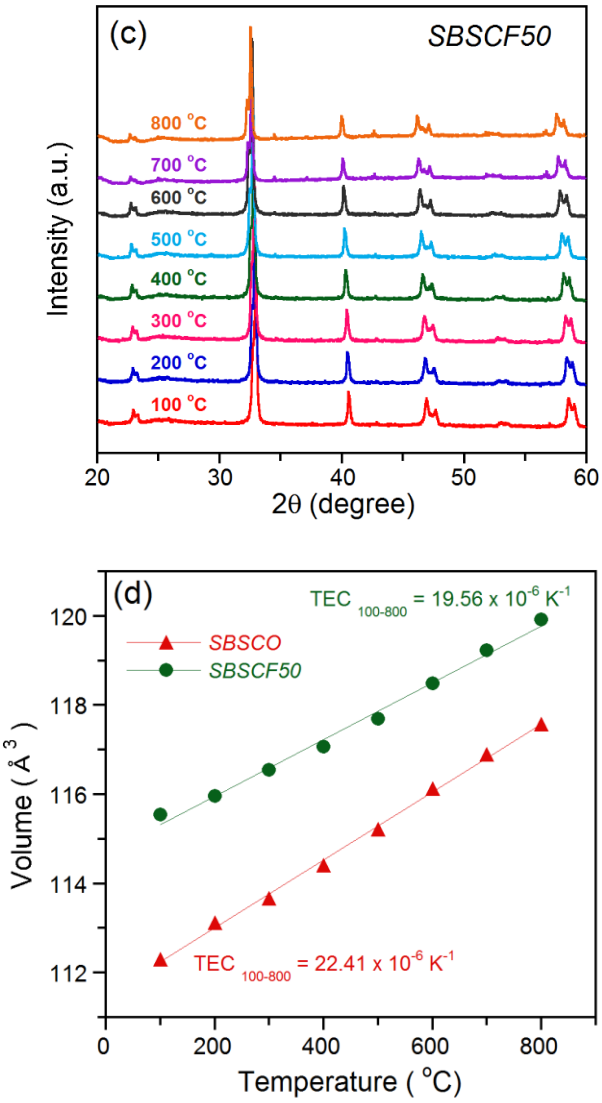

Figure 7.1. (a) XRD patterns of $SmBa_{0.5}Sr_{0.5}Co_{2-x}Fe_xO_{5+\delta}$ (x = 0, 0.25, 0.5, 0.75, and 1.0) powders. (b) Observed and calculated XRD profiles and the difference between them for $SmBa_{0.5}Sr_{0.5}Co_{1.5}Fe_{0.5}O_{5+\delta}$. (c) *In-situ* X-ray diffraction patterns for $SmBa_{0.5}Sr_{0.5}Co_{1.5}Fe_{0.5}O_{5+\delta}$ in air from 100 to 800 °C. (d) Dependence of unit cell volume V (Å ^{3}) on temperature from *in-situ* X-ray diffraction patterns for $SmBa_{0.5}Sr_{0.5}Co_{2-x}Fe_xO_{5+\delta}$ (x = 0 and 0.5).

In order to confirm the phase stability of SBSCF50 at the operating conditions of a SOFC cathode, *in-situ* X-ray diffraction measurements were carried out in a temperature range of 100 - 800 °C with steps of 100 °C under ambient air and the results are presented in Figure 7.1(c). SBSCF50 is a single phase perovskite structure without other phases in the entire temperature range of measurements, indicating that it is thermally stable. Figure 7.1(d) shows the increase of the cell volume as the temperature was increased from 100 to 800 °C, determined by *in-situ* X-ray diffraction measurement. The shift of the peaks to lower 2θ values with increasing temperature indicates thermal expansion. The

thermal expansion coefficient (TEC) of SBSCF50 is 19.56 x 10^{-6} K^{-1} calculated from *in-situ* X-ray diffraction patterns; this value is lower than that (22.41 x 10^{-6} K^{-1}) of SBSCO similar to (20-25 x 10^{-6} K^{-1}) of other cobalt containing layered perovskites.[25,26]

Figure 7.2(a) is a high-angle annular dark field (HAADF) STEM image and selective area electron diffraction (SAED) pattern obtained in the region marked with a white dotted line. The ED pattern clearly shows an ordered superlattice structure through an additional diffraction spot indexed with (001) of a tetragonal structure (lattice constants of a = 3.871 Å and c = 7.757 Å). In addition, the high-resolution STEM image (Figure 7.2(b)) also confirms an ordered stacking sequence [Ba(Sr)O]-[Co(Fe)O_2]-[SmO_δ]-[Co[Fe]O_2]-[Ba(Sr)O] of the structure, showing atomic Z-contrast between Sm and Ba(Sr) columns.

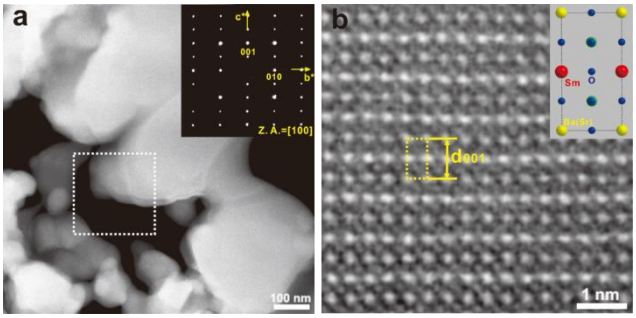

Figure 7.2. (a) High-angle annular dark field (HAADF) STEM image and corresponding selective- area electron diffraction (SAED) pattern obtained from an as-synthesized $SmBa_{0.5}Sr_{0.5}Co_{1.5}Fe_{0.5}O_{5+\delta}$ sample. (b) A high-resolution HAADF STEM image of the grain marked with a white rectangle in (a). The crystal structure of ordered $SmBa_{0.5}Sr_{0.5}Co_{1.5}Fe_{0.5}O_{5+\delta}$ is represented in the right inset.

Scanning electron microscopy (SEM) was carried out to examine the morphology of the $SmBa_{0.5}Sr_{0.5}Co_{2-x}Fe_xO_{5+\delta}$-GDC composites ($x$ = 0, 0.25, 0.5, 0.75, and 1.0). Figure 7.3(a) shows a cross-sectional SEM image of SBSCF50-GDC|GDC|NiO-GDC with an overview of the three layers, showing a thickness of approximately 15-μm for the cathode and 20-μm for the electrolyte. The interface between the cathode and electrolyte appears to be well-connected and the electrolyte is dense with no pores or cracks. More detailed microstructural images of $SmBa_{0.5}Sr_{0.5}Co_{2-x}Fe_xO_{5+\delta}$-GDC composite cathodes (x = 0, 0.25, 0.5, 0.75, and 1.0) fabricated by the screen printing method are displayed in Figures 7.3(b)-(f). The cathode has a porous and homogeneous microstructure, which will result in fast transport of gases and highly activated electro-catalytic reactions. Moreover, the microstructure of all $SmBa_{0.5}Sr_{0.5}Co_{2-x}Fe_xO_{5+\delta}$-GDC composite cathodes (x = 0, 0.25, 0.5, 0.75, and 1.0) is similar, and thus this factor appears to be insensitive to Fe substitution.

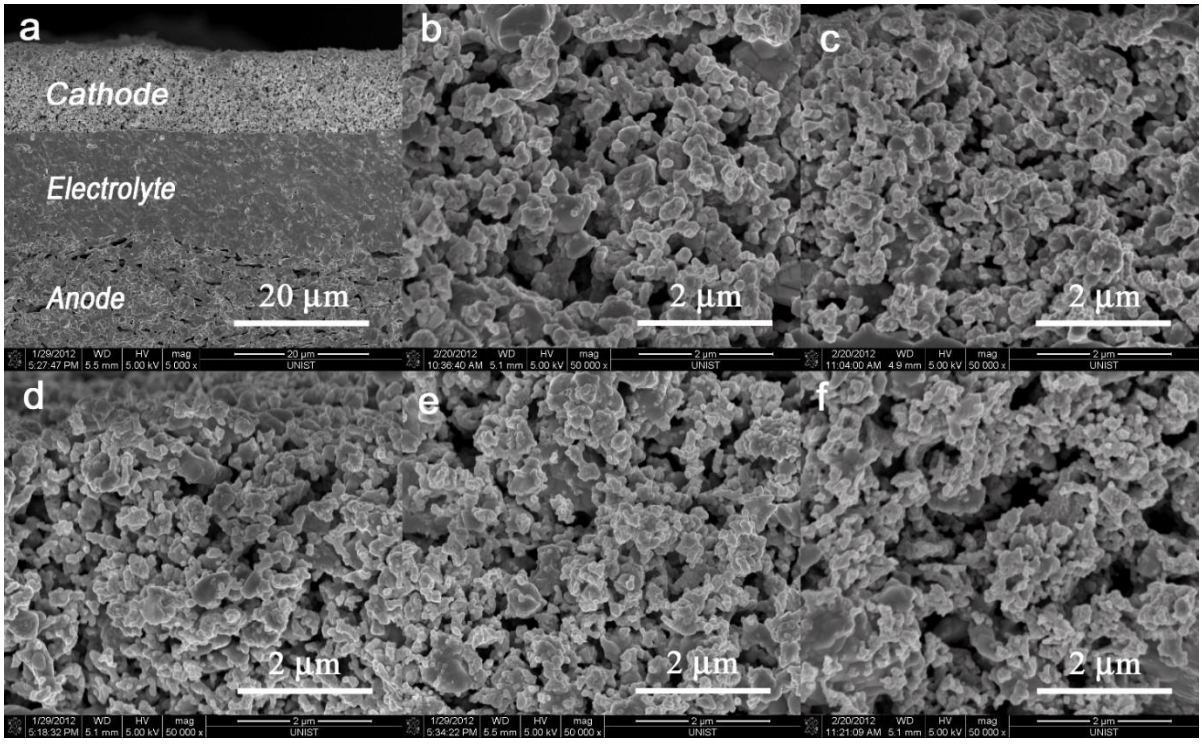

Figure 7.3. Scanning electron microscopy images of $SmBa_{0.5}Sr_{0.5}Co_{2-x}Fe_xO_{5+\delta}$ (x = 0, 0.25, 0.5, 0.75, and 1.0)-GDC cathodes: (a) a cross section consisting of the dense GDC electrolyte with the porous $SmBa_{0.5}Sr_{0.5}Co_{1.5}Fe_{0.5}O_{5+\delta}$-GDC composite cathode and NiO-GDC anode; (b)-(f) microstructure of $SmBa_{0.5}Sr_{0.5}Co_{2-x}Fe_xO_{5+\delta}$ (x = 0, 0.25, 0.5, 0.75, and 1.0)-GDC cathodes fabricated using screen printing followed by sintering at 950 °C for 4 hours.

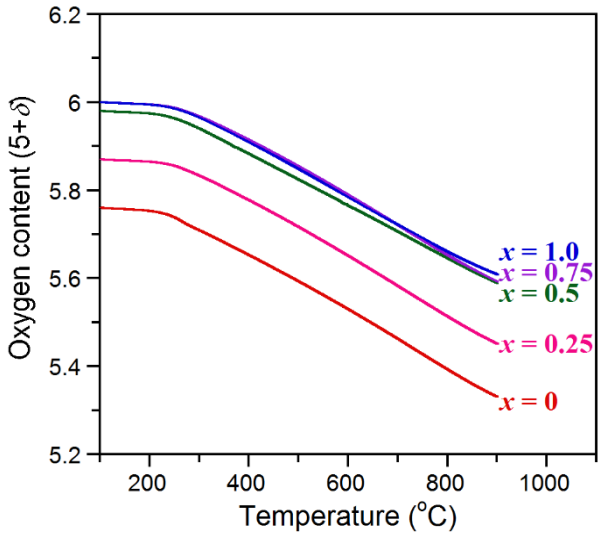

Figure 7.4. Variations of oxygen contents in $SmBa_{0.5}Sr_{0.5}Co_{2-x}Fe_xO_{5+\delta}$ (x = 0, 0.25, 0.5, 0.75, and 1.0) with temperature in air.

Figure 7.4 shows the variation of the oxygen content in the SBSCF system with temperature in air. These curves were derived using initial oxygen content values determined by iodometric titration and the TGA data. All the SBSCF samples start to lose oxygen at T > 200 °C. The data in Figure 7.4 reveal that the degree of oxygen loss decreases with increasing Fe content. The decrease in oxygen loss with Fe doping suggests stronger binding of the oxygen to the lattice with increasing Fe. This is consistent with a higher standard Gibbs free energy of formation for Fe_3O_4 (-1017.438 $kJmol^{-1}$) compared to that for Co_3O_4 (-794.871 $kJmol^{-1}$), implying a stronger Fe-O bond compared to the Co-O bond.[27]

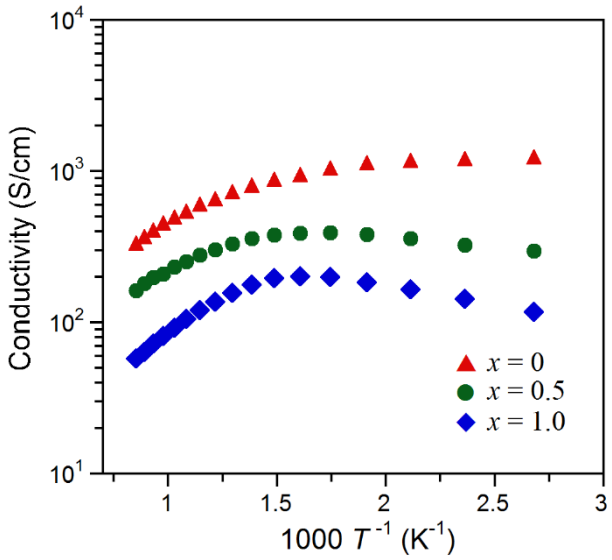

Figure 7.5. Electrical conductivities of $SmBa_{0.5}Sr_{0.5}Co_{2-x}Fe_xO_{5+\delta}$ (x = 0, 0.5, and 1.0) at various temperatures from 100 to 750 °C in air.

The temperature dependence of the electrical conductivity for $SmBa_{0.5}Sr_{0.5}Co_{2-x}Fe_xO_{5+\delta}$ (x = 0, 0.5, and 1.0) in air is presented in Figure 7.5. All of the $SmBa_{0.5}Sr_{0.5}Co_{2-x}Fe_xO_{5+\delta}$ (x = 0, 0.5, and 1.0) sample achieve their respective maximums at a range of 400-500 °C, and then decrease as the temperature is increased further, exhibiting typical semiconductor behavior. The $SmBa_{0.5}Sr_{0.5}Co_{2-x}Fe_xO_{5+\delta}$ (x = 0, 0.5, and 1.0) samples show a decrease in electrical conductivity with increasing temperature at T>200 °C due to oxygen loss from the lattice at higher temperature, as indicated by the TGA data (Figure 7.4). This can be explained by the fact that the holes are the majority charge carriers and hole-conductivity in cobaltites is usually related to the presence of Co^{4+} ions. The loss of oxygen atoms with increasing temperature not only decreases the hole concentration but also disturbs the (Co,Fe)-O-(Co,Fe) periodic potential and introduces hole localization.[28,29] This can be explained by the preferential formation of Fe^{4+}over Co^{4+} for electronic charge compensation.

At a given temperature, the electrical conductivity decreases with increasing Fe content in $SmBa_{0.5}Sr_{0.5}Co_{2-x}Fe_xO_{5+\delta}$. The oxygen and Co^{4+} ion content in the $SmBa_{0.5}Sr_{0.5}Co_{2-x}Fe_xO_{5+\delta}$ samples decreases with increasing Fe content. This leads to a reduction of the carrier concentration, resulting in a decrease of electrical conductivity. Furthermore, the covalency of the Fe^{4+}-O bond is lower than that of the Co^{4+}-O bond, implying increased electron localization and decreased electrical conductivity with increasing Fe content.[30]

In general, the cathode is in a reduced condition at $p(O_2)$ lower than 0.21 atm due to the cathodic polarization under fuel cell operating conditions.[31] Therefore, both higher redox stability and sufficient electrical conductivity at relatively low $p(O_2)$ are important factors for efficient current collection and long-term stability of the cathode performance for IT-SOFCs at operating conditions.[18,32] Characterization of the basic redox properties is therefore essential, especially under circumstances where the cathode is subjected to relatively low oxygen partial pressures. Basic redox properties including the electrical conductivity and the oxygen nonstoichiometry are also investigated in this study through a specially designed coulometric titration zig for simultaneous measurement of both properties, which has been explained in detail elsewhere.[20] The $p(O_2)$ dependence of the 4-probe electrical conductivities for $SmBa_{0.5}Sr_{0.5}Co_{2-x}Fe_xO_{5+\delta}$ (x = 0, 0.5, and 1.0) at 700 °C is displayed in Figure 7.6(a). The electrical conductivities of each sample at a given temperature increased with increasing $p(O_2)$, indicating of a typical *p*-type conductor. The electrical conductivities of $SmBa_{0.5}Sr_{0.5}Co_{2-x}Fe_xO_{5+\delta}$ are within a range of 20 to 550 Scm^{-1} under relatively low oxygen partial pressures, which are typical operating conditions of IT-SOFC cathodes.

Figure 7.6(b) shows the equilibrium oxygen nonstoichiometries for $SmBa_{0.5}Sr_{0.5}Co_{2-x}Fe_xO_{5+\delta}$ determined by coulometric titration as a function of $p(O_2)$ at 700 °C. The initial oxygen content of all samples is determined by iodometric titration and TGA data in air at 700 °C, as seen in Table 7.2. The oxidation isotherms of $SmBa_{0.5}Sr_{0.5}Co_{2-x}Fe_xO_{5+\delta}$ at 700 °C have similar shapes, suggesting that the oxidation/reduction mechanisms of all materials are quite similar. SBSCO and SBSCF50 samples start to decay at a $p(O_2)$ of approximately 10^{-5} atm and appear to decompose between 10^{-5} and 10^{-6} atm, while SBSCF100 starts to decay at 10^{-4} atm and appear to also decompose at 10^{-4} atm. A steep decrease of the slope near 10^{-6} atm and 700 °C implies that the operating $p(O_2)$ of SBSCF50 should be carefully reviewed considering the structural instability predicted from the redox behavior,[31] which also has been reported in previous studies.[10] The decomposition of SBSCF50 starts at lower $p(O_2)$ as compared with that of SBSCO and SBSCF100, indicating that SBSCF50 has higher redox stability or better durability under cathodic polarization and, consequently, a favourable property for practical application in IT-SOFCs.

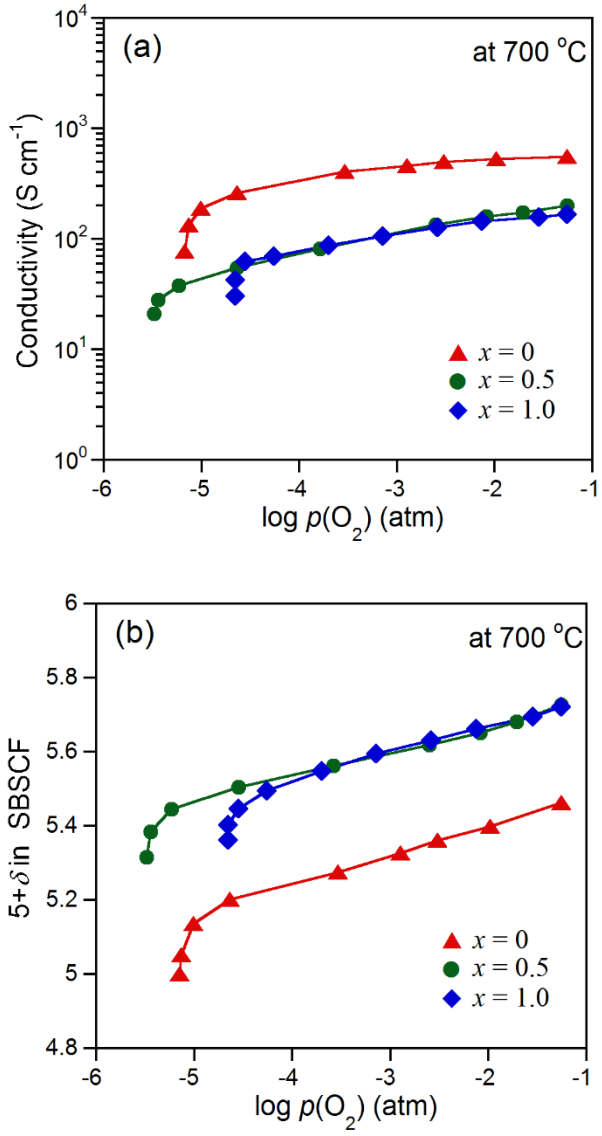

Figure 7.6. (a) Electrical conductivity of $SmBa_{0.5}Sr_{0.5}Co_{2-x}Fe_xO_{5+\delta}$ (x = 0, 0.5, and 1.0) and (b) Oxidation isotherms $SmBa_{0.5}Sr_{0.5}Co_{2-x}Fe_xO_{5+\delta}$ (x = 0, 0.5, and 1.0) in various $p(O_2)$ at 700 °C.

Figure 7.6(b) shows the equilibrium oxygen nonstoichiometries for $SmBa_{0.5}Sr_{0.5}Co_{2-x}Fe_xO_{5+\delta}$ determined by coulometric titration as a function of $p(O_2)$ at 700 °C. The initial oxygen content of all samples is determined by iodometric titration and TGA data in air at 700 °C, as seen in Table 7.2. The oxidation isotherms of $SmBa_{0.5}Sr_{0.5}Co_{2-x}Fe_xO_{5+\delta}$ at 700 °C have similar shapes, suggesting that the oxidation/reduction mechanisms of all materials are quite similar. SBSCO and SBSCF50 samples start to decay at a $p(O_2)$ of approximately 10^{-5} atm and appear to decompose between 10^{-5} and 10^{-6} atm, while SBSCF100 starts to decay at 10^{-4} atm and appear to also decompose at 10^{-4} atm. A steep decrease of the slope near 10^{-6} atm and 700 °C implies that the operating $p(O_2)$ of SBSCF50 should be carefully reviewed considering the structural instability predicted from the redox behavior,[31] which also has been

reported in previous studies.[10] The decomposition of SBSCF50 starts at lower $p(O_2)$ as compared with that of SBSCO and SBSCF100, indicating that SBSCF50 has higher redox stability or better durability under cathodic polarization and, consequently, a favourable property for practical application in IT-SOFCs.

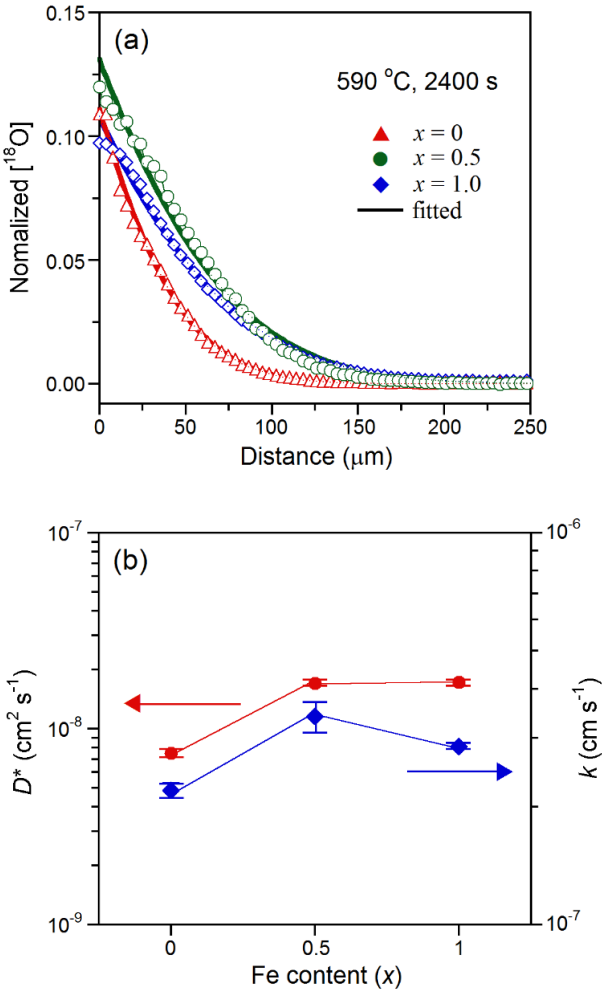

Figure 7.7. (a) Depth profile of normalized isotope oxygen fraction in $SmBa_{0.5}Sr_{0.5}Co_{2-x}Fe_xO_{5+\delta}$ (x = 0, 0.5, and 1.0) exchanged at 590 °C for 2400 sec, obtained by linescan measurement. The symbols and solid line show the measured results and fitted results, respectively. (b) D^* and k fitted values for various values of Fe content obtained from the depth profile of the normalized isotope oxygen fraction.

Figure 7.7 presents depth profiles of ^{18}O in SBSCO, SBSCF50 and SBSCF100, which are annealed at 590 °C in 200 mbar $^{18}O_2$. The normalized $^{18}O_2$ concentration of the samples was not completely homogeneous for the measured surface areas. The non-uniformity of the $^{18}O_2$ distribution may originate from differences in surface terminations and/or different grain orientations. By integrating the area of the image along the x direction, the normalized values of the $^{18}O_2$ concentration

along *y* can be calculated and fitted to Crank's solution. The obtained fitted values of D^* and *k* are presented in Figure 7.7(b). The D^* values of $SmBa_{0.5}Sr_{0.5}Co_{2-x}Fe_xO_{5+\delta}$ (x = 0, 0.5, and 1.0) are 0.75±0.04, 1.71±0.06, and 1.73±0.06 × 10^{-8} cm^2S^{-1}, respectively, confirming that Fe doping has a favorable effect on the oxygen bulk diffusion properties. In addition, the *k* value of SBSCF50 is higher than those of SBSCO and SBSCF100, and the *k* values of $SmBa_{0.5}Sr_{0.5}Co_{2-x}Fe_xO_{5+\delta}$ (x = 0, 0.5, and 1.0) are 2.2±0.1, 3.4±0.3, and 2.85±0.05 × 10^{-7} cmS^{-1}, respectively. Generally, the oxygen vacancy play a role as the oxygen ion diffusion pathway within the bulk material in simple perovskite system, such as $Ba_{0.5}Sr_{0.5}Co_{0.8}Fe_{0.2}O_{3-\delta}$, $La_{0.6}S_{0.4}C_{0.2}Fe_{0.8}O_{3-\delta}$, and $SrNb_{0.1}Co_{0.7}Fe_{0.2}O_{3-\delta}$.[9,10,33] In the case of layered perovskite system, whereas, pore channels for ion motion in the [Ln-O] and [Co(Fe)-O] planes could provide fast paths for oxygen transport. It is proposed that oxygen ion diffusion paths follow a zig-zag type trajectory through the Co(Fe)-O plane perpendicular to the Ln-O plane. The population of mobile oxygen species may relate to the enhanced oxygen bulk diffusion and surface exchange, that is, higher concentration of mobile oxygen species in the Ln-O layer can lead to faster oxygen kinetics and better electrochemical performance.[13] According to the Adler-Lane-Steele (ALS) model, the area specific resistance (ASR) is related to oxygen kinetics, such as the bulk diffusion (D_o^*) and surface exchange (k_o^0).[7] Under the assumption that the parameters of the microstructure, such as the porosity, cathode surface area, and tortuosity, are similar, high bulk diffusion and surface exchange lead to lower ASR values. Therefore, SBSCF50 is expected to provide fast oxygen diffusion in the bulk and high surface kinetics on the surface of the electrode among the $SmBa_{0.5}Sr_{0.5}Co_{2-x}Fe_xO_{5+\delta}$ (x = 0, 0.5, and 1.0) samples.

The ASR of $SmBa_{0.5}Sr_{0.5}Co_{2-x}Fe_xO_{5+\delta}$ is obtained by AC impedance spectroscopy for $SmBa_{0.5}Sr_{0.5}Co_{2-x}Fe_xO_{5+\delta}$-GDC|GDC|$SmBa_{0.5}Sr_{0.5}Co_{2-x}Fe_xO_{5+\delta}$-GDC symmetrical cells. The ASR value is determined by the impedance intercept between high-frequency and low-frequency with the real axis of the Nyquist plot, which can be expressed as the sum of the charge-transfer resistances and non-charge transfer processes. In the Nyquist plots, the high frequency arcs are equivalent to R_2, which is related to charge transfer during the migration and diffusion of oxygen ions from the triple-phase boundary (TPB) into the electrolyte. Meanwhile, the low frequency arcs correspond to R_3, which is attributed to non-charge-transfer processes including oxygen surface exchange, solid-state diffusion, and gas-phase diffusion inside and outside the electrode.[34] The experimental impedance spectroscopy patterns are shown in Figure 7.8(a) and are well fitted by the equivalent circuit model presented as an inset in Figure 7.8 (a). The inset in Figure 7.8(a) shows the R_2 and R_3 at various Fe content determined from the impedance spectra. The experimental R_2 and R_3 values of $SmBa_{0.5}Sr_{0.5}Co_{2-x}Fe_xO_{5+\delta}$ (x = 0, 0.25, 0.5, 0.75, and 1.0)-GDC based on a GDC symmetrical cell decrease with Fe content up to x = 0.5, and the R_p(=R_2+R_3) values of $SmBa_{0.5}Sr_{0.5}Co_{2-x}Fe_xO_{5+\delta}$ (x = 0, 0.25, 0.5, 0.75, and 1.0)-GDC are 0.141, 0.101, 0.081, 0.104, and 0.136 Ω cm^2 at 600 °C, respectively. In general, the population of mobile oxygen species in layered perovskites may contribute to enhanced oxygen kinetics associated with oxygen bulk

diffusion and surface exchange.[35] A higher concentration of mobile oxygen species in the Sm-O layer due to larger amount of Fe doping (up to ~50%) may lead to faster oxygen kinetics and better electrochemical performance.[13] Therefore, among the $SmBa_{0.5}Sr_{0.5}Co_{2-x}Fe_xO_{5+\delta}$samples, SBSCF50 is expected to provide fast oxygen diffusion in the bulk and high surface kinetics on the surface of the electrode.

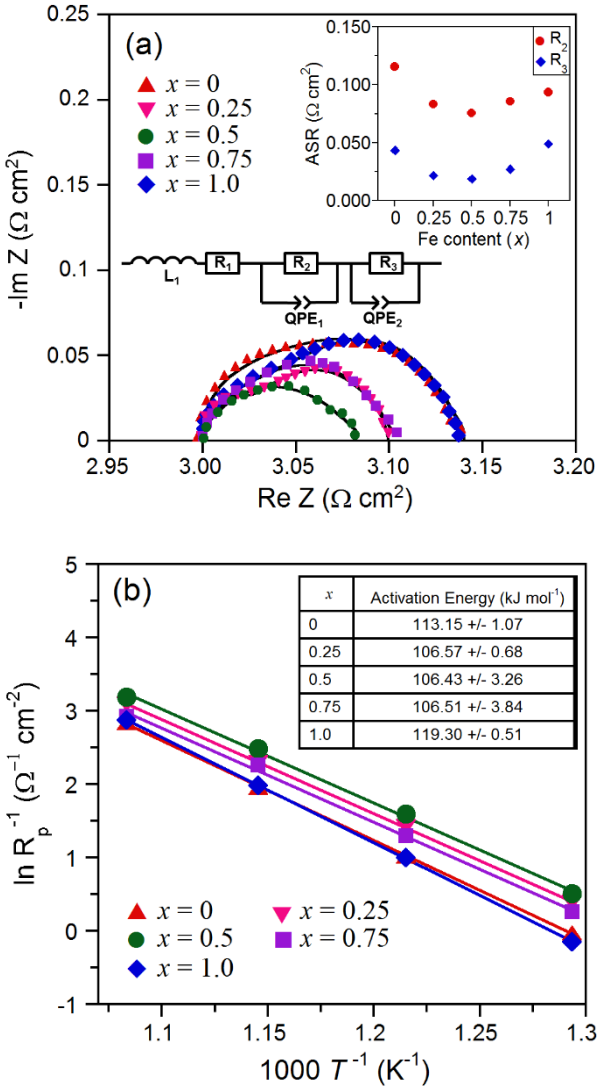

Figure 7.8. Experimental and simulated impedance plots of (a) $SmBa_{0.5}Sr_{0.5}Co_{2-x}Fe_xO_{5+\delta}$ (x = 0, 0.25, 0.5, 0.75, and 1.0)-GDC at 600 ºC by the equivalent circuit shown as an inset. The inset in (a) shows the R_2 and R_3 at various Fe content determined from the impedance spectra. Arrhenius plots of 1/ASR and activation energy of (b) $SmBa_{0.5}Sr_{0.5}Co_{2-x}Fe_xO_{5+\delta}$-GDC.

Arrhenius plots of the ASR for $SmBa_{0.5}Sr_{0.5}Co_{2-x}Fe_xO_{5+\delta}$ are shown in Figure 7.8(b). The activation energy is directly related to the cathode properties including the oxygen adsorption,

dissociation, and surface/bulk diffusion.[35,36] The activation energies of $SmBa_{0.5}Sr_{0.5}Co_{2-x}Fe_xO_{5+\delta}$ are calculated from the Arrhenius plots of the fitted line. The activation energy of $SmBa_{0.5}Sr_{0.5}Co_{2-x}Fe_xO_{5+\delta}$ (x = 0.25, 0.5, and 0.75) is around 106 kJ mol^{-1} and those samples exhibit lower activation energy than $SmBa_{0.5}Sr_{0.5}Co_{2-x}Fe_xO_{5+\delta}$ (x = 0 and 1.0).

To evaluate the performance of $SmBa_{0.5}Sr_{0.5}Co_{2-x}Fe_xO_{5+\delta}$ cathode materials in a practical fuel cell, we used anode-supported cells based on a 15-μm-thick GDC electrolyte. Figure 7.9 shows the power density and cell voltage as a function of the current density for the $SmBa_{0.5}Sr_{0.5}Co_{2-x}Fe_xO_{5+\delta}$ (x = 0, 0.5, and 1.0)-GDC|GDC|NiO-GDC cells using humidified H_2 (3 % H_2O) as a fuel and ambient air as an oxidant in a temperature range of 500 - 650 ºC. The maximum power density of SBSCO, SBSCF50, and SBSCF100 is 2.03, 2.19, and 1.81 W cm^{-2} at 650 ºC and 1.38, 1.56, and 1.28 W cm^{-2} at 600 ºC, respectively. The single cell performance improves with increasing Fe content up to x = 0.5 in the $SmBa_{0.5}Sr_{0.5}Co_{2-x}Fe_xO_{5+\delta}$ oxides, while SBSCF100 shows a sudden reduction of cell performance, consistent with the trend of the ASR and electrical conductivity results.

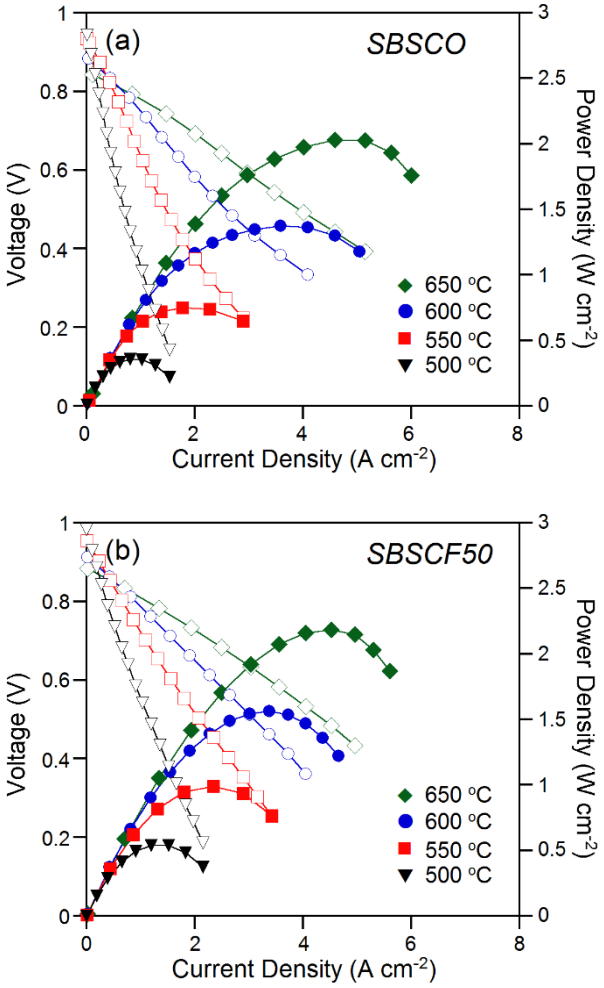

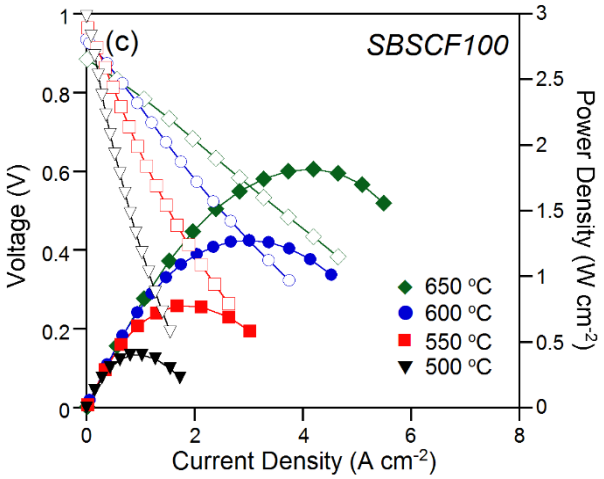

Figure 7.9. *I-V* polarization curves and the corresponding power densities of the test cells with (a), $SmBa_{0.5}Sr_{0.5}Co_2O_{5+\delta}$ -GDC (b), $SmBa_{0.5}Sr_{0.5}Co_{1.5}Fe_{0.5}O_{5+\delta}$ -GDC (c), $SmBa_{0.5}Sr_{0.5}CoFeO_{5+\delta}$ -GDC as the cathodes, using humidified H_2 (3% H_2O) as a fuel and static ambient air as an oxidant in a temperature range of 500 - 650 °C.

In conclusion, SBSCF50 is a promising material as a cathode for IT-SOFCs with Fe substitution in SBSCO enhancing the performance and redox stability, and it also shows satisfactory electrical properties and electrochemical performance under typical fuel cell operating conditions.

7.4. Conclusions

In this study, we focus on the catalytic effect of Fe doping into $SmBa_{0.5}Sr_{0.5}Co_{2-x}Fe_xO_{5+\delta}$ for the oxygen reduction reaction (ORR) and optimize the amount of Fe substitution by investigating the structural characteristics, electrical properties, redox properties, oxygen kinetics, and electrochemical performance of $SmBa_{0.5}Sr_{0.5}Co_{2-x}Fe_xO_{5+\delta}$ (x = 0, 0.25, 0.5, 0.75, and 1.0) in terms of application as an intermediate-temperature solid oxide fuel cell (IT-SOFC) cathode material. SBSCF50 shows higher redox stability at lower $p(O_2)$ compared with that of SBSCO and SBSCF100 from the coulometric titration results. Furthermore, it exhibits lower ASR values of 0.081 $\Omega\,cm^2$ and excellent cell performance of 1.56 W cm^{-2} at 600 °C. Its enhanced electrical performance is ascribed to fast oxygen diffusion in the bulk and high surface kinetics from the depth profile of normalized isotope oxygen fraction. SBSCF50 provides a combination of fast oxygen diffusion and high surface kinetics, and also shows enhanced redox stability and electrochemical performance under typical fuel cell operating conditions. SBSCF50 is indeed a promising material as a cathode for IT-SOFC systems.

References

(1) Gross, M. D.; Vohs, J. M.; Gorte, R. J. Recent Progress in SOFC Anodes for Direct Utilization of Hydrocarbons. *J. Mater. Chem.* **2007**, *17*, 3071–3077.

(2) Sengodan, S.; Choi, S.; Jun, A.; Shin, T. H.; Ju, Y.-W.; Jeong, H. Y.; Shin, J.; Irvine, J. T. S.; Kim, G. Layered Oxygen-Deficient Double Perovskite as an Efficient and Stable Anode for Direct Hydrocarbon Solid Oxide Fuel Cells. *Nat. Mater.* **2014**, *14* (2), 205–209.

(3) Dong, F.; Ni, M.; Chen, Y.; Chen, D.; Tadé, M. O.; Shao, Z. Structural and Oxygen-Transport Studies of Double Perovskites $PrBa_{1-x}Co_2O_{5+\delta}$ (x = 0.00, 0.05, and 0.10) toward Their Application as Superior Oxygen Reduction Electrod. *J. Mater. Chem. A* **2014**, *2*, 20520–20529.

(4) Steele, B. C.; Heinzel, A. Materials for Fuel-Cell Technologies. *Nature* **2001**, *414*, 345–352.

(5) Yoo, S.; Jun, A.; Ju, Y.; Odkhuu, D.; Hyodo, J.; Jeong, H. Y.; Park, N.; Shin, J.; Ishihara, T.; Kim, G. Development of Double-Perovskite Compounds as Cathode Materials for Low-Temperature Solid Oxide Fuel Cells. *Angew. Chemie Int. Ed.* **2014**, *53*, 13064–13067.

(6) Jung, W.; Gu, K. L.; Choi, Y.; Haile, S. M. Robust Nanostructures with Exceptionally High Electrochemical Reaction Activity for High Temperature Fuel Cell Electrodes. *Energy Environ. Sci.* **2014**, *7* (5), 1685–1692.

(7) Adler, S. B.; Lane, J. A.; Steele, B. C. H. Electrode Kinetics of Porous Mixed-Conducting Oxygen Electrodes. *J. Electrochem. Soc.* **1996**, *143* (11), 3554–3564.

(8) Ried, P.; Holtappels, P.; Wichser, A.; Ulrich, A.; Graule, T. Synthesis and Characterization of $La_{0.6}Sr_{0.4}Co_{0.2}Fe_{0.8}O_{3-\delta}$ and $Ba_{0.5}Sr_{0.5}Co_{0.8}Fe_{0.2}O_{3-\delta}$. *J. Electrochem. Soc.* **2008**, *155* (10), B1029–B1035.

(9) Shao, Z.; Haile, S. M. A High-Performance Cathode for the next Generation of Solid-Oxide Fuel Cells. *Nature* **2004**, *431* (7005), 170–173.

(10) Jun, A.; Yoo, S.; Gwon, O.; Shin, J.; Kim, G. Thermodynamic and Electrical Properties of $Ba_{0.5}Sr_{0.5}Co_{0.8}Fe_{0.2}O_{3-\delta}$ and $La_{0.6}Sr_{0.4}Co_{0.2}Fe_{0.8}O_{3-\delta}$ for Intermediate-Temperature Solid Oxide Fuel Cells. *Electrochim. Acta* **2013**, *89*, 372–376.

(11) Park, S.; Choi, S.; Shin, J.; Kim, G. Electrochemical Investigation of Strontium Doping Effect on High Performance $Pr_{1-x}Sr_xCoO_{3-\delta}$ (x = 0.1, 0.3, 0.5, and 0.7) Cathode for Intermediate-Temperature Solid Oxide Fuel Cells. *J. Power Sources* **2012**, *210*, 172–177.

(12) Xia, C.; Rauch, W.; Chen, F.; Liu, M. $Sm_{0.5}Sr_{0.5}CoO_3$ Cathodes for Low-Temperature SOFCs. *Solid State Ionics* **2002**, *149*, 11–19.

(13) Choi, S.; Yoo, S.; Kim, J.; Park, S.; Jun, A.; Sengodan, S.; Kim, J.; Shin, J.; Jeong, H. Y.; Choi, Y.; et al. Highly Efficient and Robust Cathode Materials for Low-Temperature Solid Oxide Fuel Cells: $PrBa_{0.5}Sr_{0.5}Co_{2-x}Fe_xO_{5+\delta}$. *Sci. Rep.* **2013**, *3*, 2426.

(14) Jun, A.; Kim, J.; Shin, J.; Kim, G. Optimization of Sr Content in Layered $SmBa_{1-x}Sr_xCo_2O_{5+\delta}$ Perovskite Cathodes for Intermediate-Temperature Solid Oxide Fuel Cells. *Int. J. Hydrogen*

Energy **2012**, *37* (23), 18381–18388.

(15) Broux, T.; Bahout, M.; Hanlon, J. M.; Hernandez, O.; Paofai, S.; Berenov, A.; Skinner, S. J. High Temperature Structural Stability, Electrical Properties and Chemical Reactivity of $NdBaCo_{2-x}Mn_xO_{5+\delta}$ ($0 \leq x \leq 2$) for Use as Cathodes in Solid Oxide Fuel Cells. *J. Mater. Chem. A* **2014**, *2* (40), 17015–17023.

(16) Park, S.; Choi, S.; Shin, J.; Kim, G. A Collaborative Study of Sintering and Composite Effects for a PrBa0.5Sr0.5Co1.5Fe0.5O5+δ IT-SOFC Cathode. *RSC Adv.* **2014**, *4* (4), 1775.

(17) Kim, J.; Choi, S.; Jun, A.; Jeong, H. Y.; Shin, J.; Kim, G. Chemically Stable Perovskites as Cathode Materials for Solid Oxide Fuel Cells: La-Doped $Ba_{0.5}Sr_{0.5}Co_{0.8}Fe_{0.2}O_{3-\delta}$. *ChemSusChem* **2014**, *7* (6), 1669–1675.

(18) Jun, A.; Shin, J.; Kim, G. High Redox and Performance Stability of Layered $SmBa_{0.5}Sr_{0.5}Co_{1.5}Cu_{0.5}O_{5+\delta}$ Perovskite Cathodes for Intermediate-Temperature Solid Oxide Fuel Cells. *Phys. Chem. Chem. Phys.* **2013**, *15* (45), 19906–19912.

(19) Tsvetkov, D. S.; Ivanov, I. L.; Urusov, I. V.; Zuev, A. Y. Thermodynamics of Formation of Double Perovskites $GdBaCo_{2-x}M_xO_{6-\delta}$ (M = Fe, Mn; x = 0, 0.2). *Thermochim. Acta* **2011**, *519*, 12–15.

(20) Yoo, S.; Shin, J. Y.; Kim, G. Thermodynamic and Electrical Characteristics of $NdBaCo_2O_{5+\delta}$ at Various Oxidation and Reduction States. *J. Mater. Chem.* **2011**, *21* (2), 439–44.

(21) De Souza, R. A.; Chater, R. J. Oxygen Exchange and Diffusion Measurements: The Importance of Extracting the Correct Initial and Boundary Conditions. *Solid State Ionics* **2005**, *176*, 1915–1920.

(22) Crank, J. T. The Mathematics of Diffusion. Oxford. Clarendon press 1975.

(23) Maignan, A.; Martin, C.; Pelloquin, D.; Nguyen, N.; Raveau, B. Structural and Magnetic Studies of Ordered Oxygen-Deficient Perovskites$LnBaCo_2O_{5+\delta}$, Closely Related to the "112" Structure. *J. Solid State Chem.* **1999**, *142* (2), 247–260.

(24) Shannon, B. Y. R. D.; H, M.; Baur, N. H.; Gibbs, O. H.; Eu, M.; Cu, V. Revised Effective Ionic Radii and Systematic Studies of Interatomie Distances in Halides and Chaleogenides. *Acta Crystallogr. Sect. A* **1976**, *A32*, 751–767.

(25) Kim, J. H.; Cassidy, M.; Irvine, J. T. S.; Bae, J. Advanced Electrochemical Properties of $LnBa_{0.5}Sr_{0.5}Co_2O_{5+\delta}$ (Ln = Pr, Sm, and Gd) as Cathode Materials for IT-SOFC. *J. Electrochem. Soc.* **2009**, *156* (6), B682–B689.

(26) Park, S.; Choi, S.; Shin, J.; Kim, G. Tradeoff Optimization of Electrochemical Performance and Thermal Expansion for Co-Based Cathode Material for Intermediate-Temperature Solid Oxide Fuel Cells. *Electrochim. Acta* **2014**, *125*, 683–690.

(27) MW Chase, J.; Davies, C.; Downey, J.; Jr., D. F.; McDonald, R.; Syverud, A. Tables, JANAF Thermochemical. *J. Phys. Chem. Ref. Data* **1985**, *14* (Suppl 1).

(28) Lee, K. T.; Manthiram, A. $LaSr_3Fe_{3-y}Co_yO_{10-\delta}$ ($0 \leq y \leq 1.5$) Intergrowth Oxide Cathodes for Intermediate Temperature Solid Oxide Fuel Cells. *Chem. Mater.* **2006**, *18*, 1621–1626.

(29) Takahashi, H.; Munakata, F.; Yamanaka, M. Ab Initio Study of the Electronic Structures in $LaCoO_3$-$SrCoO_3$ Systems. *Phys. Rev. B* **1998**, *57* (24), 15211–15218.

(30) Kim, Y. N.; Kim, J. H.; Manthiram, a. Effect of Fe Substitution on the Structure and Properties of $LnBaCo_{2-x}Fe_xO_{5+\delta}$ (Ln = Nd and Gd) Cathodes. *J. Power Sources* **2010**, *195* (19), 6411–6419.

(31) Adler, S. B. Factors Governing Oxygen Reduction in Solid Oxide Fuel Cell Cathodes. *Chem. Rev.* **2004**, *104*, 4791–4843.

(32) Bastidas, D. M.; Tao, S.; Irvine, J. T. S. A Symmetrical Solid Oxide Fuel Cell Demonstrating Redox Stable Perovskite Electrodes. *J. Mater. Chem.* **2006**, *16* (17), 1603–1605.

(33) Zhu, Y.; Sunarso, J.; Zhou, W.; Jiang, S.; Shao, Z. High-Performance $SrNb_{0.1}Co_{0.9-x}Fe_xO_{3-\delta}$ Perovskite Cathodes for Low-Temperature Solid Oxide Fuel Cells. *J. Mater. Chem. A* **2014**, *2* (37), 15454.

(34) Bevilacqua, M.; Montini, T. T.; Tavagnacco, C.; Fonda, E.; Fornasiero, P.; Graziani, M. Preparation, Characterization, and Electrochemical Properties of Pure and Composite $LaNi_{0.6}Fe_{0.4}O_3$-Based Cathodes for IT-SOFC. *Chem. Mater.* **2007**, *19* (24), 5926–5936.

(35) Kim, G.; Wang, S.; Jacobson, A. J.; Reimus, L.; Brodersen, P.; Mims, C. A. Rapid Oxygen Ion Diffusion and Surface Exchange Kinetics in $PrBaCo_2O_{5+x}$ with a Perovskite Related Structure and Ordered A Cations. *J. Mater. Chem.* **2007**, *17* (24), 2500–2505.

(36) Lü, S.; Meng, X.; Ji, Y.; Fu, C.; Sun, C.; Zhao, H. Electrochemical Performances of $NdBa_{0.5}Sr_{0.5}Co_2O_{5+x}$ as Potential Cathode Material for Intermediate-Temperature Solid Oxide Fuel Cells. *J. Power Sources* **2010**, *195* (24), 8094–8096.

Chapter 8. Achieving high efficiency and eliminating degradation in solid oxide electrochemical cells by using high oxygen capacity perovskite

8.1. Introduction

In recent years, there has been strong demand in clean and renewable energy sources such as solar energy, wind energy, hydropower or geothermal energy due to heavy dependence on finite fossil fuels which has led to serious energy and environmental problems globally.[1,2] The renewable energy supply is, however, intermittent depending on weather conditions, site-specific, and also hard to match demands all times. Therefore, these problems have motivated researchers to develop energy storage devices e.g., secondary batteries, ultracapacitors, and water electrolyzer. But, among those energy storage devices, secondary batteries and ultracapacitors have been serious problems related with the limited energy storage capacity, cost ineffectiveness, and loss of charge over time.[3] In this regard, the water electrolysis can be a leading technology for the large-scale and highly efficient energy storage. Up to now, most of the work in electrolysis has focused on the low temperature proton exchange membrane (PEM) and alkaline electrolysis cells.[4] At present, high temperature solid oxide electrolysis cells (SOECs) have received great attention as a promising energy storage device. Compared to low temperature alkaline and PEM electrolysis cells, high temperature solid oxide electrolysis cells (SOECs) have shown higher hydrogen production efficiency because electrolysis at elevated temperatures is advantageous to both thermodynamics and kinetics.[5] The electrical energy demand considerably decreases as the operating temperature rises due to the increase of provided thermal energy. In addition, high operating temperature is favorable to the faster kinetics of the electrolysis reactions, resulting in the improvement of electrochemical properties and hydrogen production efficiency for the SOEC.[1]

SOECs and solid oxide fuel cells (SOFCs), which are referred to as solid oxide cells (SOCs), can operate reversibly as schematically shown in Figure 8.1. Briefly the electrical energy is converted as hydrogen in electrolysis mode (green line) and the electricity is produced from hydrogen through fuel cell mode (orange line).[6] In SOECs, hydrogen is produced via electrolysis of steam with electrons at the fuel electrode side, and then oxygen anions (O^{2-}) diffuse through the electrolyte toward the air electrode side. These anions are oxidized to oxygen gas to complete the reaction. The reactions in the fuel and the air electrode are:[7]

$$\text{Fuel electrode: } H_2O + 2e^- \rightarrow H_2(g) + O^{2-} \qquad \text{Eqn. 8.1}$$

$$\text{Air electrode: } O^{2-} \rightarrow \frac{1}{2}O_2(g) + 2e^- \qquad \text{Eqn. 8.2}$$

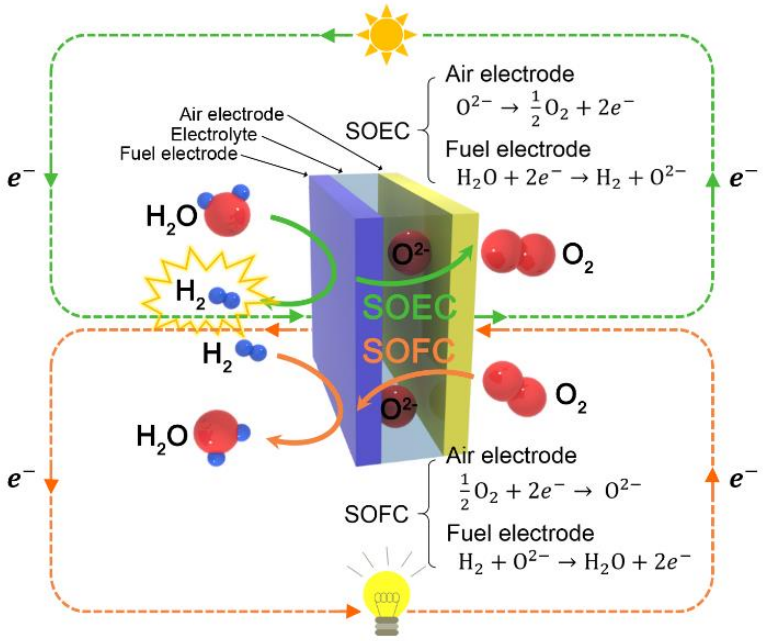

Figure 8.1. Schematic illustration of a SOC system.

Generally, the state-of-the-art commercial or lab-studied SOECs use Ni-YSZ (yttria-stabilized zirconia) and LSM (strontium-doped lanthanum manganites)-YSZ as fuel and air electrodes, respectively.[8] However, these electrodes suffer from several important limitations such as an inherent redox instability and coarsening of nickel particles for Ni-YSZ and delamination and insufficient electrolysis performance of LSM-YSZ during steam electrolysis.[9,10,11] In particular, LSM exhibits apparent oxygen excess nonstoichiometry in an oxidation environment (*i.e.*, the electrolysis mode). This excess oxygen in LSM gives rise to the formation of cation vacancies, which is thermodynamically unfavorable in the LMO ($LaMnO_3$) perovskite structure.[12,13] The cation vacancies would cause the disintegration of LSM and the formation of cation oxides or LSM nanoparticles. It results in severe microstructural damage near the air electrode/electrolyte interface, eventually, leading to degradation and delamination.[14,15]

Recently, one research group found that reversible cycling between electrolysis and fuel-cell modes can eliminate severe electrolysis-induced degradation. Reversible cycling with time periods of 1h in electrolysis mode and 5h in fuel-cell mode reduce the internal oxygen pressure at the air electrode/electrolyte interface during electrolysis operation, which would inhibit the delamination and microstructural damage.[16] But for continuous hydrogen production, reversible cycling is not an optimal method for electrolysis, because the SOE mode must be switched to SOFC mode to maintain stability.

Accordingly, it is of great significance to develop novel fuel and air electrode materials that can provide more active and stable performance without any degradation during SOEC operation. In recent years, many researchers have focused on layered perovskite as electrode materials for solid oxide fuel

cells (SOFCs) due to their fast oxygen kinetics and high and stable performance.[17,18] A-site layered perovskite $PrBaMn_2O_{5+\delta}$ (PBM) exhibited high and durable performance and excellent redox stability and can be potentially utilized as ceramic fuel electrode for SOFCs.[6] Also, a layered $PrBa_{0.5}Sr_{0.5}Co_{1.5}Fe_{0.5}O_{5+\delta}$ (PBSCF50) perovskite was reported to provide excellent electrochemical performance and stability as a novel air electrode material for IT-SOFCs.[19] Furthermore, the PBSCF50, in contrast to the LSM electrode, can accommodate more oxygen as oxygen interstitials within the Pr-O plane without structural changes, which certainly overcomes drawbacks of the LSM in the electrolysis mode.

In this study, we successfully fabricated and demonstrated the SOEC with layered perovskites as both-side electrodes for the first time. This SOEC shows high durability and high performance without any coarsening and delamination of electrodes for a long time.

8.2. Experimental

8.2.1. Synthesis of electrode and electrolyte powders

$PrBa_{0.5}Sr_{0.5}Co_{1.5}Fe_{0.5}O_{5+\delta}$ (PBSCF50) and $Pr_{0.5}Ba_{0.5}MnO_{3-\delta}$ were prepared by the Pechini method. The desired composition was obtained by each dissolving nitrate salts in distilled water with the addition of quantitative amounts of citric acid and ethylene glycol. After a viscous resin was formed, the mixture was heated to roughly 250 ºC in air, followed by combustion to form powders, which were calcined at 600 ºC for 4 h and ball-milled in acetone for 24 h. $La_{0.9}Sr_{0.1}Ga_{0.8}Mg_{0.2}O_{3-\delta}$ (LSGM) powder was prepared by the solid state reaction method and a dense electrolyte substrate was prepared by dry pressing followed by sintering at 1475 ºC. Stoichiometric amounts of La_2O_3 (Sigma 99.99%), $SrCO_3$ (Sigma, 99.99%), Ga_2O_3 (Sigma, 99.99%), and MgO (Sigma, 99.9%) powders were ball milled in ethanol for 24 h. After drying, the mixture was calcined at 1000 ºC for 6 h. The thickness of the LSGM electrolyte was adjusted to about 250 μm by polishing. $La_{0.4}Ce_{0.6}O_{2-\delta}$ (LDC) was also prepared by ball milling stoichiometric amounts of La_2O_3 and CeO_2 (Sigma, 99.99%) in ethanol and then calcined for 6 h. For preparation of the fuel electrode slurry, $Pr_{0.5}Ba_{0.5}MnO_{3-\delta}$ was mixed with an organic binder (Heraeus V006) (1:2 weight ratio). A PBSCF50-GDC air electrode slurry was prepared by mixing a pre-calcined fuel electrode and GDC powders (at a weight ratio of 6:4) using ball milling, together with an organic binder.

8.2.2. Preparation of sample for XRD and SEM analysis

In order to test the chemical stability between the electrode and electrolyte, the PBSCF50-GDC

and PBM slurries were applied on the LSGM pellet by a screen printing method, and then fired at 950 °C in air for 4 hours. Fifteen weight percent of $Co_{0.5}Fe_{0.5}$ (Co-Fe) alloy as a reduction catalyst was infiltrated onto the PBM electrode side and heated in air at 450 °C. An A-site layered $PrBaMn_2O_{5+\delta}$ fuel electrode was obtained by annealing $Pr_{0.5}Ba_{0.5}MnO_{3-\delta}$ oxide in H_2 at 800 °C. The chemical reactivity of each electrode with LSGM electrolyte was evaluated by analyzing the X-ray diffraction (XRD) patterns. The PBSCF50-GDC air electrode onto the LSGM electrolyte sintered at 950 °C for 4 hours in air and the PBM(Co-Fe) with a LDC buffer layer on LSGM after being reduced in H_2 were analyzed by using an XRD diffractometer (Rigaku diffractometer, Cu Kα radiation). The cross-sections of PBM(Co-Fe)/LDC/LSGM/PBSCF50-GDC before and after electrolysis test were investigated using a field emission scanning electron microscope (Nova Nano SEM, FEI, USA).

8.2.3. Fabrication of electrolysis cell

The LSGM electrolyte-supported cell was fabricated to measure the electrolysis performance. The LDC layer was used as the buffer layer between the air electrode and the electrolyte to prevent inter-diffusion of ionic species between PBM and LSGM.[6] The electrode slurry was applied on the LSGM pellet by the screen printing method, and then fired at 950 °C in air for 4 hours. The porous electrode had an active area of 0.36 cm^2 and a thickness of about 20 μm. 15 wt.% of $Co_{0.5}Fe_{0.5}$ (Co-Fe) catalyst solution was infiltrated onto the fuel electrode side and heated in air at 450 °C.

8.2.4. Electrolysis performance and stability test

For electrolysis performance tests, Ag wires were attached at both electrodes of the PBM(Co-Fe)/LDC/LSGM/PBSCF50-GDC cell using Ag paste as a current collector. The cells were mounted on alumina tubes with ceramic adhesives (Ceramabond 552, Aremco). The entire cell was placed inside a furnace and heated to the desired temperature. At 800 °C, fuel electrode side was exposed to nitrogen whereas air electrode side was exposed to air. Nitrogen gas was switched to humidified hydrogen (3 % H_2O), changing the phase from $Pr_{0.5}Ba_{0.5}MnO_{3-\delta}$ oxide to A-site layered $PrBaMn_2O_{5+\delta}$. The PBM(Co-Fe)/LDC/LSGM/PBSCF50-GDC cell was tested from 700 to 800 °C. A H_2 gas containing 10 % steam was fed as the inlet gas to the fuel electrode side and the air electrode side was exposed to an air atmosphere with a flow rate of 100 mL min^{-1}.

In order to assess the stability of the PBM(Co-Fe)/LDC/LSGM/PBSCF50-GDC cell at high current density, the voltage of the cell was recorded as a function of time under a constant high current of -0.7 A cm^{-2} at 700 °C under 10% steam and 90% H_2 fed in the fuel electrode side and air exposed in the air electrode side.

For reversibility and long-term stability, the PBM(Co-Fe)/LDC/LSGM/PBSCF50-GDC cell was tested at 700 °C under 10% steam and 90% H_2 fed in the fuel electrode side and air exposed in the air electrode side. During the period of 15-30 hours, the reversibility of operation was confirmed through the cycling test between steam electrolysis at - 0.25 A cm^{-2} and fuel cell operation at + 0.25 A cm^{-2}. After reversible cycling, the voltage of the PBM(Co-Fe)/LDC/LSGM/PBSCF50-GDC cell was recorded with applied current density of - 0.25 A cm^{-2}, at 700 °C for over 600 hours. Impedance spectra, *I-V* curves and stability of the electrolysis cell was examined using a BioLogic Potentiostat at operating temperature. Impedance spectra were recorded under OCV in a frequency range of 1 mHz to 500 kHz with AC perturbation of 14 mV from 700 to 800 °C.

8.3. Results and Discussions

In general, the phase reaction between the electrode and electrolyte can generate an undesired insulating layer at the interface, which obstructs the oxide-ionic and electronic transport.[20] Therefore, it is essential to avoid any insulating phases during electrochemical reaction for the reliable operation of the SOEC. The chemical reactivity of each electrode with LSGM electrolyte was evaluated by analyzing the X-ray diffraction (XRD) patterns. Figure 8.2(a) and (b) shows XRD patterns of the PBSCF50-GDC air electrode onto the LSGM electrolyte sintered at 950 °C for 4 hours in air and PBM(Co-Fe) with a LDC buffer layer on LSGM after being reduced in H_2. There are no observed interfacial reactions or undesirable secondary phases between each electrode and LSGM.

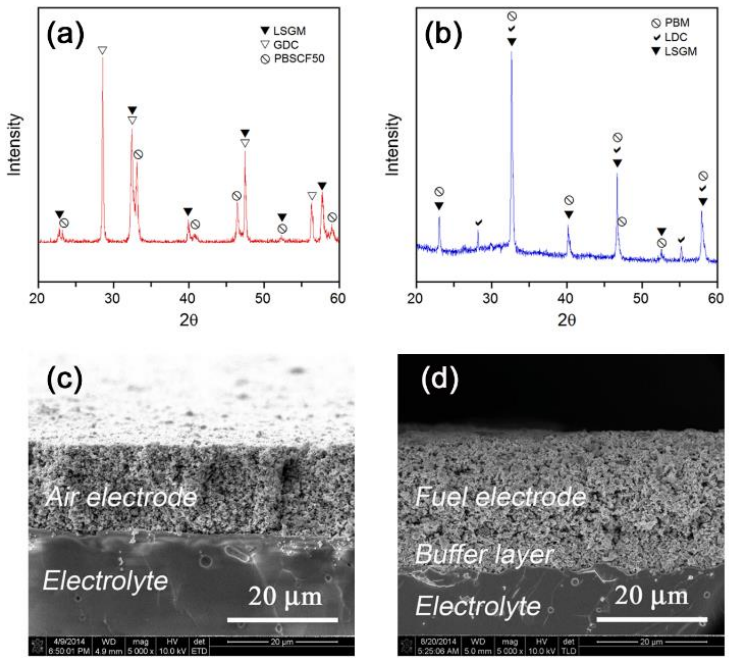

Figure 8.2. XRD patterns of a) PBSCF50-GDC/LSGM and b) PBM (Co-Fe)/LDC/LSGM. SEM

micrographs of c) PBSCF50-GDC/LSGM and d) PBM (Co-Fe)/LDC/LSGM interfaces of the single cell before electrolysis test.

The cross sectional view of the microstructure of the pristine solid oxide electrolysis cells is shown in Figure 8.2(c) and (d). Figure 8.2(c) presents a cross section of PBSCF50-GDC as an air electrode onto LSGM and Figure 8.2(d) shows a cross section of PBM(Co-Fe)/LSGM as a fuel electrode and a $La_{0.4}Ce_{0.6}O_{2-\delta}$ (LDC) buffer layer onto LSGM. It can be seen that the cell has ~ 20 μm porous electrodes and a ~5 μm LDC buffer layer which prevents any inter-diffusion of ionic species between the PBM and LSGM,. The interface between the electrode/buffer layer and the electrolyte appears to be well-connected without any delamination and the electrolyte is dense with no pores or cracks.

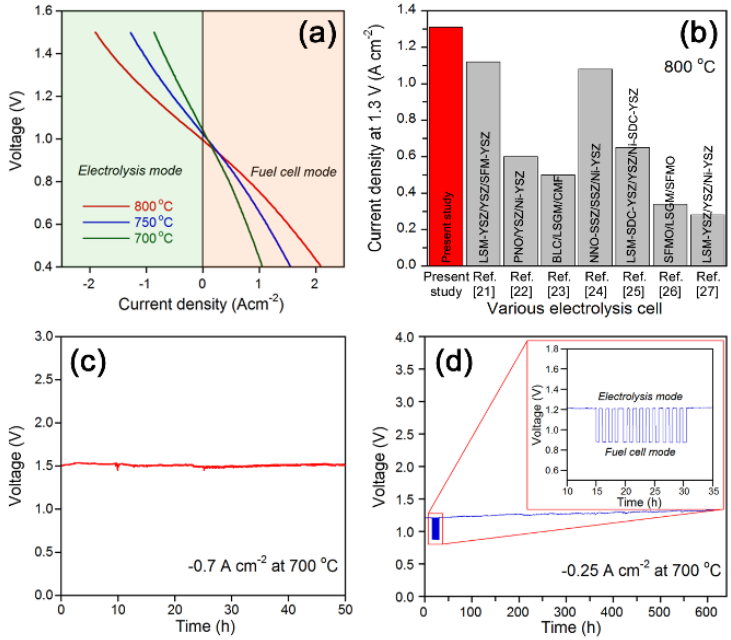

Figure 8.3. a) *I-V* curves for the single cell measured at various temperatures. b) Comparison of the current density at 1.3V and 800 °C of the present work and other literature study. c) The short-term stability of the single cell under a -0.7 Acm^{-2} at 700 °C. d) The long-term stability and reversible cycling test for -0.25 Acm^{-2} at 700 °C. The inset shows the reversible cycling result that was performed at -0.25 A cm^{-2} (electrolysis mode) and at +0.25 A cm^{-2} (fuel cell mode).

Figure 8.3(a) shows the *I-V* curves for a PBM(Co-Fe)/LDC/LSGM/PBSCF50-GDC cell at different temperatures. A H_2 gas containing 10 % steam was fed as the inlet gas to the fuel electrode side and the air electrode side was exposed to an air atmosphere with a flow rate of 100 mL min^{-1}. Current densities of 1.31, 0.81, and 0.52 A cm^{-2} were obtained at 800, 750, and 700 °C, respectively, at 1.3 V close to the thermoneutral voltage. At thermoneutral voltage which is 1.29 V for steam electrolysis,

the electricity input into the cell and the total energy demand for electrolysis reaction are equal. Therefore, the electricity-to-hydrogen conversion efficiency is 100 % at this voltage.[8] A Nyquist plot of the impedance data measured at OCV in electrolysis mode is presented in Figure 8.4. The ohmic resistance of the cell corresponds to the high frequency intercept, which mainly results from the ionic resistance of the LSGM electrolyte. The non-ohmic resistance is determined by the impedance intercept between the high frequency and low frequency intercepts, including charge transfer and non-charge transfer processes for the electrode electrolysis reaction.[20] The non-ohmic resistance of the electrolysis cell decreases with increasing temperature, which were 0.074, 0.118, and 0.161 Ω cm^2 at 800, 750, and 700 °C, respectively.

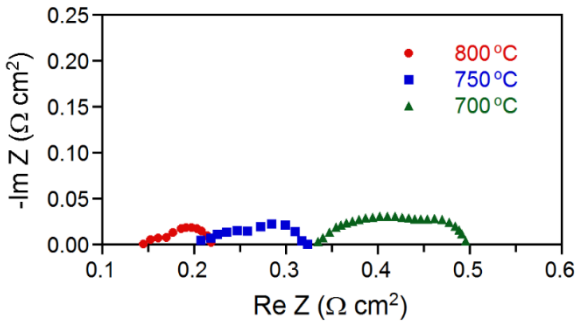

Figure 8.4. Nyquist plot of the impedance data for the PBM(Co-Fe)/LDC/LSGM/PBSCF50-GDC cell at OCV at various temperatures under 10% steam and 90% H_2 fed in the fuel electrode side.

Table 8.1. Comparison of the performance of SOEC reported in the literature and in the present study.

Year [ref.]	Electrode material (air electrode /fuel electrode)	Electrolyte material and thickness (μm)	Gas condition	Current density at 1.3 V(A cm^{-2})
Present study	PBSCF50-GDC/PBM	LSGM, 250 μm	H_2O/H_2=10/90	1.31 (at 800 °C) 0.52 (at 700 °C)
2016 [21]	LSM-YSZ/YSZ/ $Sr_2Fe_{1.5}Mo_{0.5}O_{6-\delta}$-YSZ	YSZ, 10 μm	H_2O/H_2=10/90 H_2O/H_2=30/70	1.12 (at 800 °C) 1.35 (at 800 °C)
2016 [22]	$Pr_2NiO_{4+\delta}$/Ni-YSZ	YSZ, 20 μm	H_2O/H_2=50/50	0.60 (at 800 °C) 0.26 (at 700 °C)
2016 [23]	$Ba_{0.6}La_{0.4}CoO_{3-\delta}$ /$Ce_{0.6}Mn_{0.3}Fe_{0.1}O_{2-\delta}$	LSGM, 300 μm	H_2O/H_2/Ar=20/1/79	0.50 (at 800 °C)

2015 [24]	$Nd_2NiO_{4+\delta}$-$Zr_{0.88}Sc_{0.22}Ce_{0.01}O_{2.12}$ (SSZ, scandia stabilized zirconia)/Ni-YSZ	SSZ, 12 μm	H_2O/H_2=50/50	1.08 (at 800 °C)
2015 [25]	$(La_{0.8}Sr_{0.2})_{0.95}MnO_3$(LSM)-SDC-YSZ/Ni-SDC-YSZ	YSZ, 130 μm	H_2O/H_2=50/50	0.65 (at 800 °C)
2011 [26]	$Sr_2Fe_{1.5}Mo_{0.5}O_{6-\delta}$/ $Sr_2Fe_{1.5}Mo_{0.5}O_{6-\delta}$	LSGM, 165 μm	H_2O/H_2=20/80	0.34 (at 800 °C)
2010 [27]	$(La_{0.8}Sr_{0.2})_{0.95}MnO_3$(LSM)-YSZ/Ni-YSZ	YSZ, 15 μm	H_2O/H_2 = 30/70	0.28 (at 800 °C)
2013 [28]	LSM-YSZ/$La_{0.4}Sr_{0.4}Ni_{0.06}Ti_{0.94}O_{2.94}$	YSZ, 8 μm	H_2O/N_2=47/53	0.13 (at 900 °C)
2008 [29]	$La_{0.8}Sr_{0.2}FeO_3$-YSZ/$La_{0.8}Sr_{0.2}Cr_{0.5}Mn_{0.5}O_3$-YSZ	YSZ, 65 μm	H_2O/H_2=10/90	0.40 (at 700 °C)
2006 [30]	LSM-YSZ/Ni-YSZ	YSZ, 10-15 μm	H_2O/H_2=50/50	1.00 (at 850 °C)

Figure 8.3(b) and Table 8.1. summarize the comparison of the performance between this work and the literatures using state-of-the-art electrodes or other ceramic electrodes. The performance of the present work (1.31 A cm^{-2}) is higher than that of the nanostructured $Sr_2Fe_{1.5}Mo_{0.5}O_{6-\delta}$-YSZ and LSM-YSZ electrode based single cell (1.12 A cm^{-2}) under the same steam feeding condition.[21] The electrolysis performance in the present work is more than 10-fold better than that of prior report for perovskite LSM and $La_{0.4}Sr_{0.4}Ni_{0.06}Ti_{0.94}O_{2.94}$ electrode based SOECs (*i.e.*, 0.13 A cm^{-2} at 900 °C and 1.3 V with 47 % steam and 53% N_2).[28] Recently, Chen *et al.*[24] reported that the Ni-YSZ supported single cell with a $Nd_2NiO_{4+\delta}$ air electrode as an oxygen excess material exhibited high performance (*i.e.*, 1.08 A cm^{-2} at 800 °C and 1.3 V with 50% steam and 50% H_2). Also, the results in this work are superior to those reported in the literature for Ni-YSZ supported cells with LSM-YSZ composite air electrodes (*e.g.*, 1.0 A cm^{-2} at 850 °C and 1.3 V with 50% steam and 50% H_2).[30] The electrolytic performance in this study is even better than those of other SOECs consisting of state-of-the-art Ni-YSZ and LSM electrodes or various ceramic electrodes. The outstanding cell performance demonstrates that SOEC with PBM (Co-

Fe)/LDC/LSGM/PBSCF50-GDC is one of the most promising electrolytic systems in terms of practical high temperature electrolysis.

In general, the interface between the air electrode and the electrolyte is exposed to a reducing condition under lower $p(O_2)$ than 0.21 atm during the fuel cell operating conditions due to the oxygen reduction. In contrast with fuel cell operating conditions, electrolysis operating conditions gives higher $p(O_2)$ to the interface between air electrode and electrolyte, *i.e.*, > 0.21 atm, due to the oxygen evolution [Eq. (2)]. Figure 8.5 shows the oxygen nonstoichiometry of the PBSCF50 and LSM as a function of $p(O_2)$ at 700 ºC. At 0.21 atm, PBSCF50 shows oxygen deficient nonstoichiometry while LSM shows oxygen excess nonstoichiometry. Excess oxygen in LSM can form cation vacancies because oxygen ions do not participate in the interstitial position of the closed packed ABO_3 type perovskite structure due to their larger ionic radius. From a neutron diffraction study, Tofield and Scott reported the existence of cation vacancies at both La and Mn sites.[15,31] Hence, it is assumed that metal vacancies on both La and Mn are predominant defects in the higher $p(O_2)$ region. In the oxygen excess region, the formation of cation vacancies in LSM may be expressed as,

$$6Mn_{Mn}^{X} + \frac{3}{2}O_2 \leftrightarrow V_{La}''' + V_{Mn}''' + 3O_O^X + 6Mn_{Mn}^{\cdot} \qquad \text{Eqn. 8.3}$$

Therefore, the cation vacancies would cause disintegration of LSM and the formation of cation oxide or LSM nanoparticles, resulting severe microstructural damage near the air electrode/electrolyte interface, eventually, leading to degradation and delamination.[32] However, the layered perovskite, PBSCF50, can accommodate excess oxygen as the form of oxygen interstitials within the Pr-O plane in the electrolysis region, thereby effectively inhibiting the creation of any cation vacancies.[19] It certainly excludes some drawbacks of the LSM electrode,[33] leading to improved stability in the electrolysis mode.

Operation under high current densities results in the increase of the H_2 production rate and efficient use of the surplus electricity. In the LSM-YSZ/YSZ/Ni-YSZ cell operated at high current densities, anodic polarization of the LSM-YSZ air electrode increases the oxygen partial pressure at the air electrode/electrolyte interface, resulting in a more accelerated degradation along with delamination at an electrode/electrolyte interface.[11] In order to assess the stability of the single cell at high current density, the voltage of the cell was recorded as a function of time under a constant high current of -0.7 A cm^{-2} at 700 ºC under 10% steam and 90% H_2 fed in the fuel electrode side, as shown in Figure 8.3(c). The voltage of the electrolysis cell is almost constant with no degradation at high current of - 0.7 A cm^{-2} for 50 hours, demonstrating that the PBM(Co-Fe)/LDC/LSGM/PBSCF50-GDC cell can operate at high current densities and produce more hydrogen.

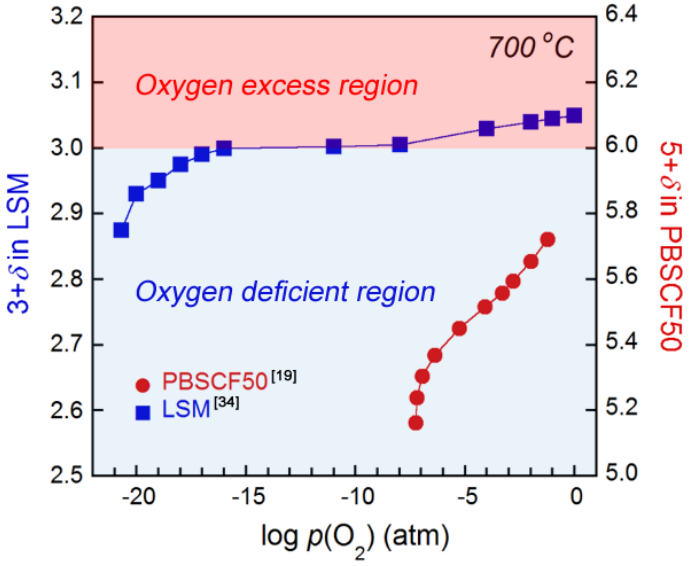

Figure 8.5. The oxygen non-stoichiometry of the PBSCF50 and LSM as a function of $p(O_2)$ at 700 °C.[19,34]

Ideally, SOECs can operate in a reversible mode as a SOFC; that is, reversible solid oxide cells (SOCs) produce hydrogen from steam (electrolysis mode) and subsequently use the produced hydrogen to generate electrical energy (fuel cell mode).[8] However, the SOEC is obviously different from the SOFC considering the fuel electrode reaction under high humidity conditions. Figure 8.3(d) shows the reversibility and long-term stability of the SOEC at 700 °C under 10% steam and 90% H_2 fed in the fuel electrode side. During the period of 15-30 hours, the reversibility of operation (Figure 8.3(d) inset) is confirmed through the cycling test between steam electrolysis at - 0.25 A cm^{-2} and fuel cell operation at + 0.25 A cm^{-2}. The cell shows stable performance in both electrolysis and fuel-cell mode without noticeable degradation during 14 cycles. After reversible cycling, with applied current density of - 0.25 A cm^{-2}, the voltage of the single cell remained almost constant without observable degradation for over 600 hours. It is speculated that the better redox stability, high mixed oxide ionic and electronic conductivity, and fast oxygen kinetics of PBM and PBSCF50 affect the high electrolysis performance and stability of the SOEC consisting of PBM and PBSCF50 as electrodes.[6,19]

To compare the microstructural stability of layered perovskite electrodes and conventional electrodes, Figure 8.6 shows the microstructure of conventional LSM[32] and Ni[35] electrode reported in the literature and PBSCF50 and PBM electrode before and after the SOEC stability test. In the case of conventional LSM and Ni electrode, a delamination between LSM air electrode and YSZ electrolyte and the coarsening of Ni particle in the fuel electrode are observed. As depicted in the inset of Figure 8.6 (a), the LSM electrode delaminates from the YSZ electrolyte. In inset of Figure 8.6 (b), Ni electrode exhibits coarsening after ageing test on account of their inherent poor redox stability. As a result, Ni

electrode coarsening causes a decrease of active site where electrochemical reaction occurs, leading the performance degradation. On the contrary, layered perovskites, PBM and PBSCF50, maintain fine particles with no delamination between electrodes and LSGM electrolyte after long term stability test (> 600 hrs) as shown in Figure 8.6 (c) and (d) due to their high oxygen capacity and excellent redox stability.

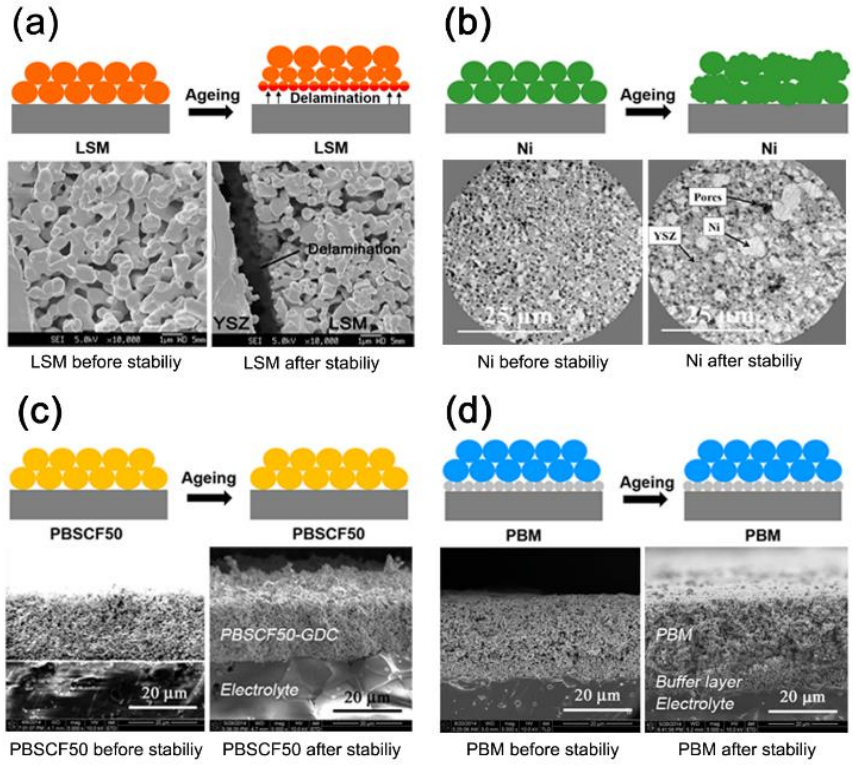

Figure 8.6. The SEM micrographs and illustration of microstructure change after ageing test of a) LSM [32] and b) Ni-YSZ [35] electrode before and after stability test in the literature and c) the PBSCF50-GDC and d) PBM electrode before and after stability test for over 600 hours.

8.4. Conclusions

In this study, we reported the successful application of the layered perovskite PBM and PBSCF50 as fuel and air electrodes for the efficient and continuous production of hydrogen as a SOEC. Current densities of 1.31, 0.81, and 0.52 were obtained for the SOEC using PBM and PBSCF50 as both electrodes at 800, 750, and 700 ^{o}C, respectively, with an applied voltage of 1.3 V. Generally, the SOEC using conventional LSM and Ni as electrode resulted in performance degradation because of delamination of LSM and poor redox stability and coarsening of Ni. In contrast, the SOEC based on PBM and PBSCF50 electrodes shows very stable hydrogen production without observable degradation for more than 600 hours. The remarkable electrolysis performance and stability demonstrate that a

SOEC with a configuration of PBM/LDC/LSGM/PBSCF50 is one of the most potential systems in terms of practical SOEC applications.

References

(1) Hauch, A.; Ebbesen, S. D.; Jensen, S. H.; Mogensen, M. Highly Efficient High Temperature Electrolysis. *J. Mater. Chem.* **2008**, *18* (20), 2331–2340.

(2) Zhu, Y.; Zhou, W.; Chen, Y.; Shao, Z. An Aurivillius Oxide Based Cathode with Excellent CO_2 Tolerance for Intermediate-Temperature Solid Oxide Fuel Cells. *Angew. Chemie Int. Ed.* **2016**, *55*, 8988–8993.

(3) Jun, A.; Ju, Y.-W.; Kim, G. Solid Oxide Electrolysis: Concluding Remarks. *Faraday Discuss.* **2015**, *182*, 519–528.

(4) Pavel, C. C.; Cecconi, F.; Emiliani, C.; Santiccioli, S.; Scaffidi, A.; Catanorchi, S.; Comotti, M. Highly Efficient Platinum Group Metal Free Based Membrane-Electrode Assembly for Anion Exchange Membrane Water Electrolysis. *Angew. Chemie Int. Ed.* **2014**, *53* (5), 1378–1381.

(5) Wang, W.; Huang, Y.; Jung, S.; Vohs, J. M.; Gorte, R. J. A Comparison of LSM, LSF, and LSCo for Solid Oxide Electrolyzer Anodes. *J. Electrochem. Soc.* **2006**, *153* (11), A2066–A2070.

(6) Sengodan, S.; Choi, S.; Jun, A.; Shin, T. H.; Ju, Y.-W.; Jeong, H. Y.; Shin, J.; Irvine, J. T. S.; Kim, G. Layered Oxygen-Deficient Double Perovskite as an Efficient and Stable Anode for Direct Hydrocarbon Solid Oxide Fuel Cells. *Nat. Mater.* **2014**, *14* (2), 205–209.

(7) Jun, A.; Kim, J.; Shin, J.; Kim, G. Perovskite as a Cathode Material: A Review of Its Role in Solid-Oxide Fuel Cell Technology. *ChemElectroChem* **2016**, 511–530.

(8) Minh, N. Q. Reversible Solid Oxide Fuel Cell Technology for Hydrogen/Syngas and Power Production. In *Hydrogen Science and Engineering : Materials, Processes, Systems and Technology*; Prof. Dr. D. Stolten and Dr. B. Emonts, Ed.; Wiley-VCH Verlag GmbH & Co. KGaA: Weinheim, Germany, 2016; pp 359–390.

(9) Wang, S.; Tsuruta, H.; Asanuma, M.; Ishihara, T. Ni-Fe-La(Sr)Fe(Mn)O_3 as a New Active Cermet Cathode for Intermediate-Temperature CO_2 Electrolysis Using a $LaGaO_3$-Based Electrolyte. *Adv. Energy Mater.* **2015**, *5*, 1401003.

(10) Sharma, V. I.; Yildiz, B. Degradation Mechanism in $La_{0.8}Sr_{0.2}CoO_3$ as Contact Layer on the Solid Oxide Electrolysis Cell Anode. *J. Electrochem. Soc.* **2010**, *157* (3), B441–B448.

(11) Knibbe, R.; Traulsen, M. L.; Hauch, A.; Ebbesen, S. D.; Mogensen, M. Solid Oxide Electrolysis Cells: Degradation at High Current Densities. *J. Electrochem. Soc.* **2010**, *157* (8), B1209–B1217.

(12) Kuo, J. H.; Anderson, H. U.; Sparlin, D. M. Oxidation-Reduction Behavior of Undoped and Sr-Doped $LaMnO_3$: Defect Structure, Electrical Conductivity, and Thermoelectric Power. *J. Solid State Chem.* **1989**, *83* (1), 52–60.

(13) Zuev, A. Y.; Tsvetkov, D. S. Oxygen Nonstoichiometry, Defect Structure and Defect-Induced Expansion of Undoped Perovskite $LaMnO_{3\pm\delta}$ *Solid State Ionics* **2010**, *181* (11–12), 557–563.

(14) Chen, K.; Ai, N.; Jiang, S. P. Performance and Stability of (La,Sr)MnO_3–Y_2O_3–ZrO_2 Composite Oxygen Electrodes under Solid Oxide Electrolysis Cell Operation Conditions. *Int. J. Hydrogen*

Energy **2012**, *37* (14), 10517–10525.

(15) Sengodan, S.; Ahn, S.; Shin, J.; Kim, G. Oxidation–reduction Behavior of $La_{0.8}Sr_{0.2}Sc_yMn_{1-y}O_{3\pm\delta}$ (y = 0.2, 0.3, 0.4): Defect Structure, Thermodynamic and Electrical Properties. *Solid State Ionics* **2012**, *228*, 25–31.

(16) Graves, C.; Ebbesen, S. D.; Jensen, S. H.; Simonsen, S. B.; Mogensen, M. B. Eliminating Degradation in Solid Oxide Electrochemical Cells by Reversible Operation. *Nat. Mater.* **2014**, *14* (2), 239–244.

(17) Yoo, S.; Jun, A.; Ju, Y.; Odkhuu, D.; Hyodo, J.; Jeong, H. Y.; Park, N.; Shin, J.; Ishihara, T.; Kim, G. Development of Double-Perovskite Compounds as Cathode Materials for Low-Temperature Solid Oxide Fuel Cells. *Angew. Chemie Int. Ed.* **2014**, *53*, 13064–13067.

(18) Jun, A.; Yoo, S.; Ju, Y.-W.; Hyodo, J.; Choi, S.; Jeong, H. Y.; Shin, J.; Ishihara, T.; Lim, T.; Kim, G. Correlation between Fast Oxygen Kinetics and Enhanced Performance in Fe Doped Layered Perovskite Cathodes for Solid Oxide Fuel Cells. *J. Mater. Chem. A* **2015**, *3*, 15082–15090.

(19) Choi, S.; Yoo, S.; Kim, J.; Park, S.; Jun, A.; Sengodan, S.; Kim, J.; Shin, J.; Jeong, H. Y.; Choi, Y.; et al. Highly Efficient and Robust Cathode Materials for Low-Temperature Solid Oxide Fuel Cells: $PrBa_{0.5}Sr_{0.5}Co_{2-x}Fe_xO_{5+\delta}$. *Sci. Rep.* **2013**, *3*, 2426.

(20) Jun, A.; Shin, J.; Kim, G. High Redox and Performance Stability of Layered $SmBa_{0.5}Sr_{0.5}Co_{1.5}Cu_{0.5}O_{5+\delta}$ Perovskite Cathodes for Intermediate-Temperature Solid Oxide Fuel Cells. *Phys. Chem. Chem. Phys.* **2013**, *15* (45), 19906–19912.

(21) Li, Y.; li, Pan; Hu, B.; Xia, C. Nanotructured Ceramic Fuel Electrode for Efficient CO_2/H_2O Electrolysis without Safe Gas. *J. Mater. Chem. A* **2016**, *4*, 9236–9243.

(22) Laguna-Bercero, M. A.; Monzón, H.; Larrea, A.; Orera, V. M. Improved Stability of Reversible Solid Oxide Cells with a Nickelate-Based Oxygen Electrode. *J. Mater. Chem. A* **2016**, *4* (4), 1446–1453.

(23) Hosoi, K.; Sakai, T.; Ida, S.; Ishihara, T. $Ce_{0.6}Mn_{0.3}Fe_{0.1}O_{2-\delta}$ as an Alternative Cathode Material for High Temperature Steam Electrolysis Using $LaGaO_3$-Based Oxide Electrolyte. *Electrochim. Acta* **2016**, *194* (3), 473–479.

(24) Chen, T.; Liu, M.; Yuan, C.; Zhou, Y.; Ye, X.; Zhan, Z.; Xia, C.; Wang, S. High Performance of Intermediate Temperature Solid Oxide Electrolysis Cells Using $Nd_2NiO_{4+\delta}$ Impregnated Scandia Stabilized Zirconia Oxygen Electrode. *J. Power Sources* **2015**, *276*, 1–6.

(25) Yang, C.; Li, J.; Newkirk, J.; Baish, V.; Hu, R.; Chen, Y.; Chen, F. Co-Electrolysis of H_2O and CO_2 in a Solid Oxide Electrolysis Cell with Hierarchically Structured Porous Electrodes. *J. Mater. Chem. A* **2015**, *3*, 15913–15919.

(26) Liu, Q.; Yang, C.; Dong, X.; Chen, F. Perovskite $Sr_2Fe_{1.5}Mo_{0.5}O_{6-\delta}$ As Electrode Materials for Symmetrical Solid Oxide Electrolysis Cells. *Int. J. Hydrogen Energy* **2010**, *35* (19), 10039–

10044.

(27) Yang, C.; Coffin, A.; Chen, F. High Temperature Solid Oxide Electrolysis Cell Employing Porous Structured $(La_{0.75}Sr_{0.25})_{0.95}MnO_3$ with Enhanced Oxygen Electrode Performance. *Int. J. Hydrogen Energy* **2010**, *35* (8), 3221–3226.

(28) Tsekouras, G.; Neagu, D.; Irvine, J. T. S. Step-Change in High Temperature Steam Electrolysis Performance of Perovskite Oxide Cathodes with Exsolution of B-Site Dopants. *Energy Environ. Sci.* **2013**, *6* (1), 256–266.

(29) Bidrawn, F.; Kim, G.; Corre, G.; Irvine, J. T. S.; Vohs, J. M.; Gorte, R. J. Efficient Reduction of CO_2 in a Solid Oxide Electrolyzer. *Electrochem. Solid-State Lett.* **2008**, *11* (9), B167–B170.

(30) Hauch, A.; Jensen, S. H.; Ramousse, S.; Mogensen, M. Performance and Durability of Solid Oxide Electrolysis Cells. *J. Electrochem. Soc.* **2006**, *153* (9), A1741–A1747.

(31) Tofield, B. C.; Scott, W. R. Oxidative Nonstoichiometry in Perovskites, an Experimental Survey; the Defect Structure of an Oxidized Lanthanum Manganite by Powder Neutron Diffraction. *J. Solid State Chem.* **1974**, *10* (3), 183–194.

(32) Chen, K.; Jiang, S. P. Failure Mechanism of (La,Sr)MnO_3 Oxygen Electrodes of Solid Oxide Electrolysis Cells. *Int. J. Hydrogen Energy* **2011**, *36* (17), 10541–10549.

(33) Orera, A.; Slater, P. R. New Chemical Systems for Solid Oxide Fuel Cells. *Chem. Mater.* **2010**, *22* (3), 675–690.

(34) Mizusaki, J.; Mori, N.; Takai, H.; Yonemura, Y.; Minamiue, H.; Tagawa, H.; Dokiya, M.; Inaba, H.; Naraya, K.; Sasamoto, T.; et al. Oxygen Nonstoichiometry and Defect Equilibrium in the Perovskite-Type Oxides $La_{1-x}Sr_xMnO_{3+\delta}$. *Solid State Ionics* **2000**, *129* (1), 163–177.

(35) Lay-Grindler, E.; Laurencin, J.; Villanova, J.; Cloetens, P.; Bleuet, P.; Mansuy, A.; Mougin, J.; Delette, G. Degradation Study by 3D Reconstruction of a Nickel-Yttria Stabilized Zirconia Cathode after High Temperature Steam Electrolysis Operation. *J. Power Sources* **2014**, *269*, 927–936.

Chapter 9. Novel system for the production of hydrogen

9.1. Introduction

Environment-friendly and clean fuels have been strongly considered with the growing concerns about global warming and environmental issues caused by the emission of CO_2 and combustion by-product arising from the consumption of fossil fuels.[1, 2] Hydrogen has been received significant attention for alternative fossil fuels because it is the cleanest fuel on the earth along with its highest energy density throughout all fuels (143 kJ kg^{-1}).[3] However, most hydrogen (>90%) is presently produced from hydrocarbons by the steam reforming, causing high cost and coproduction of the greenhouse gas emission (*i.e.*, CO_2).[4] Other hydrogen production processes, such as photoelectrochemical water splitting, thermochemical water splitting, and water electrolysis, have been considered as an environment-friendly hydrogen production system. Among these hydrogen production systems, water electrolysis is the cleanest system when it is especially combined with renewable energy sources as the electricity provider. But the water electrolysis at low operating temperature lower than 100 ^oC (*i.e.*, polymer electrolyte membrane electrolysis and alkaline water electrolysis) requires significant electricity supply and noble metal-based electrocatalysts, leading high cost and less electrolysis efficiency. On the contrary, high temperature steam electrolysis (*i.e.*, solid oxide electrolysis) is more efficient and promising hydrogen system because high operating temperature (500 – 1000 ^oC) is advantageous for both thermodynamics and kinetics.[5,6]

Solid oxide electrolysis cells (SOECs) are categorized into mainly two types of electrolysis cells based on their different ion-transport electrolyte materials: oxygen ion conducting SOECs (O^{2-}-SOECs) and proton conducting SOECs (H^+-SOECs). The conventional O^{2-}-SOECs use yttria-stabilized zirconia (YSZ, the conventional high temperature oxygen ion conductor) as the electrolyte material. SOECs based on YSZ electrolyte have to be operated at high temperatures (800 – 1000 ^oC) because YSZ shows sufficient ionic conductivity at these high operating temperatures. However, high operating temperatures have resulted in critical problems such as poor stability, fabrication challenges, and material compatibility issues. For these reasons, the development of SOECs has focused on lowering the operating temperature to an intermediate range (500 – 700 ^oC) while preserving the electrolysis performance. Proton conducting oxides such as $BaCeO_3$ and $BaZrO_3$-based materials are able to use as electrolyte for intermediate temperature H^+-SOECs due to their better ionic conductivity at intermediate temperatures.[7] But, a poor sinterability and unstability in H_2O-contaning atmospheres of $BaCeO_3$ and $BaZrO_3$-based materials make difficult to apply the H^+-SOECs.[8]

Here, to produce more hydrogen at lower operating temperature, we introduce a novel SOEC named the "Dual Solid Oxide Electrolysis Cell" (Dual-SOEC) using both O^{2-} and H^+ conducting electrolyte. We use a barium zirconate-cerate co-doped with ytterbium and yttrium, $BaZr_{0.1}Ce_{0.7}Y_{0.1-}$

$_xYb_xO_{3-\delta}$ (BZCYYb), as electrolyte for Dual SOEC. The BZCYYb oxide which contains both protonic defects and oxide ion vacancies allows transport of both protons and oxygen ions, resulting in a high ionic conductivity below 750 °C as reported.[9] Dual-SOEC is expected to benefit from the operation of both O^{2-}-SOEC and H^+-SOEC at the same time, contributing to the enhancement of hydrogen production capability.

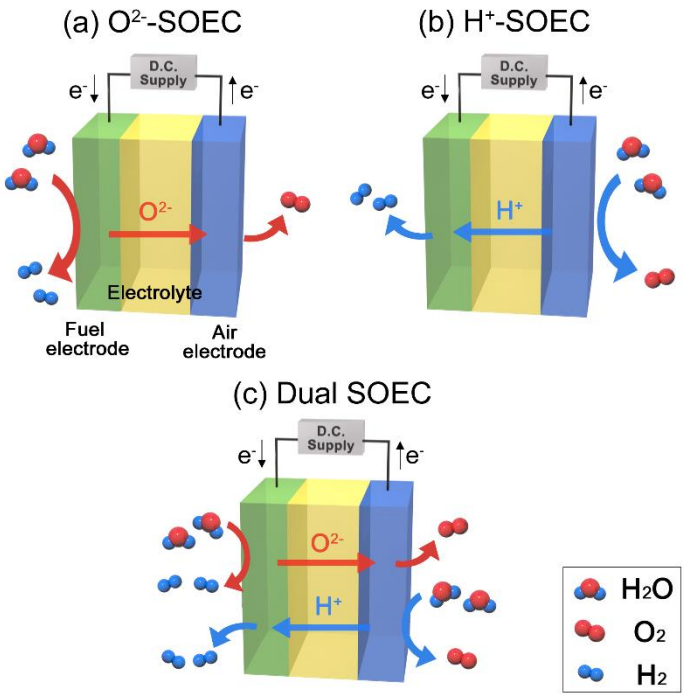

Figure 9.1. Schemes of (a) O^{2-}-SOEC, (b) H^+-SOEC, and (c) Dual SOEC.

Figure 9.1 shows a schematic illustration of the working mechanism of O^{2-}-SOEC, H^+-SOEC, and Dual SOEC. As shown in figure 9.1(a), in the O^{2-}-SOEC, steam is fed to fuel electrode side and is split into hydrogen and oxygen ions. The produced hydrogen is collected at the fuel side, while oxygen ions diffuse through the oxygen ion conducting electrolyte to the air electrode and subsequently oxidize to oxygen. On the contrary, in the H^+-SOEC (exhibited in figure 9.1(b)), the steam is supplied to the air electrode side and then it is oxidized to oxygen. Generated protons pass through the proton conducting electrolyte to the fuel electrode side and combine with electrons to form hydrogen. In the Dual SOEC, as presented in figure 9.1 (c), steam is fed to both fuel electrode side and air electrode side. Steam is split into hydrogen and oxygen ions at fuel electrode side, whereas at air electrode side, steam dissociates into oxygen and protons. Each generated oxygen ions and protons oppositely diffuse across the electrolyte to air and fuel electrode side. Finally, oxygen ions oxidize to oxygen at air electrode side while protons reduce to hydrogen at fuel electrode side. All produced hydrogen is collected at the fuel

electrode side in Dual SOEC. The overall reactions at the air and fuel electrode side can be expressed as follows for Dual SOEC:

$$\text{Air electrode: } H_2O \rightarrow 2H^+ + \frac{1}{2}O_2(g) + 2e^- \quad \text{Eqn. 9.1}$$

$$O^{2-} \rightarrow \frac{1}{2}O_2(g) + 2e^- \quad \text{Eqn. 9.2}$$

$$\text{Fuel electrode: } 2H^+ + 2e^- \rightarrow H_2(g) \quad \text{Eqn. 9.3}$$

$$H_2O + 2e^- \rightarrow H_2(g) + O^{2-} \quad \text{Eqn. 9.4}$$

As discussed below, we present the proof-of-concept of Dual SOEC and report the highest efficient current densities obtained from this system. We fabricated the Dual SOEC using the BZCYYb as a dense electrolyte, $NdBa_{0.5}Sr_{0.5}Co_{1.5}Fe_{0.5}O_{5+\delta}$ (NBSCF)-BZCYYb composite as an air electrode, and Ni-BZCYYb composite as a fuel electrode. Layered NBSCF perovskite can conduct protons, oxygen ions and electrons, leading to extend the electrochemically active sites to the entire surface of the air electrode.[10] These properties of the NBSCF may affect the improvement of the catalytic activity for steam dissociation and O_2 evolution. Also, Ni shows the excellent electrocatalytic activity, the high electronic conductivity providing pathways for electron transfer and the good compatibility with BZCYYb,[11,12] making it suitable as Ni-BZCYYb fuel electrode for the application of Dual SOEC.

9.2. Experimental

9.2.1. Synthesis of electrode and electrolyte powders

$NdBa_{0.5}Sr_{0.5}Co_{1.5}Fe_{0.5}O_{5+\delta}$ (NBSCF) were synthesized by the Pechini method. The desired composition was obtained by each dissolving nitrate salts in distilled water with the addition of quantitative amounts of citric acid and ethylene glycol. After a viscous resin was formed, the mixture was heated to roughly 250 °C in air, followed by combustion to form powders, which were calcined at 600 °C for 4 h and ball-milled in acetone for 24 h. $BaZr_{0.1}Ce_{0.7}Y_{0.1}Yb_{0.1}O_{3-\delta}$ (BZCYYb) powders were synthesized by the typical solid state reaction method. Stoichiometric amounts of barium carbonate, zirconium oxide, cerium oxide, ytterbium oxide, and yttrium oxide powders (all from Aldrich Chemicals) were mixed by ball milling, followed by sintering at 1100 °C in air for 10 h. The NiO powders for the fuel electrode were synthesized by the glycine nitrate process (GNP). Stoichiometric amounts of nitrates were dissolved in distilled water with a proper amount of glycine. The solutions were heated up to 350 °C and followed by combustion to form fine powders.

9.2.2. Preparation of sample for XRD and SEM analysis

In order to test the chemical stability between the NBSCF and BZCYYb, slurries of the NBSCF-BZCYYb composite electrode were applied on the BZCYYb electrolyte by a screen printing method, and then fired at 950 ºC in air for 4 hours. The chemical reactivity of NBSCF and BZCYYb was confirmed by using an X-ray diffractometer (Rigaku diffractometer, Cu Kα radiation). The microstructures and cross section of the Ni-BZCYYb/BZCYYb/NBSCF-BZCYYb single cell after electrolysis test were observed using field emission scanning electron microscopy (Nova Nano SEM, FEI, USA).

9.2.3. Fabrication of electrolysis cell

The NiO-BZCYYb electrode-supported cell was fabricated to measure the electrolysis performance and durability. For preparation of air electrode slurries, the calcined NBSCF powder and BZCYYb were mixed by ball-milling at weight ratio of 8:2, blended with a binder (Heraeus V006). NiO-BZCYYb supported cells were fabricated using the drop-coating method. The NiO-BZCYYb fuel electrode was prepared by a mixture of NiO and BZCYYb (weight ratio of 6.5:3.5) after being ball-milled in ethanol for 24 hours. The BZCYYb suspension was applied to a NiO-BZCYYb support by drop-coating, followed by drying in air and subsequent co-sintering at 1400 ºC for 4 hours. Air electrode slurries were applied onto the surface of the BZCYYb electrolyte by screen printing and were finally sintered 950 ºC for 4 hours in air.

9.2.4. Electrolysis performance and stability test

For the electrolysis tests, Ag wires were attached at both electrodes of the Ni-BZCYYb/BZCYYb/NBSCF-BZCYYb cell using Ag paste as a current collector. The cell was sealed fully onto one end of the alumina tube using a ceramic adhesive (Aremco, Ceramabond 552). The entire cell was placed inside a furnace and heated to the desired temperature. Nitrogen gas was switched to humidified hydrogen (3 % H_2O), changing the phase from Ni oxide to Ni metal. The cell was tested from 750 to 550ºC under three different atmosphere conditions; (1) in Dual SOEC mode: under 90% H_2 and 10% steam fed in the fuel electrode and 90% air and 10% steam fed in the air electrode (2) in O^{2-}-SOEC mode: under 90% H_2 and 10% steam fed in the fuel electrode and 100% air fed in the air electrode (3) in H^+-SOEC mode: under 100% H_2 fed in the fuel electrode and 90% air and 10% steam fed in the air electrode. In order to assess the stability of the Ni-BZCYYb/BZCYYb/NBSCF-BZCYYb cell in Dual SOEC, the voltage of the cell was recorded as a function of time under a constant high current of -0.45 A cm^{-2} at 550 ºC under 90% H_2 and 10% steam fed in the fuel electrode and 90% air and 10% steam fed in the air electrode. Impedance spectra, *I-V* curves and stability of the electrolysis

cell were examined using a BioLogic Potentiostat at operating temperature. Impedance spectra were recorded under OCV in a frequency range of 1 mHz to 500 kHz with AC perturbation of 14 mV from 750 to 550 ºC.

9.3. Results and Discussions

Generally, the phase reaction between the electrode and electrolyte materials can generate an insulating phases at the interfacial layer, which blocks ionic and electronic transport from the electrode to the electrolyte.[13] Figure 9.2 presents the XRD patterns of NBSCF-BZCYYb composite to confirm the absence of chemical reactivity as a preliminary study. All the peaks can be attributed to either NBSCF or BZCYYb, indicating that there are no obvious interfacial reactions or distinct secondary phases between them.

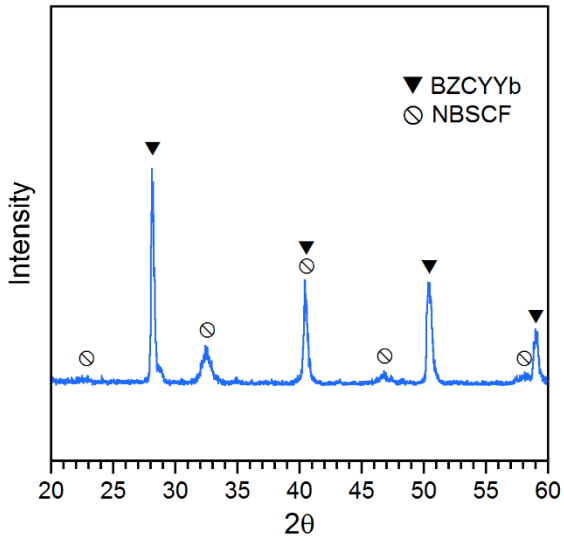

Figure 9.2. X-ray diffraction pattern of BZCYYb-NBSCF composite sintered at 950 ºC 4h.

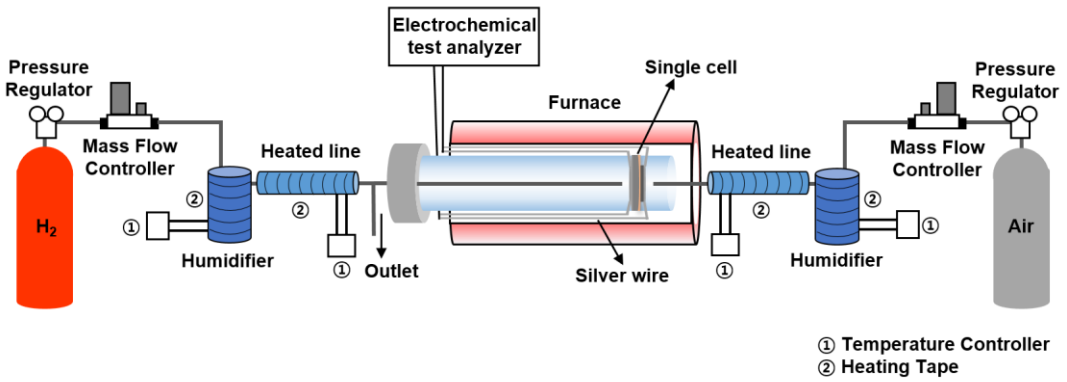

Figure 9.3. Schematic illustration of the experimental setup employed for the dual SOE experiments.

The schematic diagram and experimental details for Dual SOEC measurements is described in Figure 9.3. Hydrogen was supplied to the fuel electrode side while air was supplied to the air electrode side with a flow rate of 100 mL min^{-1}. In Dual SOEC measurements, steam was supplied to both electrode sides by the use of the gas bubbler in water surrounded by a heating tapes maintained at a constant temperature for the required amount of steam (*i.e.* 10% steam in this work). Figure 9.4 (a) shows the steam electrolysis performance of the Ni-BZCYYb/BZCYYb/NBSCF-BZCYYb cell operated as Dual SOEC at various temperatures between 550 °C and 750 °C. Current densities of 3.16, 2.41, 1.62, 0.75 and 0.42 A cm^{-2} were obtained at 750, 700, 650, 600 and 550 °C, respectively, at 1.3 V (the thermo-neutral voltage for steam electrolysis). Nyquist plot of the impedance data measured at OCV in Dual SOEC mode is shown in Figure 9.5. The ohmic resistance of the cell corresponds to the high frequency intercept, which mainly results from the ionic resistance of the BZCYYb electrolyte. The non-ohmic resistance is determined by the impedance intercept between the high frequency and low frequency intercepts, including charge transfer and non-charge transfer processes for the electrode electrolysis reaction.[14]

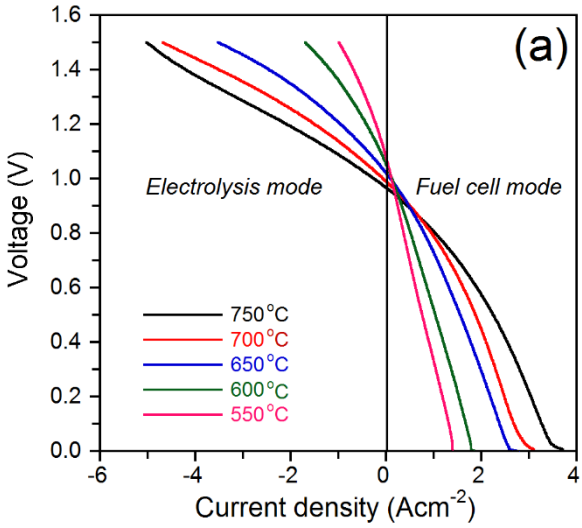

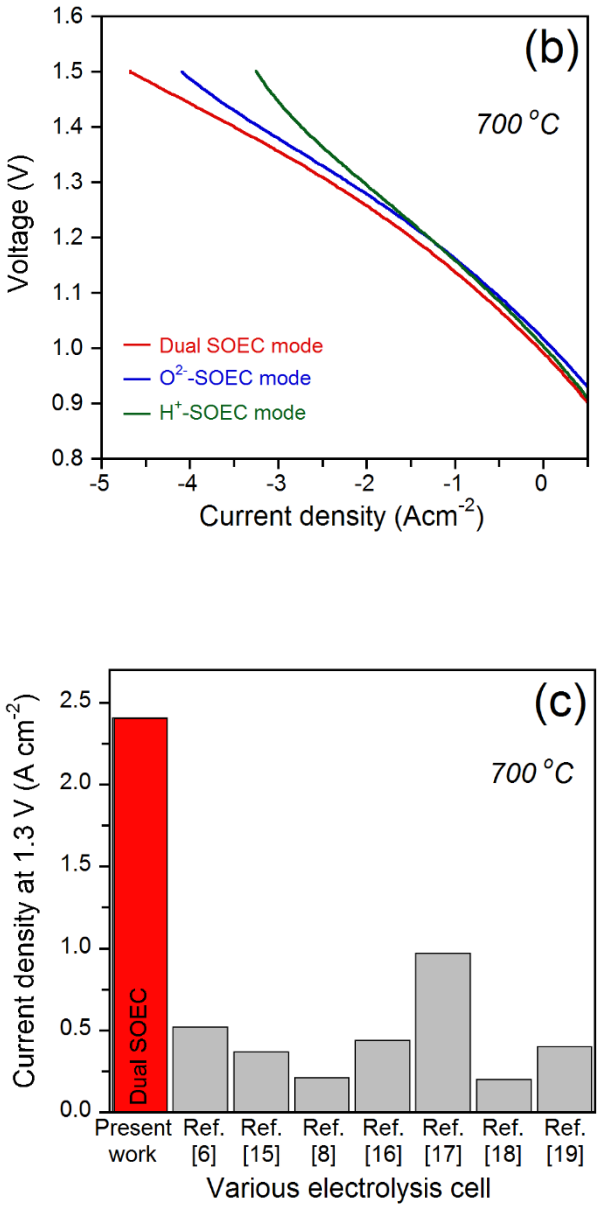

Figure 9.4. *V-i* curves for a Ni-BZCYYb/BZCYYb/NBSCF-BZCYYb cell (a) at various temperatures under 90% H_2 and 10% steam fed in the fuel side and 90% air and 10% steam fed in the air side and (b) under 90% H_2 and 10% steam fed in the fuel side and 90% air and 10% steam fed in the air side (red line, Dual SOEC mode), 90% H_2 and 10% steam fed in the fuel side and 100% air fed in the air side (blue line, O^{2-}-SOEC mode), and 97% H_2 and 3% steam fed in the fuel side and 90% air and 10% steam fed in the air side (green line, H^+-SOEC mode) at 700 °C. (c) Comparison of the current densities at 1.3V and 700 °C of the present work and other literature studies.

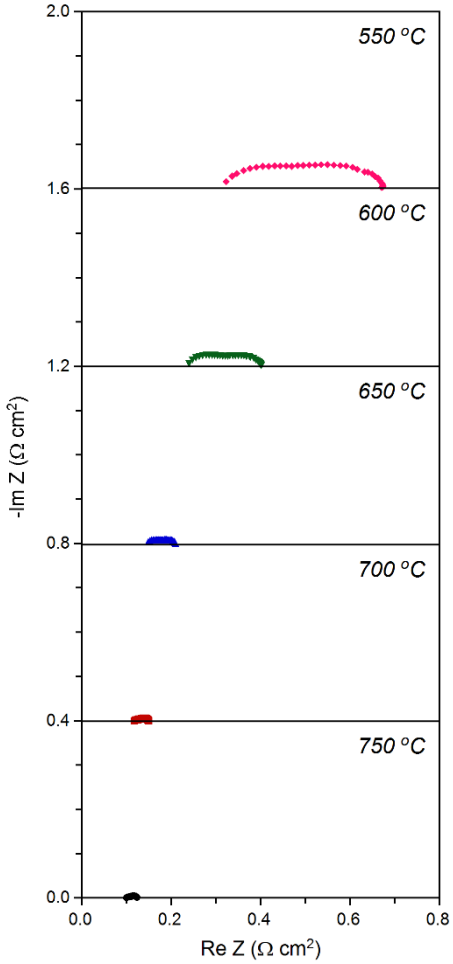

Figure 9.5. Nyquist plot of the impedance data measured at OCV in Dual SOEC mode under 90% H_2 and 10% steam fed in the fuel side and 90% air and 10% steam fed in the air side at various temperatures.

To prove the concept of Dual SOEC and investigate its outstanding performance compared to each O^{2-}-SOEC and H^+-SOEC, the Ni-BZCYYb/BZCYYb/NBSCF-BZCYYb cell was tested in three different atmosphere conditions at 700 ºC as shown in figure 9.4 (b). Current density of Dual SOEC is 2.41 A cm^{-2} in 90% H_2/10% steam (fuel electrode) and 90% air/10% steam (air electrode). Current density of O^{2-}-SOEC is 2.20 A cm^{-2} under 90% H_2/10% steam (fuel electrode) and 100% air (air electrode), while current density of H^+-SOEC in 97% H_2/3% steam (fuel electrode) and 90% air/10% steam (air electrode) is 2.04 A cm^{-2} at 1.3 V. Current density of Dual SOEC is enhanced by approximately 10% and 18% compared to O^{2-}-SOEC and H^+-SOEC, suggesting that Dual SOEC can produce more hydrogen than O^{2-} and H^+-SOEC. The amount of hydrogen produced from the SOEC operation can be estimated by Faraday's law. Assuming 100% current efficiency, the calculated amount of hydrogen production for Dual SOEC, O^{2-}-SOEC, and H^+-SOEC are 1.01, 0.92, and 0.85 L cm^{-2} h^{-1} at 1.3 V and 700 ºC, respectively.

Table 9.1. Comparison of the performance of Dual SOEC in the present study and O^{2-}-SOEC and H^{+}-SOEC reported in the literature.

Year [ref.]	SOEC type	Electrolyte	Gas condition	Current density(A cm^{-2}) at 1.3 V, 700 °C
Present work	Dual SOEC	$BaZr_{0.1}Ce_{0.7}Y_{0.1}Yb_{0.1}O_{3-\delta}$	H_2/H_2O=90/10 (Fuel side) Air/H_2O =90/10 (Air side)	2.41
2016 [6]	O^{2-}-SOEC	$La_{0.9}Sr_{0.1}Ga_{0.8}Mg_{0.2}O_{3-\delta}$ (LSGM)	H_2/H_2O=90/10 (Fuel side)	0.52
2016 [15]	O^{2-}-SOEC	$Zr_{0.89}Sc_{0.1}Ce_{0.01}O_{2-\gamma}$ (ScSZ)	H_2/H_2O=50/50 (Fuel side)	0.37
2015 [8]	H^{+}-SOEC	$BaZr_{0.9}Y_{0.1}O_{3-\delta}$	Air/H_2O=97/3 (Air side)	0.21
2015 [16]	O^{2-}-SOEC	$Zr_{0.88}Sc_{0.22}Ce_{0.01}O_{2.11}$ (SSZ)	H_2/H_2O=50/50 (Fuel side)	0.44
2012 [17]	H^{+}-SOEC	$BaCe_{0.5}Zr_{0.3}Y_{0.16}Zn_{0.04}O_{3-\delta}$ (BCZYZ)	N_2/H_2O =97/3 (Air side)	0.97
2010 [18]	H^{+}-SOEC	$BaCe_{0.5}Zr_{0.4}Y_{0.2}O_{3-\delta}$	Air/H_2O =80/20 (Air side)	0.2
2008 [19]	O^{2-}-SOEC	YSZ	H_2/H_2O =90/10 (Fuel side)	0.4

Table 9.1 and figure 9.4(c) summarized the comparison between the results of Dual SOEC in this study with the performance of H^{+}-SOECs and O^{2-}-SOECs reported in the literature. The electrolysis performance of Dual SOEC is more than quadrupled better than that of previous report for O^{2-}-SOEC (*i.e.*, 0.52 A cm^{-2} at 700 °C and 1.3 V with 10 % steam and 90% H_2 fed in the fuel electrode).[6] Furthermore, Dual SOEC shows superior performance as compared with BCZYZ electrolyte based H^{+}-SOEC in the literature (*i.e.*, 0.97 A cm^{-2} at 700 °C and 1.3 V with 3 % steam and 97% N_2 fed in the air electrode).[17] Novel hydrogen production system, Dual SOEC, exhibits significantly outstanding electrolysis performance so far when compared to other conventional SOECs consisting of H^{+} or O^{2-}

conducting electrolyte. Therefore, Dual SOEC can be considered one of the most promising electrolytic systems in terms of efficient hydrogen production.

An important aspect for promising SOEC system is the ability to produce continuously hydrogen as well as high efficiency of hydrogen production. To measure the long-term stability of the Dual SOEC, the voltage of cells was recorded as a function of time under constant current load of 0.45 A cm^{-2} at 550 ^{o}C operating in 90% H_2 and 10% steam fed in fuel electrode side and 90% air and 10% steam fed in air electrode, as shown in Figure 9.6. The voltage is almost constant for more than 60 hours with no significant degradation, indicating the Dual SOEC can produce hydrogen continuously.

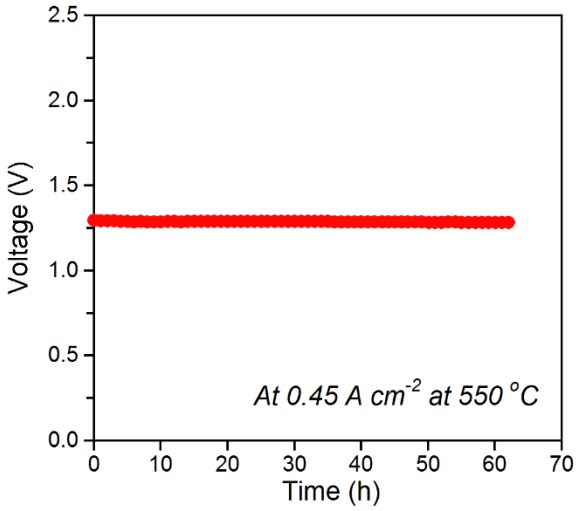

Figure 9.6. Time-dependence of the cell voltage applied 0.45 Acm^{-2} at 550 ^{o}C during Dual electrolysis under 90% H_2 and 10% steam fed in the fuel electrode and 90% air and 10% steam fed in the air electrode.

After electrolysis test, the microstructure of as-prepared electrolysis cell is examined using scanning electron microscopy (SEM). Figure 9.7 shows micrographs of the Ni-BZCYYb/BZCYYb/NBSCF-BZCYYb cells after stability test of Dual SOEC at 550 ^{o}C. The BZCYYb electrolyte is approximately 20 μm in thickness while the NBSCF-BZCYYb composite air electrode is around 15 μm in thickness. The BZCYYb electrolyte and interfaces of between electrodes and electrolytes maintained the dense electrolyte and the well-connected interface without sign of degradation such as visible cracks or delamination, indicating mechanical stability of Dual SOEC under electrolysis operating conditions (*i.e.*, high humidity conditions).

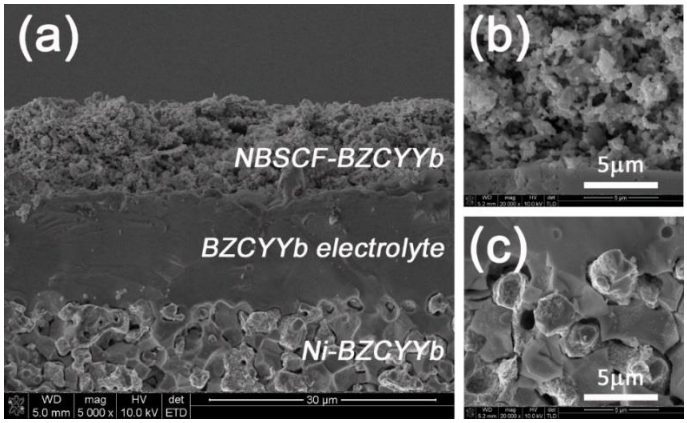

Figure 9.7. SEM micrographs of Ni-BZCYYb/BZCYYb/NBSCF-BZCYYb cell as Dual SOEC after stability at 550 ºC during over 60 hours: (a) cross-sectional SEM micrograph of the fabricated cell after stability test, with BZCYYb electrolyte supported on Ni-BZCYYb fuel electrode, and NBSCF-BZCYYb air electrode; (b) microstructure of interface between NBSCF-BZCYYb and BZCYYb electrolyte; (c) microstructure of interface between Ni-BZCYYb and BZCYYb electrolyte.

In this study, we demonstrate the proof-of-concept and achieve outstanding electrolysis performance and sufficient performance stability. In summary, the Dual SOEC shows great promise as best-in-class technology for future hydrogen production.

9.4. Conclusions

In this study, we introduce a novel solid oxide electrolyzer named the "Dual solid oxide electrolysis cell" (Dual SOEC), which is operated simultaneously both O^{2-}-SOEC and H^{+}-SOEC. Current densities of 3.16, 2.41, 1.62, 0.75 and 0.42 A cm^{-2} were obtained at 750, 700, 650, 600 and 550 ºC, respectively, at 1.3 V under 90% H_2 and 10% steam fed in the fuel electrode side and 90% air and 10% steam fed in the air electrode side. Also, the cell voltage shows stable for more than 60 h with no significant degradation under constant current load of 0.45 A cm^{-2} at 550 ºC. Therefore, the Dual SOEC shows the outstanding performance compared to O^{2-}-SOEC and H^{+}-SOEC, indicating that the Dual SOEC will be possible to apply industry after system optimization.

References

(1) Tsekouras, G.; Neagu, D.; Irvine, J. T. S. Step-Change in High Temperature Steam Electrolysis Performance of Perovskite Oxide Cathodes with Exsolution of B-Site Dopants. *Energy Environ. Sci.* **2013**, *6* (1), 256–266.

(2) Park, S.; Shao, Y.; Liu, J.; Wang, Y. Oxygen Electrocatalysts for Water Electrolyzers and Reversible Fuel Cells: Status and Perspective. *Energy Environ. Sci.* **2012**, *5* (11), 9331.

(3) Liu, W.; Cui, Y.; Du, X.; Zhang, Z.; Chao, Z.; Deng, Y. High Efficiency Hydrogen Evolution from Native Biomass Electrolysis. *Energy Environ. Sci.* **2016**, *9* (2), 467–472.

(4) Tan, Y.; Wang, H.; Liu, P.; Shen, Y.; Cheng, C.; Hirata, A.; Fujita, T.; Tang, Z.; Chen, M. Versatile Nanoporous Bimetallic Phosphides towards Electrochemical Water Splitting. *Energy Environ. Sci.* **2016**, *9*, 2257–2261.

(5) Wang, W.; Huang, Y.; Jung, S.; Vohs, J. M.; Gorte, R. J. A Comparison of LSM, LSF, and LSCo for Solid Oxide Electrolyzer Anodes. *J. Electrochem. Soc.* **2006**, *153* (11), A2066–A2070.

(6) Jun, A.; Kim, J.; Shin, J.; Kim, G. Achieving High Efficiency and Eliminating Degradation in Solid Oxide Electrochemical Cells Using High Oxygen-Capacity Perovskite. *Angew. Chemie Int. Ed.* **2016**, *55*, 12512–12515.

(7) Kim, J.; Sengodan, S.; Kwon, G.; Ding, D.; Shin, J. Triple-Conducting Layered Perovskites as Cathode Materials for Proton-Conducting Solid Oxide Fuel Cells. *ChemSusChem* **2014**, 2811–2815.

(8) Bi, L.; Shafi, S. P.; Traversa, E. Y-Doped $BaZrO_3$ as a Chemically Stable Electrolyte for Proton-Conducting Solid Oxide Electrolysis Cells (SOECs). *J. Mater. Chem. A* **2015**, *3*, 5815–5819.

(9) Yang, L.; Wang, S.; Blinn, K.; Liu, M.; Liu, Z.; Cheng, Z.; Liu, M. Enhanced Sulfur and Coking Tolerance of a Mixed Ion Conductor for SOFCs: $BaZr_{0.1}Ce_{0.7}Y_{0.2-x}Yb_xO_{3-\delta}$. *Science* **2009**, *326* (5949), 126–129.

(10) Kim, J.; Choi, S.; Jun, A.; Jeong, H. Y.; Shin, J.; Kim, G. Chemically Stable Perovskites as Cathode Materials for Solid Oxide Fuel Cells: La-Doped $Ba_{0.5}Sr_{0.5}Co_{0.8}Fe_{0.2}O_{3-\delta}$. *ChemSusChem* **2014**, *7* (6), 1669–1675.

(11) Nechache, A.; Cassir, M.; Ringuedé, A. Solid Oxide Electrolysis Cell Analysis by Means of Electrochemical Impedance Spectroscopy: A Review. *J. Power Sources* **2014**, *258*, 164–181.

(12) Bi, L.; Boulfrad, S.; Traversa, E. Steam Electrolysis by Solid Oxide Electrolysis Cells (SOECs) with Proton-Conducting Oxides. *Chem. Soc. Rev.* **2014**, *43* (24), 8255–8270.

(13) Rossignol, C.; Ralph, J. M.; Bae, J. M.; Vaughey, J. T. $Ln_{1-x}Sr_xCoO_3$ (Ln = Gd, Pr) as a Cathode for Intermediate-Temperature Solid Oxide Fuel Cells. *Solid State Ionics* **2004**, *175*, 59–61.

(14) Jun, A.; Shin, J.; Kim, G. High Redox and Performance Stability of Layered $SmBa_{0.5}Sr_{0.5}Co_{1.5}Cu_{0.5}O_{5+\delta}$ Perovskite Cathodes for Intermediate-Temperature Solid Oxide Fuel Cells. *Phys. Chem. Chem. Phys.* **2013**, *15* (45), 19906–19912.

(15) Myung, J.; Neagu, D.; Miller, D. N.; Irvine, J. T. S. Switching on Electrocatalytic Activity in Solid Oxide Cells. *Nature* **2016**, *537*, 528–531.

(16) Chen, T.; Liu, M.; Yuan, C.; Zhou, Y.; Ye, X.; Zhan, Z.; Xia, C.; Wang, S. High Performance of Intermediate Temperature Solid Oxide Electrolysis Cells Using $Nd_2NiO_{4+\delta}$ Impregnated Scandia Stabilized Zirconia Oxygen Electrode. *J. Power Sources* **2015**, *276*, 1–6.

(17) Gan, Y.; Zhang, J.; Li, Y.; Li, S.; Xie, K.; Irvine, J. T. S. Composite Oxygen Electrode Based on LSCM for Steam Electrolysis in a Proton Conducting Solid Oxide Electrolyzer. *J. Electrochem. Soc.* **2012**, *159* (11), F763–F767.

(18) He, F.; Song, D.; Peng, R.; Meng, G.; Yang, S. Electrode Performance and Analysis of Reversible Solid Oxide Fuel Cells with Proton Conducting Electrolyte of $BaCe_{0.5}Zr_{0.3}Y_{0.2}O_{3-\delta}$ *J. Power Sources* **2010**, *195* (11), 3359–3364.

(19) Bidrawn, F.; Kim, G.; Corre, G.; Irvine, J. T. S.; Vohs, J. M.; Gorte, R. J. Efficient Reduction of CO_2 in a Solid Oxide Electrolyzer. *Electrochem. Solid-State Lett.* **2008**, *11* (9), B167–B170.

List of Publications

1. **Areum Jun**, Junyoung Kim, Guntae Kim "Novel hydrogen production system: Dual Solid Oxide Electrolyzer" (2016) (To be submitted)
2. **Areum Jun**, Junyoung Kim, Jeeyoung Shin, and Guntae Kim,* "Achieving High Efficiency and Eliminating Degradation in Solid Oxide Electrochemical Cells Using High Oxygen-Capacity Perovskite" ***Angewandte Chemie Int. Ed.*** 55 (2016) 12512. ***This paper was selected the Hot Papers.***
3. **Areum Jun**, Junyoung Kim, Jeeyoung Shin, and Guntae Kim,* "Perovskite as a cathode material: A review of its role in the highly reliable SOFC technology" ***ChemElectroChem*** 3 (2016) 511.
4. Chaehyun Lim, **Areum Jun**, Hongil Jo, Kang Min Ok, Jeeyoung Shin, Young-Wan Ju* and Guntae Kim* "Influence of Ca-doping in layered perovskite $PrBaCo_2O_{5+\delta}$ on the phase transition and cathodic performance of a solid oxide fuel cell" ***J. Mater. Chem. A.*** 4 (2016) 6479.
5. Donghwi Jeong, **Areum Jun**, Young-Wan Ju, Junji Hyodo, Jeeyoung Shin, Tatsumi Ishihara, Tak-Hyoung Lim* and Guntae Kim* "Investigation of $LnBa_{0.5}Sr_{0.5}Co_{1.5}Fe_{0.5}O_{5+\delta}$ (Ln = Pr, Sm, Gd) in terms of structural, electrical, and electrochemical characteristics as an IT-SOFC cathode material" ***Energy Technology*** (2016) *Online published*
6. **Areum Jun**, Seonyoung Yoo, Young-wan Ju, Junji Hyodo, Sihyk Choi, Hu Young Jeong, Jeeyoung Shin, Tatsumi Ishihara, Tak-hyoung Lim*, and Guntae Kim* "Correlation between fast oxygen kinetics and enhanced performance in Fe doped layered perovskite cathode for solid oxide fuel cells" ***J. Mater. Chem. A*** 3 (2015) 15082. ***This paper was selected the 2015 Journal of Materials Chemistry A Hot Papers.***
7. **Areum Jun**, Young-wan Ju, and Guntae Kim,* "Solid oxide electrolysis: Concluding remarks" ***Faraday Discuss.*** 182 (2015) 519.
8. Seona Kim, **Areum Jun**, Ohhun Kwon, Junyoung Kim, Seonyoung Yoo, Hu Young Jeong, Jeeyoung Shin and Guntae Kim*, "Nanostructured Double Perovskite Cathode With Low Sintering Temperature For Intermediate Temperature Solid Oxide Fuel Cells" ***ChemSusChem*** 8(18) (2015) 3153.
9. Erik Enriquez, Xing Xu, Shanyong Bao, Zach Harrell, Chonglin Chen,* Sihyuk Choi, **Areum Jun**, Guntae Kim, Myung-Hwan Whangbo "Catalytic Dynamics and Oxygen Diffusion in Doped $PrBaCo_2O_{5.5+\delta}$ Thin Films" ***ACS Appl. Mater. Interfaces*** 7 (2015) 24353.
10. **Areum Jun**, Tak-hyoung Lim, Jeeyoung Shin*, and Guntae Kim* "Electrochemical properties of B-site Ni doped layered perovskite cathodes for IT-SOFCs" ***Int. J. Hydrogen Energy*** 39(35) (2014) 20791.

11. Young-Wan Ju,† **Areum Jun**,† Atsushi Inoishi, Shintaro Ida, Tak-hyoung Lim, Guntae Kim*, and Tatsumi Ishihara*, "Growth of thin-film layered perovskite cathodes by pulsed laser deposition and their electrochemical studies in IT-SOFCs" ***J. Electrochem. Soc.*** 161 (2014) F698. *(Authors Young-Wan Ju and Areum Jun contributed equally to this work.)*

12. Sivaprakash Sengodan, Sihyuk Choi, **Areum Jun**, Tae Ho Shin, Hu Young Jeong, Jeeyoung Shin, John Irvine, Guntae Kim*, "Layered Oxygen Deficient Double Perovskite as an Efficient and Stable Anode for Direct Hydrocarbon SOFCs", ***Nature Materials*** 14 (2014) 205.

13. Seonyoung Yoo, **Areum Jun**, Dorj Odkhuu, Young-Wan Ju, Junji Hyodo, Hu Young Jeong, Noejung Park, Jeeyoung Shin, Tatsumi Ishihara, Guntae Kim*, "A New Class for Double Perovskite Cathode for Low Temperature Solid Oxide Fuel Cells" ***Angewandte Chemie Int. Ed.*** 53(48) (2014) 13064.

14. Junyoung Kim, **Areum Jun**, Jeeyoung Shin, Guntae Kim*, "Effect of Fe doping on layered $GdBa_{0.5}Sr_{0.5}Co_2O_{5+\delta}$ perovskite cathodes for intermediate temperature solid oxide fuel cells" ***J. Am. Ceram. Soc.*** 97 (2014) 651.

15. Junyoung Kim, Sihyuk Choi, **Areum Jun**, Hu Young Jeong, Jeeyoung Shin, Guntae Kim*, "Chemically stable perovskites as a cathode material for IT-SOFCs: La doped $Ba_{0.5}Sr_{0.5}Co_{0.8}Fe_{0.2}O_{3-\delta}$" ***ChemSusChem*** 7 (2014) 1669.

16. Seona Kim, Sihyuk Choi, **Areum Jun**, Jeeyoung Shin*, and Guntae Kim*, "Scale-Down and Sr-Doping Effects on $La_4Ni_3O_{10-\delta}$–YSZ Nanocomposite Cathodes for IT-SOFCs" ***J. Electrochem. Soc.*** 161(14) (2014) F1468.

17. **Areum Jun**, Jeeyoung Shin, Guntae Kim*, "High redox and performance stability of layered $SmBa_{0.5}Sr_{0.5}Co_{1.5}Cu_{0.5}O_{5+\delta}$ perovskite cathodes for intermediate-temperature solid oxide fuel cells" ***Phys. Chem. Chem. Phys.*** 15 (2013) 19906.

18. **Areum Jun,** Seonyoung Yoo, Oh-hun Gwon, Jeeyoung Shin, Guntae Kim*, "Thermodynamic and electrical properties of $Ba_{0.5}Sr_{0.5}Co_{0.8}Fe_{0.2}O_{3-\delta}$ and $La_{0.6}Sr_{0.4}Co_{0.2}Fe_{0.8}O_{3-\delta}$ for intermediate-temperature solid oxide fuel cells" ***Electrochim. Acta*** 89, (2013) 372.

19. Sihyuk Choi, Seonyoung Yoo, Jiyoun Kim, Seonhye Park, **Areum Jun**, Sivaprakash Sengodan, Junyoung Kim, Jeeyoung Shin, Hu Young Jeong, YongMan Choi, Guntae Kim*, Meilin Liu* "Highly efficient and robust cathode materials for low-temperature solid oxide fuel cells: $PrBa_{0.5}Sr_{0.5}Co_{2-x}Fe_xO_{5+\delta}$" **Scientific Reports** 3 (2013) 2426.

20. **Areum Jun**, Junyoung Kim, Jeeyoung Shin, Guntae Kim*, "Optimization of Sr content in layered $SmBa_{1-x}Sr_xCo_2O_{5+\delta}$ perovskite cathodes for intermediate-temperature solid oxide fuel cells" ***Int. J. Hydrogen Energy*** 27 (2012) 18381.

Acknowledgements

First and foremost, I would like to gratefully and sincerely thank my advisor Professor Dr. Guntae Kim, he has been a tremendous mentor for me. I appreciate all his contributions of time, sincere advices, ideas, enormous knowledge and experience, and most importantly, the continuous support of my Ph.D study and research. The joy and enthusiasm he has for his research was motivational for me, even during tough times in the Ph.D. pursuit.

Besides my advisor, I would like to thank the all of my committee members: Prof. Jong-Beom Baek, Prof. Hyun-Kon Song, Prof. JunHee Lee, and Prof. Jeeyoung Shin for their valuable time, ideas, encouragement, and insightful comments.

My great co-advisor, Prof. Jeeyoung Shin has been always there to listen and give advice. I am deeply grateful to him for the long discussions that helped me sort out the technical details of my research.

The members of the "gunslab" have contributed immensely to my personal and professional time at UNIST. I am greatly indebted to the members of the gunslab, Dr. Seonyoung Yoo, Dr. Sivaprakashi Sengodan, Dr. Sihyuk Choi, Jiyoun Kim, Seonhye Park, Junyoung Kim, Seona Kim, Ohhun Gwon, Changmin Kim, Ohhun Kwon, Chaehyun Lim, Donghwi Jeong, Sangwook Joo, Chanseok Kim, Gihyun Kim, Jungwon Kim, Dr. Yunfei Bu, and Prof. Young-wan Ju, for all their helps during my studies.

Though only my name appears on the cover of this thesis, a great many people have contributed to its production. I owe my gratitude to all those people who have made this thesis possible and because of whom my graduate experience has been one that I will cherish forever.

Lastly, and most importantly, I would like to appreciate my parents for all their love, encouragement, understanding, and support.